Influence of Inflow Distortions on the Vibrations of a Modern Low Pressure Turbine

Doctoral Thesis

In fulfilment of the requirements for the academic degree
Doktor der technischen Wissenschaften (Dr. techn.)

Loris Simonassi

Institute for Thermal Turbomachinery and Machine Dynamics
Faculty of Mechanical Engineering
Graz University of Technology

Graz, February 2021

First Expert:
Priv.-Doz. Dipl.-Ing. Dr.techn. Andreas Marn

Second Expert:
Prof. Pietro Zunino

To my Mother and Father

STATUTORY DECLARATION

I declare that I have authored this thesis independently, that I have not used other than the declared sources/resources, and that I have explicitly marked all material which has been quoted either literally or by content from the used sources.

EIDESSTATTLICHE ERKLÄRUNG

Ich erkläre an Eides statt, dass ich die vorliegende Arbeit selbstständig verfasst, andere als die angegebenen Quellen/Hilfsmittel nicht benutzt, und die den benutzten Quellen wörtlich und inhaltlich entnommenen Stellen als solche kenntlich gemacht habe.

Graz, am .....

.....

Loris Simonassi

ABSTRACT

Aero engine and gas turbine design is continuously improving in order to achieve higher efficiency and reduce the weight, the fuel consumption and the noise emissions. The increase of the turbine inlet temperatures, higher blade loading, together with the use of lighter materials and the down-sizing of the components, reducing axial gaps between vane/blade rows and between stages, are fundamental to achieve these goals. As a consequence, the inlet conditions of a modern low pressure turbine (LPT) present significant flow non-homogeneities, which can have direct consequences on both its aerodynamic performance and vibrations. The rise in turbine entry temperatures and pressure ratios needed to achieve higher efficiencies and power output requires an increase of cooling and purge flow injections, leading to the generation of strong temperature distortions at the inlet of the LPT. Additionally, the stronger interaction between engine components due to the drastic decrease of axial spacing and to the reduction of the stage count facilitates the propagation of circumferential distortions of total pressure and temperature.

This work presents the results of an experimental investigation on the influence of total pressure and temperature inflow distortions on the aerodynamics and on the vibrations of a low pressure turbine stage. Measurements at a stable engine relevant operating condition and during transient operation were carried out in a one and a half stage subsonic turbine test facility at the Institute of Thermal Turbomachinery and Machine Dynamics at Graz University of Technology. Steady and unsteady aerodynamic measurements were performed with a five-hole-probe (5HP) and a fast response aerodynamic pressure probe (FRAPP) respectively, while the LPT rotor vibration data were acquired using strain gauges applied on different blades, in combination with a telemetry system.

Localised total pressure distortions with different intensities were generated upstream of the stage at two different axial distances from the stage inlet and in three different azimuthal positions relative to the stator vanes. With regards to the study of total temperature inlet non-homogeneities, a series of total temperature disturbances were generated upstream of the stage through the localised injection of air at different mass flow and temperature, ranging from 30% to 130% of the nominal inlet temperature.

The aerodynamic interactions between the stator and rotor rows and the circumferential perturbation were studied through the identification of the main structures constituting the flow field. This showed that the steady and unsteady alterations created by the distortion in the flow field lead to modifications of the rotor vibration characteristics. The rotor vibrations were also strongly influenced by the alterations created by the circumferential temperature perturbation in the flow. In particular, the temperature of the distortion was found to influence directly the amplitude of the rotor blade forced response. Hence, this work shows that important aerodynamic and aero-elastic effects are linked to the presence of total pressure and temperature distortions in the inlet flow field of an LPT stage.

ACKNOWLEDGEMENTS

This work would not have been possible without the help of my friends, family, and colleagues. While the list of people who have supported me during the past years is too long, I would like to take this opportunity and thank a few of them.

Prof. Franz Heitmeir and Pof. Andreas Marn for supervising this work and for guiding me during the last four years in my PhD journey.

Prof. Pietro Zunino and Prof. Davide Lengani, for agreeing to review this thesis and for their accurate and thorough work.

Dr. Peter Pirker and Prof. Emil Göttlich, who operated the compressor facility for more than 100 test runs performed during the experimental campaign. Manuel Zenz, for sharing not only the work in the lab with me but also the trips (and hotel rooms) to conferences and for being a great flatmate. Simon Pramstrahler and Philipp Bruckner also deserve a huge thank you for helping me with the measurements. Martin and Florian, for their valuable work in the workshop. Lukas Wiesinger, thank you for helping me with the more technical aspects of my work in the workshop and for being an amazing person. Stefan, Zeno, Felix, Patrick, Marios, Ena, Melanie, Magdalena, Asim, Franz and then the "Italian Connection" Federica and Filippo, thank you, the support from all of you has been invaluable during the last years.

Ettore and Riccardo, thank you for being a part of "Il Partito dalla Crocca", for the endless bike rides, for the haute cuisine dinners, for the afternoons at the park and the evenings at Parkhouse, for the crazy trips, for being my little family in Graz. You have taught me a lot. I like to think that we have grown up together. That means a lot to me. Matteo, even if it was only for a short time, you were a part of our group and you will always be a member of the party. It was a great ride!

Chiara and Tommaso, thank you for deciding to share the lockdown with me. We supported each other during this very dark time. Thank you for the yoga sessions, for the board-games, for the reading, the movie nights, for the trips with Franco and for letting me win the “Covid-Games”. Thank you for inspiring my curiosity. I am very proud of our friendship.

Gianni, Viki, Chiara, Sandra, Matia, Magda, Fede, thank you for being an amazing group of friends, for bringing a spark of Spaß in my life. Thank you for the great time we spent together.

Jo, thank you for introducing me to the beautiful world of Buschenschanks, lakeside camping trips and “avo-on-toast”. Thank you for sharing with me the genuine passion and enthusiasm with which you approach life.

Infine, grazie ai miei genitori Elena ed Egidio, a cui il mio lavoro é dedicato. Grazie perché siete sempre stati al mio fianco anche da lontano. Grazie per supportarmi con il vostro ascolto e con i vostri consigli, e con pacchi pieni di salsa e di marmellata. Siete la mia ispirazione.

NOMENCLATURE

ABBREVIATIONS

BLI	Boundary-Layer Ingesting
BPF	Blade Passing Frequency
BPP	Blade Passing Period
CFD	Computational Fluid Dynamics
CS	Compressor Station
CV	Counter rotating Vortex
E	edge-wise bending
EGV	Exit Guide Vane
EO	Engine Order
F	FLAp-wise bending
FE	Finite Elements
FRAPP	Fast Response Pressure Probe
HCF	High Cycle Fatigue
HP	High Pressure
HPT	High Pressure Turbine
HSV	Hub Secondary Vortex
HV	Horseshoe Vortex
IBPA	Inter Blade Phase Angle
IGV	Inlet Guide Vane
ITTM	Institute For Thermal Turbomachinery and Machine Dynamics
LDA	Laser Doppler Anemometry
LE	Leading Edge
LEO	Low Engine Orders
LP	Low Pressure
LPT	Low Pressure Turbine
ND	Nodal Diameter
NOX	Nitrogen Oxides
PID	Proportional Integral Derivative
PS	Pressure Side
PV	Passage Vortex
RANS	Reynolds Averaged Navier-Stokes
RMS	Root Mean Square

SDOF	Single Degree of Freedom
SG	Strain Gauge
SS	Suction Side
STTF	Subsonic Test Turbine Facility
T	Torsion
TCF	Turbine Centre Frame
TE	Trailing Edge
TEC	Turbine Exit Casing
TEGV	Turbine Exit Guide Vane
TLV	Tip Leakage Vortex
W	Wake

SYMBOLS

Latin

A,B,C	Numerical constant
B	Number of rotor blades
C	Damping
c	Speed of sound
D	Diameter
E	Young's module
f	Frequency
F	External force
f	frequency
h	Numerical constant
h	Enthalpy
I	Flexural inertia
k	Numerical constant
k	Elastic constant
M	Mass
m	Mode order
Ma	Mach number
n	Number of samples
n	Rotational speed
nn	Number of samples per revolution
P	Pressure
q	Modal movement
Q	Resistivity

R	Gas constant
r	Radius
R	Resistance
Re	Reynolds number
s	Entropy
T	Temperature
t	Time
U	Voltage
V	Number of vanes
v	Particle velocity
w	Flexural movement
x	Movement
X	Amplitude of Fourier coefficients
x,y,z	Cartesian coordinates
$\dot{m}$	Mass flow
$c_{Y,ijk}$	Calibration constants
l	Length
St	Strouhal's number
θ_{Dist}	Distortion Thickness
V	Volume of the blade
Φ	Modal matrix
p	Distributed load
E_{strain}	Strain energy
δ_{ijk}	Kroneker's delta
C_{pt}	Total pressure coefficient
H	Transfer function

Greek

α	Yaw angle
∂	Partial derivative
β	Consant
γ	Pitch angle
Δ	Variation
ε	Strain
ν	Poisson's ration
ρ	Density
σ	Stress
Ω	angular velocity

ωr	Natural frequency
Ψ	Mode shapes
φ	Eigenmodes
ζ	Critical damping factor

Subscript

a	samples in the original signal
Dist	Distortion
j	injection
m	mode order
period	revolutions in original period
r	radial
RMS	root mean square
s	sampling
t	total
t	tangential
x	axial

Superscript

‘	fluctuation
-	average
<>	periodic

TABLE OF CONTENT

1. INTRODUCTION

Aviation has drastically transformed the way we perceive the world and how we inhabit it, opening up a range of opportunities, stimulating globalisation and reducing distances and transportation time. The introduction of jet engines further facilitated fast transportation of goods and people, promoting enormous social and economic progress. Consequently, the volume of air traffic and the number of passengers have been exponentially increasing globally from the end of WWII, as shown in FIGURE 1.1. To accompany this growth rate, the price of kerosene has remained stable in recent years. In order to keep up with the rising demand for new airplanes, manufactures are faced with ever increasing orders within the next twenty years. However, as everyone knows, the socio-economic benefits of the growth of the aviation industry are offset by the emission of greenhouse gases, in particular carbon dioxide and NOx. A visualisation of the carbon dioxide emission from aviation is shown in FIGURE 1.2.

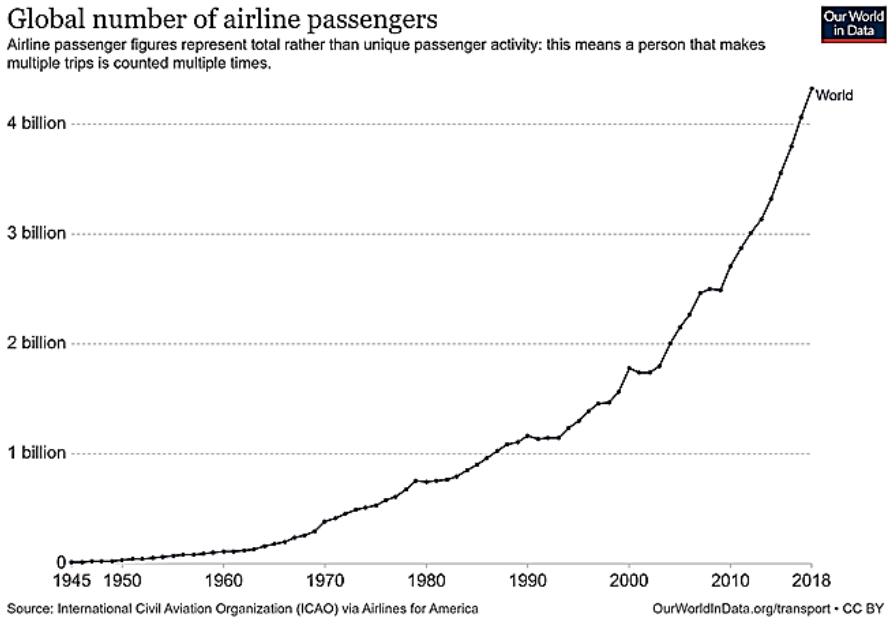

FIGURE 1.1: Global number of airline passengers. From [1]

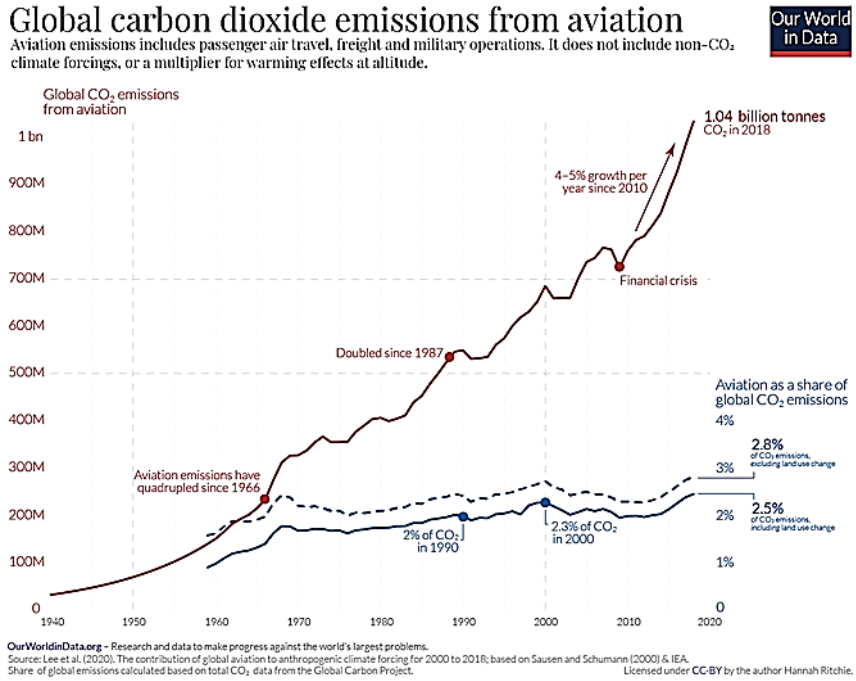

FIGURE 1.2: Global carbon dioxide emissions from aviation. From [2]

This kind of forecast was severely changed by the economic and social crisis caused by the spread of the pandemic of the new Coronavirus SARS-CoV-2, which led to the closure of national borders and the cancellation of almost all flights for a long period, reducing air traffic to an overwhelming historical low. The recession and insecurity caused by the pandemic in the global economic system is also reflected in the aviation sector. However, it is important to emphasise that although reductions in travel have led to lower emissions globally, once the pandemic is overcome, a return to normality is desirable within the industry. It then becomes imperative that resources directed to post-Covid recovery are also used to accelerate action against the climate crisis, a threat no less frightening than this pandemic. If governments are planning to spend incredible resources to kick-start economic recovery, it is only fair that these resources go to building fairer, greener and more sustainable societies and industries.

Substantial efforts to reduce the environmental impact of the aviation industry has been made in the past years. With the aim of reducing man-made climate change, following the commitments made by nations at the 2015 UN climate conference, the International Civil Aviation Organization approved an agreement in October 2016 stipulating that it would not only achieve carbon-neutral growth, but also reduce global aviation emissions in 2035 by 80% compared to 2020. The implementation of the offset and emission reduction programmes contemplated by this agreement will lead to significant competitive advantages for aircraft operators with a smaller carbon footprint.

In line with the international community's commitment to reducing emissions and tackling the climate crisis, the International Air Transportation Association has also developed a roadmap based on the previous emission targets formulated in the European Commission's 'Flightpath 2050' vision. The aim of the commission's commitment is to support and develop the European aeronautics industry, improving knowledge and advanced production capabilities, and in doing so define and shape a sustainable future.

As can be seen in the chart depicted in FIGURE 1.2, since 1950, aviation CO2 emissions increased almost nine-fold; and have reached in 2018 a level 5 times higher than 1960. However, even though emissions from aviation have increased a lot over the past half-century, the volume of air travel has in reality increased even more rapidly. The substantially slower growth of emissions means that efficiency of aviation has seen considerable improvements. In the chart depicted in FIGURE 1.3 it is possible to observe the increase in global airline traffic since 1950, and the quantity of CO2 emitted per revenue passenger kilometre travelled (a measure of the number of passengers multiplied by the travelled distance), which ultimately represents aviation efficiency. The data show that aviation is around twenty

times more efficient in 2018 than in 1950 and eleven times than in 1960, meaning that aviation efficiency increased has seen massive improvements over the past 50 years.

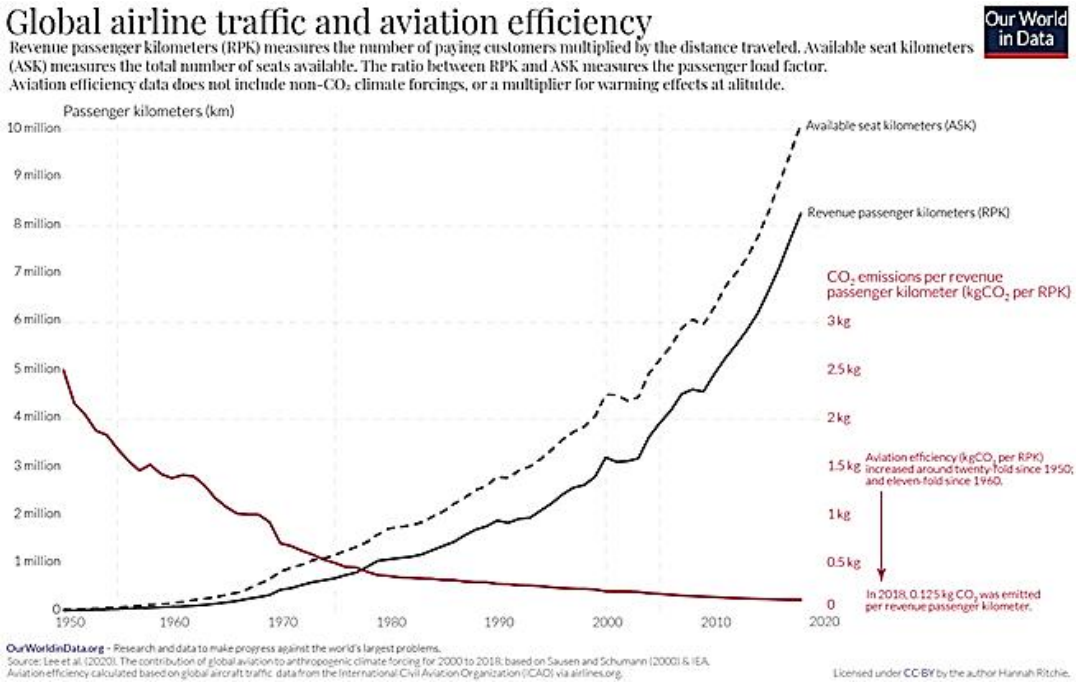

FIGURE 1.3: Global airline traffic and aviation efficiency. From [2]

The innovations introduced in the last years can be mainly classified into three categories: Measures to increase the thermodynamic cycle efficiency of the engine, measures to increase the engine's propulsive efficiency and measures to optimize the engine weight and its integration with the airframe. In a turbofan engine, the cycle efficiency is a measure of how efficiently the chemical energy available in the fuel is converted in mechanical energy to power the fan, whereas the propulsive efficiency measures how efficiently the energy contained in the fuel is converted into kinetic energy of the vehicle.

In order to optimise cycle efficiency, the focus in recent years has been on increasing the combustor outlet temperature and consequently the turbine inlet temperature, and on reducing the aerodynamic losses inherent in turbomachines. This requires the implementation of advanced cooling methods, as gas temperatures exceed the melting temperature of the turbomachine blades. In addition to the possibility of covering the blades with protective materials, the use of secondary cooling air injections for blades and cavities has become a widespread practice. In addition, the increase in computing power has recently made it possible to numerically optimise the three-dimensional shapes of the blades, allowing losses to be optimised. However, it is expected that the improvements achievable for a highly optimised system such as a turbofan engine may be limited.

With regard to the search for innovations to optimise propulsive efficiency, the most promising approach is the development of solutions to improve fan performance. Since the viscous losses created by a high velocity jet with a low mass flow rate are greater than the losses of a high mass flow rate jet with the same impulse and therefore a lower average velocity, it is possible to improve propulsive efficiency by increasing the mass flow rate so as to reduce the velocity required to obtain an equal impulse. As a result, the bypass ratio, which represents the amount of air accelerated by the fan outside the engine core relative to the mass flow of the core, has been improved from the 1:1 typical of engines produced in the 1960s to its current level of 12:1. Unfortunately, the increase in bypass mass flow results in a larger annulus area, which leads to a higher fan tip speed. In addition, the increase in diameter also results in an increase in the external surface area of the nacelle, generating a further problematic increase in drag. This problem can be solved by considering the open rotor concept, which consists of two rows of counter-rotating fans, completely outside the nacelle. While promising flight tests had already been

carried out in the 1970s, problems relating to the increased noise emission due to the absence of fan casing prevented this solution from becoming widespread. Additionally, it should not be forgotten that the mechanical loading of the fan blade root increases with larger fan diameters. Therefore, a reduction of the centrifugal forces is necessary e.g. by reducing rotational speed of the fan shaft. However, in traditional architectures, the fan and the LPT, a component that requires high rotational speed to achieve high efficiency, are mounted on the same shaft.

A possible solution for reducing the speed of rotation of the fan is to decouple its speed from that of the low-pressure turbine. In fact, if to improve the propulsive efficiency of the fan it is important to reduce its speed, the efficiency of the low-pressure turbine instead increases as the speed of rotation rises. It is therefore clear that separating the two components can lead to an overall improvement. To this purpose, the gear-driven turbofan concept was developed in the 1970s. This design alleviates the trade-off between desirable low fan speeds and high low-pressure turbine speeds by introducing a gearbox between the fan and the low-pressure shaft of the engine. Despite the various advantages of this particular design, it was not until 2016 that a geared turbofan engine for single-aisle aircraft, made by Pratt & Whitney with the PW1000G series, was launched. Reliability, weight reduction and efficiency are the key factors of this technology. A comparison between a traditional direct drive design and a geared turbofan is presented in FIGURE 1.4. The advantages of a gear-driven fan system become clear when comparing the two sections: it is evident that the number of stages as well as the number of parts in the low-pressure section is essentially reduced by half. Specifically, in this case the number of stages in the low-pressure turbine is reduced from nine to three. Consequently, the mass of the gearbox is compensated and the maintenance cost of the LPT is also reduced. This type of design has enabled the manufacturer to achieve a reduction in fuel consumption of up to 20%, according to the manufacturer. In addition, another benefit of the fan speed decrease is the reduction of the aircraft's noise emission up to 75% compared to previous generation engines [3].

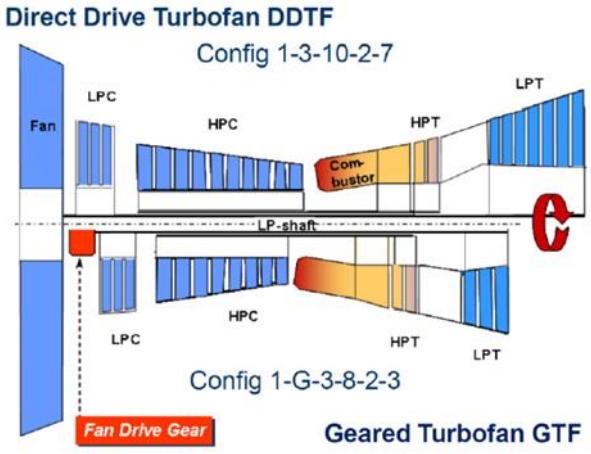

FIGURE 1.4: Comparison between the cross sections of a conventional direct drive turbofan and a geared turbofan engine. Figure from [3]

As clearly seen in FIGURE 1.4, the adoption of geared turbo fan designs leads to a drastic reduction of dimensions and weight.

Another engine component that is constantly undergoing a great deal of research and development efforts aimed at the improvement of performance is the Turbine Centre Frame. In particular, this component is located between the high-pressure turbine and the low-pressure turbine and has the purpose of facilitating the passage of fluid from the diameter of the HPT to the larger diameter of the LPT through its particular S shape. There has been a growing interest in recent years to increase the engines bypass ration through shorter ducts with more aggressive aerodynamic. One way to achieve such improvements is to eliminate the row of IGVs positioned in front of the first LPT rotor, and to integrate a series of turning vanes into the TCF, which would now act not only as a diffuser, but would also direct the flow in the optimal direction for the downstream rotor blades. This particular

configuration is named Turbine Vane Frame (TVF). A sketch representing the evolution of the TCF with the integration of turning vanes is shown in the FIGURE 1.5. This solution is particularly challenging because it increases the aerodynamic load on the vanes in the duct and favours the generation of stronger wakes. However, from the sketches in the figure it is possible to understand that a major advantage of an aerodynamically aggressive TCF with vanes is the reduction of LPT components, which results in reduced weight and engine dimensions.

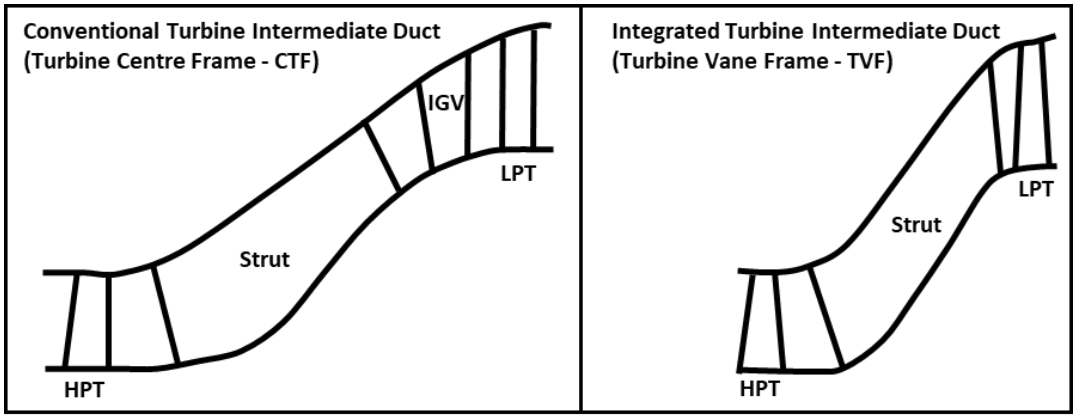

FIGURE 1.5: Schematic view of a traditional TCF (left) and a modern TVF (right).

All the solutions aimed at improving efficiency and reducing weight, such as increasing the turbine inlet temperatures, increasing the bypass ratio, geared turbofans and integrating vanes into the TCF struts, have the problem that they can generate localised flow disruptions and favour propagation through the machine. In fact, the increase in turbine inlet temperature generates an increase in the intensity of the hot-streaks generated by the combustor, which therefore propagate deeper through the HPT reaching LPT. Another consequence of the increase in operating temperatures is the need to introduce solutions for cooling the blades, through e.g. film cooling, and the cavities, through purge flows. Both cause the generation of localised zones characterised by flow distortions. Concerning the search for an ever-increasing bypass ratio, the introduction of the S-shaped duct causes the generation of separations and wakes, which modify the flow at the inlet of the low-pressure turbine. With regard to the geared turbofan, the possibility of reducing the number of turbine stages and the space between them causes the possibility of more penetration by the hot-streaks coming from the combustor and the distortions due to cooling flows and separations in the TCF, together with the increase in the blade load, which increases the interaction between rotors and stators, generating effects that differ from ideal conditions. Similarly, as for the geared turbo fan, the search for dimensions and weight reduction led to the development of the TVF, which has the characteristic of having more turning in the vanes of the duct, generating distortions at the low-pressure rotor inlet. In addition, the need to design more aggressive ducts to reduce dimensions and limit weight means increasing the possibility of the fluid not being able to follow the shape of the duct, resulting in separations and therefore localised distortions in the flow at the LPT inlet.

It can therefore be said that the design of modern aircraft engines is aimed at achieving high efficiency and low weight in order to reduce fuel consumption and therefore CO2 emissions. The use of lighter materials and component downsizing is key to achieving these goals. As a consequence of downsizing, the shortening of axial distances between engine components can promote the propagation of localized distortions of total pressure and temperature through the machine. The scope of this work is to study the effects of inlet flow distortions on the aerodynamic and aeroelastic performance of a modern low pressure turbine stage. In particular, a thorough experimental activity regarding the total pressure, the total temperature inlet distortion and the combination between them were carried out at the Subsonic Test Turbine Facility for Aerodynamic, Aeroacoustic and Aeroelastic Investigations (STTF-AAAI) located at the Institute of Thermal Turbomachinery and Machine Dynamics of Graz University of Technology. The measurement campaign was carried out by means of steady and unsteady

aerodynamic measurements. Additionally, the rotor blade vibrations were studied for all the tested configurations by strain gauges applied on the rotor blade surface.

Concerning the total pressure inlet distortion (P_t distortion), the focus lies on the forced response of the LPT rotor blading under the influence of inlet flow distortion. Aerodynamic and vibration experimental data, acquired during steady and transient operations are used to determine what is the nature and what are the effects onto the vibrations of the rotor blades of a circumferential total pressure inhomogeneity, generated at the stage inlet. Moreover, the effects of the azimuthal position of the total pressure inflow distortion relative to the stator vanes ("Distortion-Stator-Clocking") on the propagation of the flow disturbances through a low pressure turbine stage and on the resulting rotor blade vibratory response are investigated. With regards to inlet distortions of total temperature (T_t distortion), a series of experimental investigations characterised by localised flow injection at different temperatures and different injection air mass flows were performed. This thesis focusses on the generation of total temperature distortions at the inlet of a modern low pressure turbine stage and on the propagation of such inflow disturbances through the stage, with a particular focus on both the aerodynamic and aero-elastic performance of the turbine. Finally, the total temperature and total pressure distortions combination (T_t and P_t distortion) was also investigated. The temperature and pressure distortions were generated at the inlet of the stage in order to study the effects of their combination on the propagation of the inhomogeneity through the stage and the modifications determined on turbine performance and rotor blade vibratory behaviour.

1.1 OBJECTIVE OF THE RESEARCH

With regards to the generation and propagation of inlet distortions through a LPT stage, and to the effects that these inhomogeneities have on the machine aerodynamic and aeroelastic performance, the research presented in this thesis is focused addressing the following objective using extensive experimental investigations.

- Generate total pressure and temperature distortions at the inlet of a one and a half representative low pressure turbine stage, with the possibility to modify the intensity of the distortions, on their axial and azimuthal positions and on their number.

- Characterize stage performance with clean inflow. In particular, the aim of this section of project is to study the stage aerodynamics at the inlet and after the rotor row, as well the blade vibrations in nominal operating conditions, with clean inflow.

- Study the nature and the effects of a circumferential total pressure inhomogeneity generated right upstream of the LPT stage onto the vibrations of the rotor blades. Additionally, define the effect of clocking on the propagation and on the effects of the inflow pressure distortions.

- Research the effects of the non-uniform temperature circumferential distribution on the stage aerodynamics and provide insights on the relationship between characteristics of the inhomogeneity such as the intensity of the temperature distortion on the vibrations of the rotor blades.

- Combine the generation of total pressure and temperature distortions at the stage inlet with the aim to study the effects this combination on the propagation of the inhomogeneity through the stage and the modifications determined on turbine performance and rotor blade vibratory behaviour.

2. FUNDAMENTALS

2.1 AEROELASTICITY

Vibration-related failures of structures are very important in mechanical engineering. Problems may arise as a sudden failure or can be due to structural fatigue and they may be related to the presence of flow of fluid around the structure. This effect in particular is referred to as "flow induced vibrations", "flow-structure interaction" or "fluid-elasticity". It has been extensively documented that flow induced vibrations are of major concern in modern engineering design, as high stresses can be caused by the interaction between a vibrating structure and the continuously changing flow characteristics, leading to fatigue failure. Especially in aeronautics, failing to consider flow induced vibrations can have a significant influence on the operability of the final product.

Aeroelasticity is the science which treats of the interaction of inertial, elastic and aerodynamic forces. In 1978 Collar [4] defined the simplest form of aeroelastic saying: “if an increase in aerodynamic load distorts a structure in such manner that the incidence changes and increases the aerodynamic load further, then we have an aeroelastic problem”. Previously, in 1946 he described the aeroelastic interaction for the first time graphically, defining a “triangle of forces”, still known today as Collar-Triangle, in which the inertial, elastic and aerodynamic forces each occupies a vertex, as shown in FIGURE 2.1.

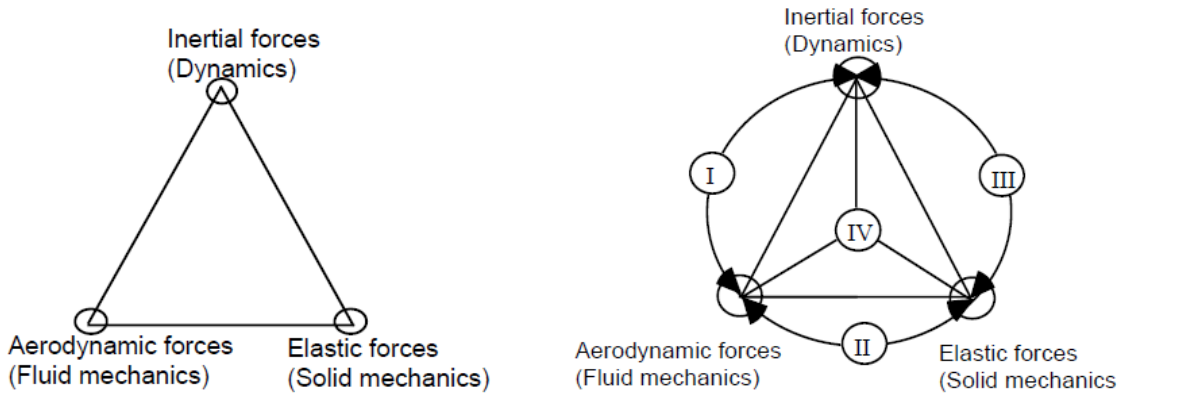

a: Forces considered [Collar, 1946, p. 62]. b: Relations between the different forces

I: Rigid-body aerodynamics; Stability; Control
II: "Static" aeroelasticity
III: Mechanical vibrations; Impact
IV: "Dynamic" aeroelasticity

FIGURE 2.1: Collar’s triangle of forces. From [5].

In the case aerodynamic and inertia forces acting together, the loading on the structure is considered in its static aspects (domain "I"). If the aerodynamic and elastic forces are considered together, the resulting problem is defined as a "static aeroelasticity" (domain "II"). A third domain ("III") contemplating the relationship between the inertial and elastic forces is referred to mechanical vibrations. Finally, a problem considering the interaction between all three forces (aerodynamic, inertia and elastic forces), is part of the "dynamic" aeroelasticity domain ("IV").

2.1.1 CLASSIFICATION OF DIFFERENT TYPES OF AEROELASTIC PHENOMENA

The flow through turbomachines is associated with many different time-dependent phenomena. The main aspects of disturbances when the flow passes through a turbomachine blade row will be extensively described in section 3.1 Regarding the relation between aerodynamic phenomena and blade mechanics, the unsteady effects influencing the flow through the blade rows and the highly time-dependent approaching inflow that characterise all the blade rows rotating relatively to each other are the main sources of excitation. Moreover, potential flow interactions between passing blade rows can also determine strong pressure amplitudes patterns, and distortions from the ideal uniform inlet flow are always present (for example from upstream struts, partial flow admissions or combustor-turbine interaction). Tip leakage flows, as well as secondary flow structures develop in the axial direction and interact with wakes of the blade and vanes creating highly distorted flow effects. Furthermore, aero- and thermodynamic gradients in both radial and circumferential direction are responsible for the flow migrations and accumulations. Transonic and supersonic flow originate highly three-dimensional shock structures that can be reflected and interact with the blade and casing boundary layers to create unsteady pressure effects on the blade surface. Finally, flow instabilities can be caused as well by flow separations at large incidence angles, for example in stall and surge conditions.

The interaction of all these time-dependent flow phenomena with the blades can generate vibrational patterns of different shape and amplitude. To all this is added the complication determined by the phenomenon of "self-excited" blade vibrations, i.e. the interaction of uniform and steady flow and a structure vibrating because of one cause or another. While some of the above mentioned phenomena are periodic, others can excite a blade stochastically or have a discrete nature. Finally, All the above phenomena appear with different magnitude at various operating points in a turbomachine.

Regarding the classification as well as definition of vibrations, there is a multitude of formulations in literature. An overview of flow-excited oscillations was given by Holzinger et al. in [6]. A scheme extracted from this work can be found in FIGURE 2.2. Firstly, the main separation within flow-induced blade vibration is between synchronous vibration and nonsynchronous vibration.

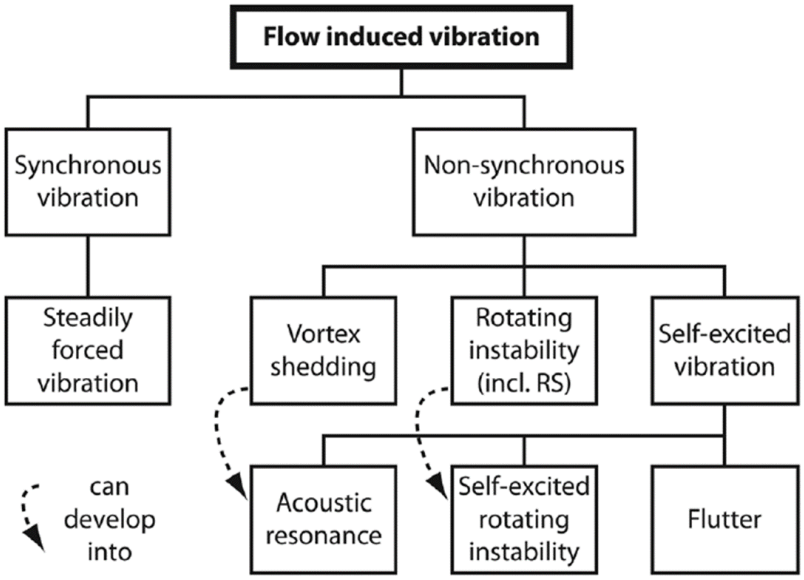

FIGURE 2.2: Flow-induced vibrations. According to [6].

2.1.1.1 SYNCHRONOUS VIBRATION

Synchronous vibration may occur at frequencies that are integer multiples of rotational frequency, called engine orders (EO). Resonance conditions causing peak amplitudes are reached when the speed of the rotor blades crossing a periodically non-uniform flow field determines that the periodic excitation of the non-uniform flow field coincides exactly with the blade eigenfrequency. In practice, steady blade row interaction mechanisms, such as wakes from upstream blade rows and potential fields from downstream blade rows, or non-uniform inflow conditions are the common cause of synchronous vibrations.

The frequency of the engine order excitation can be defined as:

$$f = EO \cdot \frac{n}{60} \tag{2.1}$$

Where EO represents the Engine Order and n the rotational speed in rpm. Considering the excitation due to non-uniform flow field generated by upstream vane/blade rows, substituting EO with the number of stator vanes or rotor blades gives directly the frequency of the excitation at a given rotational speed.

In addition to the effect of single blade or vane rows, also the forcing due to the interaction between blades and vanes generated flow structures are relevant and must be taken into account. According to Schönleitner [7] the characteristics of this excitations can be analysed based on the acoustic theory of Tyler and Sofrin [8], Which will also be discussed in more detail in section 3.1.3. The circumferential pressure patterns in the flow field responsible for this kind of excitation, are defined as a linear combination of the effect of the rotor blades B and the stator vanes V:

$$m = h \cdot B + k \cdot V \tag{2.2}$$

In this formulation the higher harmonic frequencies of the rotor blades are taken into account by the index h (1, 2, 3, etc.), while k represents an integer index ranging from $\pm\infty$.

Consequently, the frequency of the interaction modes can be evaluated extending Equation (2.1) as:

$$f_m = (m) \cdot \frac{n}{60} \tag{2.3}$$

The Campbell diagram is the most commonly used tool for the assessment of synchronous blade vibrations. The Campbell diagram shows the natural frequencies in relation to the rotor speed. This can include both experimental and numerical data. The excitation frequencies can be plotted as Engine Order lines according to Equation(2.1). Being linearly dependent on the speed, he EO excitation is represented as rising straight lines in the diagram as highlighted by EO1, 2 and 4 in the Campbell diagram depicted in FIGURE 2.3.

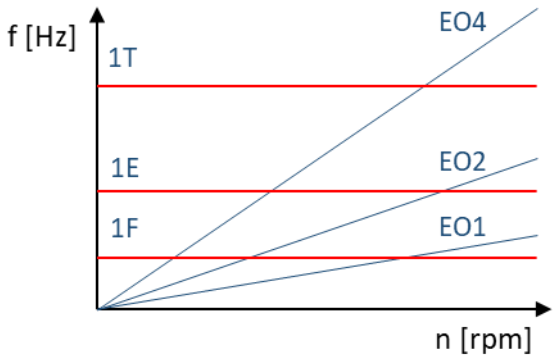

FIGURE 2.3: Experimental Campbell diagram obtained from the data of a strain gauge applied on a rotor blade.

Intersections between the natural frequency line and the EO line represent a resonance point that must be carefully avoided during operation. Particularly during start-up or shut-down of a machine, care must be taken to ensure that these resonance points are passed quickly.

2.1.1.2 NONSYNCHRONOUS VIBRATION

In contrast to synchronous vibration, nonsynchronous vibrations are not linked to integer multiples of the rotational frequency, making their prediction more difficult. A further division according to the causal mechanisms is necessary in order to establish criteria for the recognition of nonsynchronous vibration. Therefore, nonsynchronous vibrations are typically divided into vortex shedding, rotating instability, and self-excited vibration. The latter is defined as a vibration for which the frequency is not an integer multiple of the rotational frequency and the alternating force disappears as soon as the vibration ends. Instead, since both vortex shedding and rotating instabilities can occur as simple aerodynamic effects without any vibratory response, they are normally excluded from the category of self-excited vibration, but depending on the amplitudes of the aerodynamic fluctuations, they both can excite blade vibrations.

According to Camp [9],vortex shedding-driven acoustic resonance can occur if three frequencies coincide approximately: a natural vortex shedding frequency, an acoustic resonant frequency of the duct, and a blade eigenfrequency. Since the occurrence of vortex shedding from blade and vanes or struts profiles, as well as cavities, is linked to overloading and off-design conditions, acoustic resonance is likely to appear outside of the machines nominal operating condition.

Rotating instabilities have been recognised to occur in particular in axial compressors, when operated at high operating points close the aerodynamic stability limit. This vibratory behaviour has always been reported together with the presence of a large tip or hub clearance. Rotating instabilities originate from a single blade row, excited by pressure fluctuations occurring in a narrow frequency band at about half the blade passing frequency. In this frequency band several peaks are present, each representing an aerodynamic mode. If one of the aerodynamic modes locks-on to a blade eigenmode, then a sudden rise in blade vibration amplitude occurs. This determines the change from forced to self-excited vibration

Flutter was defined by Franson [10] as “a sustained oscillation due to the interaction between aerodynamic forces, elastic response, and inertia forces”. The main characteristics of Flutter vibrations are its strict bound to the blade eigenmode with no vibration below or above the blade eigenfrequency

and the exponential growth of the vibration amplitudes. This vibrational pattern can only be stopped by structural failure or by nonlinear effects leading to a limitation of the oscillations. Flutter occurs when the damping of the vibrating system is negative, determining the exponential rise of the blades vibration amplitude.

Buffeting and galloping are two other phenomena that can be grouped amongst nonsynchronous vibrations. Buffeting is a high-frequency instability, caused on a blade/ vane by airflow separations or shock waves induced oscillations, originating in another blade/vane. It is caused by a sudden impulse of load increasing.

Galloping, is instead typically a low frequency high frequency movement parallel to the direction of the flow forcing happening at a specific natural frequency. Self-excited oscillations of the galloping kind are connected to the aerodynamic instability of the airfoil cross section, in a way that the motion of the body generates forces that lead to an increase of the initial amplitudes. Continuously increasing amplitudes with increasing flow velocities are typical of galloping vibrations.

2.1.2 MATHEMATICAL MODEL

2.1.2.1 SINGLE DEGREE OF FREEDOM

The simplest mathematical model of a single degree of freedom oscillator is depicted in FIGURE 2.4. The classic depiction of the mass-spring-damper system has been here modified to represent the dynamic of an air-foil under the effect of aerodynamic load. The SDOF system in FIGURE 2.4 is composed a mass m, a spring with the spring constant k and a damper with damping constant c. The flow around the airfoil is characterised by velocity U(t) resulting in a pressure distribution over the profile p(t). This pressure distribution integrated over the blade surface corresponds to the resulting aerodynamic force F(t).

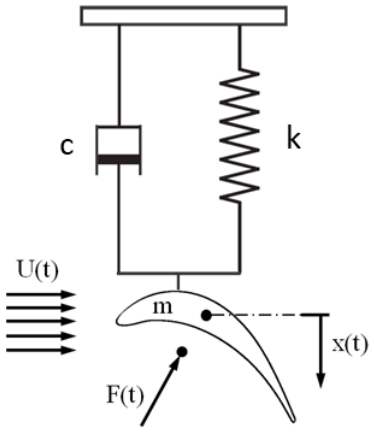

FIGURE 2.4: Single degree of freedom vibratory blade model

Assuming that the mass oscillates in vertical direction with the deflection x(t), it is possible to write the equation of motion of the airfoil as:

$$m \cdot \ddot{x} + c \cdot \dot{x} + k \cdot x = F_x(t) \tag{2.4}$$

With:

$$F(t) = \oint_A p(t) \cdot dA \tag{2.5}$$

Considering the harmonic excitation with pulsation ω, $F(t) = F \cdot e^{i\omega t}$, the response of the system will be of the type:

$$x(t) = X \cdot e^{i\omega t} \tag{2.6}$$

Inserting this in Equation (2.4) one obtains:

$$(-\omega^2 m + i\omega c + k)Xe^{i\omega t} = F_x e^{i\omega t} \tag{2.7}$$

This equation can be re-written as:

$$\mathrm{X} = \frac{F}{(-\omega^2 m + i\omega c + k)} \tag{2.8}$$

Where X is a complex value. The response of the system is therefore: $x(t) = |X| \cdot e^{i(\omega t - \varphi)}$. The amplitude and phase of the response are:

$$|\mathrm{X}| = \frac{F}{k\sqrt{\left[1 - \left(\frac{\omega}{\omega_n}\right)^2\right]^2 + \left[2\zeta\left(\frac{\omega}{\omega_n}\right)^2\right]^2}} \tag{2.9}$$

And:

$$\tan\varphi = \frac{2\zeta\left(\frac{\omega}{\omega_n}\right)}{1 - \left(\frac{\omega}{\omega_n}\right)^2} \tag{2.10}$$

The transfer function that relates the amplitude of the response of the system to the excitation can be evaluated from Equation (2.9):

$$|\mathrm{H}(\omega)| = \frac{1}{k\sqrt{\left[1 - \left(\frac{\omega}{\omega_n}\right)^2\right]^2 + \left[2\zeta\left(\frac{\omega}{\omega_n}\right)^2\right]^2}} \tag{2.11}$$

A fundamental parameter in this discussion is the critical damping factor ζ. In turbomachinery, damping is composed by three main components: structural damping, material damping and aerodynamic damping. Structural damping accounts for the energy dissipated during contacts between parts and its magnitude directly depends on the geometry and pressure of the contacts between components. Material damping instead is a characteristic of the material which represents the dissipation of energy during cyclic strain. Because significantly smaller than the other two contributors, it is typically ignored. Finally, aerodynamic damping characterises the dissipation due to the relative motion between the blade and the fluid.

2.1.2.2 MULTIPLE DEGREES OF FREEDOM

The equation of motion of the mass point system according to equation (2.4) can be converted into matrix form for complex systems as follows:

$$[M] \cdot \{\ddot{x}\} + [C] \cdot \{\dot{x}\} + [K] \cdot \{x\} = \{F(t)\} \tag{2.12}$$

A thorough presentation of the solution of the equation of motion for multiple degrees of freedom system was included by Ewins and Henry in [11], on which the discussion below is based.

2.1.2.2.1 Free vibration solution for the undamped system

It is possible to derive the basic properties considering the equations of motion for an undamped system in the absence of any force. Equation (2.12) reduces to:

$$[M] \cdot \{\ddot{x}\} + [K] \cdot \{x\} = \{0\} \tag{2.13}$$

It is possible to assume simple harmonic motion, similarly to the section above, in the form:

$$\{x(t)\} = \{x\}e^{iw_r t} \tag{2.14}$$

If we substitute the simple equation of the harmonic motion in the general equation of motion we obtain that Equation (2.14) is indeed a possible solution, provided that the frequency belongs to a specific set of frequencies ω_r named natural frequencies and that the displacement follows a particular pattern or mode shape $[\Psi]$ defined by the equation:

$$([K] - {\omega_r}^2[M])\{\Psi\}_r = \{0\} \tag{2.15}$$

The obtained displacement amplitudes are not unique. Because the equations are homogeneous, only relative amplitudes are obtained. The mode shapes have orthogonality properties expressed by the matrix equations:

$$\begin{aligned} \{\Psi\}^T[M]\{\Psi\} &= [m_r] \\ \{\Psi\}^T[K]\{\Psi\} &= [k_r] \end{aligned} \tag{2.16}$$

In which m_r and k_r represent the modal masses and the modal stiffnesses of the r-th eigenmode. Considering that it is possible to write the system of equation of motion in Equation (2.13) using any set of coordinates, it is possible to introduce the following coordinate set:

$$\{p\} = [\Psi]^{-1}\{x\} \tag{2.17}$$

Substituting in Equation (2.13) and pre-multiplying by $\{\Psi\}^T$ gives us:

$$\{\Psi\}^T[M][\Psi]\{p\} + \{\Psi\}^T[K][\Psi]\{p\} = \{0\} \tag{2.18}$$

Which can be reduced to:

$$[m_r]\{\ddot{p}\} + [k_r]\{p\} = 0 \tag{2.19}$$

In which each individual equation looks like:

$$m_r\ddot{p}_r + k_r p_r = 0 \tag{2.20}$$

This leads directly to the solution that:

$${\omega_r}^2 = \frac{k_r}{m_r} \tag{2.21}$$

According to the scaling of the mode shapes, the values for k_r and m_r vary, differently from they ratio, which is uniquely equal to the square of the natural frequency.It is convenient to scale the modes in a specific way known as mass-normalisation. This requires to divide all the elements of $[\Psi]_r$by $\sqrt{m_r}$, obtaining:

$$\{\Phi\}_r = (m_r)^{-1/2}\{\psi\}_r \tag{2.22}$$

From this normalisation it is possible to obtain a more effective from of the orthogonality statement presented in Equation (2.16):

$$\begin{aligned}\{\Phi\}^T[M]\{\Phi\} &= [I]\\ \{\Phi\}^T[K]\{\Phi\} &= [{\omega_r}^2]\end{aligned} \tag{2.23}$$

Were $[{\omega_r}^2]$ is a diagonal matrix.

2.1.2.2.2 Forced vibration solution

Considering a damped system under the effect of harmonic excitation forces allows us to study the frequency response properties of the system. Similarly to the single degree of freedom case presented above, if we consider that the excitation forces are represented by a simple harmonic function:

$$\{f(t)\} = \{f\}e^{i\omega t} \tag{2.24}$$

This gives reasonably origin to a sinusoidal response of the type:

$$\{x(t)\} = \{x\}e^{i\omega t} \tag{2.25}$$

The excitation and response functions are related by the frequency response function matrix $[H(\omega)]$ as follows:

$$\{x\}e^{i\omega t} = [H(\omega)]\{f\}e^{i\omega t} \tag{2.26}$$

Substituting Equations (2.24) and (2.25) in (2.12) it is possible to obtain:

$$[H(\omega)] = (-\omega^2 \cdot [M] + i \cdot \omega \cdot [C] + [K])^{-1} \tag{2.27}$$

Applying the modal transformation already seen for the free vibration undamped case, the last matrix equation becomes:

$$[H(\omega)] = [\Phi]\left[\left({\lambda_r}^2\right) - \omega^2\right]^{-1}[\Phi]^T \tag{2.28}$$

And the individual element results:

$$H_{jk}(\omega) = \sum_{r=1}^{N} \frac{r\Phi_j \, r\Phi_k}{{\lambda_r}^2 - \omega^2} \tag{2.29}$$

This equation gives the harmonic response per unit of harmonic excitation. It can be demonstrated that the harmonic response provides all the necessary information to evaluate the forced response of a system to any kind of excitation (such as periodic but non-harmonic or transient and non-periodic).

The advantage of the modal transformation is that with large systems (many masses or degrees of freedom) the amplitude of the forced response can be calculated with ease. In addition, the system can be reduced with the modal transformation, by omitting higher eigenmodes that make only a small contribution to the overall oscillation. This is the so-called modal reduction, widely used in modern numerical analysis FE software.

The frequency response equation can be also used to evaluate the natural frequencies and modes of structures by means of experimental measurement. Essentially the frequency response matrix can be calculated by measuring the vibration amplitude, e.g. with an accelerometer or laser vibrometer, and the force amplitude of the excitation (e.g. with an impulse hammer) by dividing the Fourier transforms of the time signals of the displacement and the force. This procedure is the basis of the so-called experimental modal analysis.

To conclude, an illustrative representation of the equilibrium of forces according to Equation (2.27) in the complex plane can be seen in FIGURE 2.5.

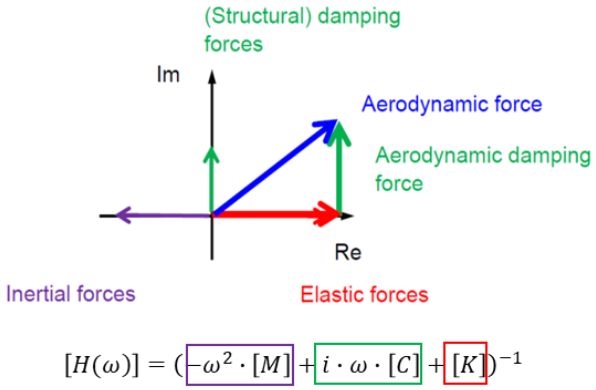

FIGURE 2.5: Aeroelastic force equilibrium in the complex plane. Adapted from [8]

2.2 VIBRATIONS IN TURBOMACHINERY

The attention of this section is focussed on the combined effects of the aerodynamic and structural dynamics phenomena in turbomachinery. The typical rotor in any turbomachinery application is structured as a bladed-disc assembly with a number of Blades mounted on a support structure, typically a disc. In this discussion the characteristics of the two components will be examined separately.

2.2.1 STRUCTURAL CHARACTERISTICS OF BLADES

Understanding the dynamic characteristics of individual blades is essential in order to be able to study the dynamics of the assembly. The geometry of the blades is undoubtedly complex. Key geometrical aspects are: the relatively thick and complex shape of the root structures; the extremely thin trailing edges; the varying heights of blades at leading and trailing edges; blade twist and tilt. Despite this, most turbomachinery blades can generally be regarded as beams or plates in respect of their vibratory behaviour. In particular, the vibration modes of rotor blades can be well represented by simple 1D or beam models. Only in particular cases the extra dimension provided by a 2D plate-like model is required. In both cases, the vibratory movement is normal to the blade longitudinal coordinate (the radial axis of the machine). Special cases exhibiting a significant displacement along the radial direction need full 3D modelling, but represent only a small fraction of the cases.

2.2.1.1 VIBRATION OF CONTINUOUS BEAMS

A typical beam-like structure is depicted in FIGURE 2.6. The mode shapes can typically be grouped in three families: flap-wise bending, edge-wise bending and torsion around the longitudinal axis.

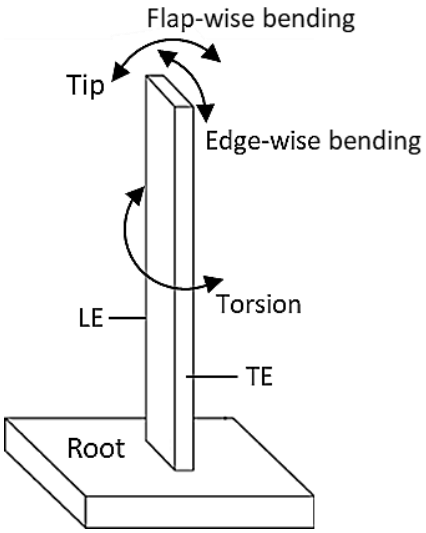

FIGURE 2.6: Uniform cantilever beam blade model and first three mode shapes.

In order to study the dynamic behaviour of the blade, the case of bending of the Bernoulli-Euler beam with a constant cross-section will be considered. An explanatory scheme is depicted in FIGURE 2.7.

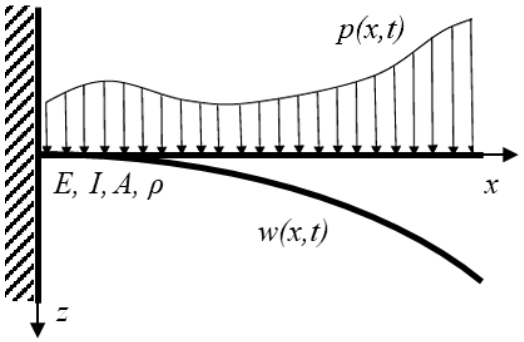

FIGURE 2.7: Cantilever beam with external time-varying load.

Studying an element of the vibrating beam, it is possible to find that the equilibrium equation is:

$$m' \frac{\partial^2 w}{\partial t^2} + EI \frac{\partial^4 w}{\partial x^4} = p(x,t) \tag{2.30}$$

Where m' represents the distributed mass and $p(x,t)$ the distributed load. Considering he homogeneous solution of the differential equation one has to solve for $p(x,t) = 0$:

$$m' \frac{\partial^2 w}{\partial t^2} + EI \frac{\partial^4 w}{\partial x^4} = 0 \tag{2.31}$$

The equation can be solved considering the separation approach, considering that the solution will be of the type:

$$w(x,t) = \psi(x) \cdot T(t) \tag{2.32}$$

By applying the derivative and then substituting in the homogenous equation, one can obtain:

$$\frac{1}{T}\frac{\partial^2 T}{\partial t^2} = -\frac{EI}{m'}\frac{1}{\psi}\frac{\partial^4 \psi}{\partial x^4} = -\omega^2 \tag{2.33}$$

This equation is only satisfied if both terms are constant and therefore we can introduce the constant $-\omega^2$. This generates two ordinary homogeneous differential equations of the second order with constant coefficients, which can be solved with the help of an exponential approach.

$$\frac{\partial^2 T}{\partial t^2} + \omega^2 T = 0 \tag{2.34}$$

$$\frac{\partial^4 \psi}{\partial x^4} - \beta^4 \psi = 0$$
$$\beta^4 = \frac{m'}{EI}\omega^2 \tag{2.35}$$

These two equations can be solved as follows.

$$T(t) = B_1 \cos(\omega t) + B_2 \sin(\omega t) \tag{2.36}$$

$$\psi(x) = A_1 \cos(\beta x) + A_2 \sin(\beta t) + A_3 \cosh(\beta x) + A_4 \sinh(\beta x) \tag{2.37}$$

With the corresponding boundary conditions and initial conditions, the eigenfunctions $\psi(x)$, i.e. the eigenmodes (up to an undetermined constant), and the eigenfrequencies ω can be determined. The eigenfunctions can be combined to form the total solution of the homogeneous differential equation:

$$w(x,t) = \sum_{n=1}^{\infty} [A_{1n}\cos(\beta_n x) + A_{2n}\sin(\beta_n x) + A_{3n}\cosh(\beta_n x) + A_{4n}\sinh(\beta_n x)] \cdot [B_{1n}\cos(\omega_n t) + B_{2n}\sin(\omega_n t)] \tag{2.38}$$

Considering the orthogonality relationship between eigenmodes, without normalisation of the eigenmodes, the following applies in general:

$$\int_o^L \psi_i(x)\psi_j(x)dx = \begin{cases} 0\,, i \neq j \\ g\,, i = j \end{cases} \tag{2.39}$$

Where g is the scaling factor. Analogously to the multi-mass oscillators, form Equation (2.39) it can be derived:

$$\int_o^L m'\psi_i(x)\psi_j(x)dx = \begin{cases} 0\,, i \neq j \\ m_{gen}\,, i = j \end{cases} \tag{2.40}$$

$$\int_o^L EI\psi_i(x)\psi_j(x)dx = \begin{cases} 0\,, i \neq j \\ c_{gen}\,, i = j \end{cases} \tag{2.41}$$

It is possible to obtain the particular solution applying the modal transformation method, since we know from the previous chapter that the total oscillation can be represented by a superposition of correspondingly scaled natural oscillations. Considering a harmonic forcing function of the form:

$$p(x,t) = \hat{p}(x)cos(\Omega t) \tag{2.42}$$

It is possible to assume that the system response will also be harmonic, particularly in the form of:

$$w(x,t) = \hat{w}(x)cos(\Omega t) \tag{2.43}$$

Substituting in the differential equation one obtains:

$$-m'\Omega^2\hat{w}(x) + EI\hat{w}^{IV}(x) = \hat{p}(x) \tag{2.44}$$

To solve this equation, it is possible use a modal approach in a form called development according to eigenfunctions:

$$\hat{w}(x) = \sum_{i=1}^{\infty} q_i \psi_i(x) \tag{2.45}$$

The external loads according to the eigenfunctions, the so-called modal loads, are expressed as:

$$\hat{p}(x) = \sum_{i=1}^{\infty} p_i \psi_i(x) \tag{2.46}$$

The definitions in Equation (2.45) and (2.46) can be inserted in (2.44), obtaining:

$$\sum_{i=1}^{\infty} q_i \left[-m'\Omega^2\psi_i(x) + EI\frac{\partial^4\psi_i(x)}{\partial x^4}\right] = \sum_{i=1}^{\infty} p_i\psi_i(x) \tag{2.47}$$

From Equation (2.33) we know that:

$$EI\frac{\partial^4\psi_i(x)}{\partial x^4} = m'{\omega_i}^2\psi_1(x) \tag{2.48}$$

This leads to:

$$\sum_{i=1}^{\infty} q_i[-m'\Omega^2\psi_i(x) + m'{\omega_i}^2] = \sum_{i=1}^{\infty} p_i\psi_i(x) \tag{2.49}$$

From the last equation, considering the orthogonality properties the modal coordinate can be calculated. It can be seen that tit is similar to the solution of a single-mass oscillator:

$$q_i = \frac{p_i}{m'[{\omega_i}^2 - \Omega^2]} \tag{2.50}$$

The value of p_i is unknown, but reorganizing the orthogonality properties, one can obtain:

$$p_i = \frac{1}{g_i}\int_0^L \psi_i\hat{p}(x)dx \tag{2.51}$$

Substituting back into Equation (2.45) yields the amplitude function as a superposition of the individual eigenmodes. Putting everything back into (2.43) gives the solution of the differential equation. The solution shows that for a system to oscillate at a certain eigenmode, this eigenmode must be contained in the forcing function to be excited. For instance, this means that if the beam is at the first eigenmode, it only oscillates with this one eigenmode and the others do not contribute to the overall oscillation.

A similar analysis can be done also for torsional and axial vibration of the beam, leading as well to partial equations of motions. The general solution takes different form in each case, but a general similarity can be found in all of them.

According to [11], the strain vector can be linked to the stress vector with the following definition:

$$\{\sigma\} = [E]\cdot\{\varepsilon\} \tag{2.52}$$

Integrating over the whole structure gives an expression for the strain energy:

$$E_{strain} = \frac{1}{2}\int_{\tau} \{\varepsilon\}^T\{\sigma\}\, d\tau = \frac{1}{2}\int_{\tau} \{\varepsilon\}^T[E]\{\varepsilon\}\, d\tau \tag{2.53}$$

This quantity represents the energy stored in a system undergoing deformation. Considering linearly elastic materials, integrating over the structure leads to:

$$E_{strain} = \frac{1}{2}VE\varepsilon^2 \tag{2.54}$$

Where V is the volume of the structure.

2.2.1.2 FACTORS INFLUENCING THE VIBRATION PROPERTIES OF BLADES

As real blades are generally more complex than the simple beam model, several design feature influence their vibration properties, primarily the natural frequency and the mode shapes. In particular, the complex geometry, including non-symmetric and non-uniform cross sections; the root attachment flexibility; the effects of real operating conditions, such as rotation and thermal effects.

Regarding the complication arising from complex geometry needed for aerodynamic performance, the blades geometry varies in several aspects along the height. The section area can vary if the blade is tapered, the geometrical centre of each section may not be aligned on one longitudinal axis and the orientation of each section may differ in the case of twisted blades. All this common geometrical features have a direct effect on the blade vibratory characteristics, as reported by Ewin and Henry in [12]. In details, tapered blades exhibit a modification of the eigenfrequencies, while longitudinal twist and non-symmetries both determine more complex mode shapes but affect less the natural frequencies.

Even though it is common to consider that the blade root presents a grounded or cantilever base, this is hardly the realistic configuration of an actual design. Both the disc and the blades possess some degree of flexibility, as will the contact between the two components. These flexibilities generally reduce the rigidity of the boundary condition at the root of the blade lowering its natural frequencies with respect to those of an ideal cantilever beam. It has been observed that short and very stiff blades are the most affected by root flexibility effects. This must be considered for the correct prediction of mode shapes and eigenfrequencies. Furthermore, the effects of the disc and contact flexibility must be taken into account for a complete modelling of the entire assembly.

A number of additional factors interact with the blade structural dynamics while the blade operates in its environment. Centrifugal forces generated by the rotation is one of the most relevant. One result of centrifugal forces is the influence on the blades geometry. However, the most relevant consequence is the stiffening effect, which causes an increase in the natural frequency and a modification of the mode shapes. Vibrations normal to the plane of rotation are more influenced, since the radial forces generate a restoring force that counteracts the blade displacement. Instead, for vibrations in the plane of rotation the restoring component of the centrifugal force is small and therefore the stiffening effect is negligible.

The effect of the centrifugal forces can be evaluated considering the mass point system defined in Equation (2.12) and adding the effect of the centrifugal force:

$$\{F_c\} = \Omega^2[M]\cdot\{x\} \tag{2.55}$$

Substituting this last definition in the system of Equation (2.12) one obtains:

$$[M]\cdot\{\ddot{x}\} + [C]\cdot\{\dot{x}\} + ([K] - \Omega^2[M])\cdot\{x\} = \{F(t)\} \tag{2.56}$$

Considering the case in which the Coriolis effect can be neglected, the solution of the system can be related to the solution of a classical un-damped system. If the motion is therefore assumed to be simple harmonic, the effect of the rotational speed on the eigenfrequencies can be derived from:

$$\omega_n = \sqrt{\frac{k}{m} - \Omega^2} \tag{2.57}$$

Another important element of real operating conditions is the temperature. A significant temperature change determines a change in the elastic modulus, effecting the eigenfrequencies. According to [12], the effect of high temperatures is generally to reduce the material stiffness, in some cases even to override the effect of centrifugal stiffening, determining a reduction of the natural frequencies. An accurate knowledge of the operating temperature and modulus-temperature relation of the blade material are key to correctly evaluate the blades vibration modes.

2.2.2 STRUCTURAL CHARACTERISTICS BLADED-DISC ASSEMBLIES

The purpose of the "disc" in the blade-disc assembly is purely structural, i.e., to carry the blades and to transfer the torque from the blades to the shaft. When considered as a part of the bladed-disc assembly, the disc participates in the vibratory motion of the assembly according to its flexibility. Excitation frequencies resulting from blade row interactions can excite the disc as well as the blades themselves. The oscillation of the disc naturally leads to blade oscillations. This kind of excitation is denominated contact excitation in the blade root.

The circular symmetry of the disc permits the generation of cyclically symmetrical vibration patterns, as shown in FIGURE 2.8. The figure schematically shows the diameter of the nodes. The resulting vibration patterns of a disc are generally referred to as the node diameter (ND). In the case of bladed rotors, this also depends on the number of blades.

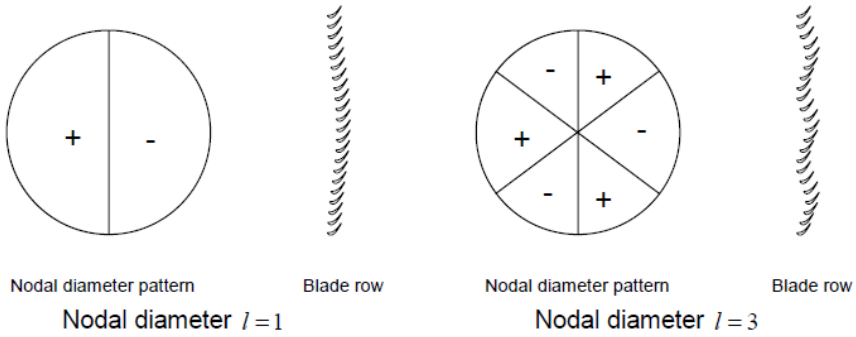

FIGURE 2.8:Schematic visualisation of the concept of Nodal Diameter. From Vogt [13]

Understanding the dynamic characteristics of blade assemblies is crucial to correctly calculate flutter and resonance of rotors. The coupling between blades due to the presence of the disc and/or shroud support structure determine different vibratory characteristics from those of individual blades. In particular, as noted by Srinivasan in [14] bladed-disc assemblies' mode shapes and eigenfrequencies are influenced by characteristics of individual blades; by the blade-disc contact type, by the contacts between support structures including part-span or tip shrouds; and the presence of mistuning.

In bladed-disc assemblies, the number of possible nodal diameters extends only to a maximum number depending on the blade count:

$$\begin{aligned} &\text{Even blade count: } ND_{max} = \frac{B}{2} \\ &\text{Odd blade count: } ND_{max} = \frac{B-1}{2} \end{aligned} \tag{2.58}$$

From the definition of nodal diameter can be obtained the concept of interblade phase angle (IBPA), representing the phase shift that is present between each blade when the bladed-disc assembly vibrates at a specific nodal diameter. The interblade phase angle is defines as:

$$\begin{aligned} &\text{Forward traveling wave: } 0°<IBPA<180° && IBPA_{forward} = \frac{2 \cdot \pi \cdot ND}{B} \\ &\text{Backward traveling wave: } -180°<IBPA<0° && IBPA_{backward} = \frac{2 \cdot \pi \cdot (B - ND)}{B} \end{aligned} \tag{2.59}$$

The vibratory patterns are not necessarily perfect and may depend on the presence of extent of irregularities in the dynamic characteristics of blades, namely the level of mistuning. If this is low and the geometrical and structural characteristics the blades are in essence identical, then the resulting vibratory pattern is regular and a certain nodal diameter and nodal circle mode can be recognised easily. On the other hand, a system with high mistuning shows a vibratory behaviour that may defy easy explanation.

Finally, FIGURE 2.9 Represents the first blade only and bladed-disc assembly mode shapes for the low pressure turbine unshrouded rotor used for the experimental activity presented in this thesis, evaluated by means of finite elements analysis

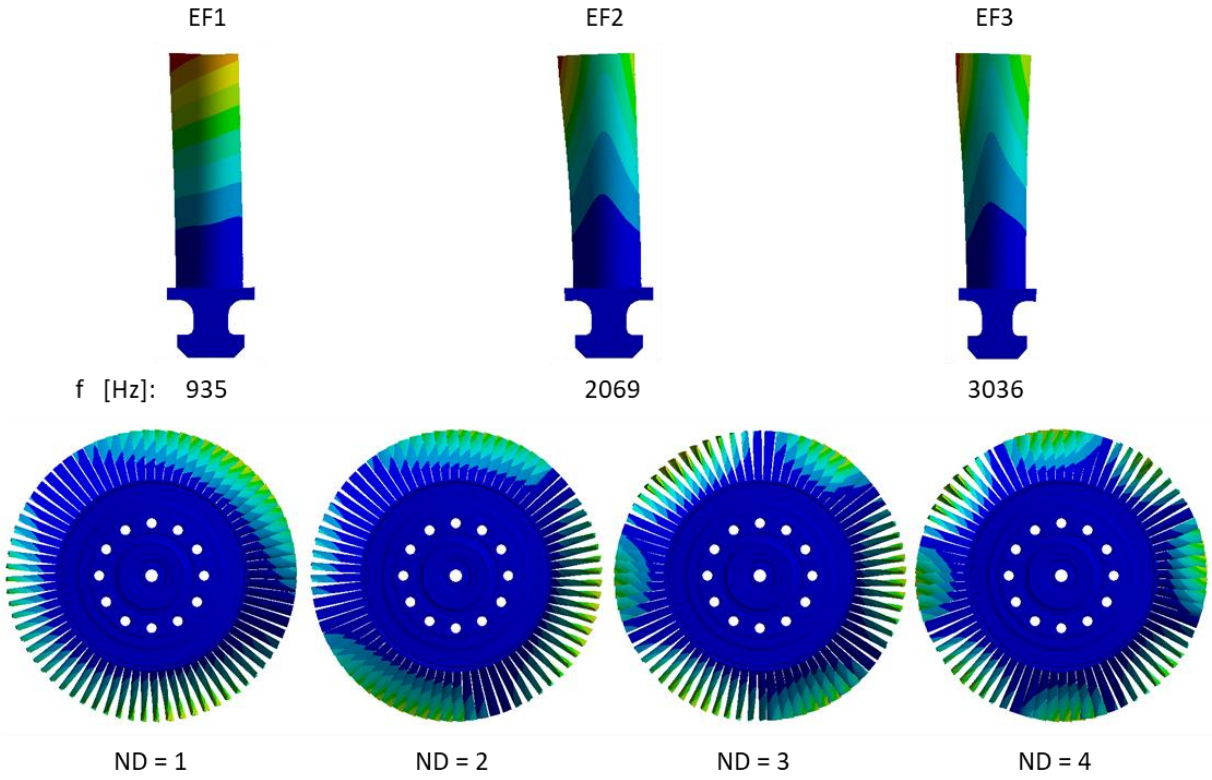

FIGURE 2.9: Blade and bladed-disc assembly mode shapes.

3. LITERATURE REVIEW

3.1 LOW PRESSURE TURBINE AERODYNAMICS

3.1.1 SECONDARY FLOWS

According to Denton [15] endwall effects generate about one third of the total aerodynamic loss in a turbine. The dissipation that occurs in the boundary layers of the hub and casing and from the secondary flow, which is generated when the non-uniform inlet flow rotates through the row of blades, is the cause of these losses. Most of the early basic studies concerning endwall flows are based on investigations carried out in linear cascades, which represent an approximate model for the behaviour of the real engines. During many decades of experimental research, a detailed understanding of the flow behaviour has been gathered. Many works summarized the knowledge on secondary flows in the past years, for instance the review papers of Sieverding [16] and Langston [17], the studies of Hodson and Dominy on three dimensional flows in LPT cascades [18] and the works of Sharma and Butler [19] on the prediction of the losses generated by secondary flows . A more recent study on the impact of key design parameters on the endwall flows and losses in turbines was presented by Coull [20]. The paper reported on a parametric study on a linear cascade and demonstrated that endwall losses can be divided in two components: one due to secondary flows and another one induced by the dissipation associated to the boundary layer.

A clear description of the causes driving the formation of endwall flows was given by Lampart [21]. In this work, the passage vortex is identified as the main type of secondary flow. The origin of the flow recirculation in the blade passage that leads to the formation of the passage vortex is found in the cross flow that forms in the boundary layer as a result the equilibrium of the forces that act on the fluid particle in its curvilinear motion. The momentum equation in the cross direction can be written as:

$$\frac{\rho v^2}{R} = \frac{\partial p}{\partial r} \tag{3.1}$$

Where v represents the velocity, p the pressure, ρ the density, R the streamline curvature radius and n the normal coordinate. Since a decrease of velocity is experienced by the flow in the boundary layer, in order to balance the cross-stream pressure gradient formed in the channel, the streamline curvature radius in the boundary layer flow needs to be reduced. Consequently, flow in the boundary layer turns more than the main flow in the blade-to-blade channel, leading to a crossflow from the pressure surface of one blade to the suction surface of the adjacent blade in the endwall boundary layer. A recirculating cross flow is then created higher in the channel, as a return flow compensating the cross flow in the boundary layer. The passage vortex originates from this recirculating flow. Due to the pressure difference existing between the pressure and the suction side channel, the passage vortex locates near the blade suction surface downstream in the blade-to-blade passage.

A schematic depiction of the resulting vortex structures that constitute endwall flows is depicted in FIGURE 3.1. The diagram is reported from Coull [20] and is based on the flow field obtained with a RANS simulation.

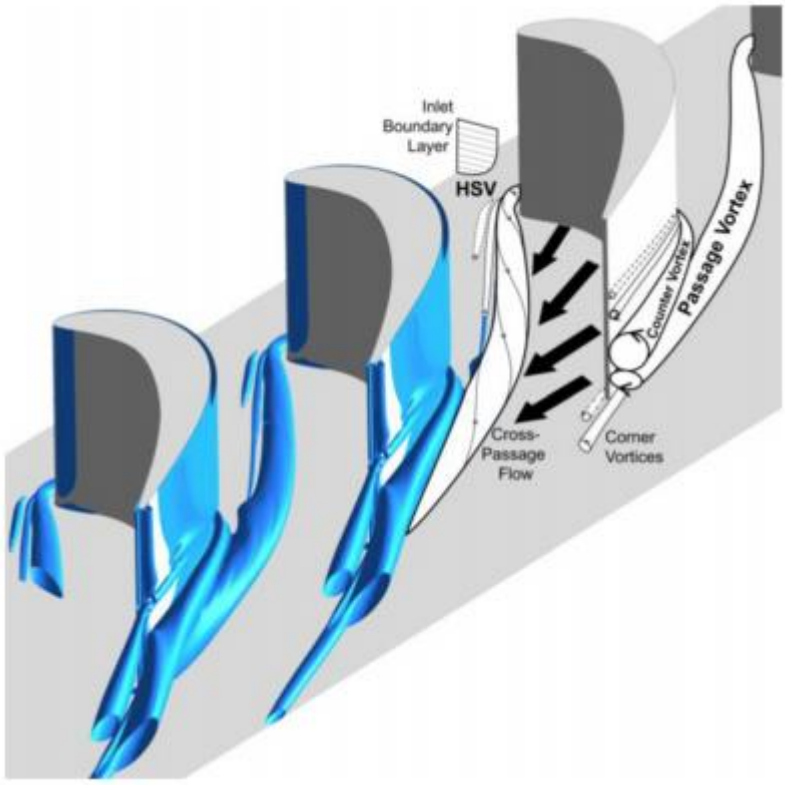

FIGURE 3.1: Three dimensional division of the boundary layer in a turbine cascade. Picture from [20].

The horseshoe vortex (HV) originates when the incoming endwall boundary layer, which is subject to the same static pressure field as the freestream flow, separates in the adverse pressure gradient approaching the blade leading edge and rolls up into two vortical structures. The static pressure gradients determine the trajectory of the HV. In particular, the suction side leg (HV-SS) remains attached to the suction surface of the blade, whereas the pressure-side leg (HV-PS) drifts toward the low-pressure region near the suction surface of the adjacent blade. Crossing the passage, the HV-PS leg interacts with the pressure-to-suction side cross flow near the endwalls joining the main passage vortex (PV). Once the passage vortex reaches the suction surface of the adjacent blade, it interacts with the blade surface and with the HS-SS from this blade, which is counter rotating respect to the passage vortex and is therefore named counter rotating vortex (CV). The two vortices then rise on the blade suction surface up until the midspan region. The HV is actually a system of counter-rotating vortices. One system of smaller vortices is created on the blade suction surface from the interaction of the passage vortex and the counter vortex. Additionally, the blade-to-blade cross flow in the boundary layer often lifts off at the blade–endwall junction, generating corner vortices. Between two passages, near the blade trailing edge, the two passage vortices, each belonging to one passage, interact with the wake flow, leading to the generation of a vortex sheet downstream of the trailing edge. This sheet of vortices is counter rotating to the corresponding passage vortex. Numerous authors reported variations from the basic description of the flow pattern given here. This suggest that the problem of secondary flow structures is actually depending on the particular design of each application.

A complication to the above-mentioned description of the endwall flows is encountered when considering purge flows. The main task of purge flows is to seal the cavities between rotating and static parts in the turbomachine, avoiding the ingress of hot air in the axial gaps. It is therefore intuitive to consider that the presence of purge flows in the region near the endwalls will consequently influence the structures related to the secondary vortices. This interaction mechanism is interesting for the scope of this work because the influence of the purge flows on the main flow features propagating from the HPT, and from the upstream components in general, can generate disturbances in the inflow field of the LPT. This can determine distortions of both temperature and pressure at the inlet of the LPT stages.

Therefore, it is interesting to study the results of the several studies published in the previous years, dealing with the interaction between purge flows and secondary vortices. The entrainment of cavity flow into the rotor hub passage vortex was observed by Paniagua et al. [22]. The vortex resulted reinforced and experienced a migration towards the midspan. This study demonstrated a 30 K decrease of the passage vortex temperature, due to the interaction with the colder purge air.

Similarly, a strong interaction of the purge with the rotor hub passage vortex was found by Jenny et al. [23], [24] and Regina et al. [25]. In their studies the authors found out that the purge flows caused a radial shift of the hub passage vortex position. These results were supported by other studies published by Ong and Miller [26], who demonstrated that the coolant injected from the cavities is entrained into the rotor secondary flows. Additionally, Jenny et al. [23] also reported higher unsteadiness, identified by means of higher total pressure root-mean-square (RMS) was observed in the vortex cores when purge flows was injected. As a consequence of the stronger secondary flow structures, both the vorticity and the flow unsteadiness increase due to the entrainment of purge flows. Furthermore, also the flow angle at the rotor exit is influenced by the interaction between the purge air injection and the secondary flows, as demonstrated by [22], [25] and Dahlqvist and Fridh [27]. In [27], a relationship between the change of Mach number and swirl angle at the rotor exit due to the intensification of secondary flow structures was obtained as well. Therefore, the influence of purge flows on the secondary vortices determines effects that can be transported downstream of the HPT and determine distortions at the LPT inlet.

Measurements focussed on the study of purge flows effects on a TCF and LPT system were carried out by Zerobin et al. [28] and by Sterzinger et al. [29]. In the first work, the measurement data illustrate the interaction of the purge flow with the main flow, determining the enhancement of the secondary flows. The aerodynamic performance of the duct depends on the amount of purge air injected in the main flow. Additionally, clocking effects were noticed. The authors ultimately demonstrate that it is convenient to reduce the amount of purge air required, in order to increase the engine system performance by increasing the TCF efficiency. Sterzinger et al. [29] focussed on the effects due to the modification of the TCF inlet conditions, generated by different purge flowrates, on the flow through the TCF duct and the effects on the LPT stage inlet flow field and performance. This study concluded that the purge flow vortices must be taken into account during the LPT design process. In particular, the effects of the purge flow vortices, which cause radial migration depending on the purge flow rate, need to be careful integrated in the design process to further improve LPT efficiency.

3.1.2 TIP LEAKAGE FLOWS

Considering that the test rig setup used within this project has an unshrouded rotor, the effects of the clearance existing between the rotor blade tip and the machine casing have to be taken into account. The unshrouded configuration is rather unusual for a low pressure turbine, this design was chosen to promote the formation of rotor-stator flow interactions, since the test rig was designed with the aim to maximise aeroacoustics and aeroelastic phenomena.

The combination of unshrouded rotor and rotor tip clearance considerably affects the secondary flow features in the tip region, as reported in the review by Sjolander [30]. A schematic view of the tip leakage flow topology is depicted in FIGURE 3.2. The driver for the creation of the leakage is the pressure difference between the suction and the pressure side of the rotor blade. This leads to a tip jet characterised by high velocity and high losses. The jet moves from the pressure side to the suction side, where it rolls up and mixes with the main flow in the blade passage, giving origin to the typical tip leakage vortex counter-rotating to the passage vortex. The flow approaching the blades tip senses the adverse gradient due to the presence of the blade and divides into two separate streams, one smaller heading to the suction side of the neighbouring blade across the blade-to-blade channel, and one main stream flowing over the blade tip towards the blade's suction side. The tip leakage vortex and the cross-flow interact in the channel with the passage vortex.

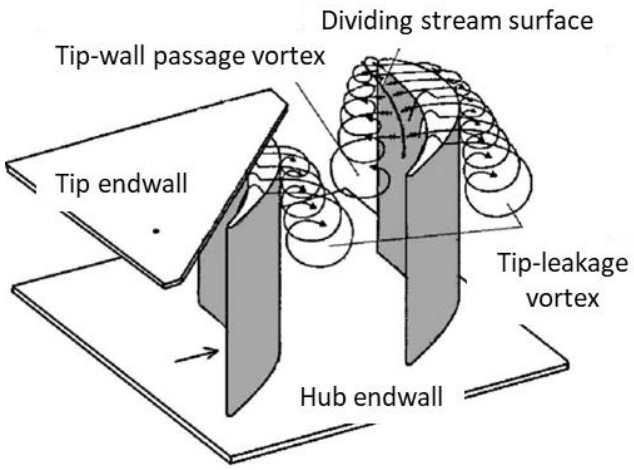

FIGURE 3.2: Sketch of the tip leakage and passage vortices at the tip endwall with clearance. Adapted from [31].

The loss performance caused by tip leakage flow has been studied extensively for many years, for instance by Bindon [32] and Moore and Tilton [33]. According to Denton [15], the simpler effect caused by flow leakage over the blades tip, is a modification of the mass flow in the blade passage. In a turbine, the jet flow leaking over the blade tip has a higher meridional velocity so that the mass flow through the rest of the blade must be reduced. This modification of mass flow results, for unshrouded blades, in a loss of lift at the blade tip which occurs both because the blade length is reduced and because the blade loading drops towards the tip.

Additionally to the in depth work of Denton [15], an extensive study of the tip leakage flows in turbines was given by Lampart [31]. According to this author, the flow typically separates from the sharp edge of the blade tip at the entrance of the tip gap. Therefore, the separation generates contraction in the tip clearance. The flow will reattach on the surface of the blade tip if the blade is thick enough. Downstream of the clearance gap the leakage flow encounters the pressure gradient of the blade-to-blade channel and forms a vortical structure that is convected downstream. Since the tip leakage flow follows the pressure gradient across the tip gap, its direction is not the same of the main flow when it re-enters the blade passage. The flow over the blade tip generates a significant increase of axial forces on the blade, between 5 and 10% depending on the geometry of the blades and the tip gap dimensions. A scheme of the flow in the tip gap region to support the explanation is given in FIGURE 3.3.

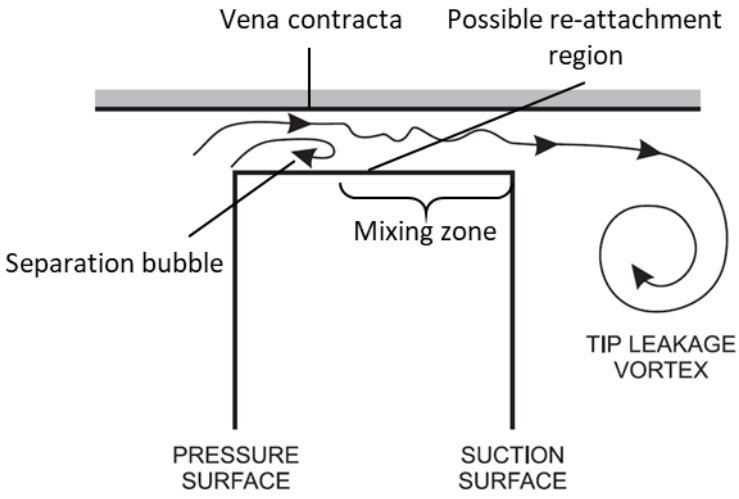

FIGURE 3.3: Tip leakage flow over unshrouded rotor. Adapted from [31].

The behaviour in the tip gap region depends on the blade tip dimension. In particular, in case on thin blades, the re-attachment is most unlikely to occur. Several flow parameters also influence the tip leakage over unshrouded blades. In particular, the gap size, the flow turning in the blade row, the flow inlet angle and the blade-casing relative motion. All these parameters were studied by several authors in recent years.

Studies on the effect of clearance on turbine rotors were performed for instance by Yoon et al. [34] and Sell et al. [35]. In their work [35] they investigated and compared four different tip gap sizes, i.e. 0%, 1%, 3% and 5%, in an annular cascade. While the smaller clearance determines the origin of a stagnation point, similarly to the case without tip gap, the largest clearance case allows the fluid to flow undisturbed over the blade. Moreover, the work of Lampart [31] suggests that the relation between the dimension of the passage vortex and the tip leakage vortex depends on the tip gap size. Results show that 25% of the axial chord downstream of the rotor trailing edge the size of the tip leakage vortex increases while the size of the passage vortex decreases with the increasing tip clearance size.

The effect of the inlet yaw angle was presented by Coull and Atkins [36] describing results obtained with numerical simulations. The incidence variation at the inlet of the blade determines a modification of the direction of the leakage flow over the blade. This caused the ejection of the leakage flow at different positions along the blade chord from the SS depending on the inlet flow angles. Moreover, the position and the intensity of the tip leakage vortex and the passage vortex depend very much on the incidence angle.

The flow turning in the blade row also influences the tip leakage flow, in particular, it affects directly the cross-flow in the endwall region. According to Lampart [31] a lower turning determines a quick dissipation of the tip passage vortex resulting from the interaction with a more intense tip leakage vortex. On the contrary, the role of cross-flow in the endwall region increases with the flow turning and the passage vortex is generally able to form before the tip leakage flow leaves the tip gap.

The effect of the relative motion between the outer casing and the blade was studied amongst others by Coull [36] and Tallman and Lakshminarayana [37]. The later work shows in particular that in turbines the relative motion decreases the mass flow through the tip gap and decreases the losses. An additional effect highlighted by this study is that some of the leakage flow is not entrained in the vortex, but is instead located around and underneath the vortex, contributing to the development of a strong secondary flow in span-wise direction.

Considering that the machine under investigation is a rotating turbine, the rotational effects must be taken into account. McCarter et al. [38] studied the modifications that the rotational effects and the Coriolis forces have on the turbulence structure in the tip leakage flow and on secondary flow as compared to cascades. The main focus of this investigation was the origin as well as the development of the leakage flow including its interaction with secondary flow features. In particular, it was observed that a scraping vortex develops due to the relative motion between blades and casing. The authors stated that the propagation of the tip leakage flow into the main flow is reduced by the scraping vortex. The presence of a scraping vortex was also observed byCoull [36], when realistic inlet conditions including the relative casing motion were considered for the numerical simulations.

The tip leakage flow is very relevant for this work because the steady and unsteady behaviour of the flow in the tip region is highly influenced by the presence of distortions in the stage inlet flow. It will be shown that both temperature and pressure disturbances have a strong effect on the tip leakage vortex. According to the already mentioned work of Coull [36], the flow angle modifications a the rotor inlet are responsible for changes in the behaviour of the tip leakage flow. Additionally, the boundary layer at the tip end wall, which influences directly the extent of the secondary vortices in this region, depends directly on the inlet total pressure and temperature.

3.1.3 WAKES AND STATOR-ROTOR INTERACTIONS

A turbine generally consists of a series of stators and rotor rows. All the secondary flow features that were introduced in the precedent sections, together with the wakes of each blade/vane row, interact with each other and with the adjacent stator or rotor. Therefore, a very complex flow field downstream of

each turbine stage originates from such interactions. The bulk of the aerodynamic results that will be presented in this thesis are representative of the flow field downstream of a LPT. Furthermore, acoustic reflections and multiple blade-row effects have an impact on aeroelastic behaviour, as stated by Sotillo and Gallardo [39].Thus, the main stator-rotor flow structure interactions will be examined in this section.

The evolution of a turbulent wake in a low pressure turbine blade passage was studied by Stieger and Hodson [40] by means of Laser Doppler Anemometry (LDA) measurements in an LPT cascade. The unsteady flow visualized by perturbation velocity vectors is visible in FIGURE 3.4. The perturbation velocity is defined as the difference between the ensemble average and the time-averaged velocities. The figure can be used to identify the main processes that characterises the convection of the wake within the blade row, namely bowing, reorientation, elongation, and stretching.

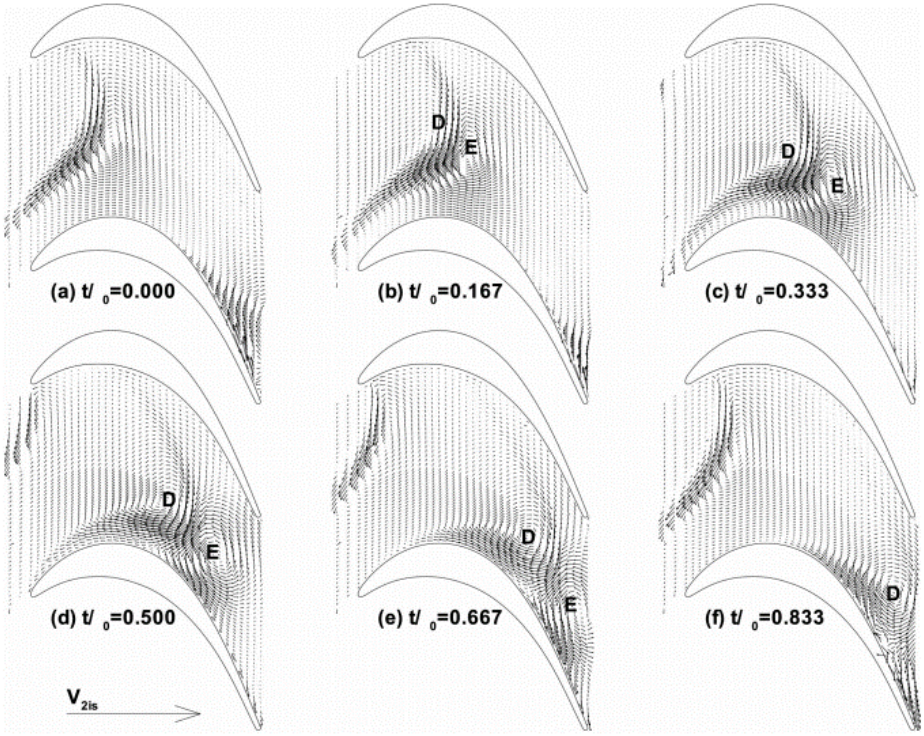

FIGURE 3.4: Perturbation velocity vectors from LDA measurements at six time instants through the wake-passing cycle. From [40].

Since the 80s, many studies have been performed in turbine research facilities in order to increase the knowledge and understanding of the unsteady flow interactions. Binder et al. [41] presented detailed measurements carried out by means of laser velocimetry near and within a single stage cold air turbine rotor. This work describes the periodical and random unsteady effects of the stator wakes impinging on the rotor blades. In particular, the non-uniform stator outlet flow impinging on the rotor blade row determined high turbulence levels in the wake regions and the in the secondary flows. The influence of the stator wakes in the rotor section was shown to generate two circulation regions, characterised by over-turning inside the wake flows and under-turning outside of it. Additionally, the authors highlighted the importance of the high turbulence intensity originating from high fluctuation of the flow in the wake region in connection with the low relative velocities measured near the pressure side of the rotor blade, that could significantly affect the boundary layer behaviour.

A work describing an investigation of stator-rotor wake interactions in axial flow turbines was also presented by Hodson [42]. This investigation focuses onto the free-stream unsteadiness caused by the interaction of the stator wakes with the rotor blades found in the rotor passages of a large-scale, single-stage air turbine. The wakes of the stator row are chopped by the rotor blades and after passing through the rotor they consist of individual segments which lie between the wakes of adjacent rotor blades.

Consequently, the flow reaching a subsequent stator row would contain both rotor and 1st-stator wake generated unsteadiness. Therefore, the complexity of the unsteady flow increases after each blade row.

Results of experiments directed at the understanding of the unsteady mean and turbulent flow in a large-scale 1.5 stage research turbine were presented by Sharma et al. [43]. While the stator exit flow was shown to be essentially steady, two different flow regimes were identified at the rotor exit, corresponding to maximum and minimum interaction of the rotor with the vane wakes. While during the maximum interaction the vane wakes merged with the rotor wakes, determining a uniform mid-channel flow and strong secondary flow vortices, during minimum interaction the vane wakes entered the rotor passages between airfoils generating lower uniformity in the mid-channel and less defined secondary vortices. Ultimately, the authors pointed out that it is important to identify and understand the interaction mechanisms as they are relevant to evaluate the losses in turbines.

The unsteady blade row interaction in multi stage low-pressure turbines were studied by Arndt [44] with hot-film probes located downstream of every blade row. This investigation showed that the rotor-rotor interactions have a profound influence on the flow through the LPT. The interactions between wake flows result in periodic and turbulent velocity fluctuations downstream of each rotor row. The work highlighted also a significant difference in wake depth and turbulence level downstream of each stage.

Using both computational and experimental evidence, Rose et al. [45] studied the thermodynamics of the vanes wakes as they interact with the rotor blades. In particular, it was observed that the wakes accelerate more than the free-stream in the rotor blade passage due to their migration towards the suction side and to the increase of relative total pressure given by isentropic work. The main implication that this results have is that the effects of unsteady interaction is to moderate the mixing losses in existing machines, therefore the authors suggest that a possible route to higher turbine efficiencies is to consider stronger unsteady interaction. Clearly this design philosophy must take into consideration the effects on forced response and noise emission.

Results obtained in the same test rig used for this work were presented by Lengani et al. [46]. Unsteady measurements with a fast response pressure probe downstream of an unshrouded low pressure test turbine with an uneven blade/vane count, allowed the author to identify the importance of the tip leakage vortex for the flow field downstream of the stage. The key outcome of this study is that the interactions between blade and vanes of the stage can be explained by means of rotating pattern according to the aero-acoustic theory presented by Tyler and Sofrin [8]. Therefore, the fluctuations downstream of the rotor can be seen as a superposition of rotating patterns due to so called spinning modes. The amplitude of the fluctuations induced by the stator/rotor interaction evaluated by means of modal decomposition is comparable to the unsteadiness induced by the rotor alone. The additional unsteadiness in the flow can be recognised employing time-space plots, which show the time history of one flow quantity over the circumferential measurement sector at one specific radial height. FIGURE 3.5 depicts the time space plots of relative exit flow angle for three radial heights and relative Mach number at the central span position reported by Lengani in [47]. Similarly to the already presented work by the same author, the measurements were taken in the flow field downstream of an LPT rotor blade row. Observing the plots, it is possible to note the effects of the stator wakes, represented by the repetition of similar structures in vertical direction. The stator wakes are chopped by the inclined traces of the rotor wakes. Furthermore, a spinning mode was recognised by the author as an inclined line connecting the regions at low momentum of the rotor wakes. This is the result of the sum of two causes: rotor-stator interaction and uneven blade/vane count.

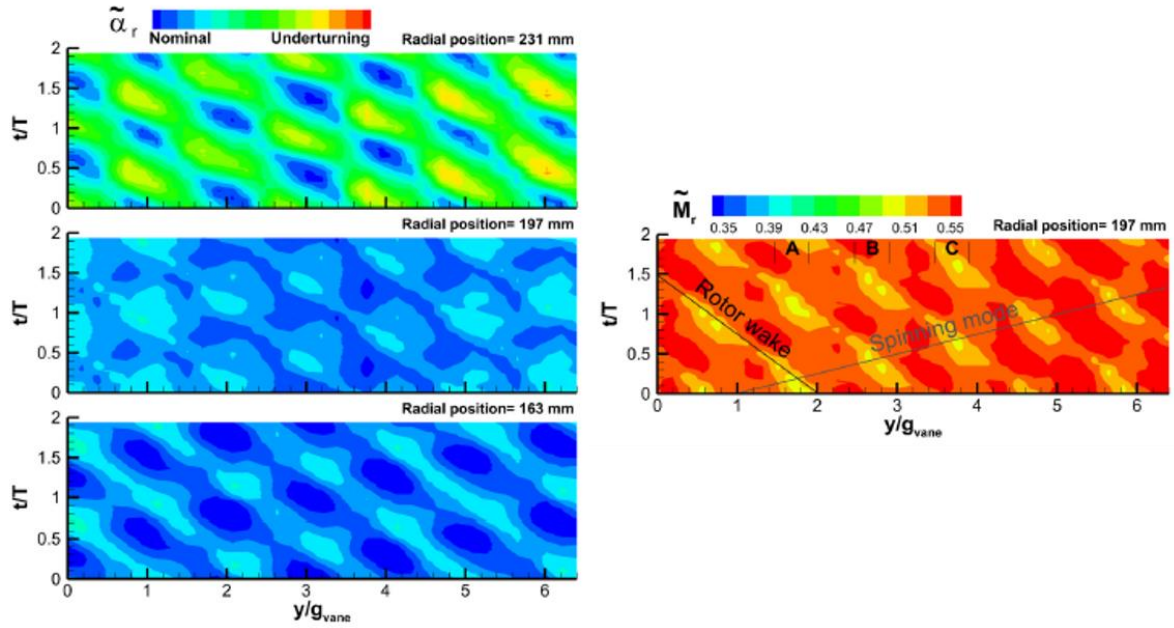

FIGURE 3.5: Time-space plots of relative exit flow angle for three radial heights and relative Mach number at the central span position. Adapted from [47]

3.2 AEROELASTICITY AND VIBRATION RESEARCH IN TURBOMACHINERY

The problem of vibration excitation has occupied engineers and researchers worldwide in all fields of technology for many decades. Regarding the turbomachinery field, the experimental research has been strongly focused on compressor development since the early 1960s. In general, experimental turbomachinery research represents a major challenge. In addition to high financial and technical costs for test rig construction and operation, difficult boundary conditions due to high speeds, temperatures, pressures and flow velocities must be taken into account. Furthermore, blade vibration measurements of rotating machines represent an exceptional challenge. This section gives a general overview of the current status of vibration research in the field of turbomachinery, including both experimental and numerical studies on vibration excitation and on the prediction of the vibrational behaviour in compressors and turbines.

3.2.1 COMPRESSORS

An extensive series of experimental and numerical investigations on compressor rotor blades aero-mechanics exist. In a very influential publication, Zielinski and Ziller [48] presented a measurement approach for blade vibration studies. In contrast to strain gauges, non-contact blade vibration measurement does not require physical contact with the blades. The methodology relies on a capacitive system and was validated in compressors environment. Having several probes distributed around the circumference of the housing, a signal is generated each time a blade passes a probe. Blade oscillations determine anticipated or delayed passage under the sensor, depending on the blade deflection. Compared to telemetry systems and strain gauges, this indirect vibration measurement technique is less complex mechanically, but more time-consuming and expensive.

The effect of the aerodynamic mistuning on the stability of a compressor cascade was investigated experimentally by Malzacher et al. [49]. Positive and negative blade mis-staggering were applied to achieve the mistuning. The author found that mis-staggering can determine a stabilizing or destabilizing effect. Even though the effect of structural mistuning could compensate the effects of the aerodynamic mistuning, the finding of this work suggests that a safety margin must be applied to account for aerodynamic mistuning.

Extensive and complex experimental investigations on a research transonic compressor were carried out by Holzinger et al [6] and [50]. Using strain gauges, tip timing and transient pressure transducers, the authors were able to measure and thoroughly explain the underlying physics of delicate phenomena such as rotating instabilities, flutter and acoustic resonance. In [50] the relationship between tip clearance and aerodynamic damping was tested. During this campaign, high vibrations limited the compressor operation range. At a closer look rotating instabilities were found to be the cause of the vibration. The authors presented data demonstrating that the rotating instabilities starts as an aerodynamic phenomenon to then develop into flutter of critical amplitude, as reported in the plots showed in FIGURE 3.6. In the figure, both the bar graph (above) and the spectrogram (below) display an increasing activity of vibrational mode M2 as the compressor back-pressure is increased, leading to the onset of flutter with forward travelling wave nodal diameter ND7.

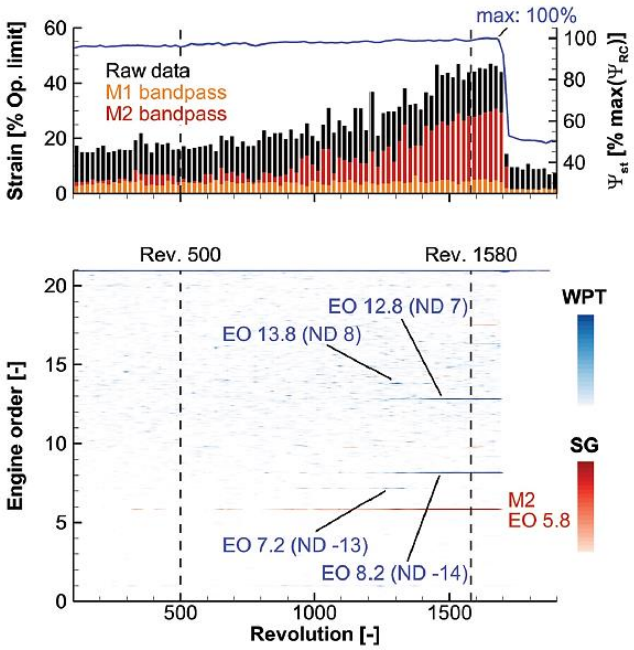

FIGURE 3.6:Measurement data representing compressor behaviour during flutter of the mode M2. From [50].

A numerical tool to analyse and predict forced response and aerodynamic damping of conventional compressor blade was developed by Mayorca et al. [51]. Within this work the authors take into account blade mistuning and compare their results with experimental measurements. The outcomes depend very much on the quality of the mapping between CFD and FE as well as on the model simplifications. In particular, to support the necessity of experimental focussed studies, the differences in aerodynamic damping between numerical simulations and experimental measurement ranged from 40% to 90%.

A numerical study aimed at the improvement of flutter stability of a fan blade was presented by Stapelfeldt et al. [52], who applied two different approaches, namely aerodynamics and aeroacoustics alterations. In the first case, radial distribution of the stagger angle was applied to stabilise the blade. In the second approach, the flutter margin of the fan was improved significantly by bleeding air from the casing above the blade tip, in order to weaken the pressure waves propagating from the trailing edge to the leading edge of the blade.

A combination of numerical and experimental techniques was used by Mischo et al. [53] to assess the impact of rotating stall on the mechanical stresses of an unshrouded centrifugal compressor. Strain gauges and unsteady pressure transducers applied on both stationary and rotating parts allowed the authors to identify rotating stall patterns and the corresponding induced stress levels. In particular, resonant blade vibration induced by the rotating stall cell induced was observed for high off-design operating conditions. Additionally, FEM fluid-structure-interaction analyses were used to predict stall

induced stresses and to assess the aerodynamic damping of the vibration mode shape, with excellent agreement to the experimental data.

3.2.2 TURBINES

Since the present work deals with experimental investigations on the low-pressure turbine of a modern aircraft engine. The literature study on this subject is therefore carried out in more detail, with particular emphasis on the experimental investigations conducted in recent years.

First off all, it is important to mention the overview of numerical and experimental research and the most relevant influences on the development of gas turbines given by Srinivasan [14].

The influence of the unsteady aerodynamic loading of airfoils oscillating in the low-reduced frequency regime was investigated by Corral and Vega [54] and [55] with a theoretical and numerical study. The authors introduced a new parameter, the unsteady loading, which is strongly connected to the phase and amplitude of the unsteady pressure produced by the airfoil oscillation. This parameter can be obtained from steady analysis and can be used to predict the airfoil stability without the need of additional flutter analysis. Ultimately, effect of unsteady loading variations due to changes in both the incidence and the mode shape can be predicted with the proposed method and flutter characteristics of different airfoils can be compared.

Numerical investigations on flutter stability of an LPT rotor were conducted by Pinelli et al. [56], with particular focus on the effects of tip shroud modelling. FE models characterised by different boundary conditions were compared with regard to the mode shape frequency and to aerodynamic damping curves. The results were validated with previous experimental data and showed the effects of contact interface modelling of the tip shroud.

The effect of multi row geometries on flutter and aerodynamic damping was studied independently by Gallardo [39] and Müller et al. [57]. The first work presents a comparison between a detailed flutter analysis for a representative LPT geometry and a single row case, highlighting the impact of upstream and downstream blade rows, as well as spinning modes. Müller instead, proposed a methodology for the evaluation of modal aero-damping based on the extraction of vibration induced pressure perturbations. The application of this procedure allowed the authors to study the influence of the steady and unsteady flow field as well as the influence of acoustic wave reflections at the adjacent stator row on the evaluated aerodynamic damping.

The problem of mistuning was the focus of several past studies. In particular, Ewins [58] and [59], as well as Castanier and Pierre [60], gave a comprehensive overview of the subject of mistuning, while Chan [61] summarised thoroughly the research status quo in the field of mistuning.

Experimental investigations were primarily carried out in cascades due to the higher simplicity of both test set-up and test execution. Nowinski and Panovsky [62] carried out several experiments in an annular cascade aimed at the understanding of the flutter mechanism and at the identification of key flutter parameters. A major result of this study was that small variations of the vibration mode shape torsion axis location had a strong effect on the blade stability. Another series of experimental studies were presented by Vogt and Fransson [13], who analysed the influence of variations of reduced frequency, flow velocity, and inflow incidence on the natural shape of vibrating blades. Their experiments were carried out in an annular sector cascade in which the middle blade was excited to vibrate in three-dimensional rigid-body modes. A sketch of the test facility is reported in FIGURE 3.7. Additionally, the figure also shows plots representing the aeroelastic stability factor as a function of the interblade phase angle, which are a typical tool for the representation of vibration stability. In this instance, the plots summarise the results obtained by Vogt regarding off design incidence (below) and reduced frequencies (above). The authors found that the main influence of a single oscillating blade is limited to the directly adjacent blades. Flow velocity was found to have only limited effect on stability, whereas increase in reduced frequency determined increased stability. Separation caused by off-design conditions was found to destabilise the axial-bending modes but to stabilise the flap-wise bending ones. Hardly any influence was observed for the torsion-dominated modes.

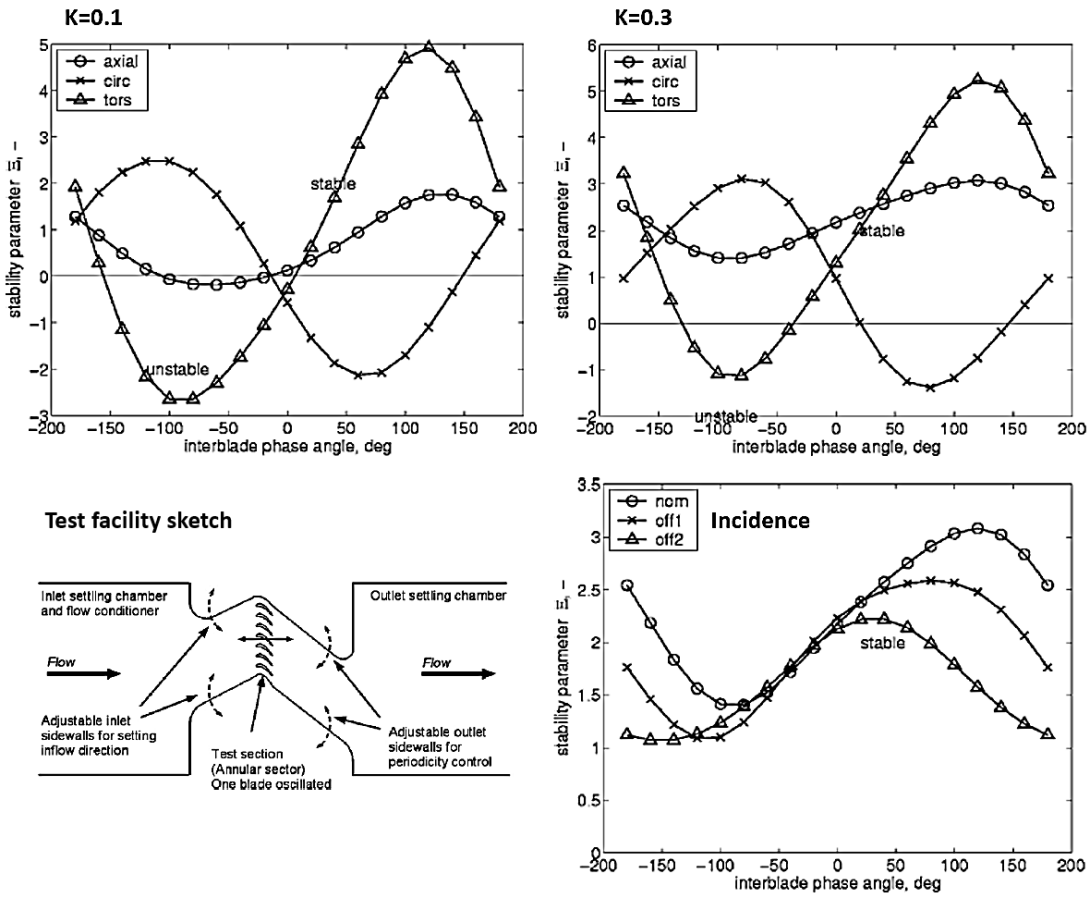

FIGURE 3.7: Variation of stability factor with interblade phase angle for two reduced frequency cases (above) and three incidence cases (below).

The influence of mistuning caused by blade stagger angle variations on the aerodynamic damping of the same oscillating LPT cascade used in the previously described study was investigated by Glodic et al. [63]. The study shows that variations in incidence angle affect the aeroelastic stability similarly to the results presented in Fransson [13].

Experimental work on a model LPT stage focused on aerodynamic excitation was presented by Megerle et al. [64]. The authors studied the very particular conditions of ventilation in last stage low pressure blades of steam turbines. Analysis of unsteady pressure measurements performed under ventilation conditions revealed that the typical rotating excitation mechanism observed in operating steam turbines is well reproduced in the model stage. The comparison with CFD results provided more detail insights in the flow features connected to the blade excitation observed during the experiments. LP steam turbine operating at high part load were studied also by Bessone et al. [65] by comparing numerical simulations with experimental data collected in a downscaled steam turbine test plant. By exciting the blade with a magnet, the authors were able to evaluate the overall damping and to separate the mechanical and aerodynamic contributions. The acquired data were used to validate a numerical tool, that was confirmed capable to evaluate blade flutter stability at low load condition properly.

An important study reporting simultaneous structural and aerodynamic damping measurement under engine relevant operating conditions in a full scale rotating turbine was presented by Kielb and Abhari [66]. Measurement of the structural and aerodynamic damping were carried out for different modes and operating conditions, including vacuum and air loaded, variations in rotor speed, inlet pressure and rotor/stator spacing. The variation of structural damping with rotational speed was analysed to understand the effect of friction damping at the interface between blade root and disc. Results of the experiments in the full scale rig showed that aerodynamic damping was a large component of the blade total damping for all modes and that different axial rotor/stator spacing and different inlet pressure resulted in similar damping levels.

Hennings and Elliot [67] conducted an experimental campaign on a single stage HPT in order to generate a data set for validation and calibration of calculation tools. A rotor with modes excitable in the operating range of the stage was instrumented with strain gauges and fast response pressure taps and tests were conducted for two stage pressure ratio. Forced response results were presented for all blades showing a large scatter both in frequency and amplitude of the maximum response. The frequency and max amplitudes scatter can be observed in the plots presented in FIGURE 3.8, reported from the authors' original work.

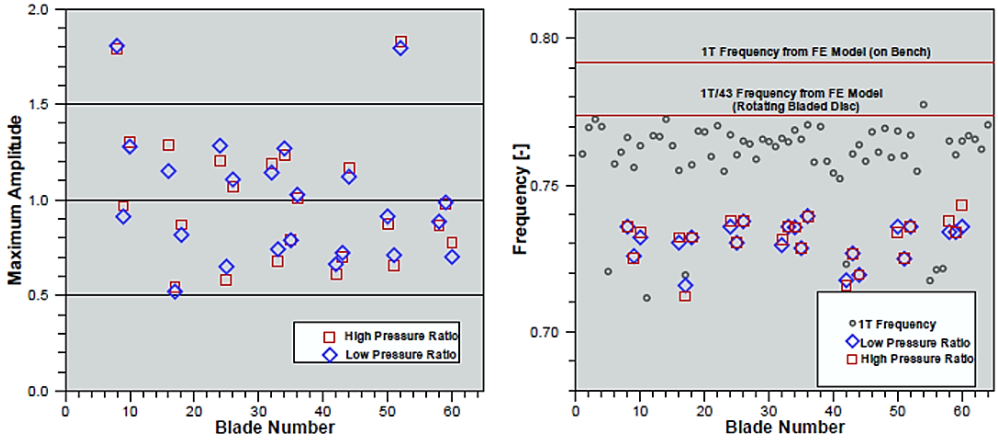

FIGURE 3.8: Comparison of the maximum blade forced response amplitude and frequency for the instrumented blades obtained for the high and low stage pressure ratio. Adapted from [67].

Finally, the previous experimental activity carried out at the Institute of Thermal Turbomachinery and Machine Dynamics of the TU Graz, on the same test rig used for the present work, must be mentioned. Several works focussed on LPT blade vibration and aerodynamic excitation were published by Schönleitner [7], Schönleitner et al. [68] and Marn et al [69]. All these works were performed analysing the aerodynamic and blade vibration data acquired in a 1.5 stages low pressure turbine rotating test rig. The flow field characteristics were studied by means of steady aerodynamic probes, while a telemetry system was operated in combination with strain gauges applied on the rotor blades to sample the blade vibrations.

The effect of different exit guide vanes design philosophies on the vibration of the rotor blades was the focus of the experimental activity presented by Schönleitner in [7] and Schönleitner et al. [68]. The blade vibration results showed that the upstream effect of the turbine exit guide vanes (TEGV) on the forced response amplitude increases with the number of vanes. This effect can be noticed in the plots representing frequency spectra of the blade vibration amplitude displayed in FIGURE 3.9. Consequently, design features that promised aerodynamic and acoustic improvements led to unfavourable aerodynamic conditions and higher blade excitation in comparison to a standard TEGV design.

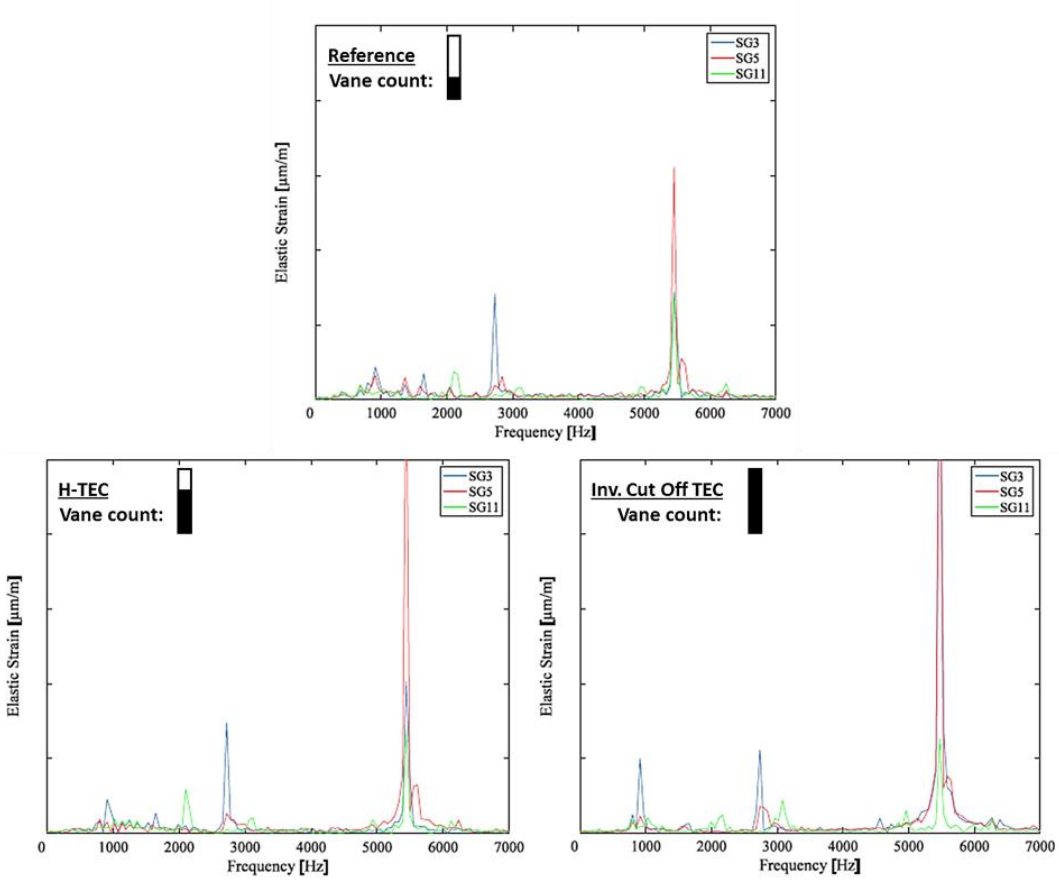

FIGURE 3.9: Adapted visualisation of the forced response spectra for the three tested TEGV design presented in [68] by Schönleitner.

Applying a similar methodology, Marn et al. [69] studied the effect of axial spacing between rotor and stator onto the blade vibrations at engine relevant conditions. By analysing the flow field upstream and downstream of the LPT stage, the authors investigated the aerodynamic excitation in relation to the forced response of the blading. The aerodynamic measurements showed a shift in the swirling flow field due to the modification of the axial gap. This modification in the flow field was connected to an amplification of the vibration amplitude. The authors therefore conclude that even though reducing axial spacing is a valid solution for engine weight reduction, the associated aeroelastic penalty must be carefully taken into consideration in the design process of modern LPT.

3.3 INLET DISTORTION IN TURBOMACHINERY

The design of modern aero engines is aimed at achieving high efficiency and low weight, in order to reduce fuel consumption and therefore CO2 emissions. The use of lighter materials and the down-sizing of the components is crucial to achieve these goals. A disadvantage of reducing axial distances between engine components is the propagation of circumferential distortions of total pressure and temperature through the machine. In fact, disturbances propagating from the combustion chamber or from the upstream stages may cause direct consequences on the forced response and flutter of the turbine rotor blades. Additionally, also flow injections, or fixed instrumentation, as well as manufacturing and assembling tolerances may produce steady and unsteady perturbations in the flow field. In many cases, such distortions could lead to resonance at low engine order excitation. Further, in certain applications turbomachines are subject to frequent alteration of the operating conditions, leading to an increase of possible resonance crossings.

3.3.1 PRESSURE INLET DISTORTIONS

3.3.1.1 FANS AND BOUNDARY LAYER INGESTION

Most of the research conducted in the past on pressure inlet distortions in aero engines has been focussed on fan blades and the effects of boundary-layer ingesting (BLI) design concepts. BLI propulsion systems aim to take advantage of the integration of the engine in the airframe body to generate improvements in propulsive efficiency, by producing thrust from the reduced velocity boundary layer air. The benefit of boundary layer ingestion (BLI) comes from re-energizing the aircraft wake. This enables less energy to be produced and then wasted by the engine, as stated by Plas et al. [70].

The aerodynamic and aeromechanical performance of BLI fan has been extensively studied in particular by NASA. The aim of the study was to design and test a distortion tolerant fan system for operation in representative BLI conditions. The main results of this work were presented by Florea et al. [71], Arend et al. [72] and Cousins et al. [73]. The impact of the distortion on the aerodynamics of the fan blades were studied by means of CFD calculations, showing that the BLI distortion propagates through the fan with little attenuation. The distortion is gradually reduced as the flow propagates through the EGV.

The fan-distortion interaction has a relevant role on both aerodynamic and aeromechanic performance and in addition it influences efficiency, as it affects the overall fuel burn benefit according to Perovic [74]. The effect of the boundary layer at the fan inlet can be explained considering that the effect of the fan is stronger in the region of low momentum. This causes the distortion in the pressure field and the induction of a region of low pressure in the low momentum area. This pressure field acts on the fluid particles which migrate towards the low momentum region, creating co-swirl and counter-swirl. This was observed by several authors, such as Longley [75] Jerez Fidalgo et al. [76] and Gunn and Hall [77]. Jerez Fidalgo et al. [76] in particular showed that the upstream redistribution introduces swirl and variation in incidence, leading to a variation in local work input. The most important contribution to the understanding of work and loss distribution in a BLI fan was made by [77]. A noteworthy result of this investigation is that efficiency is highest in the low momentum region. Studying transonic fans, this work also showed that the main feature of the BLI flow in a transonic fan is the variable shock structure between co-swirl and counter-swirl region. This leads to non-uniform variation in loss, work input, and loading, and consequently mechanical forces. A visualisation of the incidence variation and the consequent modification of the local work input obtained by [77] is shown in FIGURE 3.10.

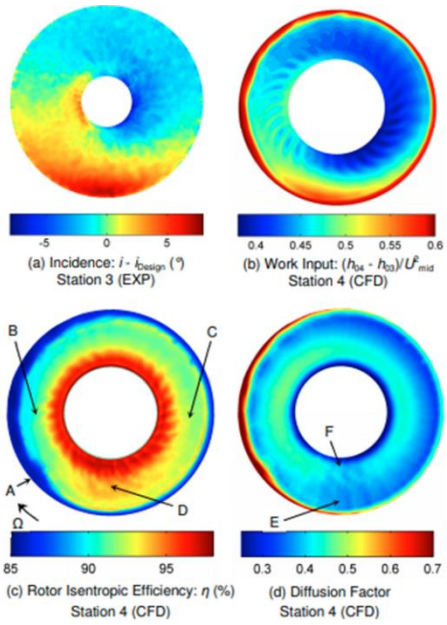

FIGURE 3.10: Rotor incidence, work, loss and diffusion factor. From [77].

Attempts to manage the non-uniformity at the inlet, by adjusting each blade to local operating conditions, were presented again by [78], who demonstrated that significant improvement in performance can be achieved by employing non-axisymmetric design. Also Hall et al. [79] investigated a series of stage design parameters and suggested that non-axisymmetric stator design was the most important for stage performance improvements in BLI. An effort to develop a distortion tolerant design was presented also in [72] and Provenza et al. [80]. The aim of the research was to design an aero-mechanically stable blade that could sustain the distorted flow environment. As a disadvantage, the efficiency of the stage was reduced compared to the original blade.

Furthermore, high cycle fatigue is a fundamental issue for BLI fans. Previous works by Bakhle et al. [81] and Min et al. [82] have shown that inlet distortion causes significant forcing at low EOs and excitation of low vibratory modes. A plot representing the EO excitation contained in the unsteady pressure load on the blades as presented by [82] is shown in FIGURE 3.11. As a result of these investigations, several design modifications including for example blade thickening at the root were employed to reduce increased dynamic stresses due to forced response. The impact of the strengthening of rotor blades on aerodynamic performance was investigated by Perovic [74], who also studied how the performance can be improved by modifying the fan rotor design and how BLI fans can operate within their stability margin even when regions outside of the clean flow stability limit are present.

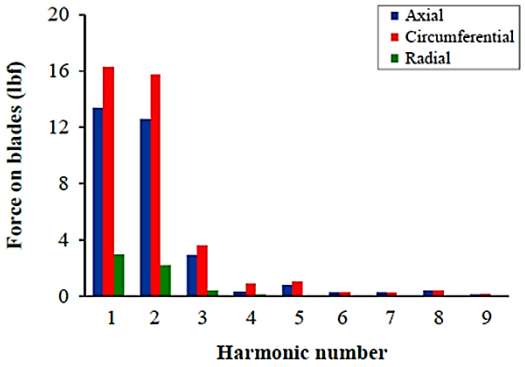

FIGURE 3.11: Blade unsteady pressure load EO excitation, at design speed. From [82].

A series of experiments were performed by Manwaring et al. [83], using screens to create distorted flow conditions at the inlet of a transonic fan and measuring the unsteady pressure loadings and the resulting blade vibration. The goal of this study was to recognise the driving mechanism of the aerodynamic excitation and of the unsteady response of a three-dimensional transonic fan rotor. The authors observed that the perturbations created at the inlet had primarily a vortical component, with also a moderate entropic content and a weak acoustic part.

A study on the prediction of low engine order resonance of fan blades, driven by inlet distortions was presented by Marshall et all. [84]. The authors used the results presented in [83], directly comparing experimental data with different evaluation methods and to assess their validity and indicate the areas that require further research effort.

3.3.1.2 PRESSURE DISTORTIONS IN COMPRESSORS AND TURBINES.

The effects of pressure inhomogeneities in the flow field has been the focal point of numerous works dealing with the flow in the inner components of the engine. The pure aerodynamic performance and the aeromechanic interaction between the pressure distortions and the force response of the blades were both studied. In a series of works focussed on centrifugal compressors, inlet distortions were used to excite blade vibrations and resonance, in order to investigate the blades forced response and damping. Kammerer and Abhari [85] [86] [87] in particular, studied the effects of inlet distortions on the blade

forcing function, the aerodynamic work and the blade damping in a high speed centrifugal compressor. Grids were installed before the impeller to generate a non-uniform inlet flow and originate unsteady blade forcing. The resulting velocity distribution at the machine inlet is reported in FIGURE 3.12. Aerodynamic probes and strain gauges were used to measure the flow properties and the blades response during three resonant crossings. The results presented by the authors indicated that the inflow distortion generated additional harmonics on top of the fundamental frequency. A single degree of freedom system was proposed as model to study the resonant response of the blades, according to the data of the first and second mode of vibration.

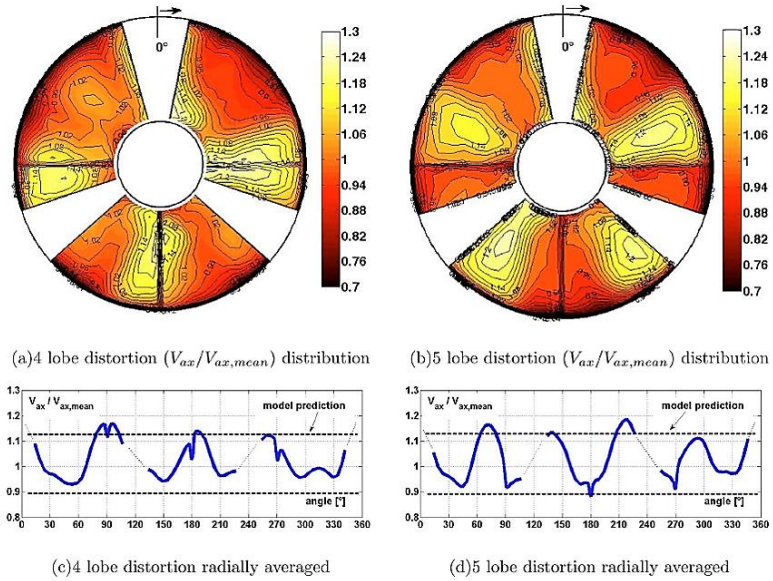

FIGURE 3.12: Distorted field of normalized velocity at the inlet of the impeller presented by Kammerer in [85].

In the second part of the study [86], a curve-fit procedure was applied to fit the blade strain response, acquired during sweeps through several resonant points, to estimate the critical damping ratio. The aerodynamic damping was found to be the dominant contributor to the overall dissipation process in this application. FIGURE 3.13 shows the damping obtained with the SDOF curve fitting procedure of the resonant response to two engine order for mode 2. Additionally, it was also observed that incidence angles and pressure distribution at the blade LE affect the aerodynamic damping value. Finally, in [87], Kammerer and Abhari describe measurements of blade surface pressure and strain gauges carried out under the effect of inlet distortions, aimed at the determination of the forcing function and the aerodynamic work.

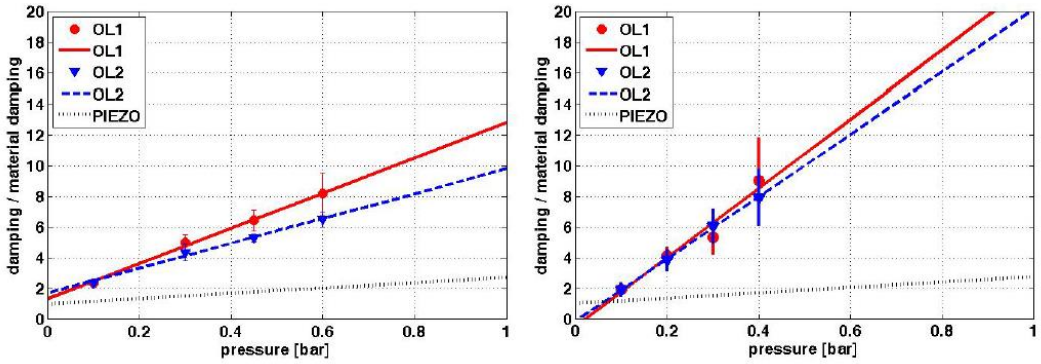

(c) Damping estimates for Mode2 and EO12 excitation. (d) Damping estimates for Mode2 and EO10 excitation.

FIGURE 3.13: Damping estimated for mode 2 as a function of inlet pressure. From [86].

The effects of upstream components on rotor blade structural dynamics and on turbine aerodynamic performance was studied in recent year by Iyengar and Simmons [88] and Simmons et al. [89], Oettinger et la. [90] and Biagiotti et al. [91]. In part 1 of their two-parts paper Iyengar and Simmons [88] investigated the aerodynamic excitation produced by stator vane and the role this has on the excitation of blade vibration by means of CFD simulations. The second part of this work [89], instead deals with the development of an empirical dynamic stress model aimed at the assessment of the material endurance strength, and ultimately at the estimation of criteria for HCF failure. Impulse response method tests were applied in combination to strain gauges, accelerometer and microphone measurements to elaborate a structural dynamic model of the blade under investigation, which was then used to assess the blade stress response for each of the flow distortions considered in this investigation. The evaluated stress levels were then compared to the endurance strength of the blade in Goodman diagrams. The authors concluded that stator and rotor interactions affect the unsteady pressure field and the performance of the machine. In particular, stator vane misalignment enhances wake pulsation, generating additional resonance frequencies. Ultimately, stress levels leading to fatigue damage may occur in presence of IGV misalignment.

The works presented so far were concentrated on the analysis of flow non-uniformities in compressors and fans. Moving our focus downstream in the machine, the impact of turbine centre frame (TCF) wakes on the downstream components was studied by Biagiotti et al. [91]. In particular, the paper focussed on the TCF wakes effect on the aeromechanical behaviour of the downstream LP rotor blades. The authors analysed a small industrial turbine, composed of a TCF followed by the two LP stages and a turbine rear frame, by means of full-annulus unsteady simulations at two operating points and compared the results with experimental data. Regarding the aerodynamic results, off-design operating conditions determine a strong incidence deviation, which generates strong separation on the TCF struts, associated to a strong distortion pattern in the downstream blade rows. This is evident in the upper plots in FIGURE 3.14, where the intensified separation is highlighted by the comparison between entropy contours at midspan obtained for the two load cases. The unsteady pressure fields were used to evaluate the harmonic amplitude and phase at the engine order corresponding to the excitation due to the TCF struts. The comparison with strain gauge acquired data showed higher modal forces and corresponding higher strain response amplitude for the part-load case characterised by separation and flow distortion. The modal amplitudes evaluated with numerical force response analysis and with the strain gauge data presented by the authors is shown in the lower chart in FIGURE 3.14. In concluding their work, the authors added some design solutions, including chord reduction of the struts or their clocking optimisation.

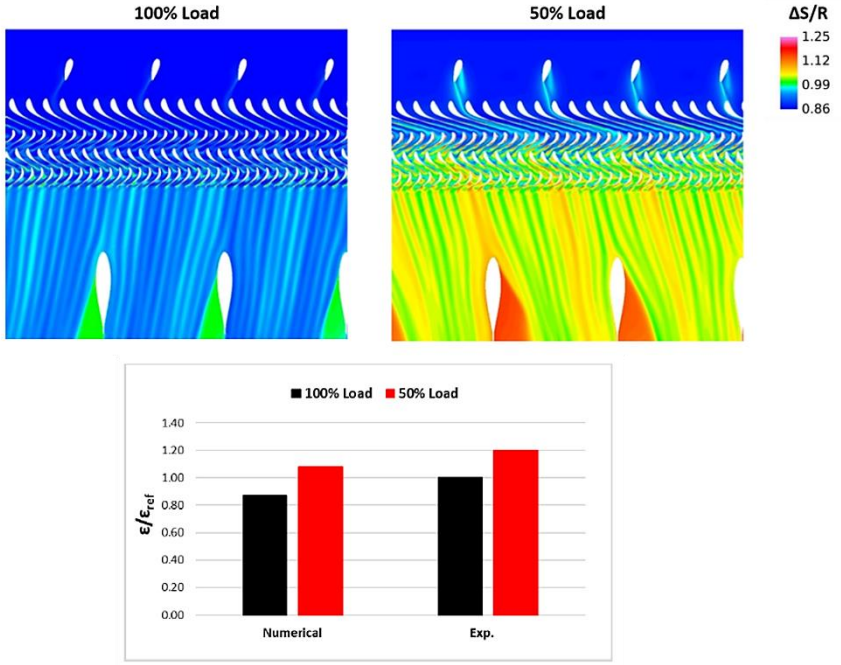

FIGURE 3.14: Entropy contours and modal blade response in terms of strain for of the two operative conditions tested by Biagiotti [91].

Furthermore, secondary flow injections, as well as manufacturing and assembling tolerances may produce relevant flow alterations, as demonstrated by Jenny et al. [23] and Lee et al. [92] respectively. The main details of the first work have been already discussed in section 3.1.1, when dealing with endwall flows. Instead, the work of Lee presented a discussion on the impact of manufacturing tolerance on the aerodynamic performance and the secondary flows of a high-pressure turbine. The authors used a 1.5 stage CFD model and tested a series of HPT rotor blade geometries to study the impact of different changes on the stage performances. With the introduction of production variability, not only the performance of the investigated HPT was altered, but most importantly the exit flow angle and the flow features in the tip region were directly influenced.

In the work of Oettinger et al. [90] the focus lied on the effect of diffusor flow inhomogeneity on the upstream axial turbine rotor row. Analysing the results of experimentally validated full annulus simulations of a 1.5 stage turbine with diffuser and exit guide vanes, the authors observed a distortion in the static pressure at diffuser inlet. The amplitude of such distortion was observed to increase for high swirl angles. Additionally, a variation of blade loading and an increase in unsteadiness in the rotor outflow were found. Similarly to the suggestion already given by several other authors cited in this thesis, the conclusions of this work stressed how important it is to include the evaluation of the interaction between turbine components in the design process.

3.3.1.3 PARTIAL ADMISSION IN STEAM TURBINES

The combination of aerodynamic effects and unsteady forcing of the rotor row due to inlet inhomogeneities have been addressed in some works dealing with partial admission. Partial admission is a technique that allows high efficiency off-design operation of turbines by admitting the fluid only into defined circumferential sectors of the inlet. This method has been consistently applied for the regulation of small gas turbines and steam turbines. The main drawback of partial admission is the generation of losses and additional blade excitation on the downstream stages.

The unsteady forces acting on the rotor blades due to partial admission were studied experimentally in a model turbine by Boulbin et al. [93]. The authors observed that the cyclic loading and unloading originating when the blade enters and leaves the arc of admission determine peaks of aerodynamic forces. An early method to analyse the vibrations during partial admission was proposed by Pigott [94].

This thorough analysis on the different factors that influence blade forcing was based on the separation between the effect of the loading due to the crossing of the arc of admission and the loading due to the upstream wakes.

More recently, a study aimed to the determination of the impact of unsteady aerodynamic forces deriving from partial admission onto the control stage rotor was carried out by Fridh et al. [95] and Hushmandi et al. [96] in a two-stage axial test turbine. In the work of Fridh et al. [95], the effects of partial admission, achieved by blocking inlet arcs with aerodynamically shaped filling blocks, were studied using unsteady data acquired during speed sweeps by means of pressure transducers and strain gauges applied on the rotor blades. The authors proposed a qualitative forcing function and compared the experimental results with previous numerical data, finding good agreement. A visualisation of the comparison is shown in FIGURE 3.15. The analysis of this forcing function in the frequency domain, and the study of the sensors response in Campbell diagrams allowed the recognition of a high quantity of added or amplified low engine orders in the forced response due to the blockage and to the loading-unloading process.

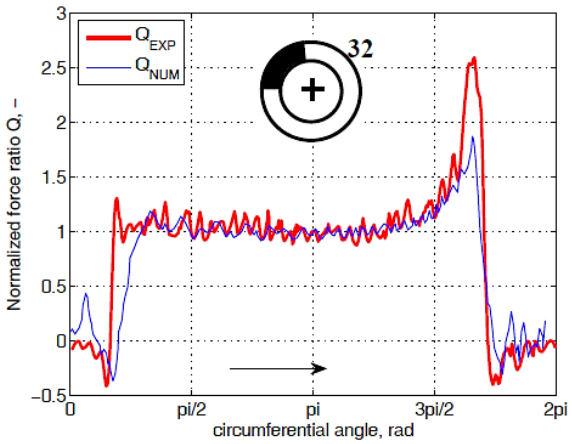

FIGURE 3.15: Qualitative forcing function due to partial admission as evaluated by [95].

The results presented in [95] are based on the numerical study by Hushmandi et al. [96]. The full annulus of the turbine was modelled, including shroud and disc cavities. Studying the unsteady forces in the frequency domain, the authors observed that partial admission caused high amplitudes at the first and second engine orders. This was due to the presence of the blockage and to the change in direction of the excitation during the loading and unloading process. Furthermore, the second stage also resulted largely influenced by the distortion in the first stage admission. The authors concluded by highlighting how important is the knowledge of the frequency content of the unsteady force acting on rotating blades during partial admission, as this could be the cause of high cycle fatigue and unexpected failures.

3.3.2 TEMPERATURE INLET DISTORTIONS

Regarding inlet temperature non-uniformities, until now the focus has been predominantly on the effects on turbine aerodynamics. But, as it will be shown, temperature distortion in the flow field were also related to effects on forced response vibrations.

Kerrebrock and Mikolajczak [97] were the first to describe the primary mechanism that controls temperature redistribution in the blade-to-blade plane in turbomachinery stages. It was observed that the high temperature non-uniformities passing through the stators are transported towards the pressure side of the stator passage. The difference of the absolute velocity at the inlet of the rotor, due to the temperature difference, is the cause of this migration and is identified as segregation effect. This phenomenon has been observed both for wakes and for temperature distortions.

The relationship between temperature and velocity described by the definition of the Mach number presented in the following equation can be exploited to describe the origin of the segregation effect.

$$Ma = \frac{c}{\sqrt{\gamma RT}} \tag{3.2}$$

According to Munk and Prim [98], the Mach number in the vane passage remains unchanged in presence of a temperature inhomogeneity without a change in inlet stagnation pressure. In the case of a high temperature non-uniformity entering the rotor frame, the only variable is the increased temperature when compared to the neighbouring colder main flow. Consequently, a difference in axial velocity induces a relative slip between the hot and cold fluid at the entrance of the rotational frame, with the hot fluid migrating toward the rotor PS. The different direction of the relative velocity at rotor inlet between cold and hot flow is highlighted in the velocity triangles shown in FIGURE 3.16.

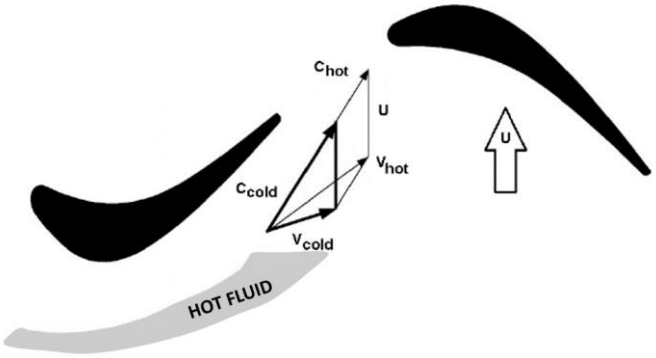

FIGURE 3.16: Velocity triangles and segregation effect. Adapted from [99]

Early experimental studies on the effects of inlet flow distortion in turbine rows were done by Munk and Prim [98]. The modifications of performance in an axial turbine stage under the influence of radial non-uniform inlet temperature profile were studied by Schwab et al. [100]. The results of an experimental campaign carried out in a large-scale low speed axial turbine presented by Butler et al. [101] demonstrated the tendency of separation of hot and cold fluid when entering the rotor row, following the segregation effect. This resulted in the hot fluid moving towards the pressure side of the rotor and the cold towards the suction side, with a consequent heating of the rotor blades pressure side. In addition to this effect, the increase of secondary flows due to temperature gradients originating from temperature distortions propagating from the turbine inlet was observed.

Extensive studies on temperature distortions, in particular hot streaks, were undertaken by Povey and Qureshi [102]. In his works, he analysed combustor representative hot streak profiles in a comprehensive review of six combustor simulators, providing realistic data useful to describe engine-representative high temperature flow path in axial turbines. An example of the temperature field at the turbine inlet, showing radial and circumferential variation extracted from this work is presented in FIGURE 3.17

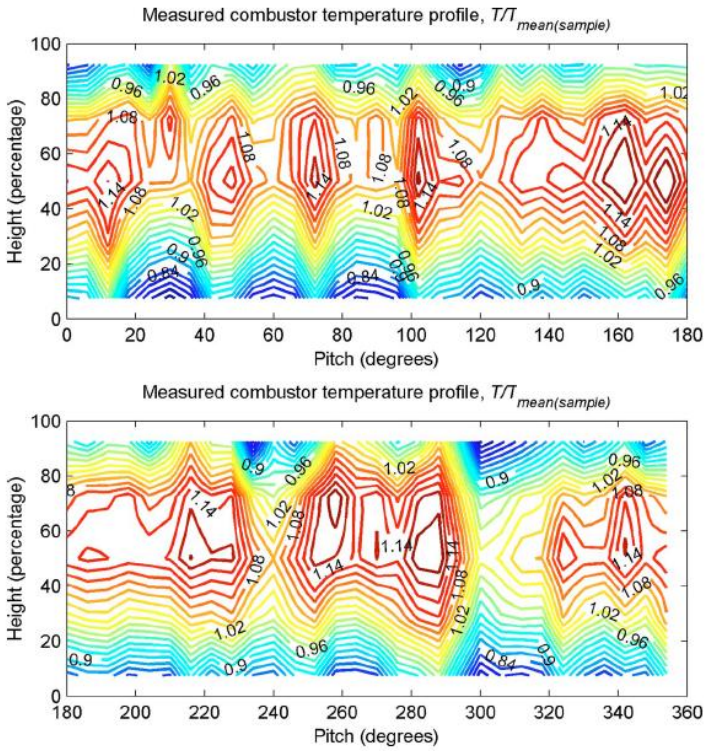

FIGURE 3.17: 360 degrees combustor exit temperature field. From [102].

Gaetani and Persico [103] and Geatani et al. [104], presented experiments and numerical simulations aimed at discussing the migration, the interaction with the blades, and the attenuation of hot streaks as they propagate through the first HP turbine stage. The results showed that the weakening of the temperature distortion during the transport across the stage rows, was not only consistent, but also highly dependent on the circumferential position of the injection. Additionally, a loss of spatial coherence and a strong spanwise migration of the perturbations were observed, especially through the crossing of the rotor row. The authors proposed the possibility of exploitation of clocking in the design process with the aim to minimize thermal loads and temperature distortions on the following stages. This was suggested since the stage-outlet temperature field resulted significantly different depending on the circumferential position of the hot streak.

Regarding secondary flows, the mechanisms that drive temperature inhomogeneities transport in turbine rotor with respect to 3D effects were studied by Prasad and Hendricks [105]. They found that the flow density variation due to the temperature differences is responsible for a modification in the secondary flows in the rotor passages. The already cited work of Ong and Miller [26] was also focussed on the superposition of blade row interaction and temperature driven phenomena on the production of rotor hub secondary vortices in the rotor passage. It was shown that the stator wake has a stronger effect of hub passage vortex enhancement compared to the hot streaks used in this study. The major effect of the enhanced secondary flow in rotor passage is the distortion of the hot streak profile on the rotor PS, the magnitude of which is dependent on the turbine and combustor design, and the compression of the hot flow streamlines on the rotor SS, the importance of which is highlighted in terms of performance and coolant effectiveness.

An experimental study of the effect of unsteady blade row interaction on the migration of hot streaks in an axial turbine was carried out by Jenny et al. [106] in a highly loaded one-and-half-stage model axial turbine. A hot spot was generated to match nondimensional parameters of real engines at the turbine inlet. Time resolved flow field measurements showed enhancement of the mixing process, demonstrated by a reduction in the maximum relative entropy difference between the free stream and the hot gasses in the control volume from inlet to outlet of the machine. The authors connected this to a region of heat loss. Moreover, the analysis of the flow at the rotor exit demonstrated that the hot gases migrate towards the end walls on the blade PS and interact with the secondary flow structures in the hub

region. A space-time visualisation of total temperature and radial velocity from the results of [106] are grouped in FIGURE 3.18. Since the highest measured total temperatures were measured at lower span compared to their position at rotor inlet, the authors concluded that the hot spot travels radially inwards crossing the rotor. This migration is visible also in the radial velocity plot. The two arrows highlight fluid moving towards the hub in the lower span and fluid moving towards the casing at higher span, demonstrating radial transport of fluid.

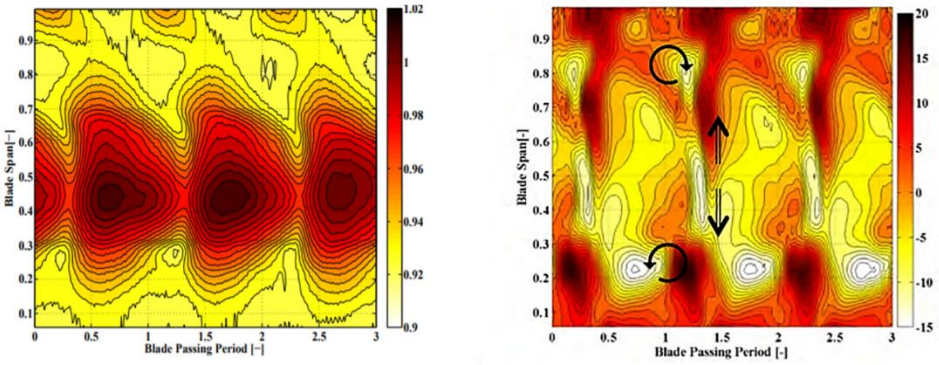

FIGURE 3.18: Space time diagrams of normalised total temperature (left) and radial velocity (right), measured at the exit of a rotor stage by [106].

The hot streak effects on thermal loads in HP turbine was the focus of a numerical study by Simone et al. [107]. This work suggested that the propagation of the temperature distortions is important not only for the first HP stage, but its effects on the stages further downstream should be considered. In particular, the authors investigated the segregation effect happening in second stage stator blades, stressing the importance of this type of analysis for the accurate evaluation of the propagation of temperature inhomogeneities through the turbine. The need to investigate further the hot streak migration pattern into the second turbine stage was also pointed out earlier by Dorney et al. [108]. The propagation of temperature non-uniformities in the machine is considered in this thesis, as the effect of inlet distortions of both pressure and temperature is investigated in an LPT stage.

All the studies presented above dealt with the aerodynamic aspect of temperature inhomogeneities in turbines, rather than with forced response analysis. In truth, forced response studies focussed on aeromechanic excitation and blade vibration due to turbine inlet temperature distortions are very sparse in the open literature. However, effects driven by temperature non-uniformities in the turbine inlet flow have been linked to forced response vibration in few studies, for example Ong and Miller [26], but have not been researched further.

Manwaring and Kirkeng [109] attempted to discern the effect of temperature distortions on the excitation at low engine orders (LEO) in a low pressure turbine. The inhomogeneities were based on the temperature field measured downstream of an HPT stage (inlet of LPT). The study considered both effects due to temperature distortions and total pressure variations, showing equally important role on the evaluation of the unsteady blade loading. Therefore, the study concluded that the analysis of blade vibrations response to turbine inlet flow variations need to be implemented in the design process.

The aeromechanical effect of temperature non-uniformities with interest on rotor blade excitation was investigated by Breard et al. [110] using 3D full-annulus simulations. This study concluded that the total blade excitation forcing can be modified substantially when the effects of temperature distortion are considered.

Mayorca et al. [111] investigated the excitation levels on LPT blades due to temperature distortions at the outlet of the fourth stage of an axial turbine. The fact that the hot streaks coming from the combustor were still present determining considerably strong temperature distortions at the LPT inlet was linked to the higher excitation. However, the authors were not able to directly connect the temperature inlet profiles to the blade excitation at the first BPF in their numerical simulations. According to the authors, this was due to the consideration of cooling flows and to the different scaling

of the blade rows adopted, which caused a modification of the potential effect and the excitation of different engine orders according to the authors

Finally, a study on the effect of temperature distortions on low engine order excitation in LPT was presented by Ioannou [99]. The author carried out a thorough analysis of the hot streak migration, with respect to the streaks shape and injection location, coolant configuration and combined effects on the secondary flow development. This was achieved using full annulus multi-blade row unsteady 3D simulations and applying combustor representative outlet temperature fields. As shown in FIGURE 3.19, the results showed significant levels of hot streak induced low engine order excitation compared to the burners and stator related blade passing frequency vibration. In particular, the EO19 and EO24 visible in the figure are directly excited by the temperature streaks. This indicate that the design process needs to take into consideration any possible inlet distortion if the aim is to obtain reliable forced response and high cycle fatigue evaluations.

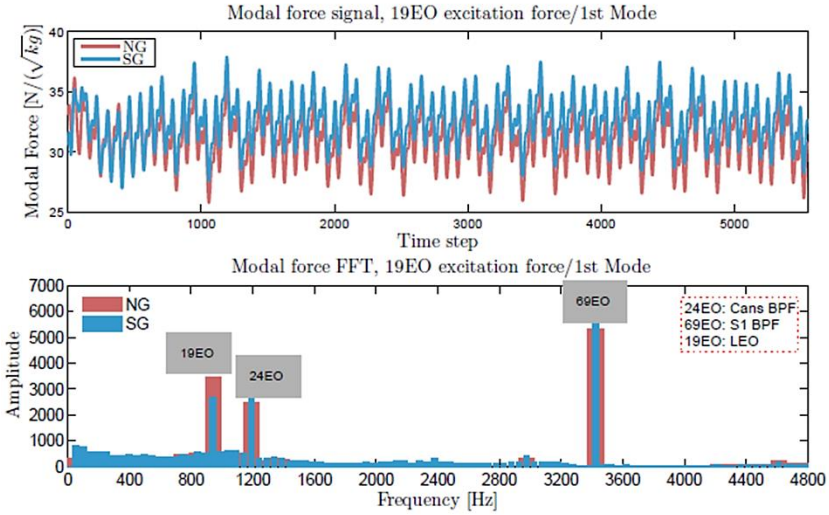

FIGURE 3.19: Comparison of first mode force amplitude for two hot streaks configurations. Adapted from [99].

3.4 LITERATURE REVIEW SUMMARY

In summary, it can be said that in the field of turbomachinery research only a few works dealt with the problems of aeroelasticity and blade vibrations with an experimental approach. A large number of past publications in the field of aeroelasticity were based on theoretical or numerical investigations. In particular, flutter phenomena were mostly assessed on the basis of aerodynamic aspects with numerical techniques. Regarding structural dynamics, mistuning and damping are among the main studied topics. Very few, if any, studies relative to the area of expertise of turbines dealt with the vibration behaviour and the assessment of the entire machine during engine relevant operations. Most experimental investigations were carried out in cascades, with the disadvantage that essential phenomena and effects do not occur due to the lack of rotation.

The effects of inlet distortions of both temperature and pressure were also largely investigated with respect to their transport through stages and the consequences on the aerodynamic performance. However, only few studies took into consideration possible structural dynamic aspects such as blade vibrations and forced response that could be connected to the presence of inflow in-homogeneities. Dealing with these aspects, both from the aerodynamic and aeroelastic point of view, this work covers an important gap in the field of aerodynamic excitation and forcing of turbomachinery blades.

4. EXPERIMENTAL FACILITY

This chapter introduces the experimental facility of the Institute for Thermal Turbomachinery and Machine Dynamics and discusses in particular the Subsonic Test Turbine Facility used for the experimental work presented in this thesis. A schematic view of the experimental facilities available at the Institute can be seen in FIGURE 4.1.

The facility is based on an electrically driven 3,3 MW compressor station providing pressurised air for all test rigs. The compressor station consists of two radial and one double screw compressors with two coolers. The machines can be operated in different configurations (serial, parallel and mixed types, with and without cooling) so that air can be provided continuously from 2.5 kg/s up to nearly 16.0 kg/s with a pressure ratio up to 2.9 bar in parallel operation and up to 7.0 kg/s at 10.0 bar in serial operation. The compressed air temperature can be regulated from 35 °C up to about 140 °C. More details on the facility can be found in Pirker et al. [112].

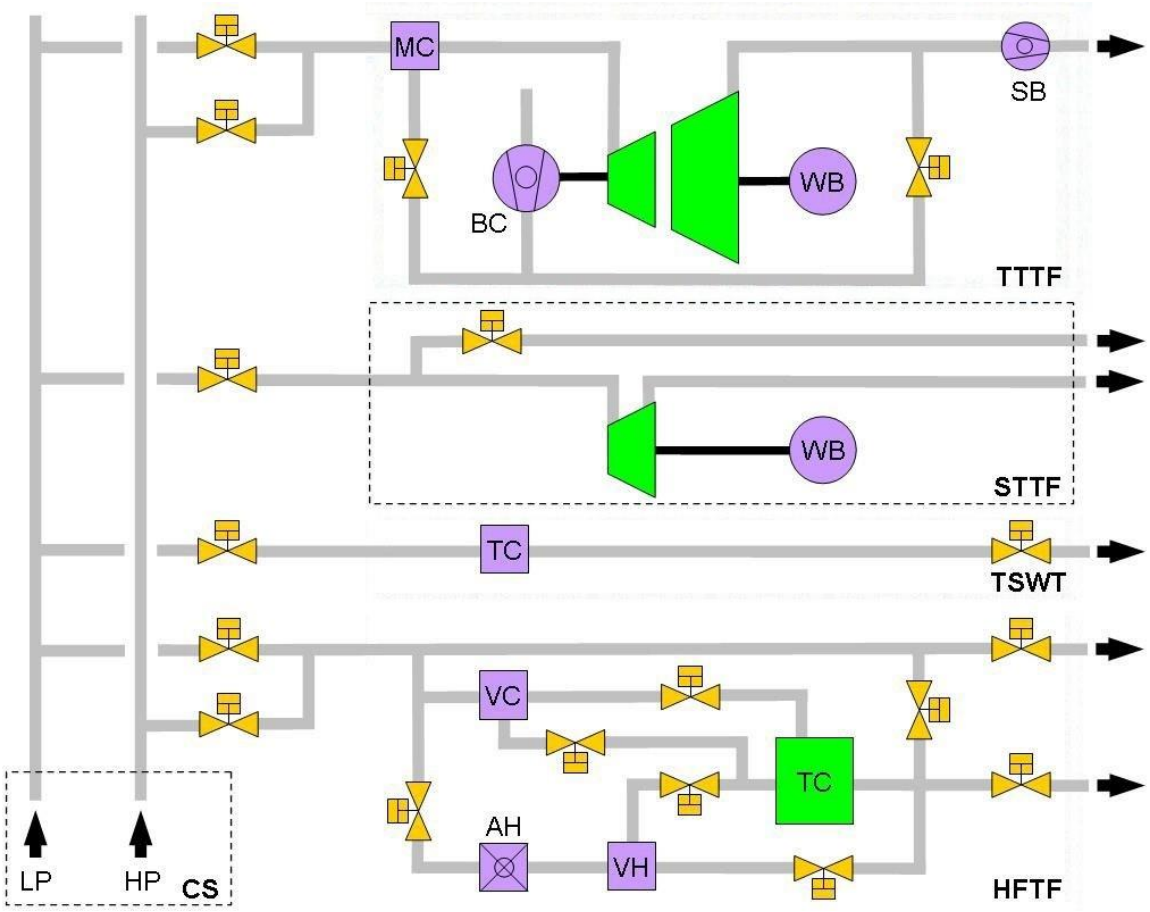

FIGURE 4.1: Schematic view of the compressor facilities at the ITTM.

4.1 SUBSONIC TEST TURBINE FACILITY FOR AERODYNAMIC AEROACOUSTIC AND AEROELASTIC INVESTIGATIONS

The test rig operated to collect the experimental data for this thesis is the so called subsonic test turbine facility (STTF), which was put in operation during the European project VITAL. The LP line of the compressor station supplying the air allows for a mass flow between 2.5 and 15 kg/s. The maximum inlet pressure of the rig is 2 bar with a max inlet temperature 100 °C due to the rotor blade material operating limit. The rig is designed for a maximum operating rotational speed of 6300 rpm and a maximum power of 500 kW.

The general view of the test rig is depicted in FIGURE 4.2. The airflow enters through a spiral inlet casing into the test facility. Then, the inlet flow passes through a de-swirler, a perforated metal plate and a set of inlet guide vanes (IGVs) before reaching the stage inlet, in order to provide well-defined and uniform inflow conditions. The air then flows through the test LPT stage, which is representative of the last stage of a commercial engine and consists of a stator row and of a high aspect ratio unshrouded rotor. To avoid any influence of potential effects on the measurements, a vane-less TEC is mounted downstream of the LPT. A 360 deg rotatable aero-acoustic measurement section is located downstream of the TEC. Finally, the air leaves the rig through the exhaust casing of the facility.

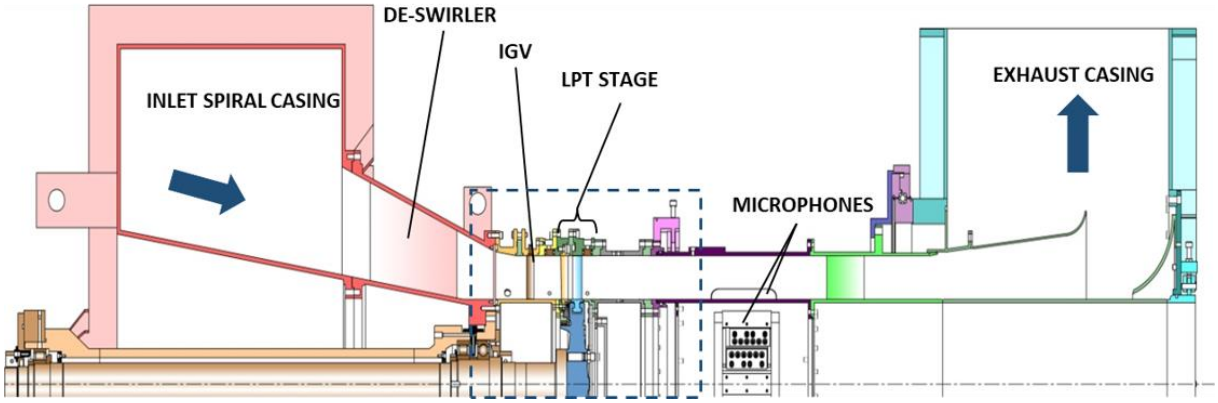

FIGURE 4.2: Cross section of the Subsonic Test Turbine Facility.

The acoustic measurement section is mounted on the exhaust casing rather than on the rotor casing, allowing for an axial movement of the section and enabling easy access to the TEC/LPT section. Instead, the TEC is mounted on the rotor casing and can easily be assembled and disassembled. Details on the construction can be found in Moser et al. [113].

In order to better depict the LPT stage used for this study, a sketch of the blades and vanes profiles at midspan is presented in FIGURE 4.3. The direction of the flow is shown as a blue arrow, the rotational direction of the LPT as a red arrow.

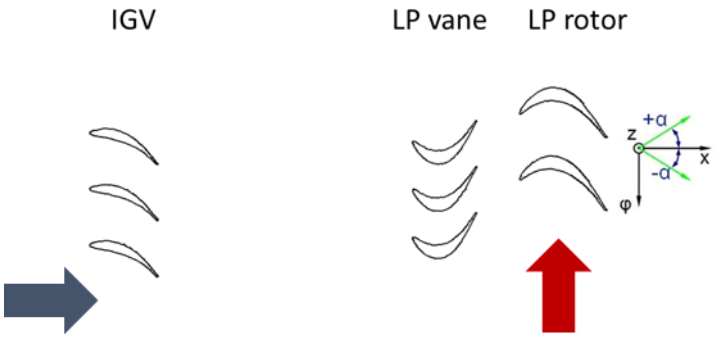

FIGURE 4.3: Sketch of the profile sections at midspan, not to scale.

4.2 STAGE SETUP AND OPERATING CONDITIONS

The test rig consists of an IGV with 83 vanes and an LPT stage. The inlet guide vanes provide a typical pre-swirl of approximately 46° across the span. The stator itself has 96 vanes and the rotor 72 blades. The details of the stage are presented in TABLE 4.1. The profiles of the vanes and blades were defined using an aero design point of the last stage LPT derived from current LPT design practice using scaling along reduced speed, reduced mass flow (both referred to 288.15 K and 1013.25 mbar) and pressure ratio. Uncommonly, the rotor used in this application is unshrouded. This results in a tip gap of 1% channel height for the operating point used in this work. The tip-leakage resulting from the tip gap results in the formation of a tip leakage vortex that influences the downstream stages.

TABLE 4.1: LPT stage geometry details.

STAGE GEOMETRY				
		IGV	**Stator**	**Rotor**
Blade Count	-	83	96	72
Axial chord length	mm	20	17	23
Aspect ratio	-	4	4.74	3.48
Stator-rotor axial gap/ rotor axial chord	-	0.565	-	
Hub to tip ratio	-	0.6596	-	

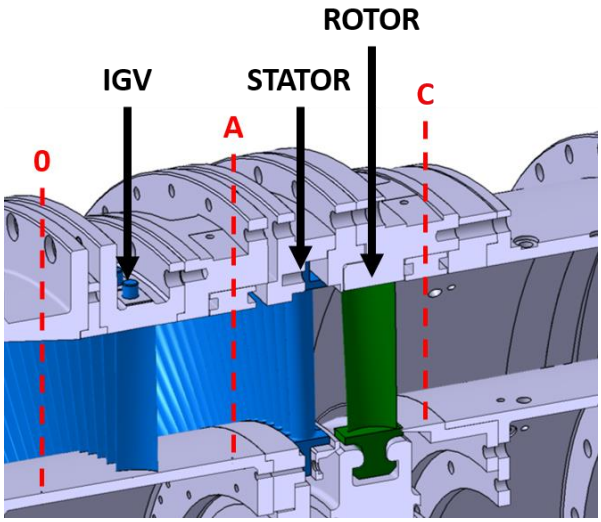

FIGURE 4.4: LPT stage.

4.3 OPERATING CONDITIONS

The aerodynamic measurements were performed at a stable operating point. TABLE 4.2 groups the reduced speed, reduced mass flow (both referred to 288.15 K and 1013.25 mbar) and pressure ratio of the nominal operating point. Due to the fact that the facility is operated as an open loop only the stage pressure ratio is set and not the absolute pressure levels at the inlet of the stage.

The vibration measurements were conducted both at the nominal operating point presented below, and during transient operation. The rotor speed was progressively increased from 90% to 125% of the nominal operating point speed at a sweep rate of approximately 5 rpm/s, while maintaining the nominal inlet total pressure constant.

TABLE 4.2: Nominal stage operating conditions.

NOMINAL OPERATING CONDITIONS		
Stage pressure ratio	pt_{IN}/pt_{OUT}	**1.16**
Corrected speed	rpm	2999
Corrected mass flow	kg/s	6.82
Inlet total pressure	K	348.65

4.4 INLET DISTORTION GENERATION

4.4.1 TOTAL PRESSURE INLET DISTORTION

In order to study the effect of different inlet distortion intensities on the LPT stage under investigation, two different concepts of pressure distortion generators were conceived. In particular, the dimensions and the distance between the distortion generator and the stage were modified. Therefore, the section of this work dealing with total pressure distortion can be separated in two parts, one regarding the generation of the non-uniformity in Plane 0 and another featuring the distortion generator in Plane A. Both systems are based around cylindrical distortion generators inserted in four equi-spaced holes around the machine circumference. Other than for the axial position of the generators, the two cases mainly differed also for the dimensions of the cylinders. In the two following sections, the differences and the specific characteristics of the two cases will be described in detail.

4.4.1.1 PLANE 0

The inlet distortion is achieved by introducing a series of cylinders with a diameter of 15 mm in the duct in plane 0, upstream of the IGVs as depicted in FIGURE 4.5. The geometry of the inlet distortion and the angular position of the cylinders is shown in FIGURE 4.6, where the red lines represent the distortion generators positioned at 45 degrees from the top position of the machine. Flowing around the cylinder, the inlet air generates a thick wake, causing a defect of velocity and therefore total pressure over the circumference. The extent of the inlet distortion generated with this method was studied with both steady and unsteady measurements in plane A, upstream of the LPT stage under investigation.

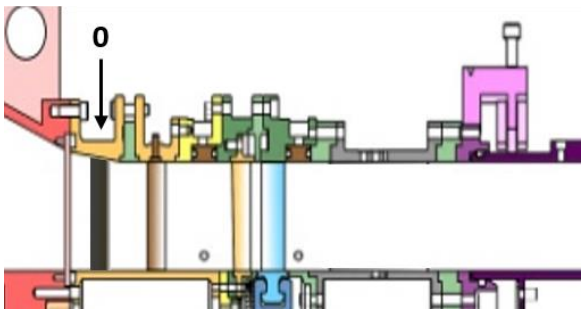

FIGURE 4.5: Schematic view of the axial position of the distortion generator positioned in plane 0.

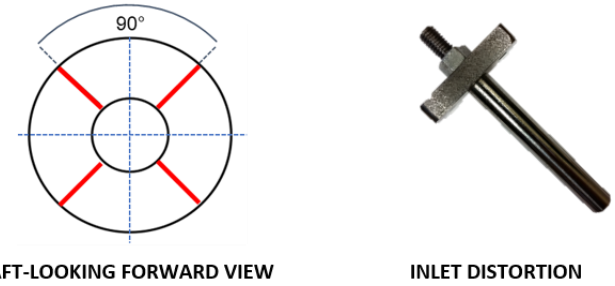

FIGURE 4.6: inlet distortion generator and aft-looking forward schematic view of the circumferential position.

4.4.1.2 PLANE A - CLOCKING

The generation of a total pressure distortion in Plane A was based on the same idea developed for Plane 0. The circumferential distortion was obtained in the inlet flow field by introducing a cylinder with a diameter of 8 mm in a plane upstream of the LPT stator row in plane A. A view of the distortion generator positioned in the machine is shown in in FIGURE 4.7. In order to expand the study carried out in plane 0, the effect of clocking was considered with the distortion generated in plane A. Three different azimuthal positions relative to the stator vanes were chosen for the generation of the localised total pressure disturbance. The locations were chosen in order to align the distortion directly with the vane leading edge (case LE), suction side (case SS) and pressure side (case PS) of the stator vane. A detailed view of the relative clocking position between the stator vanes and the distortion generator and their angular location referred to the machine top is shown in FIGURE 4.8 for the three investigated cases.

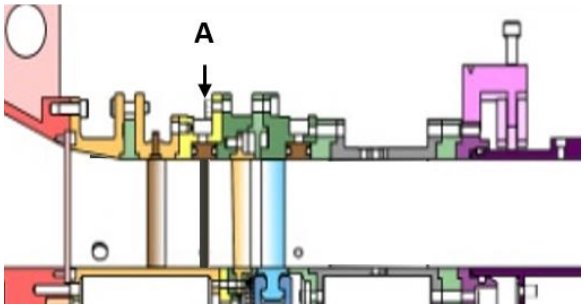

FIGURE 4.7: Schematic view of the axial position of the distortion generator positioned in plane A

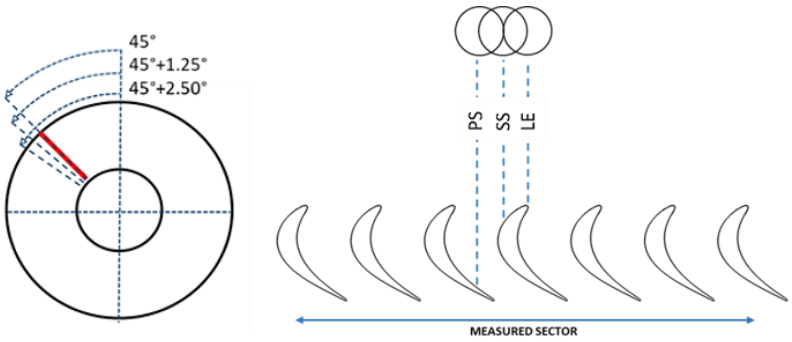

FIGURE 4.8: Detailed view of the relative position between the stator vanes and the distortion generator.

4.4.2 TEMPERATURE INLET DISTORTION – AIR INJECTION IN PLANE 0

The aim of the temperature inlet distortion generator is to create a localised total temperature distortion in the inlet flow field of the LPT stage under investigation. The temperature inlet distortion was obtained injecting air at a specific temperature through the specifically designed injector mounted in plane 0, as depicted in FIGURE 4.9.

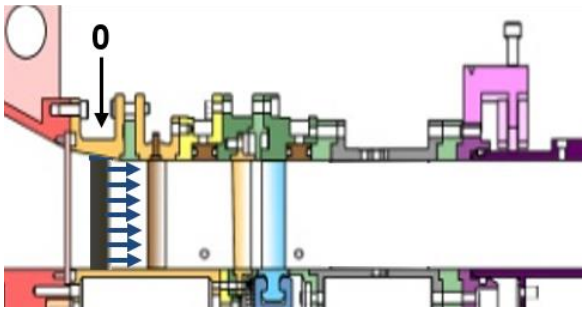

FIGURE 4.9: View of the stage and axial position of the temperature inlet distortion generator.

In order to create an even temperature distortion along the span, the distortion generator needed to be as high as the flow channel, therefore 7 equally spaced air pipes where used along the injector height. Additionally, four different injectors were built and can be fitted in the machine contemporary to achieve four different distortions along the circumference in Plane 0. The air injection system developed can provide and injection of air at a temperature ranging from 298 K to 373 K, equal to 33% to 133% of the mean undisturbed inlet flow temperature. Therefore, both positive ($T_{inj} > T_{0,avg}$) and negative ($T_{inj} < T_{0,avg}$) total temperature distortion can be generated with the current system. In order to create distortions with different intensities, different mass flows and temperature were used for the air injected in plane 0. In a preliminary series of test-runs, several temperatures and mass flow configurations were investigated, leading to the selection of the final injection characteristics used throughout the rest of this work. Ultimately, it was chosen to study two mass flows and a series of temperature ranging from 25 °C to 100 °C. TABLE 4.3 resumes all the selected configurations.

TABLE 4.3: Details of the temperature distortion injected air configurations in plane 0.

Mass flow [g/s]	**Temperature [K] ([°C])**					
2	298 (25)	310.5 (37.5)	323 (50)	363 (90)	368 (95)	373 (100)
2.5	298 (25)	310.5 (37.5)	323 (50)	363 (90)	-	-

4.4.2.1 INJECTOR DESIGN

A schematic cross-section of the injector is shown in FIGURE 4.10. The air is processed by the heating system, used to precisely regulate the injection temperature, and is then divided between the 7 pipes to generate a homogeneous injection in radial direction. A thermocouple and a static pressure tap are mounted in the air supply line just before the air is divided to control the temperature and velocity of the injected flow.

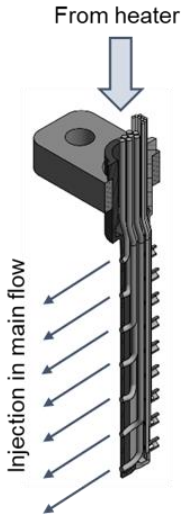

FIGURE 4.10: Cross section of the air injector.

In addition, the injector body is equipped with 9 measuring heads to allow the measurement of total pressure and total temperature in the inlet plane 0. This was necessary since the injection plane is also used for the evaluation of the inlet flow conditions of the stage. The injector body has been produced by means of Selective Laser Melting to allow the realization of its complex shape. A picture of the completed injector body taken after the use in the machine is presented in FIGURE 4.11.

FIGURE 4.11: Injector rake for air injection in plane 0

4.4.2.2 SUPPLY LINE

The air for the injection is supplied by the workshop compressed-air line. In order to provide a stable supply of air to be injected, an air-supply and heating system was designed and built. A scheme of the system is presented in FIGURE 4.12.

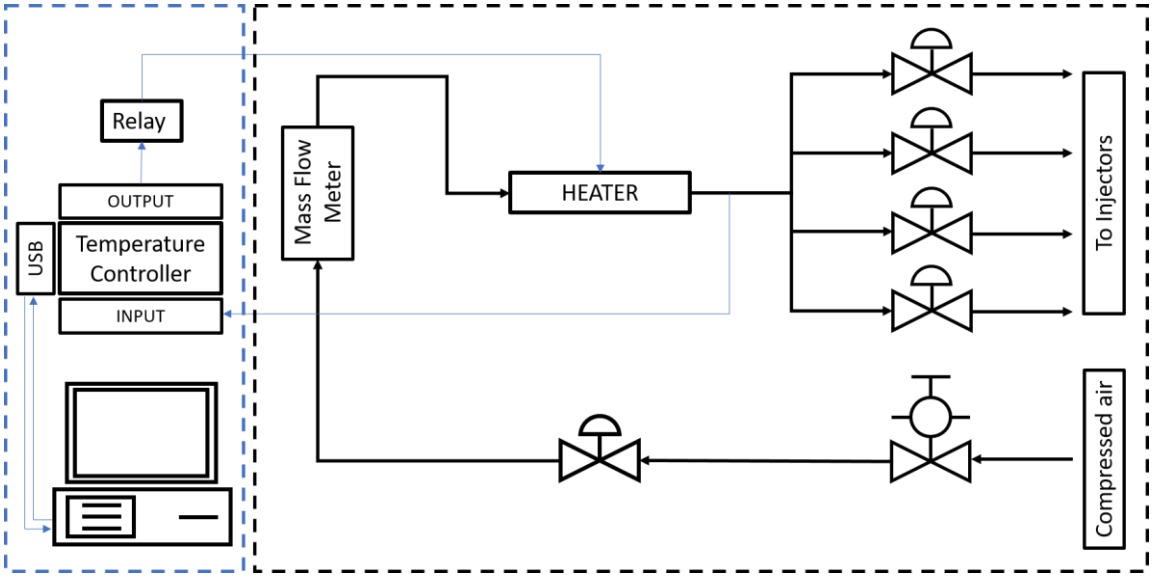

FIGURE 4.12: Scheme of the air supply and heating system with control.

The air flows from the shop compressed line into a filter fitted with a pressure regulation valve before encountering the fine regulation valve, used to precisely set the mass flow needed for the desired inlet temperature distortion. Subsequently, the temperature, pressure and mass flow are measured with a mass flow meter (Omega FMA 1600). Then, the air enters the heater used to regulate the injection temperature. The heater was supplied by Omega and is characterised by a power of 400 W (Omega AHPF-062 with 400 W - 240 V). After, the supply air is then split in four lines in order to reach the four injectors mounted around the machine inlet circumference. The complete system is visible in FIGURE 4.13. The thermocouple used for the regulation of the injection air temperature in visible fitted at the exit of the heater.

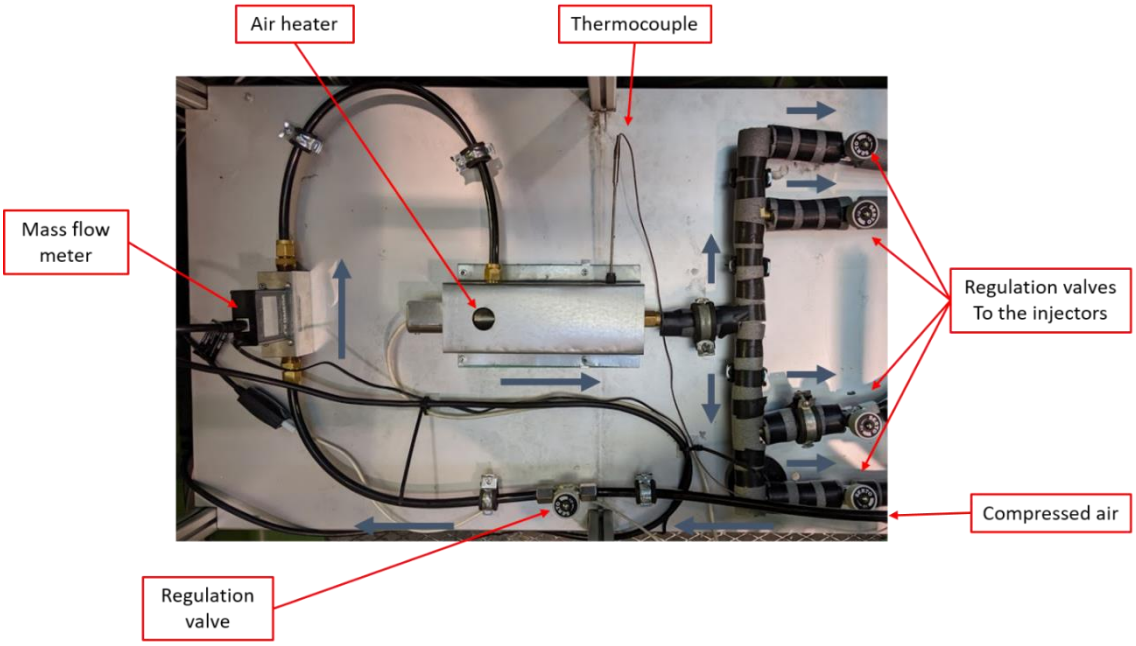

FIGURE 4.13: Air supply and heating system.

4.4.2.3 CONTROL

FIGURE 4.12 shows as well a schematic view of the control system used to regulate the air temperature. The brain of the regulation system is the temperature controller Omega CN32PT-145. A PID control loop was implemented in the temperature control. A thermocouple was mounted at the exit of the heater to measure the air temperature and the signal was used as input for the controller loop. The output control signal from the controller was directed to a solid state relay (Omega SSRL-240-660), responsible to pilot the power supply of the air heater. Furthermore, the temperature controller was connected to a regulation software running on the control-PC, in order to remotely adjust the temperature of the air supply. A scheme of a general Proportional-Integrative-Derivative control is depicted in FIGURE 4.14.

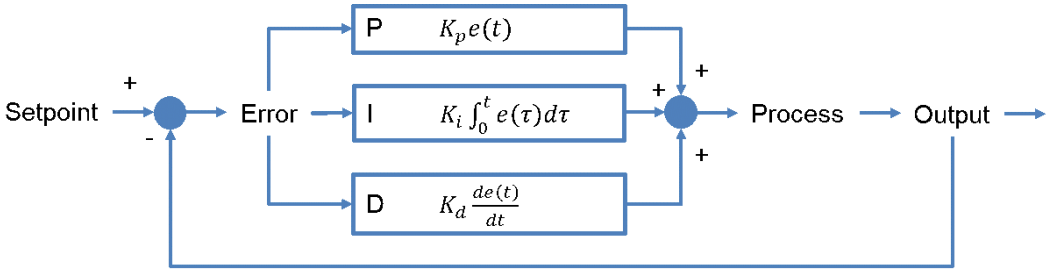

FIGURE 4.14: General scheme of PID controller implemented to regulate the air temperature.

The parameters were obtained using the auto-tune function implemented in the Omega temperature controller. FIGURE 4.15 reports a screenshot of the regulation software. One can see the temperature ramp to 90° C and the PID output control signal responsible for this temperature ramp.

FIGURE 4.15: Screenshot of the temperature control software. Upper plot: air temperature (blue)and set-point (orange). Lower plot: graph of the PID regulation output (purple).

4.4.3 TEMPERATURE INLET DISTORTION – AIR INJECTION IN PLANE A

The goal of this part of the project was to investigate the effects of the injection of secondary air in an axial position closer to the stage. The distortion generated by the injector and the air injection in the main flow create a stage inflow condition similar to the one of the configuration presented in 4.4.1.2. The additional variable introduced is the possibility to modify the intensity of both the pressure and temperature distortions, by varying the mass flow of the temperature of the injected air. The presence of the injector allows the generation of a series of inflow inhomogeneities characterised by the combination of different total temperatures and total pressures. The results obtained for the previous configurations were taken as a starting point for this last step. It was chosen to create a new device to generate the air

injection where it could be most effective and where it allows the modification of the intensity of the inflow distortion very close to the stage inlet. Therefore, it was chosen to generate the new P_t and T_t distortions in plane A, following the outcome of the investigations done for the total pressure only case and combining the injection of compressed air with warmer/colder temperature in the same plane and circumferential position. FIGURE 4.16 shows a meridional section of the turbine with a detailed sketch of the distortion generator positioned in Plane A. The circumferential position of the injector was chosen in order to align the injector to a stator vane LE, i.e. the injection angle was 45 degrees from the top.

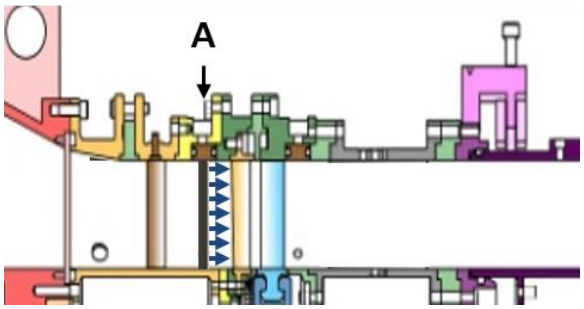

FIGURE 4.16: View of the stage and position of the air injector in plane A.

In order to maintain reliable and robust operation of the air injection system, and in order to facilitate comparisons between cases, the two mass flow rates used for the injection in plane A were used also for this configuration. Two different temperatures were chosen for each mass flow rate, corresponding to the temperatures already used in the configuration regarding the generation of temperature distortion in plane 0. The details of the injected air mass flow and temperature are presented in TABLE 4.4.

TABLE 4.4: Details of the temperature distortion injected air configurations in plane A.

Mass flow [g/s]	**Temperature [K] ([°C])**	
2	310.5 (37.5)	373 (100)
2.5	310.5 (37.5)	363 (90)

4.4.3.1 INJECTOR DESIGN

The main factors for the injector rake body design were its structural stability and ability to route the needed seven injection lines through its centre, as well as maintaining the same shape of the plane A P_t distortion generator. Additionally, the body was severely constrained because of the small rake insertion hole on the casing, which measures 8 mm in diameter. The position of the holes for the injectors along the channel height was needed to be the same as for the rakes designed for the injection in Plane 0.

As a basis for rake body design, a cylinder with a diameter of 7,8 mm was chosen, to give the rake the necessary tolerance to be inserted in the mounting hole. Supporting the choice of a cylindrical shape, round body geometries proved to be better in terms of internal space and regarding the mounting. In order to guarantee the correct angle of the air injection, a squared end was designed at the top of the injection rake, this also enabled to facilitate the mounting and assembly procedure. The direction of the injections holes is angled at 45 degrees with respect to the axial direction, in order to follow the angle of the flow in Plane A, therefore aligning the direction of the air injection to the average angle of the main flow. Two views of the final design of the injector rake are shown in FIGURE 4.17.

The compressed air necessary for the injection has been supplied using the same supply line and control system described in section 4.4.2.

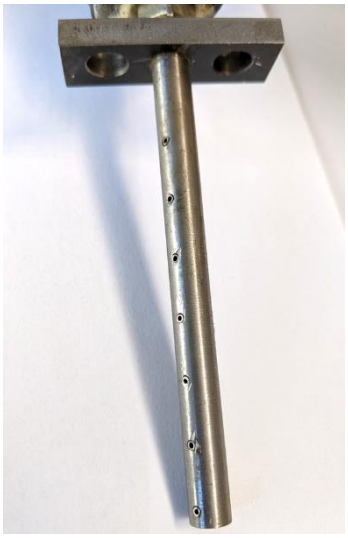

FIGURE 4.17: Injector rake for air injection in plane A.

5. MEASUREMENT SETUP

This chapter introduces the measurements techniques, probes and instruments used during the experimental campaign. Aerodynamic, acoustic and aeroelastic measurement techniques will be introduced separately.

5.1 AERODYNAMIC

The equipment and setup used for the aerodynamic measurements is discussed here. This includes the 5-hole probe, the Fast Response Aerodynamic Pressure Probe (FRAPP), static pressure taps and the data acquisition system.

5.1.1 MEASUREMENT PLANES AND SECTORS

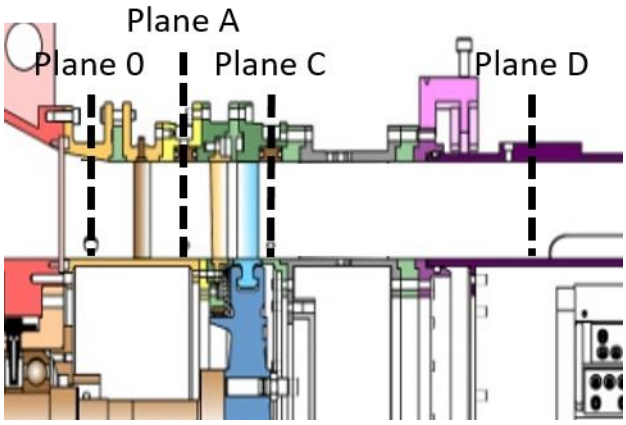

FIGURE 5.1: Measurement planes for probe measurements.

FIGURE 5.1 shows the location of the planes that are suitable for probe measurements. The available measurement planes are named 0, A, C, and D. the following list describes the details of each measurement plane:

- Plane 0: located approximately 2.4 IGV axial chords upstream of the IGV leading edge and equipped with total pressure and temperature rakes for the monitoring of the rig inlet conditions.
- Plane A: located downstream of the IGV and approximately 1.5 stator axial chords upstream of the stator vanes. This plane is used in this study to characterise the inlet conditions of the stage.

- Plane C: located 0.43 rotor axial chords downstream of the rotor trailing edge. The measurements related to the rotor exit flow conditions are acquired in this plane.
- Plane D: located at the inlet of the acoustic measurement section. The characterisation of the flow leaving the stage and entering the acoustic rig is done in this plane.

In planes A and C a rotating ring that is attached to the traversing system in order to move the probe in both circumferential and radial direction. Instead, plane D is located in the acoustic measurement section and does not need a separate system for circumferential traversing since the acoustic measurement section itself is rotatable by 360 degrees. The radial traversing unit is still needed in plane D for the movement of the probe in radial direction.

The probes were traversed in counter-clockwise direction in all the planes. The angular distance between two radial lines in the measurement grid is 0.75 deg. Consequently, one stator pitch is covered every 5 radial traverses.

5.1.1.1 MEASUREMENT SECTOR PLANE A

The sectors used for the measurements are different for the two aerodynamic probes used in this work. The difference is due to the fact that the FRAPP measurement is more time consuming than the 5HP measurements and therefore the probe is traversed only in the region of interest. FIGURE 5.2 shows the location of the two measurement sectors. Staring from the top of the test-rig, the 5HP sector starts at 37.5 deg in counter-clockwise direction and extends to 60 deg. The sector investigated with the FRAPP instead, ranges from 45 deg to 60 deg, again in counter-clockwise direction. For both probes, the radial coverage of these sectors is of 95%, due to geometrical reasons.

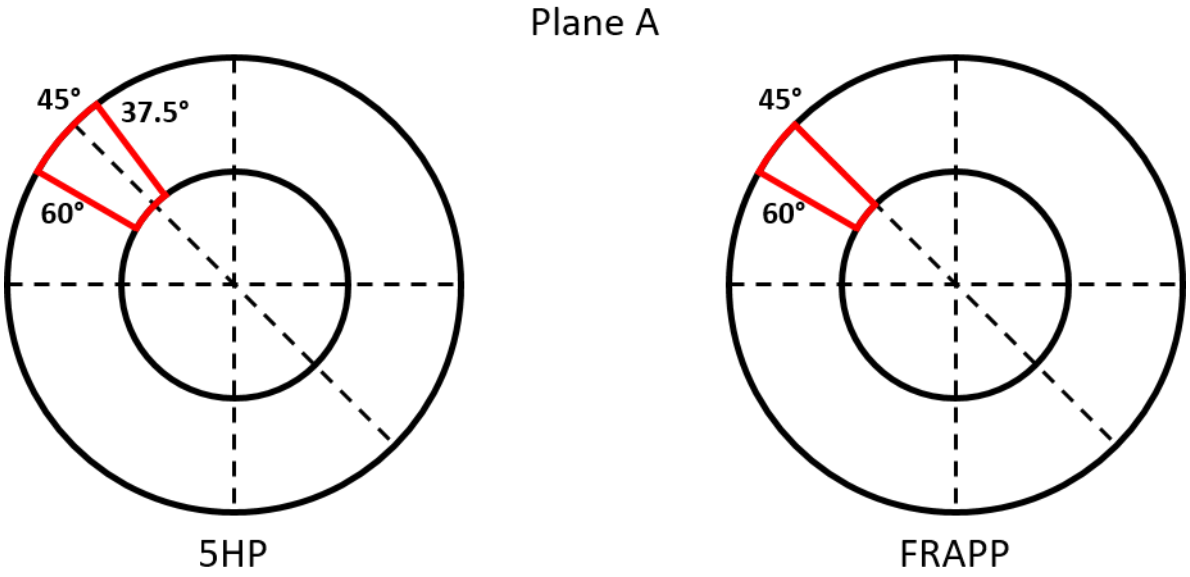

FIGURE 5.2: Schematic drawing of the measurement sectors in plane A for 5HP and FRAPP. The view is to be intended from downstream to upstream.

5.1.1.2 MEASUREMENT SECTOR PLANE C

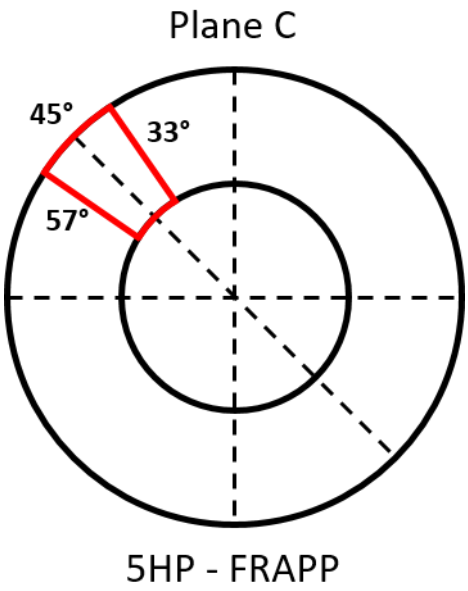

FIGURE 5.3: Schematic drawing of the measurement sector in plane C for both 5HP and FRAPP.

The measurement sector in plane C is the same for both 5HP and FRAPP. It extends from 33 deg to 60 deg, as can be seen in FIGURE 5.3. Considering that the stator pitch is 3.75 deg, this measurement sector includes 6.4 stator pitches, and is considered adequate for the purpose of including the totality of the distorted flow in one single measurement, giving the possibility to achieve well representative measurements downstream of the stage rotor. The probe traversing was always performed in counter-clockwise direction.

5.1.2 5-HOLE PROBE

A five-hole probe was used to obtain the time-averaged flow parameters like total and static pressure, total and static temperature, Mach number, as well as yaw and pitch angle. The particular probe was manufactured and calibrated at the “Institut für Strahlantriebe und Turboarbeitsmaschinen” of the RWTH University Aachen. To enable the calculation of the static temperature and pressure and the flow velocity, a type K thermocouple is mounted on the bottom of the probe head, as shown in FIGURE 5.4. A schematic view of the 5-hole probe used can be found in FIGURE 5.5. The flow quantities are obtained from the total temperature and pressure using the calibrated recovery factor provided by the probe producer. The ranges within which the calibration for the five-hole-probe is valid are shown in TABLE 5.1. To guarantee the angular position of the probe relative to the flow angle to be within the calibration range, during the acquisition the probe was turned into the flow for each measurement point.

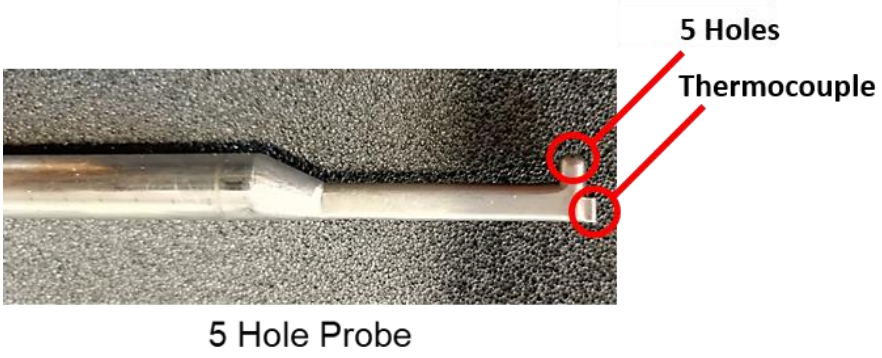

FIGURE 5.4: Five-hole-probe

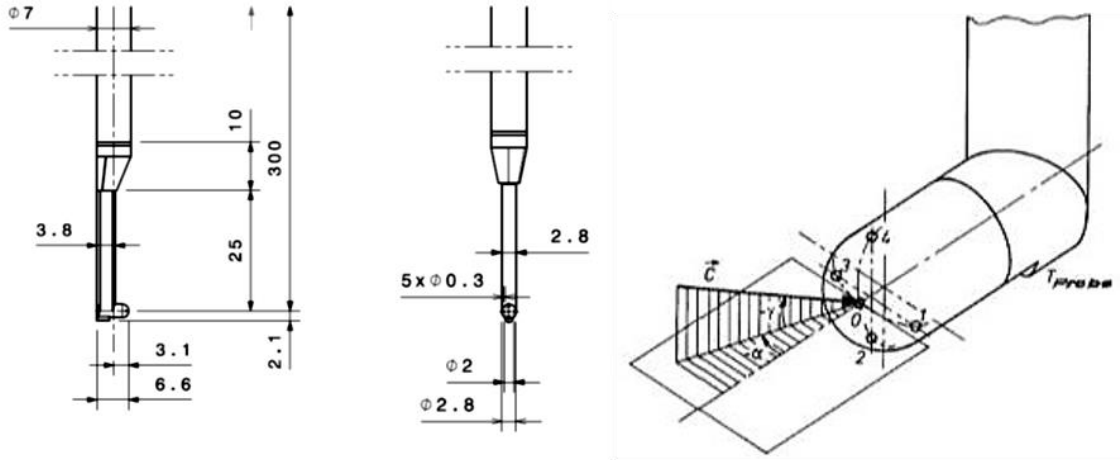

FIGURE 5.5: CAD drawings of the 5HP. From Selic et al. [114]

TABLE 5.1: Calibration range of the 5HP.

5HP CALIBRATION RANGE			
Flow parameter	**Minimum**	**Maximum**	**Step**
Mach number - Ma	0.1	0.8	0.1
Yaw angle - α	-20	20	4
Pitch angle - γ	-20	20	4

The pressure values acquired from the 5 holes on the probe's head are used to calculate 4 non-dimensional parameters used for the determination of the flow quantities. The non-dimensional parameters are defined as follows:

Mach number parameter

$$k_{Ma} = \frac{\Delta p}{p_0} \tag{5.1}$$

Yaw angle parameter

$$k_{\alpha} = \frac{p_3 - p_1}{\Delta p} \tag{5.2}$$

Pitch angle parameter

$$k_\gamma = \frac{p_4 - p_2}{\Delta p} \tag{5.3}$$

Where Δp is defined as:

$$\Delta p = p_0 - \frac{p_1 + p_3}{2} \tag{5.4}$$

The evaluation of these parameters allows us to calculate the flow quantities as Mach number, yaw angle, pitch angle, recovery factor, static pressure and total pressure, according to the multi-parameter approximation as given in the following equation (where Y indicates the variable of interest between the ones named above):

$$Y = \sum_{i=0}^{l}\sum_{j=0}^{m}\sum_{k=0}^{n} \delta_{ijk} c_{Y,ijk} k_{Ma}^{i} k_{\alpha}^{j} k_{\gamma}^{k} \tag{5.5}$$

Where$c_{Y,ijk}$ are the calibration coefficients and δ_{ijk} is evaluated according to the following definition:

$$\delta_{ijk} = \begin{cases} 1 \;\forall\; i+j+k \leq \max(l,m,n) \\ 0 \;\forall\; i+j+k > \max(l,m,n) \end{cases} \tag{5.6}$$

A total pressure and static pressure coefficients can subsequently be evaluated:

$$k_{pt} = \frac{p_t - p_0}{\Delta p} \tag{5.7}$$

$$k_p = \frac{p_0 - p}{\Delta p} \tag{5.8}$$

However, Arnold [115] in the probe calibration report suggest that it is more accurate to calculate the static pressure according to the isentropic flow relation:

$$p = \frac{p_t}{\left(1 + \frac{\kappa-1}{2} Ma^2\right)^{\frac{\kappa}{\kappa-1}}} \tag{5.9}$$

The total and static temperature of the flow as well as the recovery factor and flow velocity can be evaluated starting from the temperature measured in the probe head with the thermocouple, the evaluated Mach number and the recovery factor:

$$r = \frac{T_{probe} - T}{T_t - T} \tag{5.10}$$

$$T_t = \frac{1 + \frac{\kappa-1}{2} Ma^2}{1 + r\frac{\kappa-1}{2} Ma^2} \tag{5.11}$$

$$T = \frac{T_{probe}}{1 + r\frac{\kappa-1}{2}Ma^2} \tag{5.12}$$

$$c = Ma\sqrt{\kappa RT} \tag{5.13}$$

The following step in the analysis of the flow is the evaluation of the flow angles. To clarify the definition of the flow angles, a sketch is depicted in FIGURE 5.6. The axial direction is indicated as x, the radial direction as r and the circumferential direction as φ. The positive direction of φ corresponds to the rotational direction of the rotor. The absolute flow velocity is represented in the figure as a green arrow and can be split in an axial component c_x, a radial component c_r and a circumferential component c_t.

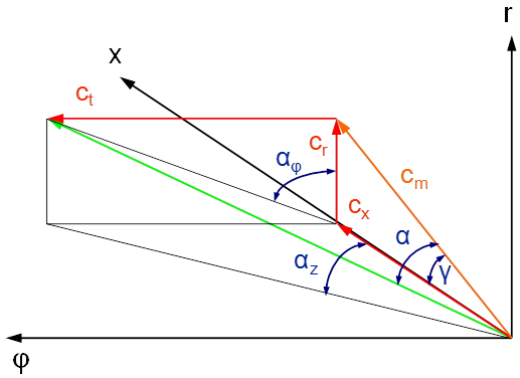

FIGURE 5.6: Definition of the flow angles. Selic [116]

Therefore, according to this definition, when the measurement plane is perpendicular to the axis of the machine, the yaw angle can be evaluated as:

$$\tan \alpha = \frac{c_t}{c_x} \tag{5.14}$$

And the pitch angle as:

$$\tan \gamma = \frac{c_r}{c_x} \tag{5.15}$$

Positive values of the yaw angle indicate that the circumferential component of the velocity vector is in the direction of the rotor revolution, whereas a positive pitch angle means that the flow is directed toward positive values of the radial coordinate.

Regarding the accuracy of the 5-hole probe data, TABLE 5.2 reports the steady pressure measurement uncertainties (within a 95% confidence interval). The five pressure values of the 5-hole probe are measured using a PSI 9016 module. The uncertainties reported here include the error due to the approximation, random error and the systematic error of the pressure transducers. The system is calibrated and has a guaranteed error according to the manufacturer of ±0.05% of full scale, ±1,034 mbar. Due to the approximation surface received during calibration the probe uncertainties are not symmetrical.

TABLE 5.2: 5-Hole probe measurement uncertainties from calibration report.

5-HOLE PROBE MEASUREMENT UNCERTAINTIES				
Mach number	Ma	0.005	-0.004	[-]
Yaw angle	α	0.3	-0.3	[deg]
Pitch angle	γ	0.5	-0.4	[deg]
Total pressure	P_t	3	-3	[mbar]
Static pressure	p	5.4	-5.1	[mbar]
Total temperature	T_t	0.6	-0.5	[K]
Static temperature	T	0.7	-0.8	[K]

5.1.3 FAST RESPONSE AERODYNAMIC PRESSURE PROBE (FRAPP)

The fast response probe here presented is a cylindrical single sensor pressure probe designed, manufactured and calibrated at the Polytechnic of Milano. The probe is composed of a main body with a diameter of 7 mm a smaller head with a diameter of 1.85 mm. A piezo-resistive pressure sensor (Kulite XCE-062) is mounted inside the probe head The probe can be seen in FIGURE 5.7and FIGURE 5.8. Despite having a single sensor, the probe can be operated as a virtual-three-sensors-probe to determine the total pressure, static pressure, Mach number, and yaw angle of the flow. Therefore, at each point of the measurement grid, at least three measurements were taken: one with the probe head aligned with the expected direction of the flow and two additional with the probe head turned of +45 deg and -45 deg relative to the mean flow direction. The information on the mean direction of the flow was taken from the results of the yaw angle obtained from a previous 5HP measurement in the same plane.

FIGURE 5.7: FRAPP probe used in this study.

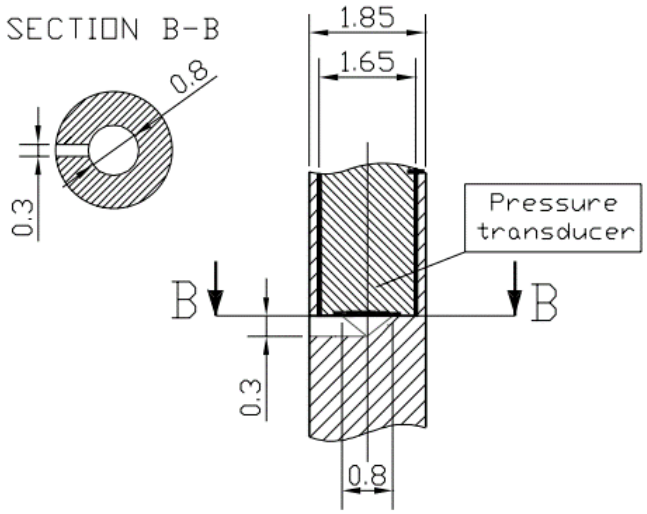

FIGURE 5.8: CAD drawings of a FRAPP from Persico et al. [117].

At each measurement piont the data was acquired for two seconds with a sample frequency of 500 kS/s. An Endevco signal conditioner (model 136) and a NI PCI-6123 data acquisition system constitute the acquisition system. The one-pulse-per-revolution shaft trigger signal was acquired simultaneously to the FRAPP data to determine the beginning and the end of a rotor revolution. Since the acquisition of the three rotational position happened at different times, the trigger information was necessary to phase-resolve the FRAPP data according to a phase-locked flow reconstruction.

A dynamic calibration has been carried out in a low pressure shock tube to characterise the dynamic behaviour of the probe. Applying the calibration to the three probe signals obtained for each measurement position, it is possible to evaluate the static pressure, the total pressure, the Mach number and the yaw angle. The probe sensitivity to the pitch angle (γ) had also been investigated, even though the device was not designed to perform measurements in radial direction. The details regarding the measurement uncertainties of the probe are reported in TABLE 5.3. All the specific of the probe are given in Persico et al. [117]

TABLE 5.3: FRAPP uncertainties from calibration report.

FRAPP MEASUREMENT UNCERTAINTIES						
Parameter	**Symbol**	**+/- Uncertainty**	**Error at γ=+10 & -10**		**Calibration Range**	**Unit**
Mach number	Ma	0.4/-0.4	0.02	0.01	0.2 to 0.8	[%]
Yaw angle	α	0.3/-0.3	0.7	0.3	-22.5 to 22.5	[deg]
Total pressure	P_t	0.5/0.5	8	1	-	[% of kinetic head]
Static pressure	p	0.5/0.5	8	1	-	[% of kinetic head]

5.1.3.1 DETERMINATION OF THE TOTAL PRESSURE RMS

The Fourier-filtering method was employed to identify the stochastic total pressure fluctuations from the unsteady FRAPP signal, as described by Lengani et al. [118]. The post-processing is based on the triple decomposition procedure of the measured value, according to the following equation:

$$p_t(t) = \overline{p_t(t)} + \langle p_t(t) \rangle + p_t'(t) \tag{5.16}$$

In this case the measured total pressure is therefore sum of the average part $\overline{p_t(t)}$, the periodic fluctuation $\langle p_t(t) \rangle$ and the stochastic fluctuations $p_t'(t)$, which depends mainly on turbulence.

In order to determine the stochastic fluctuations, both the periodic and the time-averaged parts have to be removed from the analysis. Hence, Fast Fourier Transformations (FFT) are conducted on the signals acquired at each measurement point. A sufficiently high number of samples must be chosen to reach a satisfactory frequency resolution. The spectra obtained with this procedure shows a peak at the rotor BPF and its harmonics. In order to remove the periodic part of the pressure, these amplitudes are set to zero. Additionally, the time-average part is removed as well by setting the amplitude at the frequency 0 Hz to zero, as shown in [119]. Since it is not possible to distinguish between the deterministic and the stochastic part when setting the BPF peak value to zero, a small error is made at these specific frequencies.

The resulting spectrum is then representing only the spectrum of the stochastic part of the data present in the original signal $p_t'(t)$. At this point low pass filtering and phase averaging to one rotor revolution are applied to remove high frequency content from the signal. Ultimately the RMS value to the total pressure stochastic fluctuation can be evaluated with:

$$p'_{t\,RMS} = \sqrt{\sum_m \left| \frac{P'_t[m]}{N} \right|^2} \tag{5.17}$$

Where N is the number of observations in the frequency domain and P'_t the FFT coefficients.

5.2 VIBRATION MEASUREMENTS

The experimental evaluation of the rotor blade vibration is the fundamental topic of this work. The vibration measurements were carried out by means of strain gauges applied on the surface of different blades in combination with the sensor telemetry system. The high rotational speed, together with the high operating temperature posed a particular challenge on the application of these measurement techniques. In particular, on one hand the strain gauges applied on the blades had to resist the centrifugal forces and the aerodynamic load of the flow. On the other hand, the telemetry system had to transmit a reliable electrical signal from the rotating blades to the static analysis unit at high and unstable operating speed.

5.2.1 STRAIN GAUGES AND WHEATSTONE BRIDGE

5.2.1.1 STRAIN GAUGES

A strain gauge is a device designed to convert mechanical strain into a change of electrical resistance during the measurement. Strain is defined as a measure of the relative change of length of a section. The definition of strain is:

$$\varepsilon = \frac{l - l_0}{l_0} = \frac{\Delta l}{l_0} \left[\frac{m}{m}\right] \tag{5.18}$$

By definition strain is positive when Δl is positive and negative when Δl is negative.

Strain gauges find applications in the manufacturing of transducers, i.e. force, torque and pressure transducers and load cells, and in experimental stress analysis for the determination of mechanical stress and for fatigue and residual stress analysis.

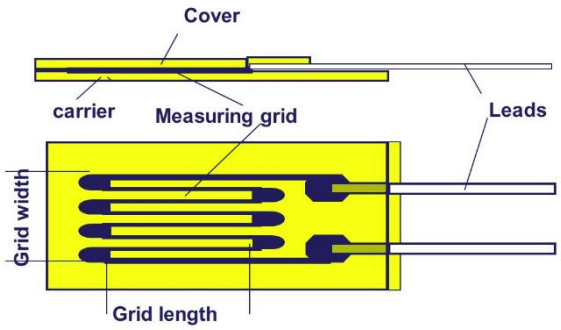

FIGURE 5.9: Strain gauge structure.

A view of the typical structure of a foil strain gauge is shown in FIGURE 5.9. A metallic measuring grid is positioned above a carrier layer, which is in direct contact with the object under investigation. the measuring grid is then covered with a protective covering layer. Two leads extend out of the device serving as electrical connection.

The measurement of strain using strain gauges assumes perfect transmission of strain from the object under investigation to the strain gauge. This requires a close bond between the strain gauge and the object. Adhesive provides the very close bond needed for strain measurements, and is widely used in this applications.

The working principle of the metal strain gage is based on the strain-resistance relationship of electrical conductors. In more details, according to Hoffmann [120] an electrical conductor changes its resistance when exposed to mechanical stress, e.g. tension or compression forces. The change in resistance due to two factors: the conductor's deformation and the change in the resistivity Q of the conductor material resulting from microstructural changes. This process is described by the following relationship:

$$\frac{dR}{R} = \varepsilon(1 + 2\upsilon) + \frac{dQ}{Q} \tag{5.19}$$

Where R is the electrical resistance of the gauge, ε the strain, ν the Poisson's ratio and Q the resistivity. The quotient of relative change of resistance $\Delta R/R_0$ and strain, also known as gauge factor is defined as:

$$k = \frac{\Delta R/R_0}{\Delta l/l_0} = \frac{\Delta R/R_0}{\varepsilon} \tag{5.20}$$

The results of different investigations into various materials have indicated material with values of k close to 2 as particularly attractive for strain gauges manufacturing.

In this study, The LPT rotor was instrumented with 12 strain gauges applied on different blades. The position of the strain gauges on the blades will be discussed in the following sections and was performed according to Schönleitner et al. [121]. The devices used for the measurements are HBM 3/350 LY63

aluminium strain gauges, with an electrical resistance of 350Ω +/-0.30%, a gauge factor k of 2.05+/-1.0%, a transverse sensitivity of 0.0% and a temperature coefficient of gauge factor of $101 \pm 10 \left[\frac{10^{-6}}{K}\right]$

5.2.1.2 WHEATSTONE BRIDGE

The change of resistance of the strain gauges is measured by a Wheatstone bridge circuit. In general, since both the strain gauge and the bridge circuit are passive elements in the physical sense, energy must be supplied to obtain the measurement signal. In this application, this is done by the sensor telemetry system, which will be explained in more detail in the following paragraphs.

A schematic view of the Wheatstone bridge is shown in FIGURE 5.10. The bridge is an electrical circuit that can be used in different ways to measure an unknown resistance:

- For the determination of the absolute value of a resistance by comparison with a known resistance
- For the determination of relative changes in resistance

The second method is used with strain gauges, enabling the detection of relative changes of resistance, which are usually very small, around the order of 10^{-4} to 10^{-2} Ω/Ω.

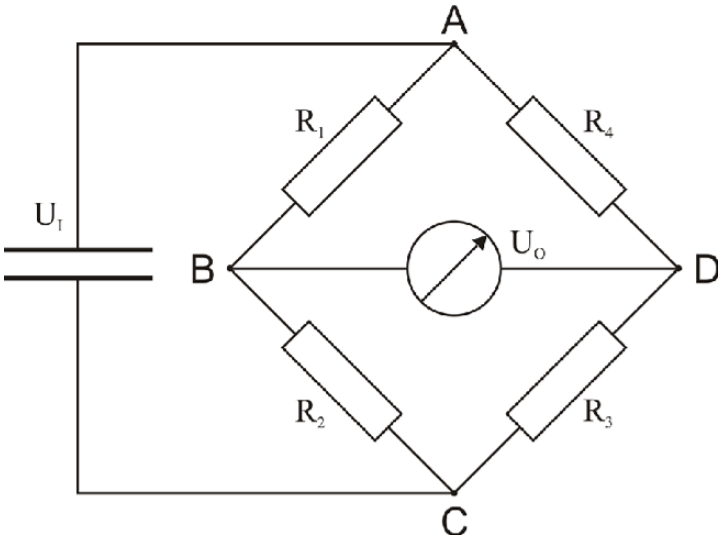

FIGURE 5.10: Schematic of the Wheatstone bridge.

In the figure, the four arms of the bridge are formed by the resistors R_1, R_2 R_3 and R_4. The points A and C represent the connection to the input voltage U_I, whereas the output voltage U_0, which the measurement signal ,is available between nodes B and D.

When a supply voltage U_I is applied to the bridge, it divides in the two halves of the bridge R1, R2 and R4, R3 as a ratio of the corresponding bridge resistances, i.e., each half of the bridge forms a voltage divider. In case the bridge results unbalanced, the output voltage can be measured between the nodes B and D and can be calculated as follows:

$$U_0 = U_I \left(\frac{R_1}{R_1 + R_2} - \frac{R_4}{R_4 + R_3}\right) \tag{5.21}$$

With a certain strain, the resistance of the strain gauges changes by a certain amount ΔR, giving us the following equation:

$$U_0 = U_I \left(\frac{R_1 + \Delta R_1}{R_1 + \Delta R_1 + R_2 + \Delta R_2} - \frac{R_4 + \Delta R_4}{R_4 + \Delta R_4 + R_3 + \Delta R_3} \right) \tag{5.22}$$

For strain measurements, the resistances R_1 and R_2 must be equal in the Wheatstone bridge. Same applies to R_3 and R_4. Therefore, the following equation can be determined:

$$\frac{U_0}{U_I} = \frac{1}{4} \left(\frac{\Delta R_1}{R_1} - \frac{\Delta R_2}{R_2} + \frac{\Delta R_3}{R_3} - \frac{\Delta R_4}{R_4} \right) \tag{5.23}$$

At this point, from equation (5.20) the term $\Delta R/R$ can be replaced by the term $(k \cdot \varepsilon)$:

$$\frac{U_0}{U_I} = \frac{k}{4} (\varepsilon_1 - \varepsilon_2 + \varepsilon_3 - \varepsilon_4) \tag{5.24}$$

In this equation it is assumed that all the resistances in the bridge are changing contemporary. This is hardly the case in experimental activities. Usually the strain gauges are contained only in some of the bridges arms and the remainder arms consist of bridge completion resistors. Various configurations are possible, such as quarter bridge, half bridge, double quarter or diagonal bridge and full bridge. The diagrams in FIGURE 5.11 show a Wheatstone bridge configured as a simple quarter bridge circuit with one active strain gauge. This configuration has the benefits of ease of installation, but the normal and bending strain are superimposed in the measurement signal and the effects of the temperature are not automatically compensated. The schematic shown in FIGURE 5.11 is taken from the user manual of the telemetry measurement system (Bär [122]) and represents exactly the configuration applied for the measurements reported in this work. The strain gauge applied on the rotor blades corresponds to a resistance in the bridge circuit. The remaining three resistors are permanently integrated in the sensor telemetry. The only decisive factor is that the resistor that is connected in series with the strain gauge must have the same basic resistance.

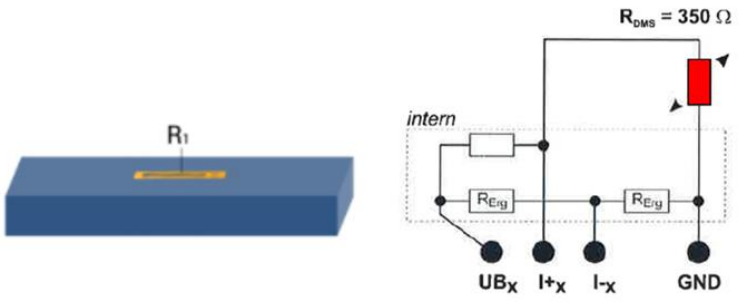

[114]

FIGURE 5.11: Schematic view of a Wheatstone bridge with simple quarter bridge configuration. From [122] and [120].

Considering that in the quarter bridge configuration only the resistor represented by the strain gauge will alter its resistance, in this application equation (5.24) becomes:

$$\frac{U_0}{U_I} = \frac{k}{4} \cdot \varepsilon_1 \tag{5.25}$$

Therefore, knowing the input voltage and the gauge factor of the strain gauge and measuring the output voltage, it is possible to obtain the value of the strain.

5.2.2 TELEMETRY SYSTEM

In the course of this work, a modular sensor telemetry system was used. The device was designed during the course of a previous project at the ITTM together with Manner Sensortelemetrie. The system consists in principles of a sensor signal amplifier, a stator and rotor antenna, an HF-line and an evaluation unit. The sensor telemetry system has a modular design, which means that modules for temperature measurements and pressure sensors can be used variably in addition to blade vibrations. A total of 20 channels are available.

FIGURE 5.12 shows the general measurement setup and FIGURE 5.13 the measurement data and powering principles. The signal from the strain sensors is fed into the rotor antenna via the signal amplifier mounted directly on the rotor disc. Then the rotor-stator principle is used to transmit the signal to the stator antenna. In other words, the rotor unit appears as a moving conductor in a magnetic field generated by the static antenna. As a result, the real-time signal from the strain gauge is transmitted to the antenna via the induction principle. The data are then transmitted from the static part of the antenna with a cable to the evaluation unit.

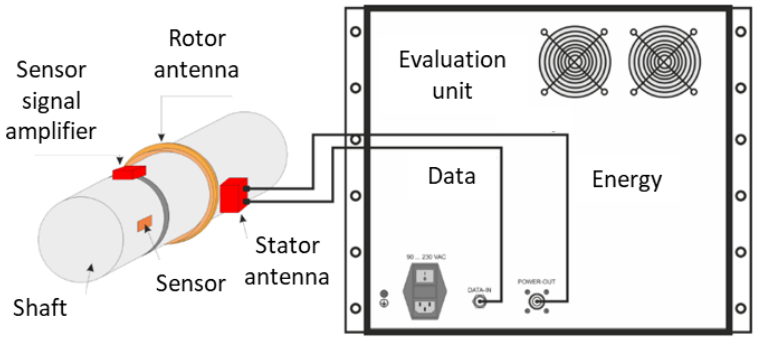

FIGURE 5.12: Complete vibration measurement system [123].

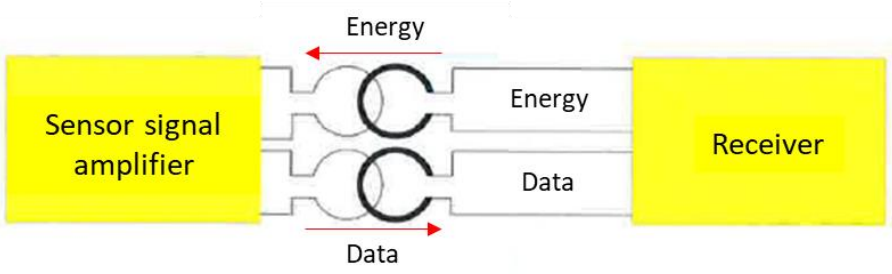

FIGURE 5.13: Data and energy flow in the telemetry system [123].

More details regarding the installation layout of the telemetry system for blade vibration measurement can be introduced from the description of FIGURE 5.14. Each strain gauge is applied to the rotor blades and is connected to a circuit board located in the centre of the rotor disc with copper wire. The signal amplifier is then connected to the pins of the circuit board and secured with screws to the rotor disc. Due to its small size and mass, the rotor unit of the telemetry system has no influence on

the rotor dynamics or structural dynamic properties of the low-pressure rotor. As already discussed above, the signal is transmitted contactless to the static unit. This part of the telemetry system is integrated in the structural part of the turbine exit casing and t is equipped with two connections, one for the data line and one for the power line.

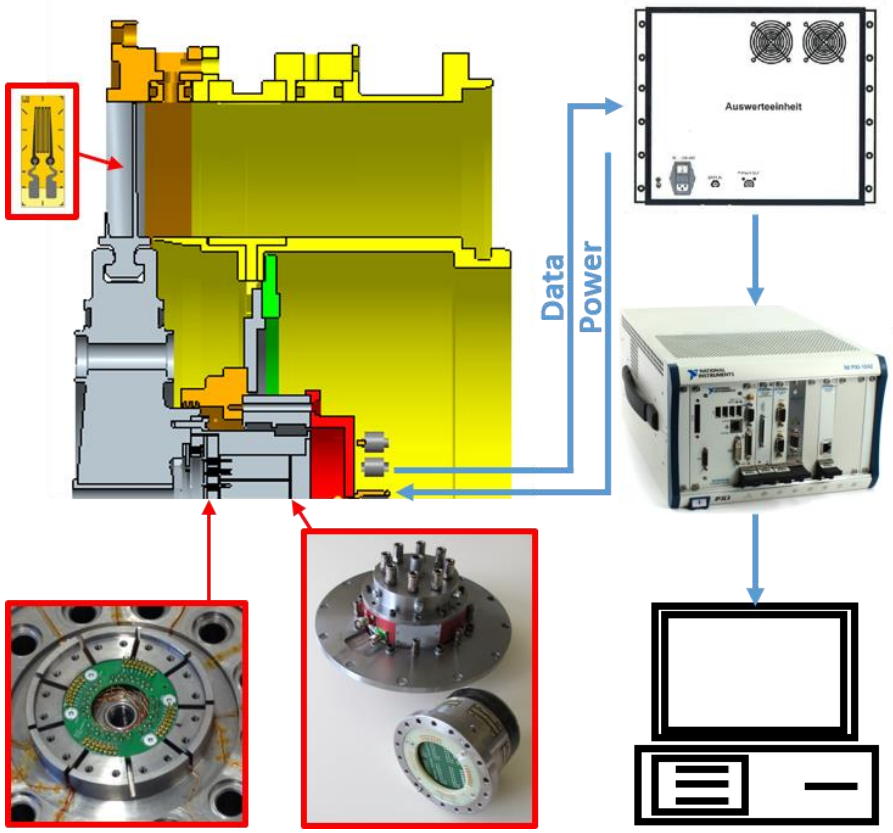

FIGURE 5.14: Schematic view of the vibration measurement system.

Regarding the technical data of the sensor telemetry system, a total of 20 channels are available. Additionally, the system has a modular design, which means that the modules for temperature measurements and pressure sensors can be used variably in addition to blade vibrations. The most important technical specifications are listed in the following list; more detailed information on this high-performance sensor telemetry can be found in the operating manual [122]:

- Sensor telemetry system with radial antenna (air gap 2mm);
- Specifically designed for turbine applications;
- Simultaneous acquisition of all signals with 12bit resolution;
- Sampling rate 400000samples/s;
- DMS resistance 350Ω (any resistance can be set);
- Quarter bridge circuit;
- Vibration analysis from 0 to 100kHz;
- Speed range up to max. 11000 rms;
- Temperature range -10 °C to +125 °C;

The signal flow during the blade vibration measurements is shown schematically in FIGURE 5.14. The data reaches the Manner evaluation unit via a high frequency cable. The signals are then transmitted as analogic tension signals (+/- 10V) via BNC cables to a BNC to ‘InfiniBand’ adapter rack, necessary to allow the connection to the acquisition system PXI-Chassis from National Instruments. The chassis is fitted with two PXIe-4498 acquisition cards with a total of 32 input channels. The signals are then transmitted via optic fibre cable to the measurement a PC equipped with a NI PXIe-8374 input card.

The unfiltered signals of the strain gauges were recorded at a sampling rate of 204800samples/s using a specific software designed with NI Labview. The measurement duration at stable operating point is about 60s. The bandwidth of the DMS channel is from 0 to 100kHz. According to the Nyquist criterion, the required sampling frequency to avoid alias effects must be at least double of the maximum frequency analysed. Considering that for the analysis presented in this work the highest frequency in the analysed spectrum is 10000Hz, the Nyquist criterion is clearly fulfilled.

5.2.3 INSTRUMENTATION OF THE ROTOR BLADES

The rotor was instrumented with twelve strain gauges (SG) applied on different blades. The final configuration of the rotor instrumented with the SGs is depicted in FIGURE 5.15. The position of the strain gauges on the blades was chosen with the aim to record as many modes of blade vibration as possible. In particular, in order to obtain a high quality signal, it was necessary to apply the strain gauges at blade surface positions with large strain gradients. To find the optimal strain gauge setup, a large number of numerical and experimental studies have been carried out during a previous project and reported in Schönleitner et al. [121] and Schönleitner et al. [123]. Other well-known works published by Szwedowicz et al [124] Sensmeir and Nichol [125] and Sensmeir and Nichol [126], which dealt intensively with the optimum strain gauge application were taken under consideration during the selection process of the strain gauge positioning.

FIGURE 5.15: Rotor instrumented with strain gauges and circuit connection board.

Before the application of the SGs on the blades, the surface was grinded slightly to ensure good adhesion of the strain gauges. Glue was then used to stick the gauges on the desired position. Once the glue cured, the copper wires for the signal transmission were soldered to the SG terminals and then routed and glued to the blade and disc surfaces. The diameter of the copper wire measures only 0.1mm in diameter. It was chosen as small as possible to limit any influence on the flow field around the blades. In addition, the soldered joints were kept as small as possible, as these parts are subject high stresses due to centrifugal force and thus may represents a possible problem for the transmission of the signal and would cause signal loss if broken.

After gluing, the wires were soldered to the connection board. The details of the board layout can be found in [122]. Finally, the entire instrumentation was sealed with a protective coating to ensure long-term operation and measuring accuracy. Since the strain gauge adhesive is hydrophilic and attracts water from the air humidity, it would lose adhesive power and additionally the strain gauge would quickly

start to corrode and thus become unusable. Two detailed pictures of the rotor blades and disc instrumented with the strain gauges and with the connection wires can be seen in FIGURE 5.16.

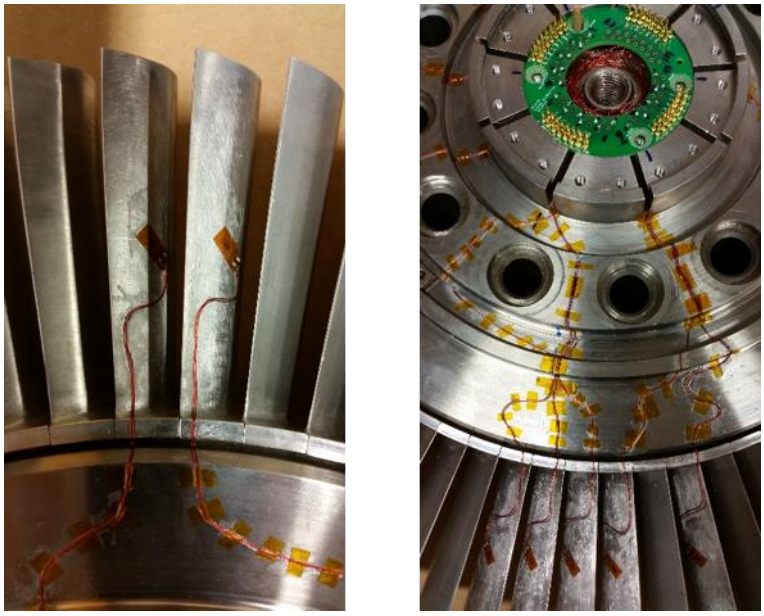

FIGURE 5.16: Photos of the rotor blades and disc during the instrumentation process.

As can be seen in FIGURE 5.16, the strain gauges were applied on the suction surface of the blades, close to the trailing edge. This position was chosen as a compromise between accessibility and the opportunity to apply the sensor in an area of large deformation. In general, since the blade profile is very stiff in the area of the leading edge, larger deformations (surface strains) on the blade surface are to be expected at the trailing edge. In more specific details, the sensors we applied with an angle of 45 degrees relative to the blade radial axis, 41 mm below the blade tip and 10 mm forward with respect to the blade TE. The distribution of the strain sensors around the rotor is reported in the scheme in FIGURE 5.17.

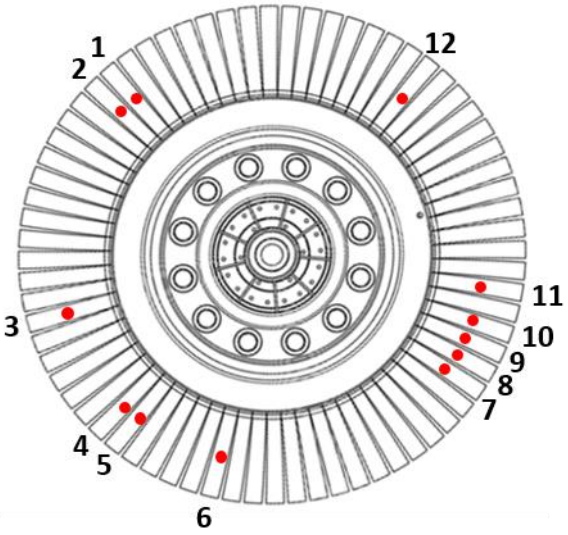

FIGURE 5.17: Position of the strain gauges around the rotor circumference.

5.2.4 VIBRATION DATA POST-PROCESSING

In this section, the post-processing methodology used for the evaluation of the blade vibration data is explained in detail. Two different routines were created, one for the analysis of the steady data and one for the unsteady measurement procedure. The first routine is composed of the following steps:

- Adaptive resampling;
- Fourier Transformation;
- Averaging;

The post-processing of the data acquired during transient operation of the machine is based on the previous steps, to which the following are added:

- Evaluation of the rotational speed;
- Data organisation and Campbell diagram plotting;

5.2.4.1 STEADY POST-PROCESSING

Adaptive resampling is a specially developed procedure to address the irregular sample distribution resulting from small fluctuations of the rotational speed around the nominal value. During a data acquisition period of 1 minute, the variation is usually less than 1%. However, since the sampling rate of the measuring system is fixed, the unequal rotational speed causes an uneven distribution of the samples for each rotor revolution. A trigger that gives a signal once per revolution is used to resample the raw recorded signal. In this instance the necessary trigger is obtained from Bently Nevada's shaft surveillance system. The trigger is used to cut the raw SG's signal into pieces corresponding to one rotor revolution. Since the rotor speed varies slightly during each revolution, the number of samples acquired during each revolution is different. Therefore, after the cutting, resampling has to be performed in order to obtain the same number of samples for each revolution. This technique was used in past works already to analyse acoustic and FRAPP data. According to the previous applications of this procedure, the number of samples per revolution in the resampled signal must be lower than the average original number of samples in one rotor revolution, as defined in the following equation:

$$nn = 2^k < \frac{f_s \cdot t}{n_{period}} = na \tag{5.26}$$

Where nn is the number of samples per revolution in the resampled signal. While not necessarily needed for the procedure, a samples number equal to a power of 2 accelerates the procedures following the resampling using the software MATLAB. The variable f_s is the original sampling frequency, t represents the measured time of the raw signal and n_{period} is the number of revolutions in the original signal. The variable na is the original number of samples per revolution. Since n_{period} is not necessarily an integer number, also na is not integer. Consequently, samples in the resampled signal will be smaller than the original number of samples.

In order to achieve a frequency resolution after the fast Fourier transformation of 5 Hz, the data relative to 5 consecutive revolutions are re-united, to be analysed together. This resolution is considered enough for the extent of this study, considering that the spectra are going to be analysed in a frequency range from 0 to 10 kHz. After the transformation in the frequency domain, the signals are averaged, obtaining a spectrum that represents the single acquisition. Considering that the nature of the signal variations due to the rotational speed fluctuations are of a stochastic nature, this procedure removes them from the resulting frequency spectrum. A schematic representation of the averaging procedure is depicted in FIGURE 5.18.

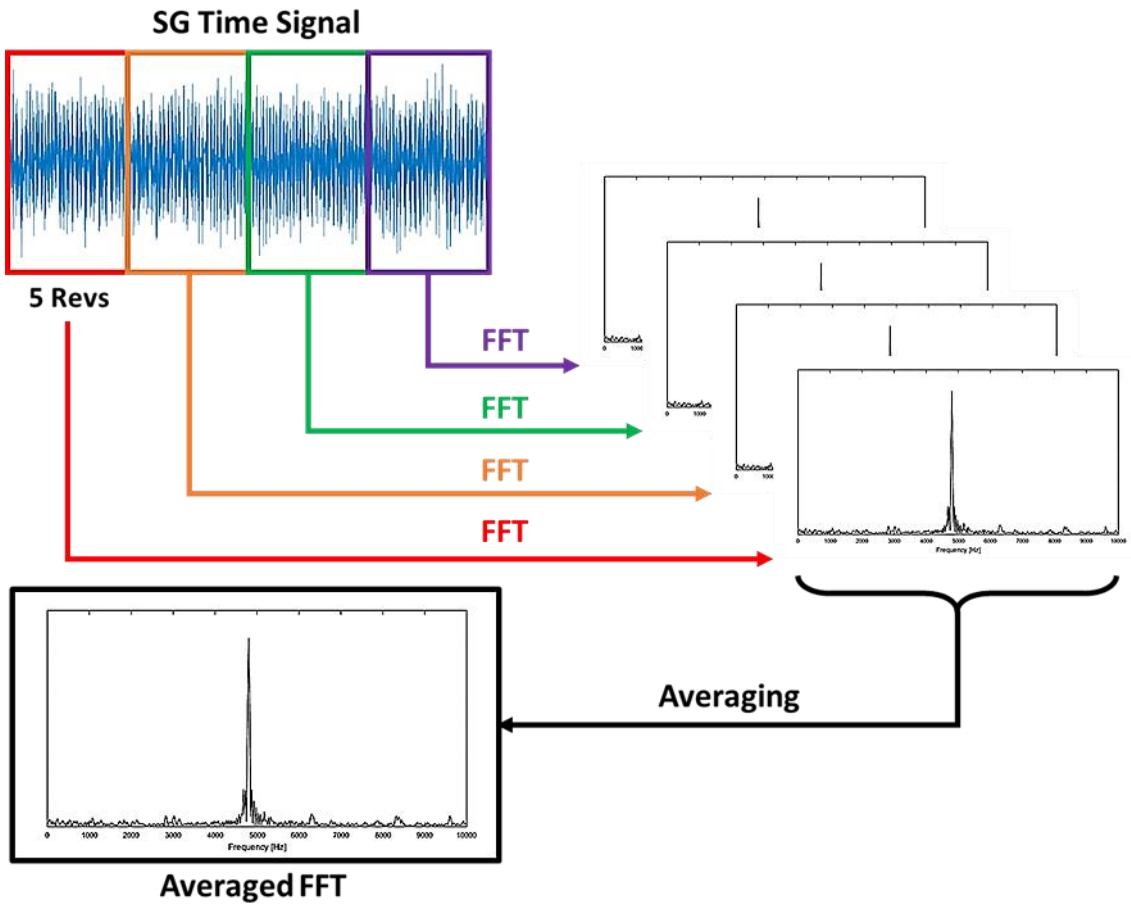

FIGURE 5.18: Schematic representation of the averaging process. Modified from [8].

To allow a more detailed study of the SG data, an estimated value of the strain energy was evaluated from the measured SG signals applying the following equation to the strain spectra.

$$E_{strain} = \sum_{m=1}^{N} |X[m]|^2 \tag{5.27}$$

Where N represents the number of observations in the frequency domain and X the FFT coefficients referred to the strain measured by means of strain gauges. Considering that all the results and evaluations presented in the following chapters of this work are referred to the same blades, the strain energy can be evaluated starting from the strain signal obtained from the strain gauges. This is valid because the geometrical and mechanical characteristics of the blade remained unchanged during the measurement campaign.

5.2.4.2 TRANSIENT POST-PROCESSING

The post-processing of the data acquired during speed sweeps is based on the steady routine. The averaging procedure is not applied in this case, since every revolution was acquired at a different rotational speed and represents a different data-set.

The first step of the transient routine consists of the evaluation of the rotational speed. The time that passed between two trigger impulses is evaluated according to the following equation:

$$n = \frac{60 \cdot f_s}{nn} \; [rpm] \tag{5.28}$$

Where n represents the rotational speed of the machine and nn the number of samples between two trigger peaks. At this point, after the signal of each resolution is resampled, an FFT is performed, according to the description presented above. The resulting spectra are therefore associated to a specific rotational speed that characterised the rotor during the acquisition.

Plotting each spectrum as a function of the rotational speed is therefore possible to obtain a spectrogram that relates the amplitudes of the FFT to the speed of the rotor. A schematic view of the described procedure is depicted in FIGURE 5.19.

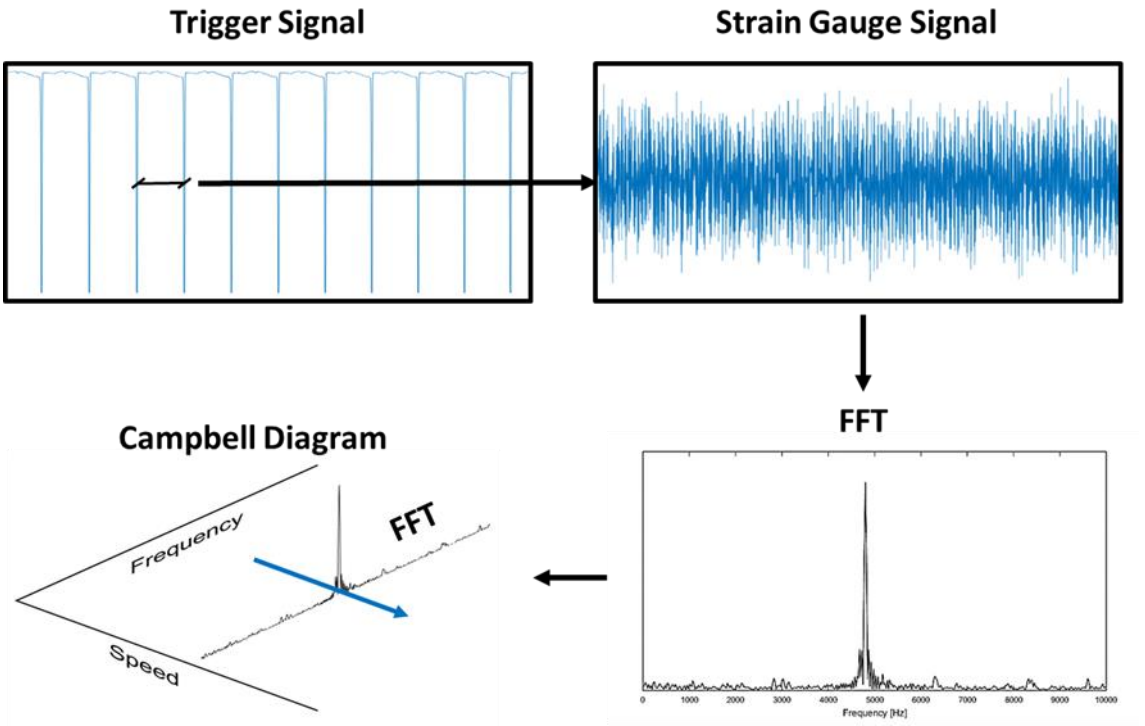

FIGURE 5.19: Transient post-processing of blade vibration data.

The resulting plot is a Campbell diagram. An explanatory example if shown in the FIGURE 5.20, where the rotational velocity of the rotor is on the x-axis and the frequency of the vibration is on the y-axis. It is interesting to observe in the figure the presence of the horizontal lines, representing the eigenfrequencies, and of the inclined line, which is a trace of the engine order 96 excitation coming from the stator wakes.

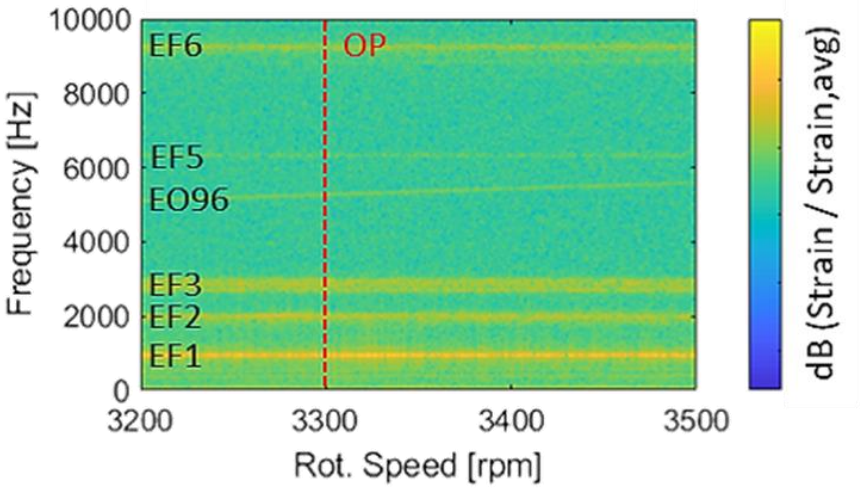

FIGURE 5.20: Experimental Campbell diagram

6. STAGE CHARACTERISATION WITH CLEAN INFLOW

The following chapters discuss the measurement results of the stage with clean inflow and with different inlet distortion configurations presented in section 4.4.

Firstly, the aerodynamic characterisation of the flow in the planes upstream and downstream the stage will be presented, together with the forced response of the rotor blades, for the clean inflow case. Thereafter, the focus will shift towards the results regarding the total pressure distortion, total temperature distortion and finally the combination of the two.

This chapter in particular deals with the description of the stage aerodynamics at the inlet and downstream the rotor row, as well as with the blade vibrations in nominal operating conditions, with clean inflow.

6.1 PLANE A

The results of the investigation carried out by means of 5HP in plane A are presented here. A contour of the total pressure distribution is presented in FIGURE 6.1. The flow field upstream of the LPT is not uniform and three main effect can be identified. Since the IGVs are mounted on the outer casing leaving a 0.5 mm gap at the hub, the generation of a leakage vortex is allowed. The presence of this vortex is the cause of the region of low total pressure near the hub, identified in the picture with the letter B. The wakes generated by the vanes prevail in the region between 10% and 90% of the passage and are marked with black dashed lines. As a consequence of the circumferential swirl determined by the flow angle at the exit of the IGV, the wakes are bent towards the outer casing. In the upper passage section, lobes of low total pressure are created by the upper passage vortices present in the casing region of the IGV. Letter A is superimposed to the plot in the figure in order to highlight these structures.

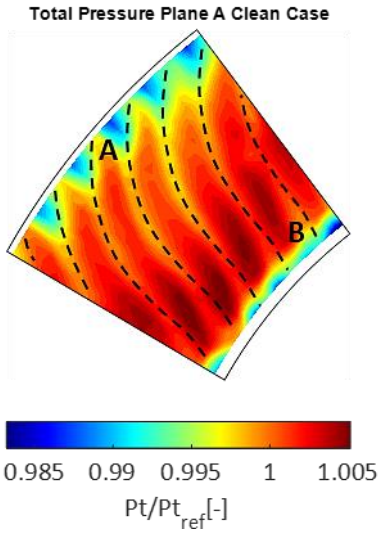

FIGURE 6.1: Distribution of total pressure in plane A for the reference case.

The temperature distribution is depicted in FIGURE 6.1. The field appears to be almost constant in the lower part of the channel, with the exception of a limited lower total temperature region in the lower-right corner of the measured sector, highlighted with the letter C in the figure. Higher temperature located in the upper region of the channel (A') can be recognised in the the secondary vortices generated by the inlet guide vanes positioned upstream of the measurement plane. This band is spatially partitioned according to the number of IGV present in the area corresponding to the measurement sector.

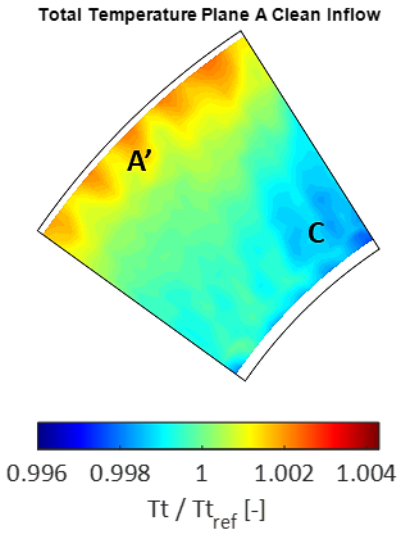

FIGURE 6.2: Distribution of total temperature in plane A for the reference case.

In order to provide an additional visualisation of the effect of the circumferential inlet air injection on the total pressure and temperature field in plane A, in the following sections the different tested configurations will be compared using circumferentially mass averaged spanwise distributions. For this reason, FIGURE 6.3 shows the radial distributions of total pressure, total temperature, static pressure and Mach number. These plots will be used in the following as a base for the comparison of the effects of temperature and pressure distortions.

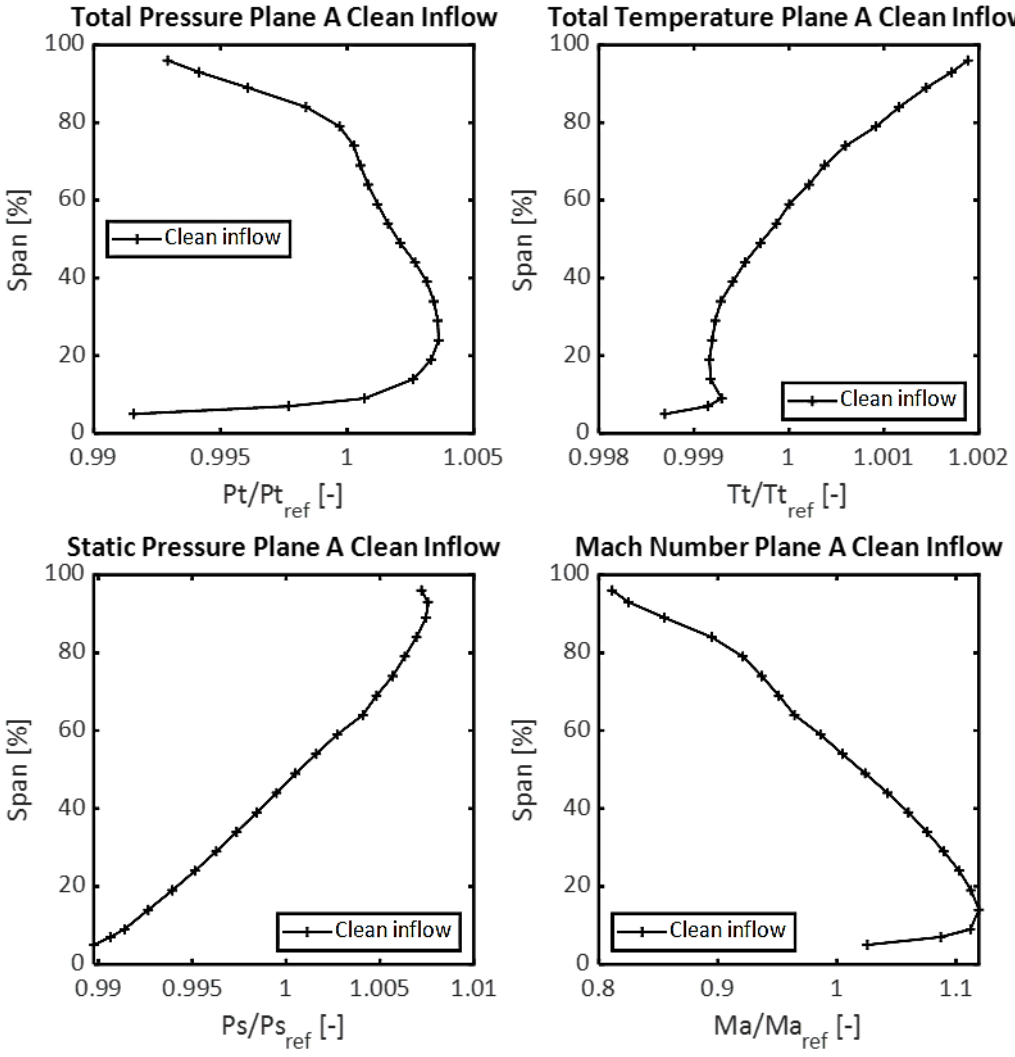

FIGURE 6.3: Radial distributions of circumferentially mass averaged quantities in plane A. Clean inflow case.

6.2 PLANE C

6.2.1 5HP MEASUREMENTS

The flow field downstream of the investigated low pressure turbine stage measured by means of 5HP will be presented in this section. FIGURE 6.4 presents an aft-looking-forward visualisation of the time-averaged total pressure of the flow measured for the reference case. The analysis of the flow field of the clean inflow case is used to identify the main flow structures that characterise the outlet of the stage.

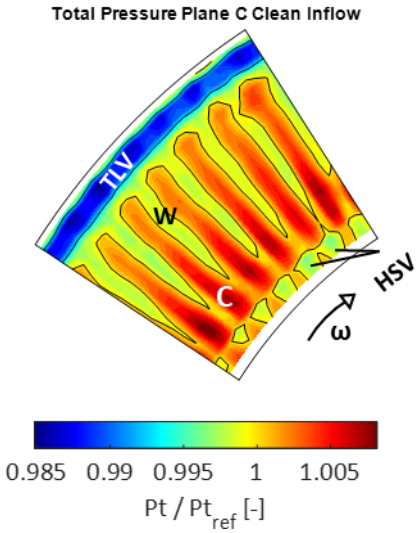

FIGURE 6.4: Total pressure distribution in plane C with black superimposed iso-contour lines of C_{pt}.

Observing the figure, one can see that the total pressure field above 80% span is dominated by the effect of the leakage flow generated by the unshrouded rotor blades, marked with TLV. The higher total pressure region visible just above the tip leakage vortex, can be linked to the presence of a wall jet leakage flow, as also described by Lengani et al. [47]. Between 20% and 80% span, the rotor exit flow is characterised by the velocity defect related to the stator vanes wakes, identified in the figure with the letter W. To highlight the position of the stator flow structures it is possible to introduce a total pressure coefficient, defined in Equation (6.1), as the non-dimensional difference between the total pressure and its circumferential average.

$$C_{pt} = \frac{p_t - p_{t,AVE}}{1/2\,\rho w_{AVE}^2} \tag{6.1}$$

Iso-contour lines of the total pressure coefficient are superimposed to the normalised total pressure plot of FIGURE 6.4. The areas enclosed inside the lines correspond to a negative C_{pt} and match exactly with the number of the stator vanes present upstream. This allows the identification of the position of the structures produced by the stator row. In the lower passage region, at approximately 15% of the span, the hub secondary vortices, named HSV can be observed. Even though the effect of the horse shoe vortices and the hub passage vortices cannot be separated in this visualisation, due to the specifics of the measurement technique, it is possible to note their combined effect in the 5HP results as the low P_t zone close to the hub. The non-uniformity of these structures is due to the uneven blade count and the clocking between the inlet guide vanes and the stator vanes. Additionally, spots of higher total pressure (C) can be observed in the core flow region above the HSV at around 20% span.

The total temperature distribution in plane C is depicted in FIGURE 6.5. As for the total pressure field, the total temperature appears to be modulated by the interaction between the stator vanes wake and the rotor tip leakage. In particular, the tip leakage is responsible for the high temperature region next to the casing. The effect of the secondary vortices generated by the stator vanes can be recognised in in the lower region of the channel. All the temperature features present in the plots are spatially divided according to the number of wakes originating from the stator vanes present in the measurement sector.

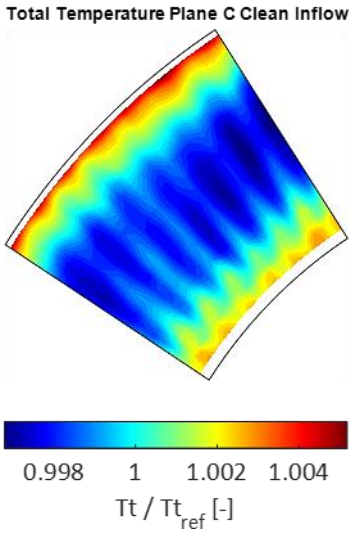

FIGURE 6.5: Distribution of total temperature in plane C for the clean inflow case.

As for the case presented above, also for plane C, the radial distributions of total pressure, total temperature, static pressure, Mach number and yaw angle are presented in FIGURE 6.6. These plots will serve as a base for the comparison of the effects of temperature and pressure distortions in the following sections.

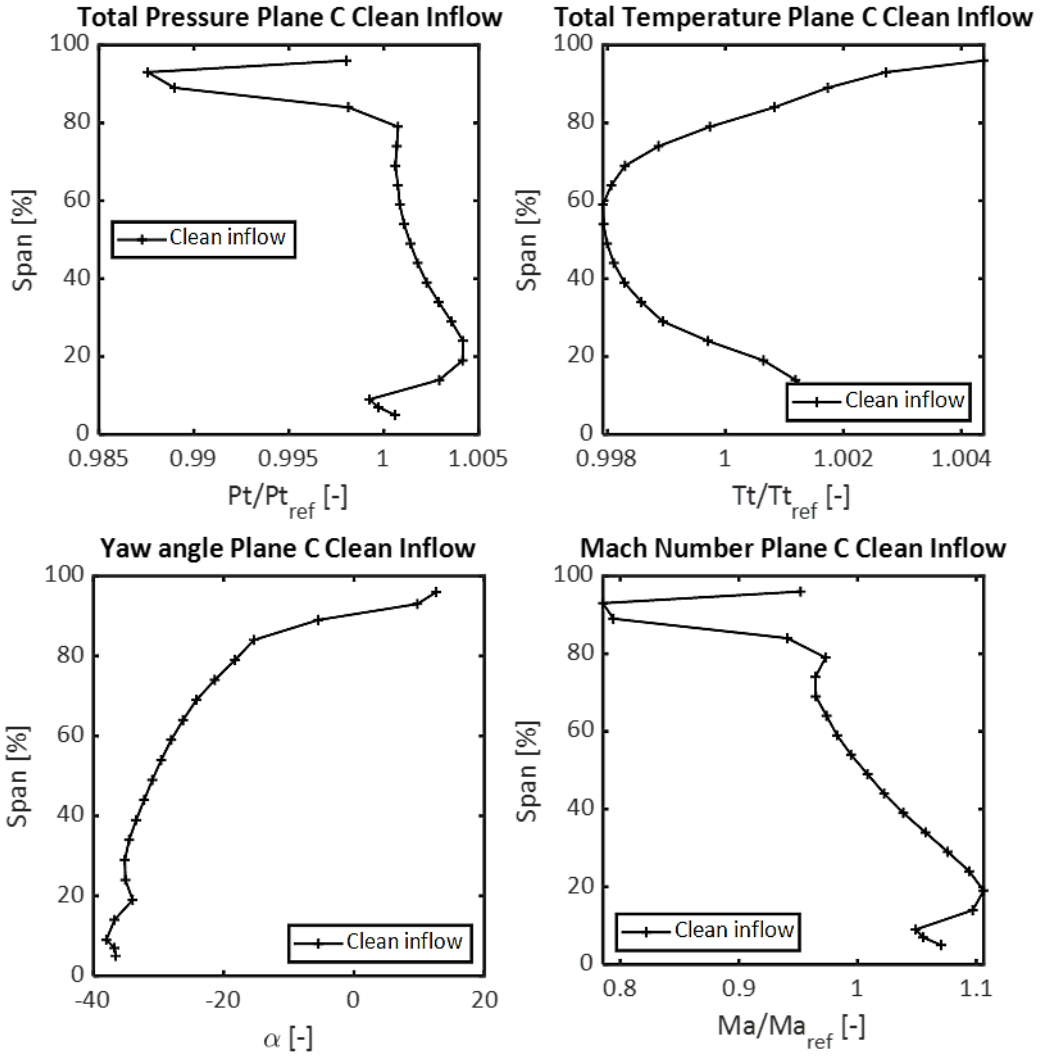

FIGURE 6.6: Radial distributions of circumferentially mass averaged quantities in plane C. Clean inflow case.

6.2.2 FRAPP UNSTEADY MEASUREMENTS

The unsteady data obtained from the FRAPP measurement downstream of the LPT stage are presented here. FIGURE 6.7 shows the development of the flow as contour plots of the normalised total pressure, where the absolute values were normalised using the time averaged mean value of the corresponding flow field. The plots are an aft-looking forward visualisation of the measurement sector described in section 5.1.1.2. The main flow features caused by the wakes, hub and tip secondary vortices, and by the rotor blades can be identified in the plots, congruently to the flow description introduced with the 5HP results. The tip leakage vortex, identified in the picture with TLV, causes a series of low total pressure regions. Just above this area, a very high total pressure area is recognizable. In the previous section this high total pressure area was already identified as wall jet leakage flow. Smaller values of total pressure due to the rotor blade wakes are dominant in the region between 20% and 80% of the passage height. These areas are indicated in the picture with the letter W. Furthermore, it can be observed the presence of hub secondary vortices, which are marked in the figure with HSV and appear to be less intense than the tip leakage vortex.

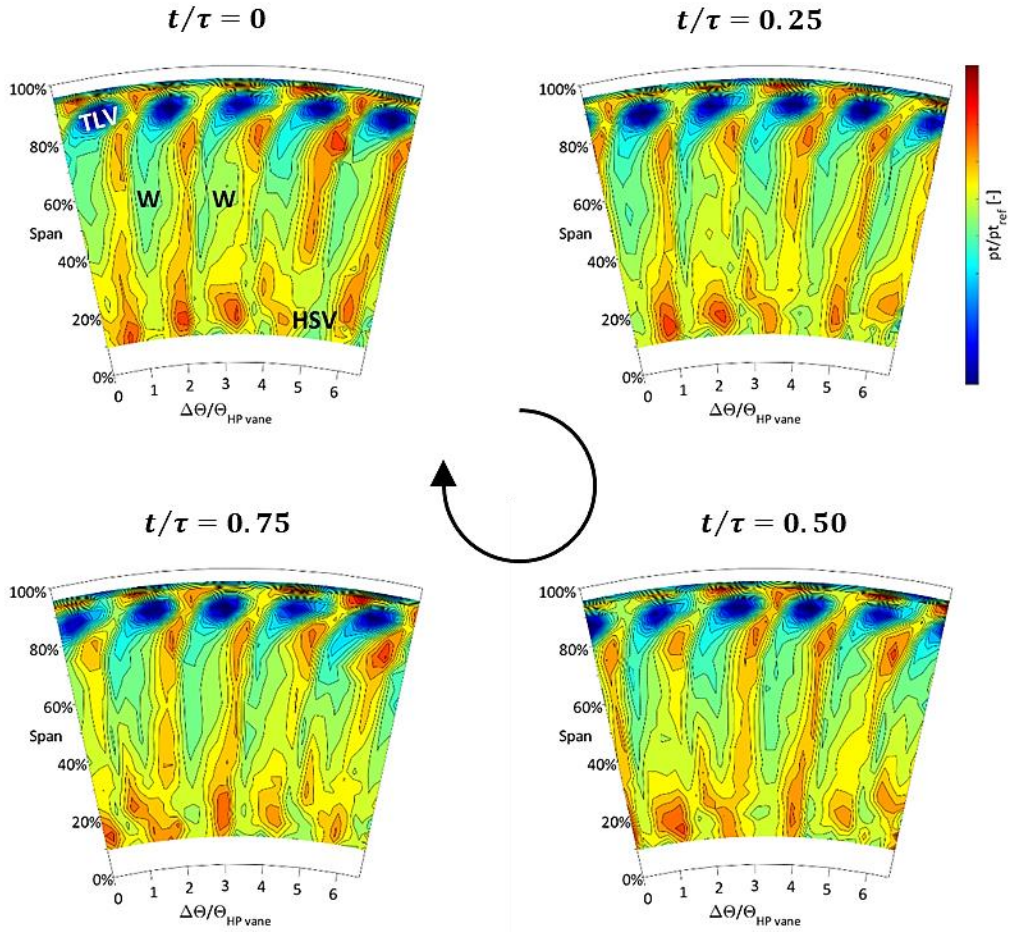

FIGURE 6.7: Time resolved distribution of the normalised total pressure downstream of the LPT rotor. Clean inflow case.

Further information regarding the flow behaviour can be obtained studying the evolution of the unsteady total pressure and is presented by means of time-space diagrams showing all the measured stator pitches and two blade passing periods in FIGURE 6.8. The radial coordinates chosen for this visualisation are 12%, 50% and 93%, representing the hub, mid-span and tip region respectively. Observing the three time-space plots, one notes that the flow field downstream of the rotor is dominated by the rotor wake and the interaction between the stator vane row and the rotor blades, independently on the span height. The rotor traces, inclined in the rotor direction of revolution, are indeed well noticeable and are highlighted in the figure with black dashed lines. Such traces appear to be periodically chopped in horizontal direction by the wakes of the stator vanes, one of which has been emphasised with a magenta dashed line. The main difference that can be found observing the three figures is the intensity of the rotor and stator related structure interaction. In the high span region, it can be seen that the tip leakage vortices related to the rotor passage represent the main feature. Instead, in the mid span region, are the rotor wakes to be dominant. In the region close to the hub, the HSV can be considered responsible for the modulation of the total pressure field.

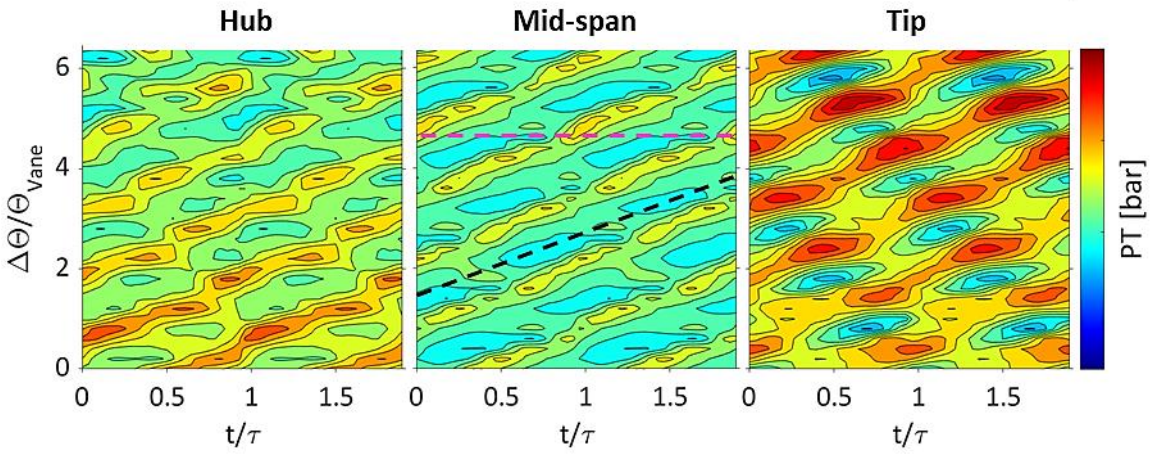

FIGURE 6.8: Time-space plots of total pressure at hub, mid-span and tip.

6.3 ROTOR BLADE VIBRATIONS

The blade vibrations frequency spectrum is presented here to identify the characteristics of the main modes. FIGURE 6.9 presents the spectrum of the analysed strain gauge (SG2) for the clean inflow case, up to a maximum of 10 kHz. The amplitude of the strain has been normalised with the amplitude of the first mode. This normalisation will be used for all the cases in order to simplify the comparisons. The main vibrational modes and the excitation determined by the stator vanes can be identified in the figure. More specifically, the highest peak is related to the first eigenfrequency (1st flap-wise bending mode – 1F) and is located around 930 Hz. The second eigenfrequency is at 1995 Hz and is the 1st edge-wise bending mode (1E). The third peak in the spectra represents the 1st torsion mode at approximately 2850 Hz (1T). Another peak can be observed at a frequency of 9220 Hz and corresponds to the 3rd flap-wise bending mode (3F). At 5280 Hz it is possible to notice the response of the rotor blades to the forcing due to the excitation corresponding to the engine order 96, originated by the stator wakes. The amplitude related to the EO 96 is very low compared to the amplitude of the other peaks. This is due to the fact that the operating point chosen for this investigation is far from a condition of resonance.

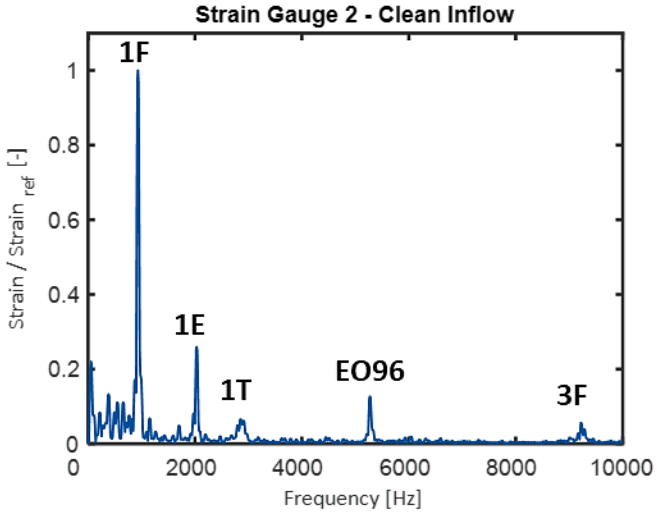

FIGURE 6.9: Forced response spectra of strain gauge 2. Clean reference case.

Numerical simulations performed using ANSYS FEM platform, were used to identify the mode shapes, according to Schönleitner et al [121]. In order to obtain the mode shapes of the rotor blades, a pre-stressed modal analysis was done on one rotor blade, in which the pressure-loadings from a previous steady-state simulation and the rotational velocity were set as boundary conditions. Further, the blade

was constraint in the root. An unstructured mesh consisting roughly of 440000 nodes was employed. The results are presented in FIGURE 6.10.

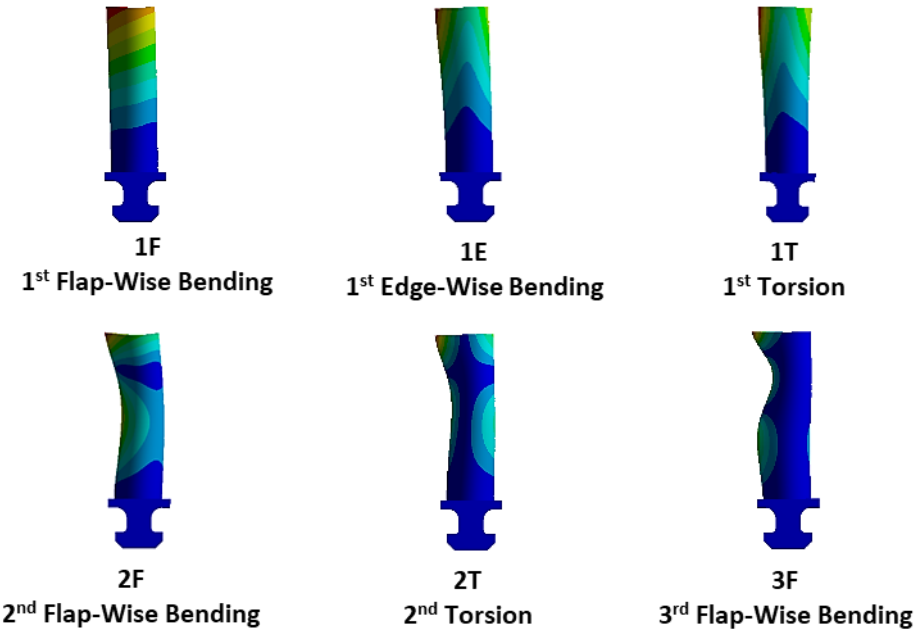

FIGURE 6.10 Mode shapes evaluated with numerical simulations.

Sweeps across a speed range around the operating speed from 3100 rpm to 4100 rpm at constant pressure ratio were performed during simultaneous strain gauges' measurements. The response of the sensors across the operating range can be illustrated in a Campbell Diagram, where horizontal lines denote the blade and disc eigenfrequencies lines originating from the origin and proportional to the rotation frequency represent excitation lines (EO excitation). Additionally, the crossings between eigenfrequencies and excitation lines imply potential resonances. FIGURE 6.11 shows the results of the measurements during transient operation (run-down) of the machine around the operating point.

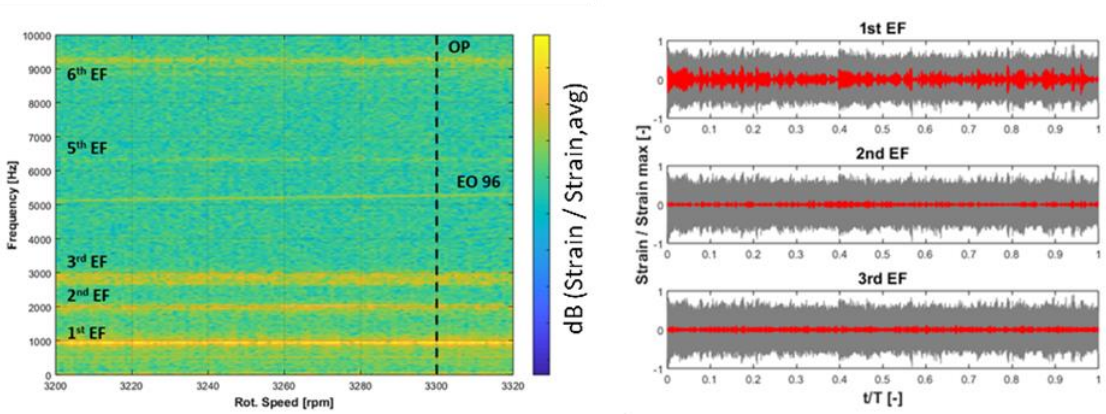

FIGURE 6.11: Campbell Diagram of strain gauge 2 (left) and vibration signature of the first three eigenfrequencies (right) during sweep between 3200 rpm and 3320 rpm.

Observing the Campbell diagram of SG2 is depicted on the left, it is possible to identify the eigenfrequencies already described in the previous part of this section. In addition, the excitation due to the stator vanes is clearly detectable and is denoted in the figure as EO96. The fact that no crossing between the eigenfrequencies and the excitation line occurs, demonstrates that no possible resonances

can arise around the operating point. Contrarily, the excitation due to the IGVs is not clearly noticeable in the Campbell diagram, as its amplitude results too small for the visualisation.

Furthermore, during the velocity sweep no evidence of unstable vibration was recorded. This is visible in signature of the first three eigenfrequencies depicted in the right hand side plot of FIGURE 6.11. To create this visualisation, the signal of SG2 was band pass filtered around the three investigated eigenfrequencies and then plotted (in red) against the total signal of the strain gauge (in grey), over the nondimensional sweep time. None of the modes show the onset of self-excited blade vibrations with an exponential growth in amplitude, which would be caused by an overrun of the aeroelastic stability limit. Therefore, the amplitudes of the vibrations measured with the strain gauges show that the blades are stable during the operation around the investigated operating point for the clean inflow case.

7. TOTAL PRESSURE INLET DISTORTION

7.1 P_T DISTORTION IN PLANE 0

The results presented in the following section are related to the configuration of the machine described in 4.4.1.1. The aerodynamic results of the 5HP and FRAPP investigation in plane A will be illustrated and a comparison between the P_t distortion case and the reference with clean inflow will be presented. This section is aimed at the determination of the nature of the effects of a circumferential total pressure inhomogeneity onto the vibrations of the rotor blades.

7.1.1 PLANE A - AERODYNAMIC RESULTS

The flow field upstream of the investigated low pressure turbine stage measured by means of 5HP will be presented in this section. The measurements were performed for the distorted inflow and for the clean inflow, which was presented in 6.1. It was chosen to report some of the plots referring to the clean inflow reference case to facilitate the direct comparison.

An aft-looking-forward visualisation of the time-averaged total pressure of the flow is presented in FIGURE 7.1. The contour plot on the left is related to the clean inflow setup results, while the results on the right hand side of the figure represent the distorted inflow case.

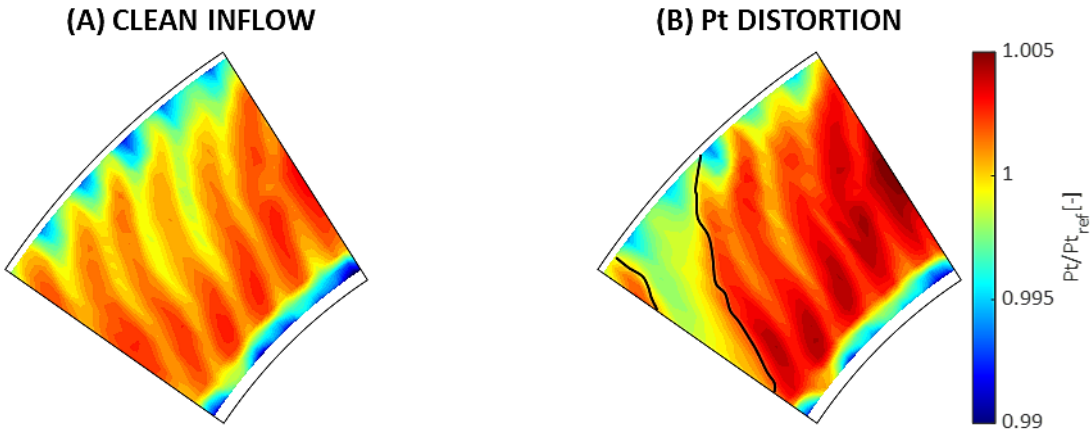

FIGURE 7.1: Total pressure distribution in plane A. Clean inflow case (left) and distorted inflow case (clean).

By comparing the two cases a number of remarkable aspects can be examined. Firstly, it is possible to clearly identify the presence of the wake of the distortion cylinder mounted upstream of the IGVs in

the P_t distortion plot. Interestingly, the low momentum fluid in the wake interacts with the inlet guide vanes and with the wakes that they generate, resulting bent with the same S-shape that characterises the wakes of the IGV for the clean inflow case. In more details, the total pressure drop in the low momentum regime is about 55% of the value in the vanes core flow. Despite this, the lower values of total pressure are still due to the leakage flow near the hub region, originating from the hub gap in the inlet guide vane row. Another visible influence of the inlet distortion is noticeable in the overall lower level shown around the blockage area. In fact, the transition between the distortion generator wake and the free stream seems to be gradual. As a result of the influence of the distortion on the neighbouring IGV passages, the wakes of the inlet guide vanes and the secondary structures at the tip become less intense closer to the wake of the distortion cylinder. Additionally, for the same reason, the blockage created by the distortion cylinder generates a redistribution of fluid, resulting into a flow acceleration around the low momentum region. A sign of this acceleration is the increased total pressure visible in the vanes core flows in comparison with the clean inflow case.

The total pressure mass averaged radial distribution is plotted in FIGURE 7.2. This plot refers only to the part of the measurement sector influenced by the distortion. Two main effects of the total pressure distortion can be seen also in this visualisation. The higher span region is characterised by the total pressure drop due to the low momentum fluid generated by the distortion cylinder. In the lower span area instead, it is possible to observe the increase of total pressure due to the flow redistribution around the distortion generator. The plot is influenced by the presence of only the upper half of the low momentum flow in the measurement sector. The higher total pressure in the lower half of the span is due to the higher mass flow pushed by the presence of the skewed wake of the distortion generator.

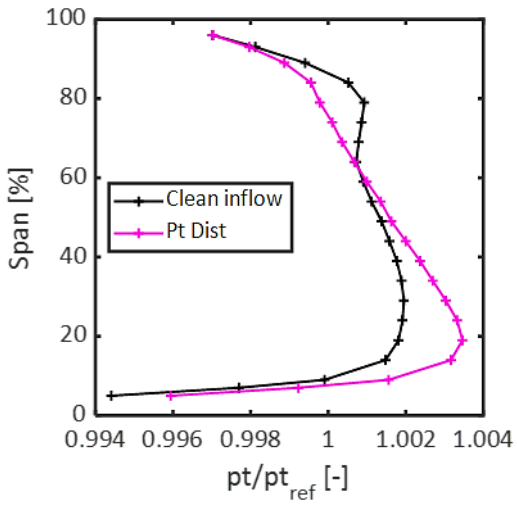

FIGURE 7.2: Radial distributions of circumferentially mass averaged total pressure. Plane C.

In conclusion, the wake generated by the cylinder creates a localised and well-defined total pressure distortion in the inlet flow of the low pressure turbine stage under investigation. The low momentum fluid entering the stage interacts with the flow features determining modifications to both the core flow and in to secondary vortices. Due to such distorted pressure pattern, a potential excitation of the low engine orders is expected and will be in fact introduced in the presentation of the blade vibrations results.

7.1.2 ROTOR BLADE VIBRATIONS

7.1.2.1 FORCED RESPONSE AT NOMINAL OPERATING POINT

Strain gauge measurements were performed during stable and transient operation of the machine, as described above. Results of the measurements at steady nominal operating conditions will be used within this work to characterise the vibration of the LPT rotor blades, and to obtain a comparison between the two investigated configurations in this first part of thesis.

FIGURE 7.3 (A) and (B) present the spectra of the analysed strain gauge for the clean inflow case and for the distorted inflow case respectively, up to a maximum of 10 kHz. The amplitude of the strain has been normalised with the amplitude of the first mode evaluated for the reference case, as already presented in 6.3. In section 6.3 the main characteristics of the rotor blade vibration spectra were presented, and therefore are not repeated here, the focus here lies on the comparison between the two cases.

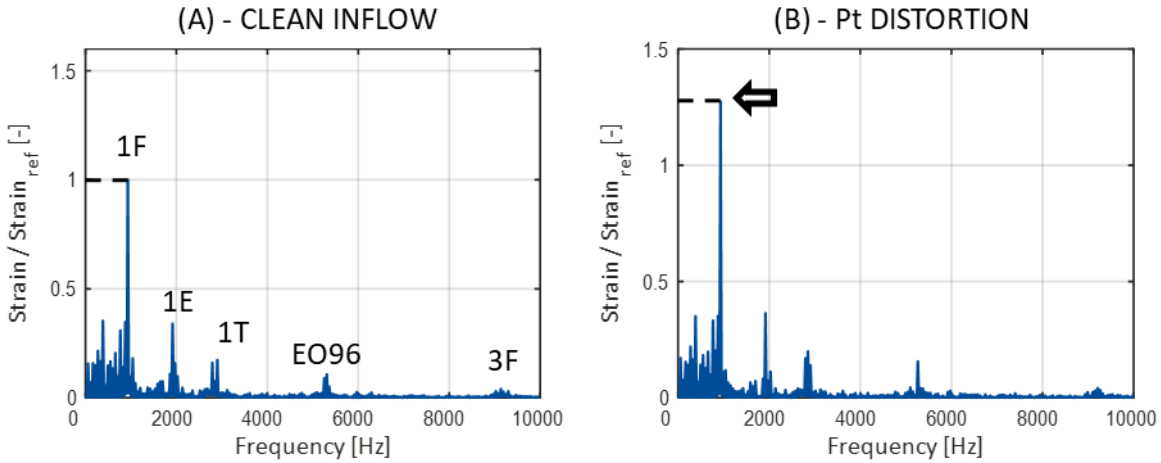

FIGURE 7.3: Forced response spectra of SG2. Clean inflow configuration (A) and P_t inlet distortion case (B).

Comparing the results obtained for the two configurations tested, a major difference can be found. The 1F amplitude appears to be the most affected by the inflow conditions change. In particular, the amplitude increment of 1F amplitude is 27.5% in the distorted inflow case. Such amplification can be linked to the increased excitation due to the vortex shedding in the wake of the distortion cylinder. Considering that the frequency of the vortex shedding can be evaluated according to Equation (7.1), for the operating conditions tested, the excitation frequency is f_s = 960 Hz. This value is particularly close to the frequency of the first mode and the vortices detaching from the cylinder are transported through the stage inlet and determine an additional source of excitation for the rotor blade forced response.

$$St = \frac{f_s \cdot D}{v} \tag{7.1}$$

More insights regarding the vibrations increase at the 1st flap-wise mode can be obtained studying the unsteady pressure data acquired with the fast response probe in plane A. For this purpose, a discrete Fourier transformation was applied on the time signal. By means of this procedure, it was possible to notice that the highest contribution in the frequency spectra is represented by the amplitude of the total pressure fluctuation at the vortex shedding frequency.

The distributions of the total pressure fluctuations at the vortex shedding frequency obtained for the measurement sector is visualised in FIGURE 7.4. The plot reveals that high fluctuation amplitudes at this specific frequency are located mainly in the region dominated by the distorted flow. Additionally, an area of high amplitude can be observed near the hub, this could be linked to the vortices generated by the hub leakage in the IGV row. However, observing FIGURE 7.4 it can be stated that the main origin of total pressure fluctuations can be found in the distorted region

Therefore, the vortices detaching from the cylinder are thought to be the origin of the excitation at a frequency close to the blades 1F mode, determining higher amplitude measured at this frequency.

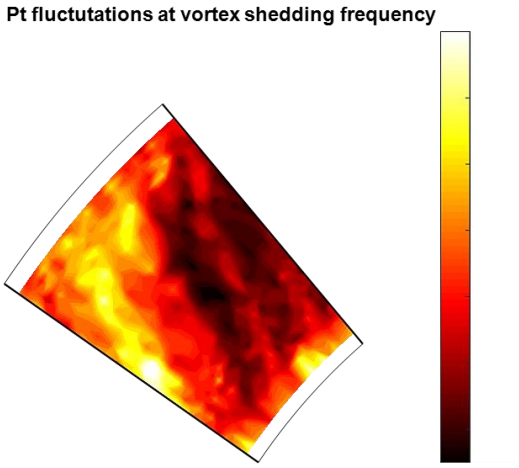

FIGURE 7.4: Distribution of total pressure fluctuations at the frequency of the vortex shedding 960 Hz. Plane A

The strain energy contained in the SG data spectrum can be evaluated according to Equation (5.27). The resulting values evaluated for the clean inflow case and for the configuration featuring a distortion generator at the inlet are presented in FIGURE 7.5. Comparing the two values, it is possible to note that the inlet distortion case presents a higher levels of strain energy. Since the value has been evaluated considering the interval from 0 to 10 kHz, this result is representative of higher overall strain amplitudes measured over the whole investigated frequency range in the P_t distortion setup. Higher unsteadiness in the flow field generated by the wake that constitutes the flow distortion causes therefore a broadband excitation on the rotor blades, as shown by the increased strain energy evaluated over the whole frequency range. Thus, the distorted inflow conditions cause an enhancement of the rotor blades excitation both at the frequency of the first eigenfrequency and across the whole frequency spectrum.

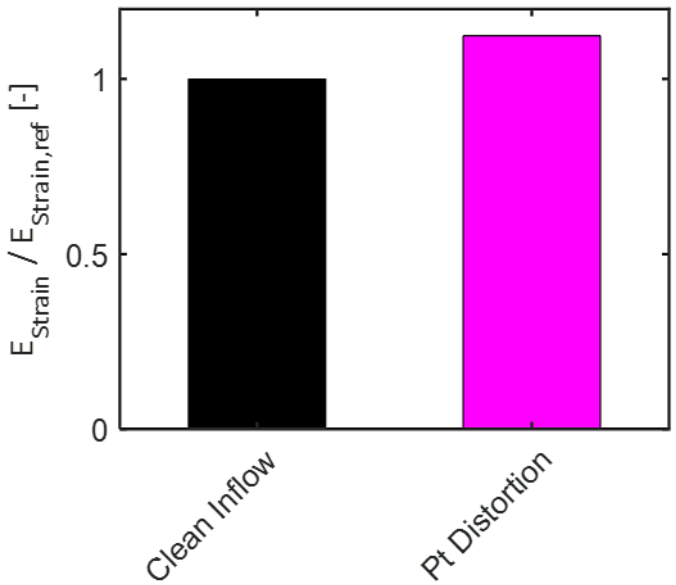

FIGURE 7.5: Strain energy evaluated from sg2 signal for the four investigated cases.

7.1.2.2 FORCED RESPONSE DURING TRANSIENT OPERATIONS

The analysis of the data acquired during transient measurements is based on the procedure presented in 5.2.4. The data were studied combining the frequency and rotational speed information. As a result of this signal processing method, the amplitude changes of each mode can be detected during continuous speed sweeps around the nominal operating rotor speed. In order to analyse the effect of the distorted flow field excitation of the 1F, the amplitude of the first mode obtained from the signal of SG2 is plotted along the speed ramp in FIGURE 7.6. It can be observed that during the velocity sweeps across the operating range of the machine, the amplitude of the 1F is higher in the P_t distortion case than in the configuration with clean inflow, across the whole speed range. Additionally, an increase in the 1F amplitude between 3300 and 3400 rpm can be noted. Also for this feature, the inlet distortion configuration exhibits a higher amplitude rise.

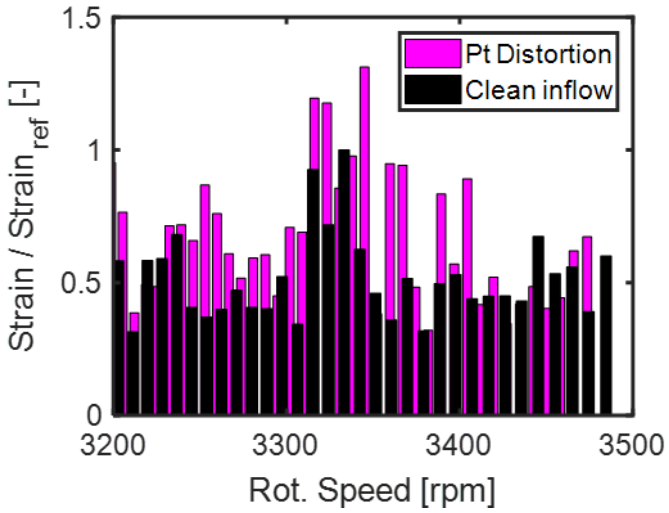

FIGURE 7.6: Amplitude of mode 1F during transient SG measurements between 3200 and 3500 rpm.

The higher amplitudes observed in the previous plot can be determined by two phenomena causing different aerodynamic excitation. On the first hand, high unsteadiness is introduced by the wake of the distortion generator in the rotor inlet flow as shown by the raised 1F amplitude at the nominal OP. On the second hand, the flow field measured at the stage inlet in the inlet distortion case is non-uniform. This spatial inhomogeneity, can be the cause of higher excitation at low engine orders, determining increased 1F amplitude during the speed sweeps.

The effect of the increase of unsteadiness caused by the wake of the inlet P_t distortion generator was discussed in the analysis of the steady SG data. In order to investigate the effect of the spatial non-uniformity introduced in the flow field by the low momentum fluid in the distortion on the rotor blade vibrations, the flow field at the stage inlet was decomposed by means of FFT. This procedure enabled the evaluation of the excitation orders present in the total pressure field in correspondence of the highest pressure drop, i.e. at 75% span. The total pressure distribution at 75% span used for the evaluation of the excitation content, measured by means of 5HP is presented in FIGURE 7.7. The left-hand side plot is reported for reference.

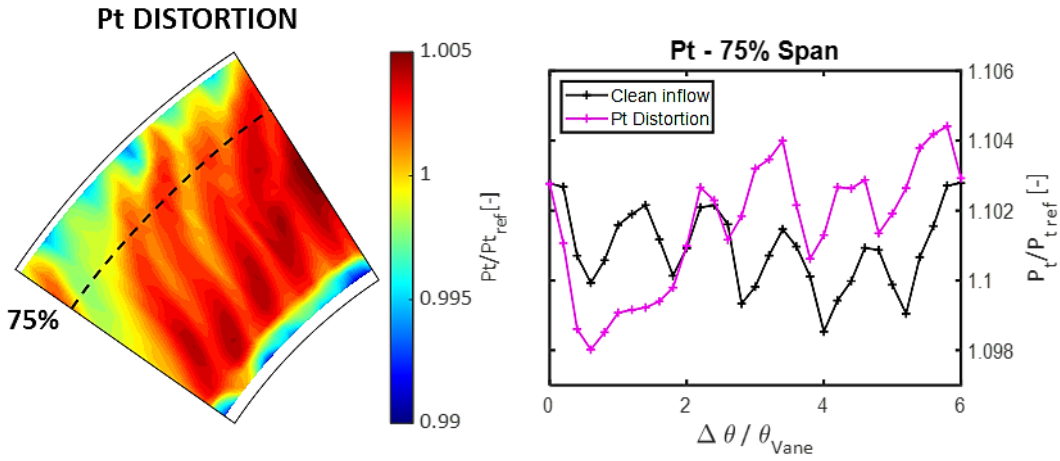

FIGURE 7.7: Total pressure contour at the stage inlet measured by means of 5HP (left) for reference and P_t circumferential distribution at 75% span (right).

By applying a Fourier transformation to the circumferential distribution of total pressure it is possible to obtain an insight on the size of the main circumferential structures that constitute the flow field at the stage inlet. The periodical pattern recognised can then be linked to the rotor blade excitation through the concept of Engine Order, presented in section 2.1.1.1.

The amplitudes evaluated for the excitation orders in the inlet flow field for the two cases tested are plotted in FIGURE 7.8. The values are normalized over the amplitude of EO83, which corresponds to the periodical inhomogeneity due to the IGV wakes. The analysis is restricted due to the circumferential extension of the measurement sector and to the angular resolution of the measurement grid. In particular, the resolution of the EO analysis is of 15 EOs, meaning that each of the values represented in FIGURE 7.8 represents the value of the EO comprised in a 15EO interval. This determines an uncertainty in the estimation of the EO excitation of the order of ±7 EO, which is considered acceptable for the purpose of this study.

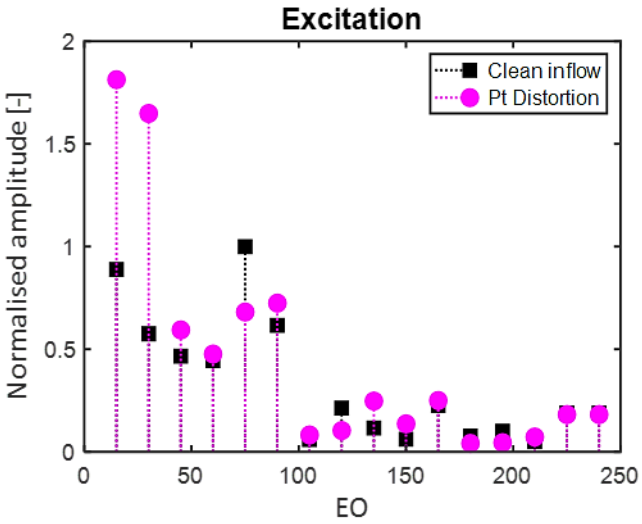

FIGURE 7.8: Engine order excitations evaluated for the clean inflow case and for the P_t distortion case in plane A.

The amplitudes of the EO excitations obtained for the clean inflow case show that, the main forcing present in the flow field at the stage inlet is due to the IGV wakes at an EO close to 83, which represents

the number of inlet guide vanes. It is also possible to observe the second harmonic of this excitation around the EO165.

The pressure distortion configuration shown in FIGURE 7.8 presents different amplitudes of the excitation orders. In fact, the wake of the distortion generator introduces in the flow field a spatial inhomogeneity that determines high excitation amplitudes at low engine orders. Moreover, for these configurations the amplitude around EO83 appears to be lower than for the clean inflow case. In particular, the EO1 and EO2 excitations result almost two times more intense than the EO83 in the P_t distortion case. This additional excitation caused by the additional pressure perturbation present in the distorted inflow configuration causes the higher responses measured at the frequency of the 1F mode during the speed-sweeps. Therefore, the vibration data and the aerodynamic excitation analysis show that the low-momentum fluid due to the wake of the distortion cylinder propagating from the inlet through the stage causes low engine order excitation, which in turn results in increased rotor blade vibratory response.

7.2 P_T DISTORTION IN PLANE A - EFFECT OF CLOCKING

This section refers to the configuration described in 4.4.1.2 Here the results of the aerodynamic measurements are presented and compared in details. In order to evaluate the effects of the inflow distortion on the rotor blade excitation, the rotor exit flow field is thoroughly studied. The aerodynamic results will be successively related to the amplitude of the blade vibrations for the three investigated distortion-stator clocking positions.

7.2.1 PLANE C - AERODYNAMIC RESULTS

7.2.1.1 STEADY MEASUREMENTS

The flow field downstream of the investigated low pressure turbine stage (Plane C) measured by means of 5HP will be presented in this section. The measurements were taken for the three distorted inflow cases with different clocking position relative to the stator vanes. FIGURE 7.9 presents an aft-looking-forward visualisation of the time-averaged total pressure of the flow measured by means of 5HP for the three investigated cases. The position of the distortion generator is reported on the P_t contours as a black dashed line. This visualization was chosen with the aim to highlight the interaction between the total pressure non-uniformities at the inlet of the stage and the stator vanes.

Areas of low momentum fluid can be noticed in the surroundings of the distortion generator concentrated in the region between 20% and 80% span. This low momentum regime is characterized by a drop in total pressure that reaches up to more than 50% of the measured range in the core flow. One can additionally note that the low total pressure flow influences both the wakes and core flow regions originating from the stator vanes. A further effect of the inflow non-uniformity can be recognised in the tip region. The areas where this is more noticeable were highlighted with arrows. The differences in the tip region between the reference case (FIGURE 6.4) and the other cases can be connected to the redistribution of mass flow due to the blockage and consequently to a modification of flow angles at the rotor inlet. Additionally, the boundary layer at the tip end wall, which influences directly the extent of the secondary vortices in this region, depends directly on the inlet total pressure.

Comparing the results obtained for the three inlet distortion cases, some differences can be found. It appears that the LE clocking case determines the pressure distortion characterised by the wider extension in circumferential direction. Additionally, for this case, the interaction between the distorted flow and the tip leakage vortex seems to be stronger than for the other cases, as suggested by the lower total pressure identified at the tip in FIGURE 7.9 (A) with the letter A. Furthermore, this case presents the highest total pressure difference also in the core flow region (indicated with the letter B).

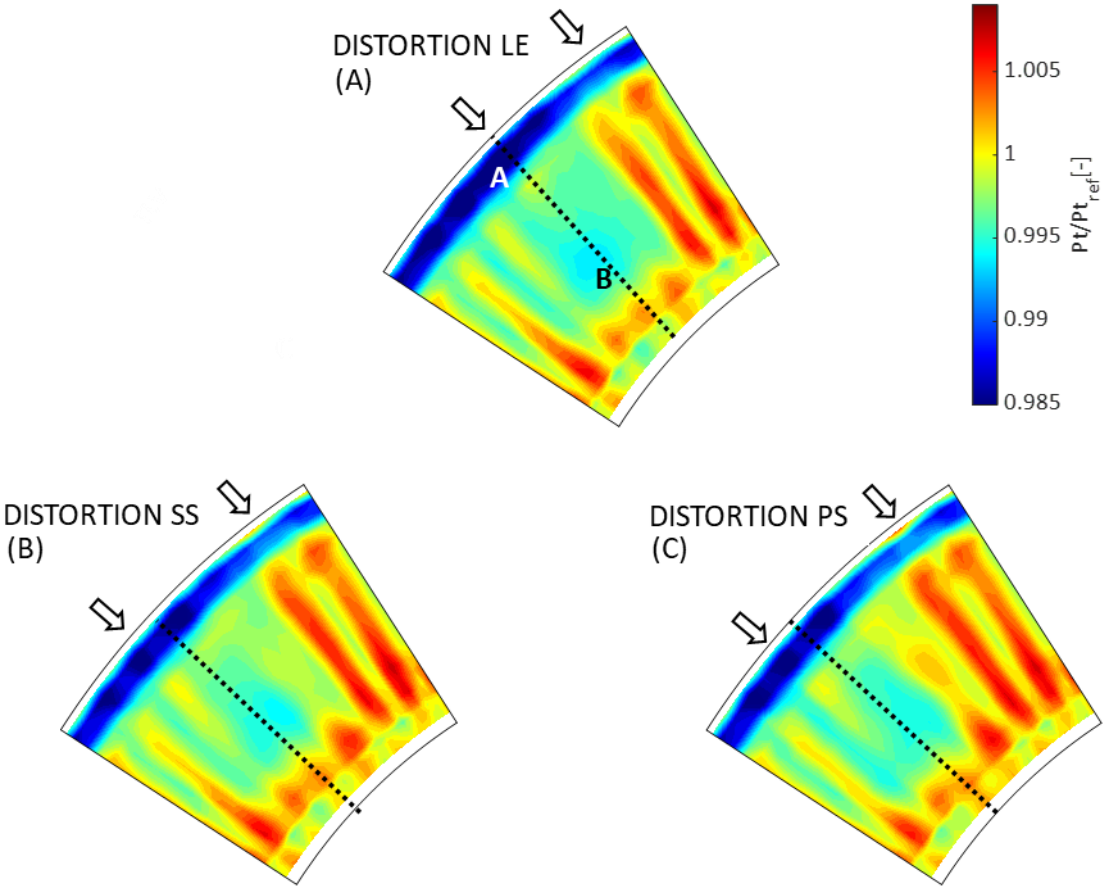

FIGURE 7.9: Total pressure distributions in plane C. Total pressure inlet distortion generated in plane A cases.

In order to provide an additional visualisation of the effect of the circumferential positioning of the inlet total pressure distortion generator, the spanwise distributions of total pressure circumferentially mass averaged over the measured sector at the rotor exit is plotted in FIGURE 7.10. The clean inflow case is depicted in black, while the LE case is orange, the SS distortion configuration red and the PS green. This colour code will be used in the rest of the chapter to distinguish and compare the cases.

The configuration which determines the highest total pressure difference relative to the clean inflow case is the LE case. Instead, the SS and PS set-ups present a very similar radial total pressure distribution. In all cases, the maximum different is registered at 39% span. These observations are in accordance with the plots described in FIGURE 7.9. Furthermore, the radial lines depicted in FIGURE 7.10 confirm that the low momentum flow generated by the distortion interacts principally with the rotor tip leakage vortex and with the core flow. In particular, the LE distortion is the case presenting the strongest total pressure reduction in the tip region. The hub secondary vortices, by contrast, seem to be only marginally affected by the distortion generator wake. A plot with the radial distribution evaluated only in the region characterised by distorted flow is depicted in FIGURE 7.11. The distributions are very similar compared to the plot in FIGURE 7.10. It can be observed that the LE case is the one configuration that determines the highest total pressure difference relative to the clean inflow case.

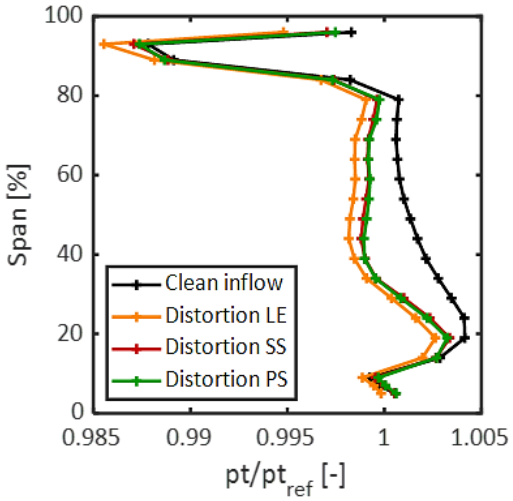

FIGURE 7.10: Radial distributions of circumferentially mass averaged total pressure. Plane C.

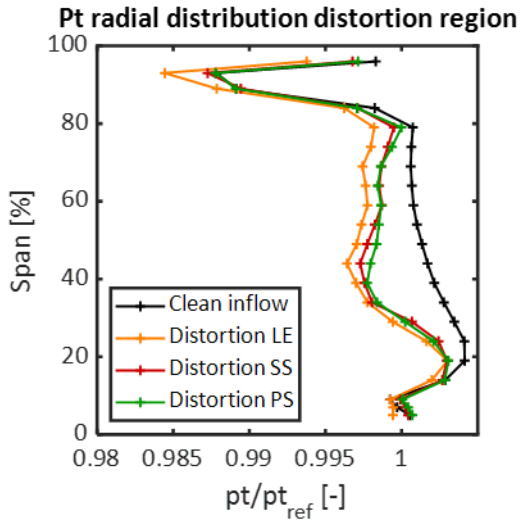

FIGURE 7.11: Radial distributions of circumferentially mass averaged total pressure in the distorted region. Plane C.

Studying the circumferential distribution of total pressure in plane C allows a better understanding of the position of the total pressure distortion downstream of the rotor, after it crossed the stage. FIGURE 7.12 reports the circumferential distribution of total pressure at hub (left), 39% span (centre) and tip (right). First of all, it can be observed that the circumferential position of the total pressure defect in the plots, caused by the chaotic flow entering the stage, is positioned accordingly to the position of the distortion generator for the three investigated cases. This is visible in particular in the 39% span plot, where the region influenced by the distortion moves from right to left for the LE, SS and PS cases respectively.

While the impact of the distortion is easily recognisable in the central plot, at the hub and tip the effect seem to be lower. However, in the tip region a modification of the P_t distribution can be observed. In particular, together with a drop in total pressure in the central region of the measurement sector, a P_t rise is visible in the right hand side of the plot. This can be connected to the redistribution of flow around the distortion generator, which determines an increase of the flow velocity in the region outside of the blockage.

Another visible difference in the plot is the circumferential shift of the distortion depending on the span height. The pressure drop is not located in the same position in the plots representing the tip and

the 39% span height. It appears that the distortion at midspan is located more towards the left side of the measured sector than at the tip. This circumferential redistribution based on the radius is due to the crossing of the rotating blade row.

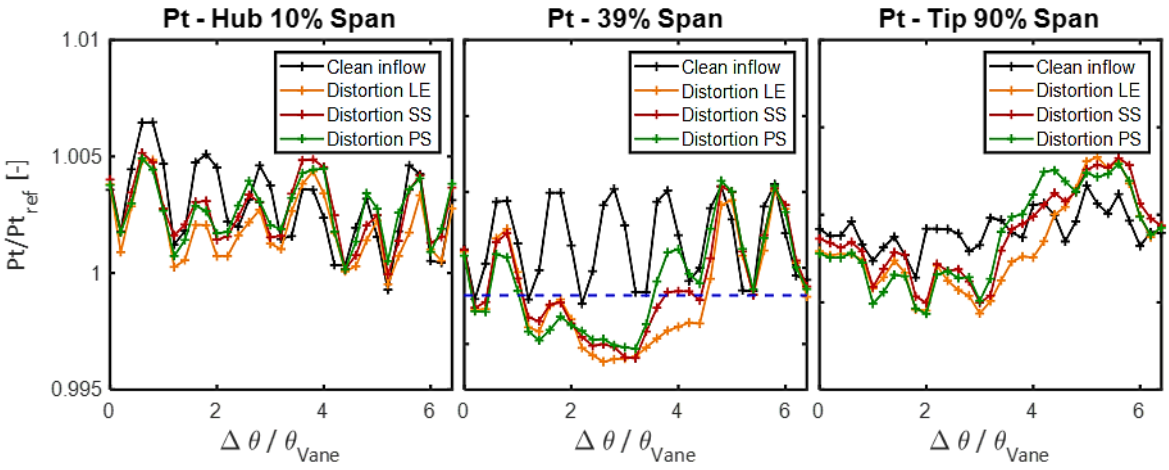

FIGURE 7.12: Circumferential distribution of total pressure at tip (right), 39% span (centre) and hub (left).

In conclusion, the artificially generated non-homogeneous inlet conditions create a well-recognisable total pressure distortion in the inlet flow of the LPT stage under investigation, which travelling through the stage interacts with the main flow features. It was shown that this interaction depends on the relative position between the inlet distortion and the stator vanes.

In order to study the repercussions of the inlet total pressure distortion on the stage performance for all the different configurations examined, the work extracted from the flow in the stage was evaluated. The details of this evaluation are explained in 5.1.2.

The experimental results regarding thermodynamic changes of the distorted flow, the wakes, the secondary flow regions and the undisturbed flow must be carefully interpreted. Therefore, according to the outcomes of the aerodynamic study presented above, three main regions were isolated in order to study the effect of the inlet distortion on the performance of the machine. Namely, the tip region, the hub region and the midspan region. The calculated extracted work was normalised over the mean Δh_t evaluated for the clean case. The results are plotted in FIGURE 7.13.

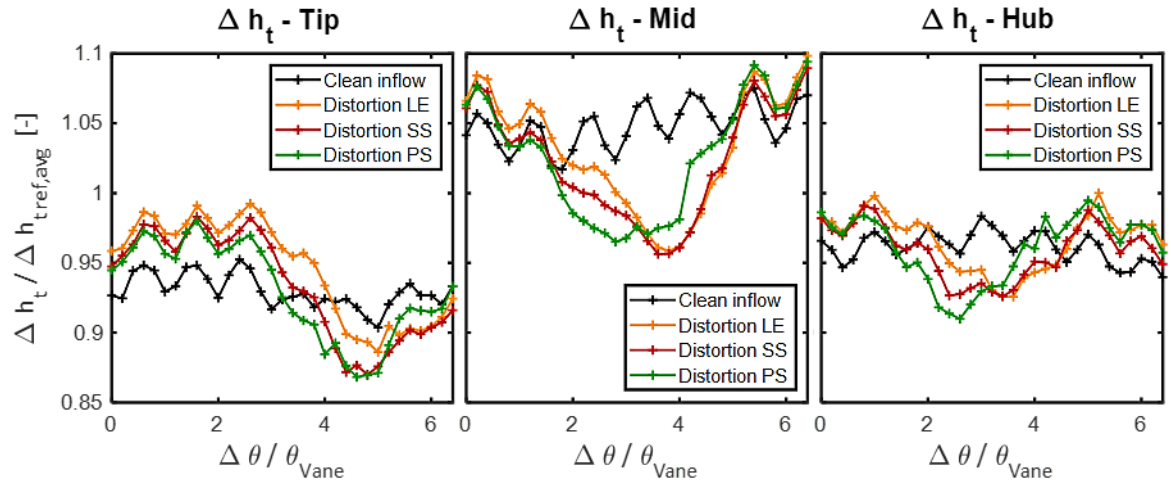

FIGURE 7.13: Circumferential distribution of total enthalpy difference evaluated at tip (left), midspan (centre) and hub (left).

In the presence of total pressure distortion, the circumferential profiles of total enthalpy variation appear altered. A higher temperature is recorded in the wake of the blockage, which is therefore exposed to a lower work extraction. Such outcome can be observed at the three investigated span heights, but the appearance of the curves clearly indicates that the reduction of exchanged work is stronger at midspan. On the contrary, due to flow redistribution around the distortion generator, the axial flow velocity of the region outside of the blockage wake increases, resulting in a higher Δh_t.

Ultimately, the inlet total pressure distortion causes a modification in the distribution of the work extracted by the rotor. It will be shown in the following how the vibrations characteristics of the rotor blades are influenced by this modification as some vibratory modes are subjected to increased excitation.

7.2.1.2 FRAPP UNSTEADY MEASUREMENTS

In this section, the results of the experimental investigation carried out by means of fast response pressure probe (FRAPP) in plane C are presented. A normalization of the absolute values is performed using the time averaged mean values of the reference flow field already shown in 6.2.2. The total pressure time evolution relative to all the inlet distortion cases is reported in FIGURE 7.14, FIGURE 7.15, FIGURE 7.16.

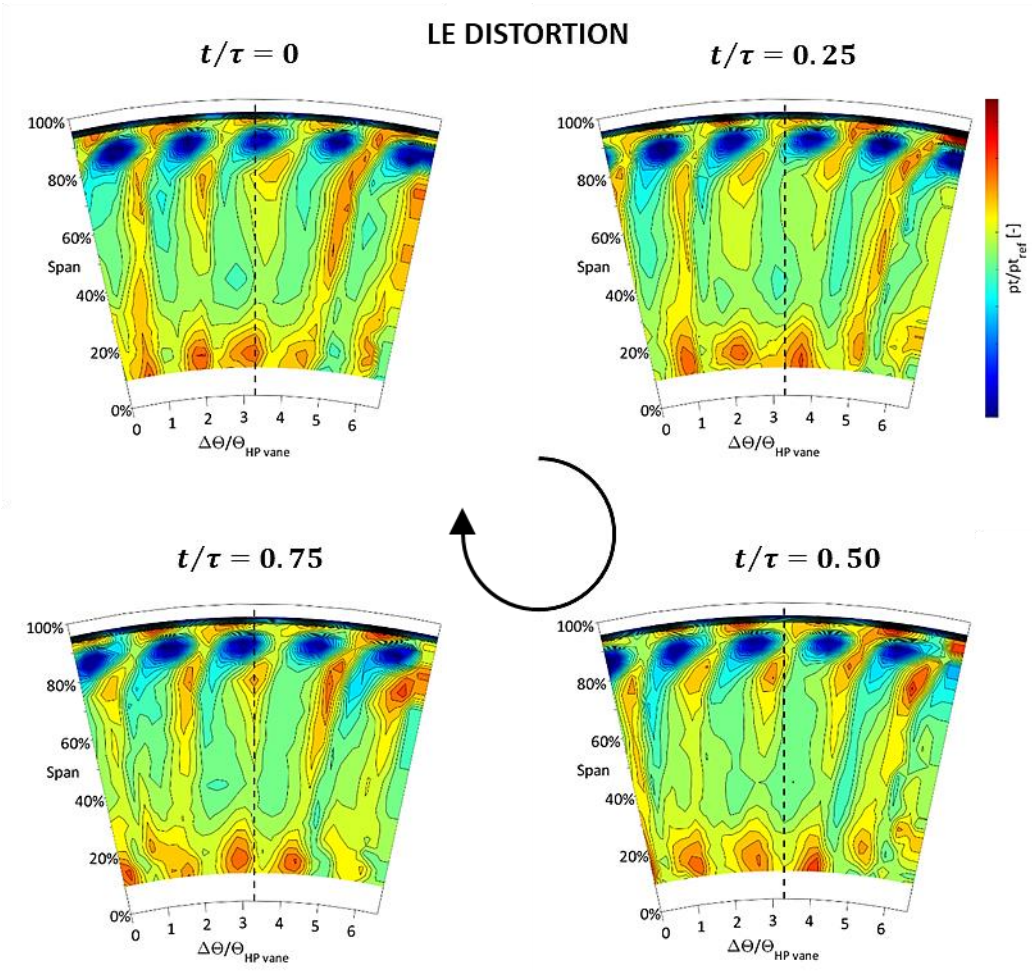

FIGURE 7.14: Time resolved distribution of the normalised total pressure downstream of the LPT rotor. LE distortion case.

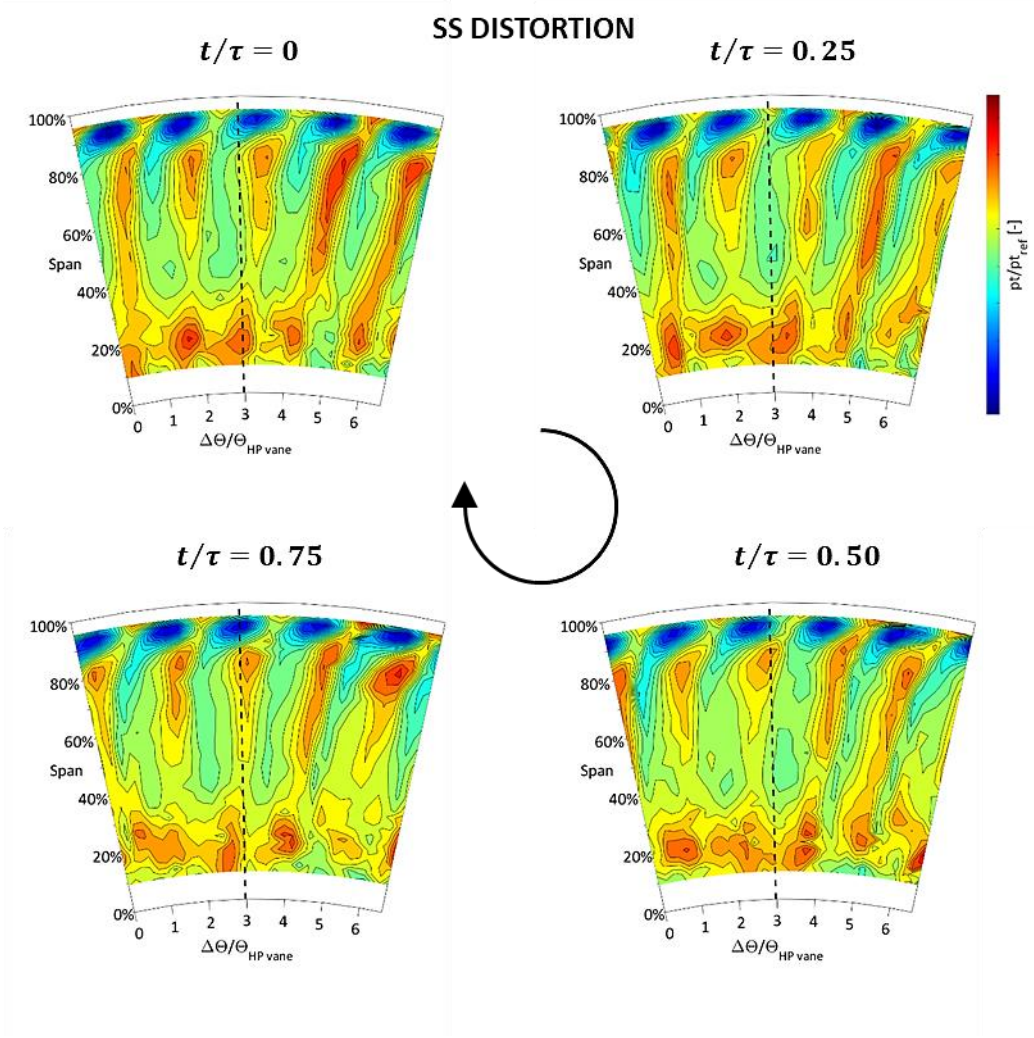

FIGURE 7.15: Time resolved distribution of the normalised total pressure downstream of the LPT rotor. SS distortion case.

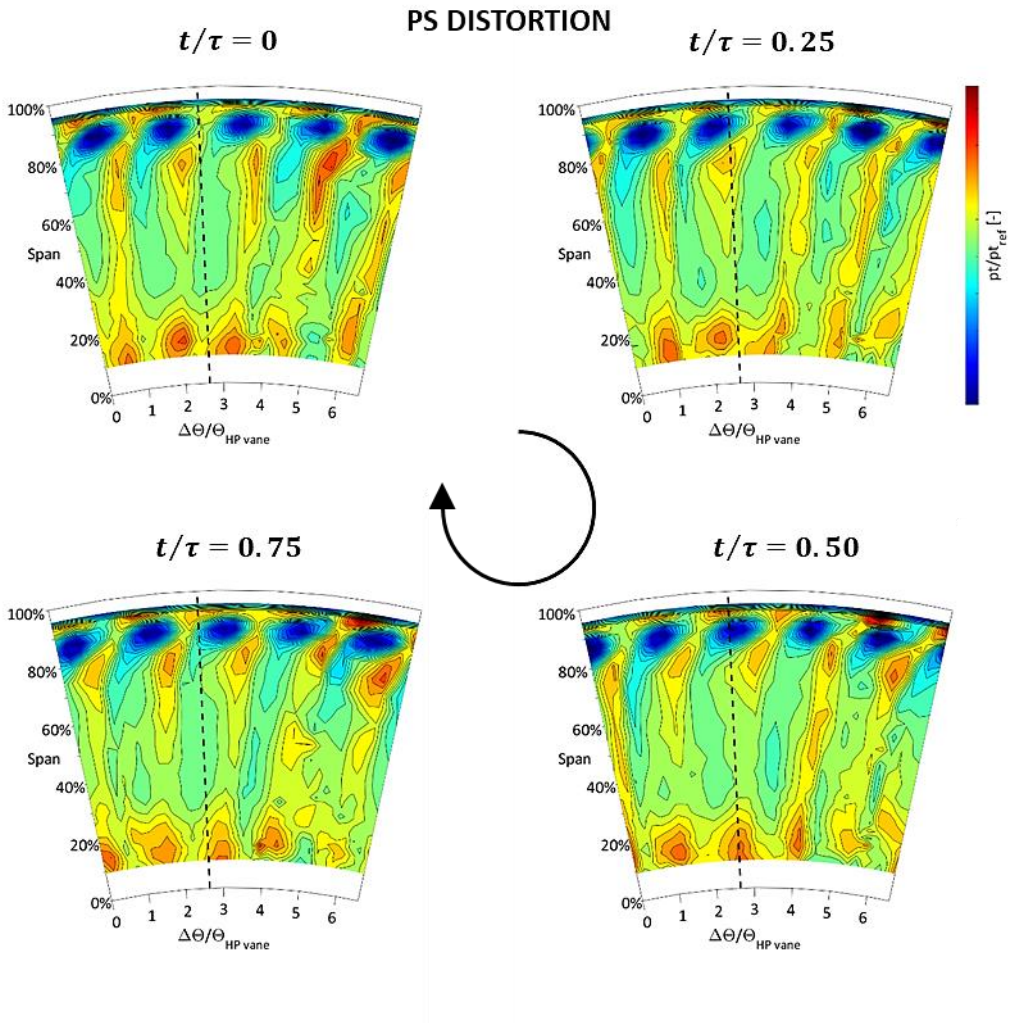

FIGURE 7.16: Time resolved distribution of the normalised total pressure downstream of the LPT rotor. PS distortion case.

In the figures, the position of the distortion generator is represented as a black dashed line superimposed to the total pressure contours. The effect of the P_t distortion is evident in the region around the black dashed lines. The low total pressure flow moves through the stage and is visible in Plane C downstream of the rotor. Analysing the FRAPP data and the time resolved P_t distribution it is possible to study the interaction between the total pressure distortion and the rotor related flow structures. In fact, one can see that the high total pressure structures representing the rotor core flow become less and less intense as they approach the low momentum flow and proceed to return to their original intensity as they leave (in circumferential direction) the distorted area.

Further information regarding the flow behaviour can be obtained studying the evolution of the unsteady total pressure is presented by means of time-space diagrams showing all the measured stator pitches and two blade passing periods at 39% span. This value of radial height was selected as this is the position where the inlet distortion cases show the maximum total pressure reduction with respect to the clean inflow case. The time-space plots of the total pressure three distortion cases under investigation and the one related to the clean case are illustrated in FIGURE 7.17. This visualisation is similar to the time-space plots presented in 6.2.2.

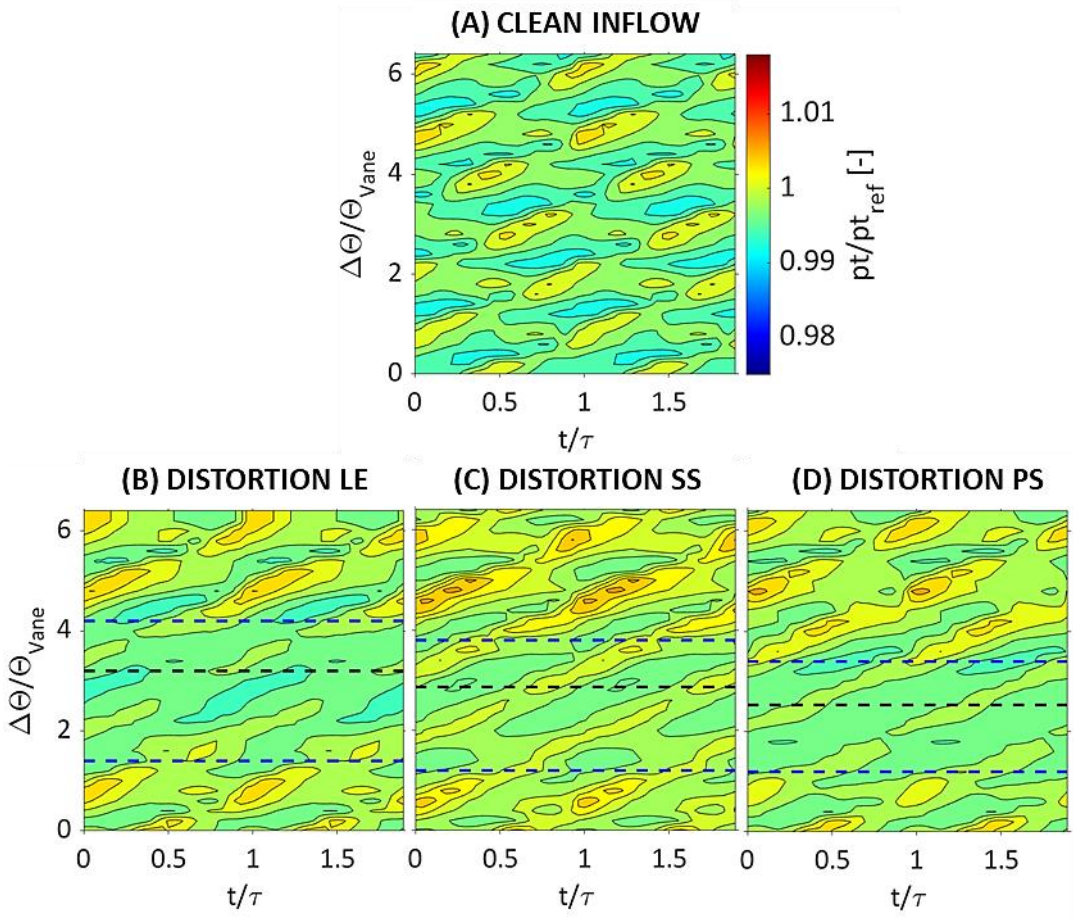

FIGURE 7.17: Time-space plots of total pressure at 39% span.

A comparison of the total pressure time-space plots with the clean inflow case shows that the low momentum fluid due to the cylinder wake interacts with the rotor flow structures, originating a horizontal band of low total pressure. The azimuthal position of this band follows the location of the inlet distortion generator indicated in the figure with a black dashed line. The effect of the distortion is particularly evident in the decrease of total pressure experienced by the rotor core flow traces.

With the aim of supporting the findings explained in the previous sections, the outer borders of the low total pressure fluid are represented in FIGURE 7.17 (B), (C) and (D) as blue dashed lines. The dashed lines were positioned in order to contain the region where the total pressure amplitude results lower than the values measured in the wakes generated by the stator vanes in the undisturbed regions. It was found that this limit value corresponds approximately to a total pressure amplitude reduction of 30% respective to the maximum amplitude in the undisturbed regions. The width of the distorted flow region seems to be larger for the LE distortion case (FIGURE 7.17 (B)). This is thought to be due to the fact that the wake fluid directed to the vane LE senses the rise in static pressure caused by the potential field of the leading edge and therefore splits, affecting the adjacent vane passage. Such separation of the wake fluid does not happen when the distortion cylinder is aligned with the vane SS or the PS, determining a narrower low momentum region in the measurements downstream of the rotor blade. Additionally, the lower border of the distorted region appears to be in a very similar position for all the cases.

The time average total pressure over one blade passing period BPP at 39% span was used to evaluate the thickness of the disturbed flow, similarly to [127], using the definition in the following equation:

$$\theta_{Dist} = \frac{1}{(\Delta\overline{p_t})_{max}} \sum_{\theta} \left(\overline{p_t}_{max} - \overline{p_t}(\theta)\right) \cdot \Delta\theta \tag{7.2}$$

Where $\overline{p_t}_{max}$ represents the peak value of total pressure in the undisturbed core flow and $(\Delta\overline{p_t})_{max}$ the difference between $\overline{p_t}_{max}$ and the minimum value of time average total pressure in the distortion region at 39% span. The results of this evaluation are reported in TABLE 7.1, normalised with the stator vane pitch. Therefore, the data shown in the table represent the number of stator pitches that the low momentum fluid occupies in plane C.

TABLE 7.1: Distortion thickness normalised over the stator vane pitch.

Distortion thickness	
Case	$\theta_{Dist}/\theta_{Vane}$ [-]
Distortion LE	2.95
Distortion SS	2.89
Distortion PS	2.88

The configuration characterised by the widest distortion is the LE distortion case with a distortion thickness of approximately 3 stator pitches. Both the PS and SS cases show a slightly smaller, and similar, width of the distorted flow region.

Interestingly, the LE configuration shows both the highest P_t reduction and the widest low-momentum flow region. This could be explained considering that the wake of the cylinder interacts with the stator vanes; and consequently, occupies a wider portion of the measurement sector, still maintaining the same intensity, as can be observed in the contour plots referring to the 5HP measurements. This determines an overall higher reduction on the total pressure field downstream of the LPT rotor. Ultimately, the result in TABLE 7.1 support the observations gathered from the study of both the steady and unsteady data sets.

The data collected by means of FRAP probe can be used to gain more insights on the effects of the inflow non-homogeneity on the rotor vibrations, studying the unsteady total pressure fluctuations, similarly to Lengani et al. [118]. The procedure applied to evaluate the total pressure RMS is described in detail in section 5.1.3. FIGURE 7.18shows the RMS values of the total pressure stochastic time averaged over one BPP and normalised with the average value obtained for the reference case. The three plots represent the three cases featuring inlet distorted flow LE, SS and PS. By analysing the three contour-plots one can observe that higher pressure fluctuations were measured for the SS and PS distortion cases than for the LE configuration. In particular, the last case, which was linked to the strongest total pressure reduction, presents lower RMS of total pressure stochastic fluctuations. This result is considered to be related to the larger width of the distorted flow and its interaction with the stator vanes observed in the LE configuration.

All presented cases exhibit the highest values of total pressure RMS at high span, connected to the presence of the tip vortex. An additional region of high unsteadiness can be noticed in the lower section of the passage. Here the core of the low momentum fluid interacts with the hub passage vortex. The high total pressure RMS in this region suggest a strengthening of the secondary flow structures due to the presence of inlet distortion.

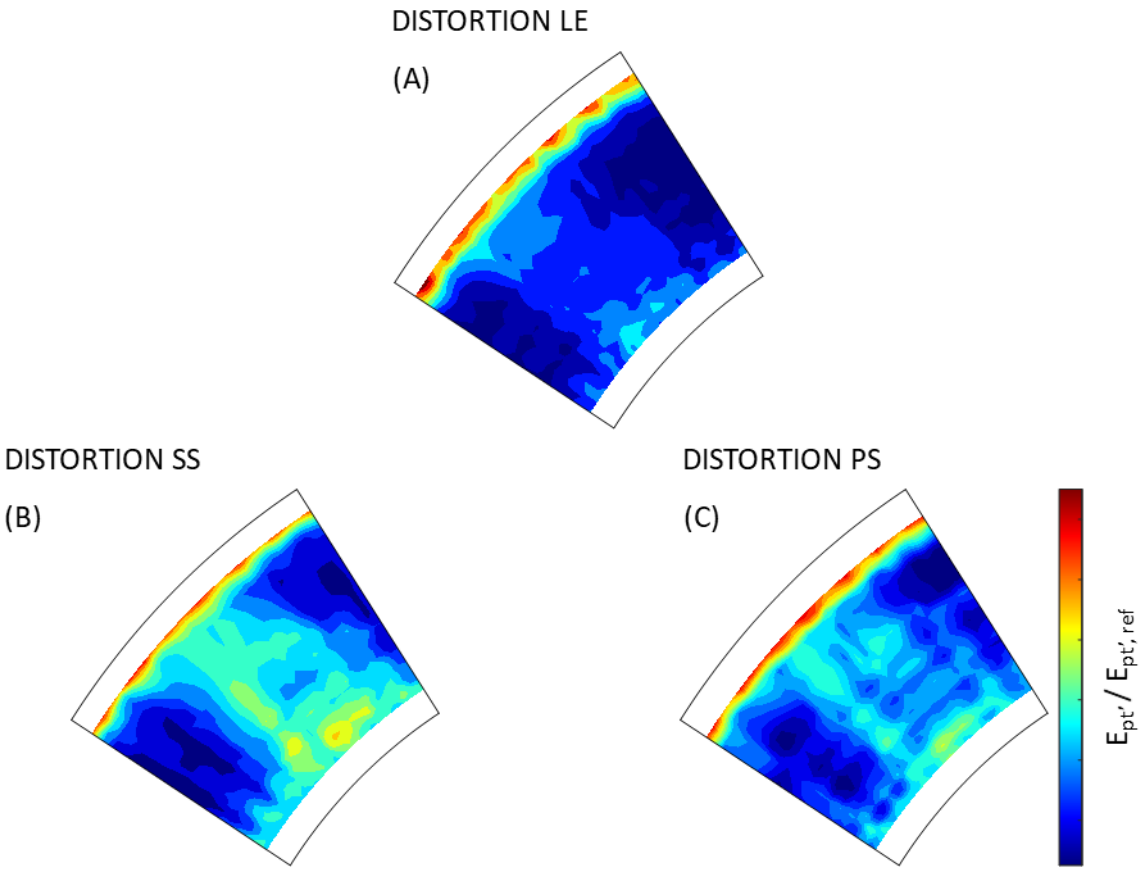

FIGURE 7.18: RMS of stochastic total pressure fluctuations time averaged over one BPP Total pressure inlet distortion generated in plane A. Measurements in Plane c.

Overall, the FRAPP data suggest that the additional unsteadiness due to the wake of the distortion generator evolving in the stage determines an alteration of the rotor-stator wakes interaction, generating a larger extent of instability in the secondary flows in the lower region of the channel.

7.2.2 ROTOR BLADE VIBRATIONS

7.2.2.1 FORCED RESPONSE AT NOMINAL OPERATING POINT

The results of the measurements at nominal operating point are presented here with the intention to characterise the LPT rotor vibrations and to study the effects of the total pressure inlet distortion and its clocking position on the vibrational amplitudes. Additionally, the data acquired during the speed sweeps around the operating point gave the opportunity to study the effects of the excitation determined by the inlet distortion on the forced response of the rotor blades. In particular, the analysis in time and frequency of the data collected during the sweeps allowed the identification of an amplification of the vibratory response occurring at the first blade eigenfrequency (1F).

FIGURE 7.19 shows a comparison of the spectra obtained from the signals measured from a single strain gauge. The results are presented in the form of strain normalised with the amplitude of the first eigenfrequency of the reference case already presented in section 6.3.

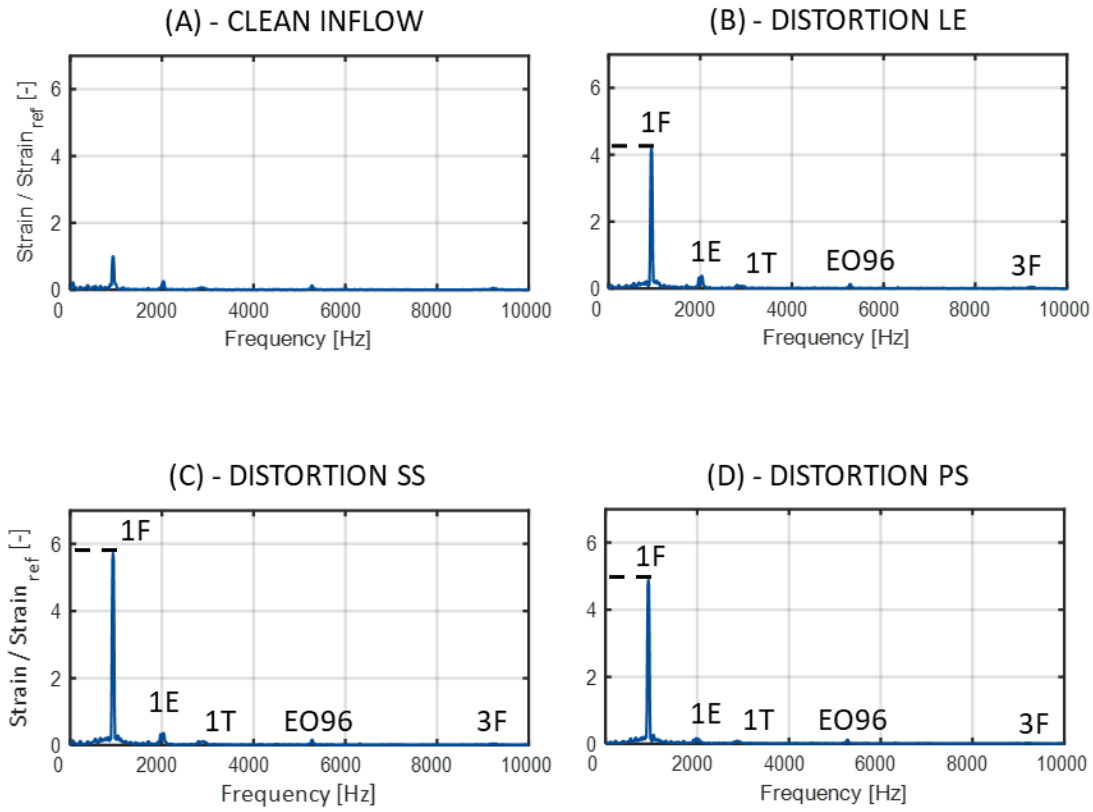

FIGURE 7.19: Forced response spectra of strain gauge 2 at nominal OP.

A comparison between the spectra enables the recognition of the impact of the distorted flow on the rotor blade vibrations. In the first place, the amplitude of the first mode obtained for all the distorted cases (FIGURE 7.19 (B), (C), (D)) is higher than the level of the 1F measured for the clean inflow configuration. Specifically, 1F amplitude is 4.2 times higher than the reference case in the LE distortion case, 5.7 times higher in the SS case and 4.9 times in the case featuring the distortion generator aligned with the pressure side of the stator vane.

To allow a better comparison of the strain gauges' data, the strain energy was evaluated according to Equation (5.27). The results of this evaluation are shown in FIGURE 7.20. The clean inflow case was taken as reference and therefore the value associated to this configuration is 1 in the bar-plot. Observing the figure, one can note that all the configurations including the inlet distortion generator present higher levels of strain energy. This result is representative of higher overall strain amplitudes measured over the whole investigated frequency range. In particular, the set-up which features the distortion generator aligned with the suction side of the stator vane exhibits the highest strain energy. In accordance to what already observed for the amplitude of the first eigenfrequency (1F), the PS case shows the second highest level. Furthermore, even though the LE case presents the lowest strain energy of the distorted cases, its value is still considerably higher than the one obtained for the reference case.

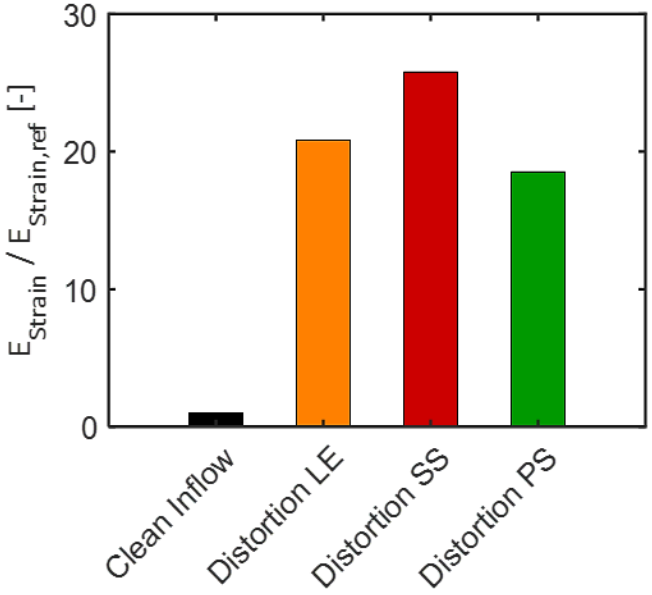

FIGURE 7.20: Strain energy evaluated from SG2 signal for the four investigated cases.

7.2.2.2 FORCED RESPONSE DURING TRANSIENT OPERATIONS

Strain gauge data were acquired during speed weeps around the nominal operating point. The results presented in this section will focus on the speed range between 3200 and 3500 rpm. Analysing the data with respect to both speed and frequency, allowed the recognition of a modification of the blade vibratory behaviour of the rotor blades in the inflow distortion cases. While the clean inlet total pressure case showed stable vibration amplitudes, as already discussed in the previous set-up vibration analysis, higher vibration amplitudes were instead experienced by the rotor blades when the distortion generator was placed in front of the LPT stator vanes in plane A. A sudden rise in amplitudes was measured at the first eigenfrequency (1F) starting from 3310 rpm until approximately 3330 rpm, followed by a rapid reduction that lasted until the rotor speed reached 3360 rpm. Using the technique presented in 7.1.2.2, it was possible to isolate the evolution of the 1F amplitude across the speed sweep. The 1F amplitudes obtained for all the investigated configurations are shown in FIGURE 7.21.

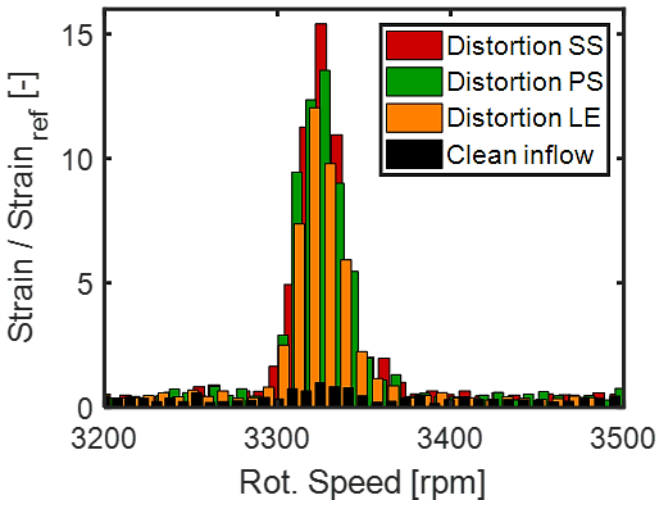

FIGURE 7.21: Amplitude of the first eigenfrequency (1F) during speed sweeps between 3200 and 3500 rpm.

By comparing the distortion cases with the reference clean inflow, the growth of the rotor blades vibratory response can be noticed. The alignment of the distortion generator with the suction side of the stator vane causes the highest 1F amplitude, followed by the PS and LE positions. Two different mechanisms can be considered responsible for the aerodynamic excitation observed during the transient measurements. Firstly, the high unsteadiness introduced by the wake of the distortion generator in the rotor inlet flow, and secondly, the spatially non-uniformity in the flow field determined by the low-momentum flow in the distorted region.

The effect of the unsteadiness increase caused by the inlet total pressure distortion on the rotor blade vibrations was already discussed in the analysis presented in the previous section. Decomposing the flow field sector measured by means of 5HP applying a spatial FFT in correspondence of the highest total pressure distortion allowed us to study the effects of the spatial non-uniformity on the aerodynamic excitation on the rotor blades. The amplitudes of the excitation orders obtained decomposing the flow field at 39% span are presented in FIGURE 7.22, normalised with the amplitude of the EO96 excitation, which corresponds to the forcing due to the stator vanes wakes. The circumferential distribution of the total pressure used for this analysis is shown in the central plot of FIGURE 7.10.

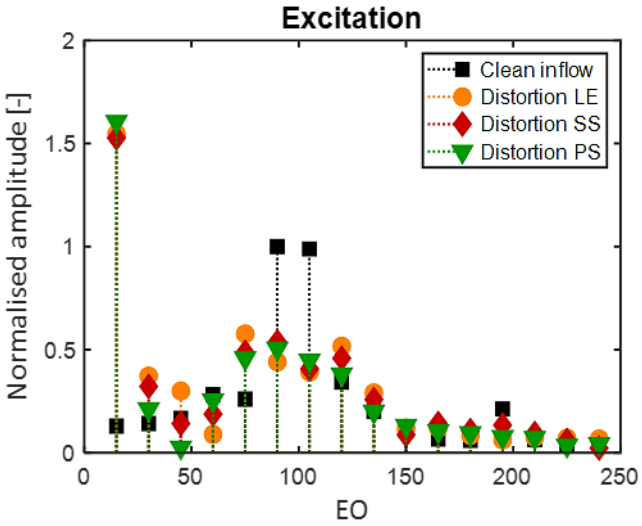

FIGURE 7.22: Engine order excitations evaluated for the clean inflow case and for the distortion cases in plane C.

Observing the amplitudes of the EO excitations obtained for the clean inflow case it is possible to note that, as expected, the main forcing is due to the wakes of the stator vanes at EO96. The second harmonic of this excitation is also visible around EO200. On the contrary, the configurations featuring the inlet distortion generator present different excitation orders. All the inlet distortion cases show high excitation amplitude at low engine orders. Moreover, for these configurations the amplitude of the EO96 appears to be lower than for the clean inflow case.

The speed range around which the 1F mode vibratory response experienced the rise in amplitude presented in FIGURE 7.21 fits well with an excitation at an engine order between 16 and 18. This range of EOs agrees well with the higher amplitude of aerodynamic excitation at low engines orders that was obtained for all the inlet distortion cases shown in FIGURE 7.22. Consequently, the additional pressure perturbation present in the distorted inflow configuration can be defined as the causes of additional flow excitation at low engine orders, which determines the higher responses measured at the frequency of the 1F mode during the speed-sweeps.

Furthermore, the higher vibration amplitudes obtained at the frequency of the first mode presented in FIGURE 7.19 were measured at the nominal operating speed, very close to the amplification of the 1F response during transient speed sweeps. Consequently, higher low engine order excitation introduced by the distortion in the flow-field can be considered the cause of the amplification of the first mode

amplitude obtained for the distorted cases. Ultimately, the propagation of the low-momentum fluid due to the wake of the distortion generator positioned in front of the stator vanes causes the excitation of the rotor blades at low engine order, resulting in an observable modification of the rotor blade vibratory response.

In conclusion, the amplification of the flow unsteadiness due to the inlet distortion is directly connected to the higher forced response of the rotor blading. Furthermore, the data showed that the spatial non-uniformity in the distorted region caused higher low engine order aerodynamic excitation, determining the intensification of the blades' vibratory response at the first eigenfrequency.

8. TOTAL TEMPERATURE INLET DISTORTION IN PLANE 0

The present chapter presents the results of the part of this experimental investigation focused on the propagation of temperature inflow distortions through a modern low pressure turbine stage, with a particular focus on both the aerodynamic and aero-elastic characteristics of the turbine. The details of the tested configurations are presented in sections 4.4.2.

The results of the investigation carried out by means of 5HP in plane A and C are presented in the following paragraphs. The most relevant tested configurations are collected in the contour plots of total temperature, in order to highlight the effect of the air injection on the total temperature field at the inlet of the LPT stage. In particular, the total pressure and total temperature measured in plane A and C will be compared with the reference case in order to study the influence of the secondary air injection on the LPT stage inlet and outlet conditions.

8.1.1 PLANE A - TOTAL PRESSURE

The present paragraph collects the total pressure radial profiles measured for the two investigated mass flow injections (2.0 g/s and 2.5 g/s). The aim of this section is to demonstrate the low impact of the air injection on the flow conditions at the inlet of the stage other than on the temperature. This is relevant since the aim of this part of the study was to create a temperature distortion without any modification of the total pressure inlet conditions.

The total pressure distributions in plane A for the 2 g/s and 2.5 g/s injection cases are presented in FIGURE 8.1. In the plots the results corresponding to different injected temperatures are compared to the P_t radial distribution obtained for the clean case (in black), presented in paragraph 6.1. Observing the first plot on the left, one can notice that all the tested configurations relative to the 2 g/s case present a very similar P_t distribution to the clean in flow case. The plot obtained for the 2.5 g/s cases, presented on the right, also show a very similar trend of total pressure in plane A, even though there are two small regions at around 80% and 20% where the inlet distortion cases show a slightly higher total pressure. It must be considered that these differences are very small and can therefore be neglected as this would not cause a noticeable modification in the operation of the turbine. Consequently, the two pressure profiles demonstrate that the localised injection of secondary air does not modify much the inlet total pressure of the LPT stage under investigation.

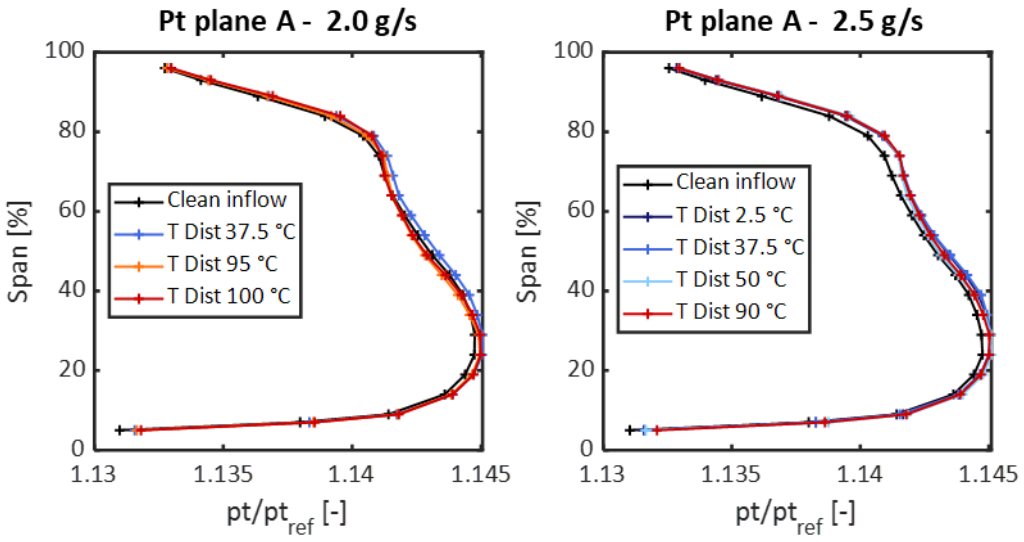

FIGURE 8.1: Radial distributions of circumferentially mass averaged total pressure. 2.0 g/s case (left) and 2.5 g/s case (right).

8.1.2 PLANE A – TOTAL TEMPERATURE - INJECTED MASS FLOW 2 G/S

The first injection mass flow that was tested was 2 g/s. The complete set of temperatures tested are represented in TABLE 4.3. Here only the most relevant one will be analysed, considering that for the other cases similar conclusions can be drawn. In particular, the presentation focusses on the cases with an injection temperature of 310.5 K (37.5 °C), 323 K (50 °C), 368 K (95 °C) and 373 (100 °C). These temperatures correspond respectively to 50%, 66%, 125% and 133% of the nominal total inlet temperature. FIGURE 8.2 presents the total temperature measured by means of 5HP in plane A, located at the inlet of the LPT stage, for the cases 310.5 K (37.5 °C), 368 K (95 °C) and 373 (100 °C). On the left column of the picture one can see the total temperature distributions and on the right column, the difference between the total temperature measured for the distorted cases and the total temperature of the clean inflow case presented in FIGURE 6.2. The percentage value presented in the plots is obtained using the definition presented in Equation (8.1), where the maximum temperature range measured in the clean inflow case ($T_{t\,max,Ref} - T_{t\,min,Ref}$) as a reference for the difference between the distorted cases ($T_{t,Dist}$) and the reference case ($T_{t,Ref}$).

$$\Delta T_{Dist} = \frac{T_{t,Dist} - T_{t,Ref}}{T_{t\,max,Ref} - T_{t\,min,Ref}} \tag{8.1}$$

Observing the figures, it is possible to identify the effect of the injection of air on the inlet flow of the turbine stage. Both the cold air injection and the hot air injection create a distinct and well recognizable region of colder or warmer temperature in the field respectively. This region appears to interest two IGV passages and its intensity depends directly on the temperature of the injected air. Interestingly, the colder flow seems to be more evident in lower half of the passage, whereas the higher temperature injection appears to have a stronger impact on the upper section of the passage. Regarding the position of the temperature distortion, the colder flow is more evident in lower half of the passage, whereas the higher temperature injection appears to have a stronger impact on the upper section of the passage. This could be due to the interaction between the injected air and the vanes, in particular with the upper passage vortex already presented in in the discussion of the results relative to the clean inflow case. Moreover, the effect of the IGVs wakes is recognizable in the skewed shape that the temperature distortion assumes after passing through them.

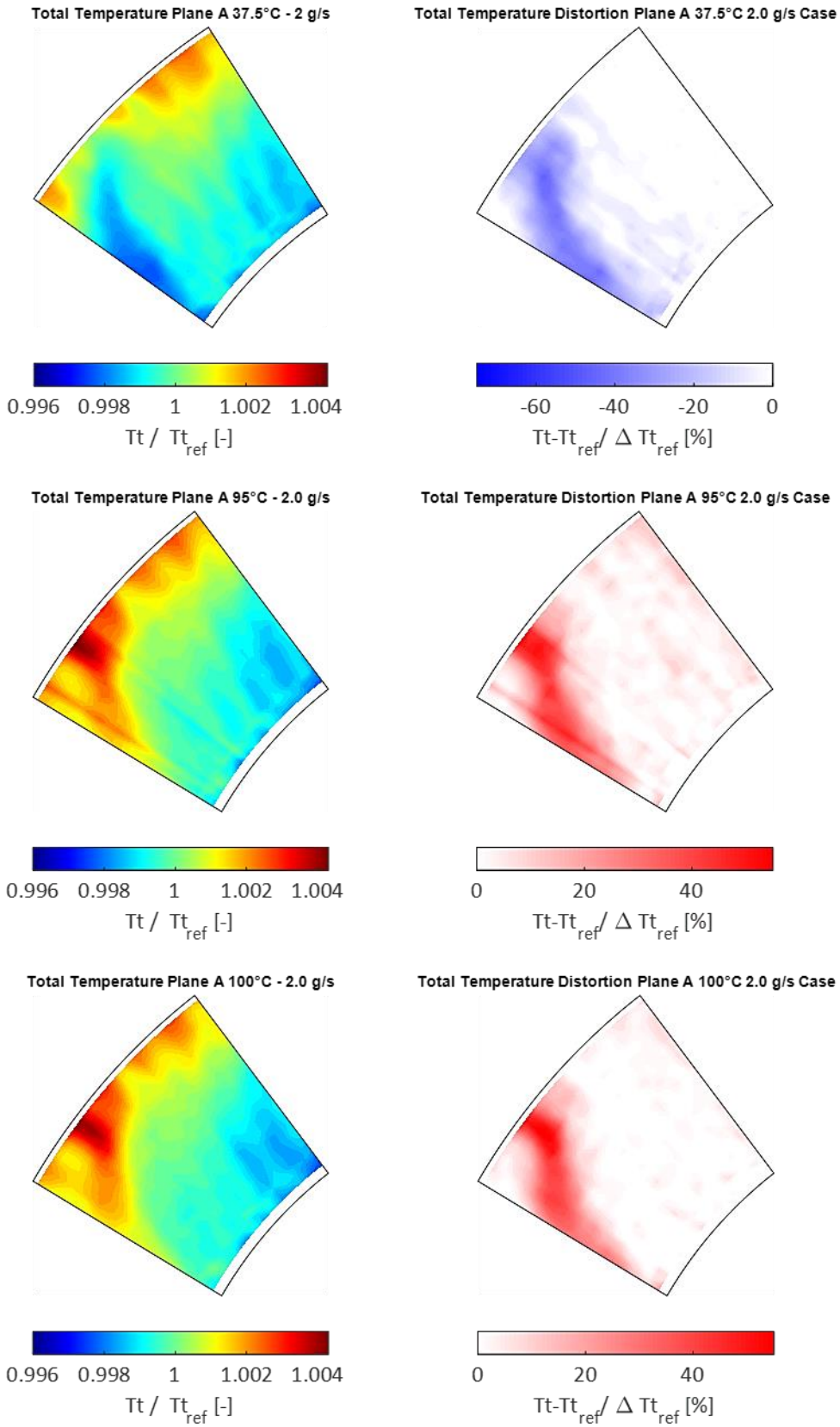

FIGURE 8.2: Total temperature distribution for the 37.5 °C (up), 95 °C (centre), 100 °C (low) cases. 2g/s injection.

The effect of the distortion on the total temperature field can be understood observing the right column of the figure. In all injection cases, the total temperature distortion travels from the injection plane (plane 0) to the measurement plane (plane A), through the IGV and is still well recognisable, representing a ΔT_{Dist} that reaches up to 70% of the reference temperature range. For this reason, it is possible to conclude that air injection in Plane 0 creates a well-defined total temperature distortion in the inlet flow of the low pressure turbine stage under investigation.

In order to provide an additional visualisation of the effect of the circumferential inlet air injection on the total temperature field in Plane A, the spanwise distributions of the total temperature fields presented above circumferentially mass averaged over the measured sector is plotted in FIGURE 8.3.

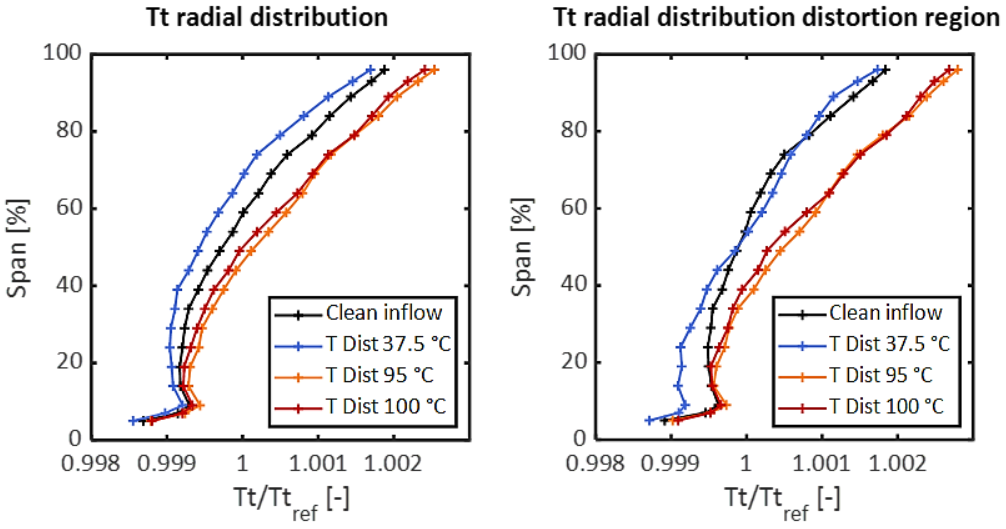

FIGURE 8.3: Radial distributions of circumferentially mass averaged total temperature in the complete measurement sector (left) and in the distorted sector only (right). Plane A. 2g/s injection.

The total temperature distributions follow accurately the temperature of the injected air, determining a colder total temperature distribution for the 310.5 K (37.5 °C) case and hotter temperature profiles for the cases 368 K (95 °C) and 373 (100 °C). Since the injected air temperature difference between the two last cases is only 5 K, these temperature profiles are very similar. Additionally, one can observe that the lower temperature air injection determines a modification in the temperature profile particularly in the lower half of the channel, while the effect of the hot injection is stronger at higher span.

Another visualisation of the total temperature distorted flow is depicted in FIGURE 8.4. The three plots represent the circumferential distribution of total temperature at midspan (centre), hub (left) and tip (right). Analysing the clean inflow case distributions al all span heights, it is possible to notice the effect of the wakes of the IGVs. The temperature distortion generated by the air injection is more evident in the midspan and tip plots. Looking at the circumferential position of the temperature distortion, a circumferential shift due to the interaction with the bended wakes of the IGVs can be noticed. In the lower section of the passage (hub) only the colder air injection case seems to have a noticeable effect on the total temperature circumferential distribution. This supports the finding that the hot air injection has a stronger effect at high span and the cold injection is more effective in the lower part of the channel. Once again, the small difference between the two cases with temperature injection of 368 K (95 °C) and 373 K (100 °C) determines a very similar circumferential total temperature profile. Furthermore, the skewed shape of the temperature distortion is recognisable once more in the different circumferential location of the temperature distortion between hub, midspan and tip.

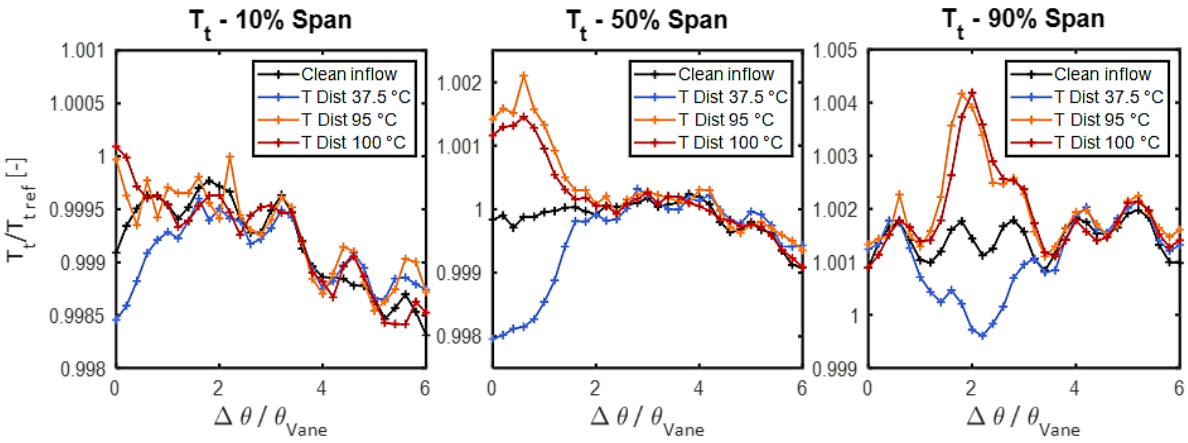

FIGURE 8.4: Circumferential distribution of total temperature at hub (10% span), midspan (50% span) and tip (90% span). 2 g/s injection.

8.1.3 PLANE A – TOTAL TEMPERATURE - INJECTED MASS FLOW 2.5 G/S

A second set of experiments with a higher mass flow was carried out, in order to study the effect of the injected air mass flow on the total temperature distortion. The mass flow of the injected air was in this second case 2.5 g/s. The complete set of temperatures tested for this mass flow is shown in TABLE 4.3. Also in this case, only the most relevant configurations will be presented here. In particular, the air injection temperature of 298 K (25 °C – 33% of T_{t0} nominal), 310.5 K (37.5°C – 50% of T_{t0} nominal), 323 K (50 °C – 66% of T_{t0} nominal) and 363 K (90 °C - 120% of T_{t0} nominal) will be used for this presentation. FIGURE 8.5 presents the total temperature measured by means of 5HP in plane A, for the cases 310.5 K (37.5 °C), 323 K (50 °C) and 363 (90 °C). The figure is organised similarly to FIGURE 8.2. The total temperature distributions are presented on the left hand side and the difference between the total temperature measured for the distorted cases and the total temperature of the clean inflow case is presented in the plots on the right. Again, the percentage value presented in the plots is obtained using the max temperature range measured in the clean inflow case as a reference for the difference between the distorted cases and the reference case, according to Equation (8.1).

The effect of the injection of air in the inlet flow of the turbine stage can be seen in the temperature contours once again. In fact, the intensity of the distortions can be compared to the intensity obtained for the 2 g/s case, resulting higher for the higher injected mass flow. This is particularly evident comparing the plots obtained for the 37.5 °C air temperature.

A similar behaviour of the distortion in relation to its radial height is noticeable in the plots, the colder flow seems again to occupy a lower region of the channel compared to the hotter air injection case, which is more evident in the upper half of the passage. The shape of the temperature distortion appears to be very similar to the 2 g/s case, resulting skewed after the interaction with the IGVs.

The intensity of the additional air injection on the total temperature field can be understood looking at the right column of the figure. The 37.5 °C case creates a T_t distortion in plane A that reaches up to 75% of the reference total temperature range, which is higher than the distortion obtained for the 2 g/s case. Instead, the distortion created by the 50 °C case results lower in intensity, as the injection temperature was closer to the main flow temperature. The hotter air injection case determines a distortion temperature up to more than 50% of the total temperature of the clean inflow case. Therefore, the effect of the higher mass flow is observable in the total temperature distributions.

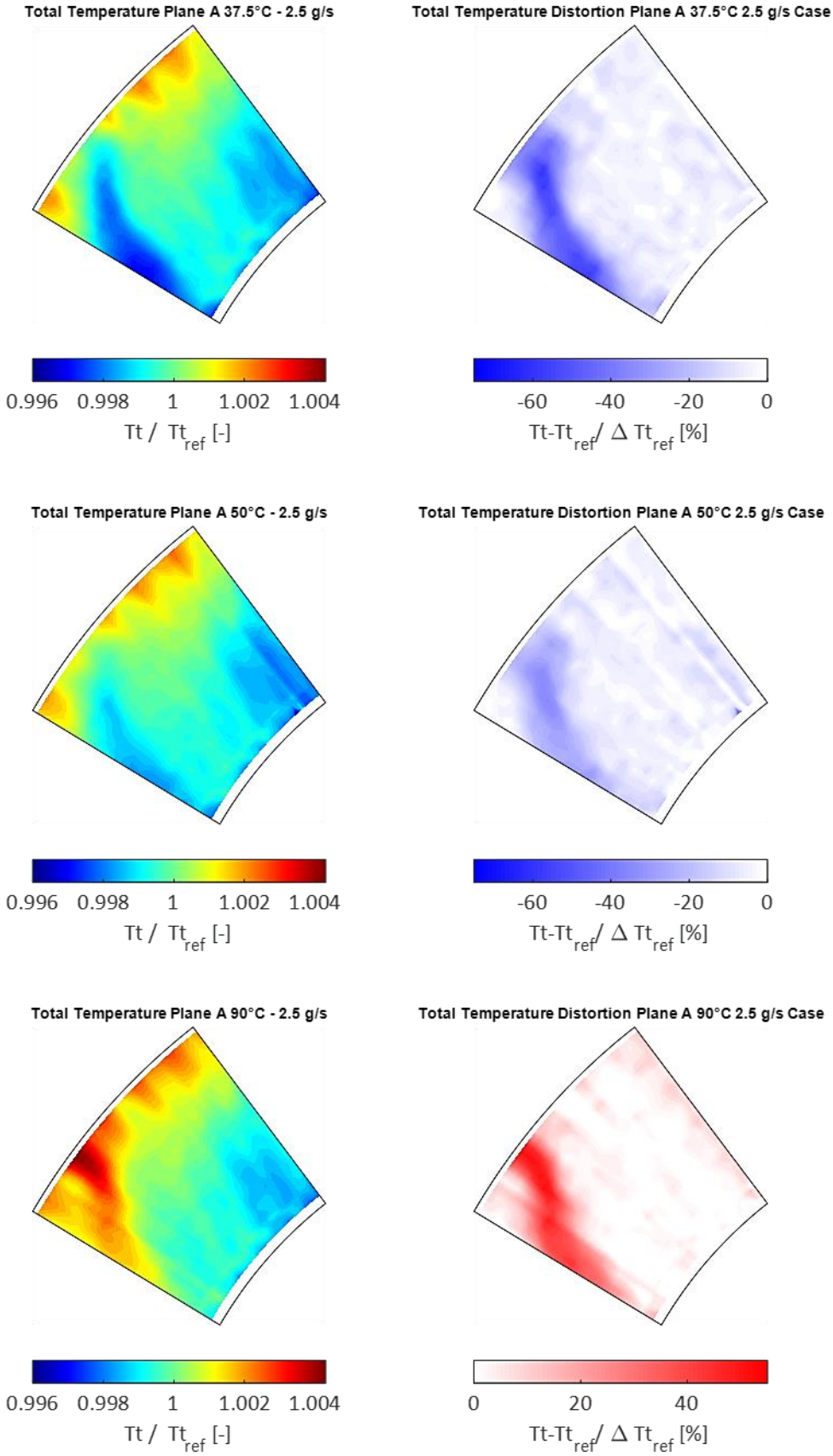

FIGURE 8.5: Total temperature distribution for the 37.5 °C (up), 50 °C (centre), 900 °C (low) cases. 2.5 g/s injection.

The spanwise distributions of the total temperature circumferentially mass averaged over the region influenced by the distortion for the 2.5 g/s cases is plotted in FIGURE 8.6.

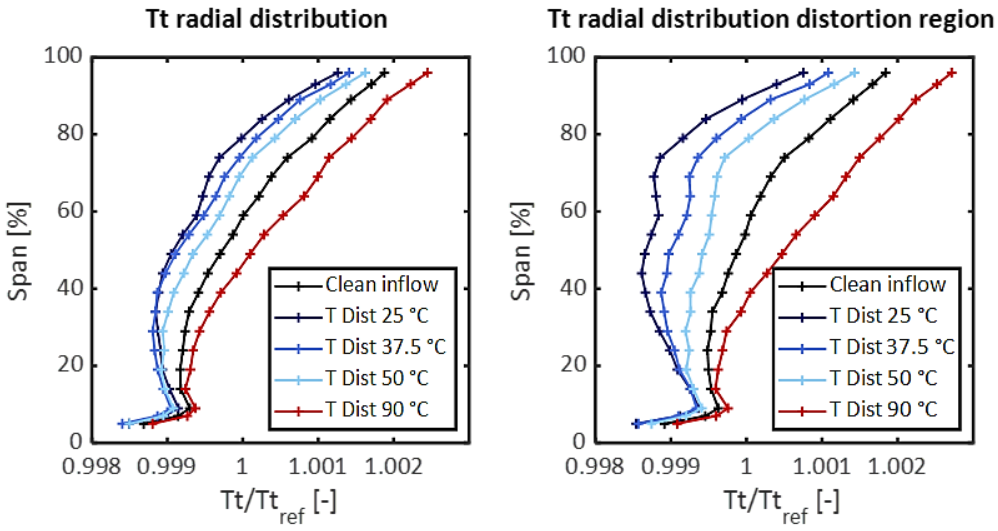

FIGURE 8.6: Radial distributions of circumferentially mass averaged total temperature in the complete measurement sector (left) and in the distorted sector only (right). Plane A. 2.5 g/s injection.

As for the 2.0 g/s case, also for this configuration it can be seen that the trend of the temperature distributions follows accurately the temperature of the injected air, determining a colder total temperature distribution for the 298 K (25 °C), 310.5 K (37.5 °C) and 323 K (50 °C) injection temperatures and hotter temperature profiles for the 363 K (90 °C) supplementary air temperature.

By comparing the radial distribution obtained for the 2.5 g/s case to the one measured for the 2.0 g/s case, one can observe that the higher injected mass flow causes a stronger variation on the total temperature profiles. In particular, the colder air cases seem to have a more intense effect on the temperature distribution along the whole span and not only in the lower passage region as it was the case for the 2 g/s injection. However, the effect of the warmer air injection results stronger at higher span also in the 2.5 g/s configuration.

The three plots in FIGURE 8.7 represent the circumferential distribution of total pressure at midspan (centre), hub (left) and tip (right) obtained from the data presented in FIGURE 8.5. As it was already observed for the 2.0 g/s case, the temperature distortion generated by the air injection can be mainly noticed in the midspan and tip plots. The circumferential skew of the temperature distortion is responsible for the only partial presence of a signature of temperature distortion in the hub plot, since the distorted region falls out of the measurement sector at this radial height.

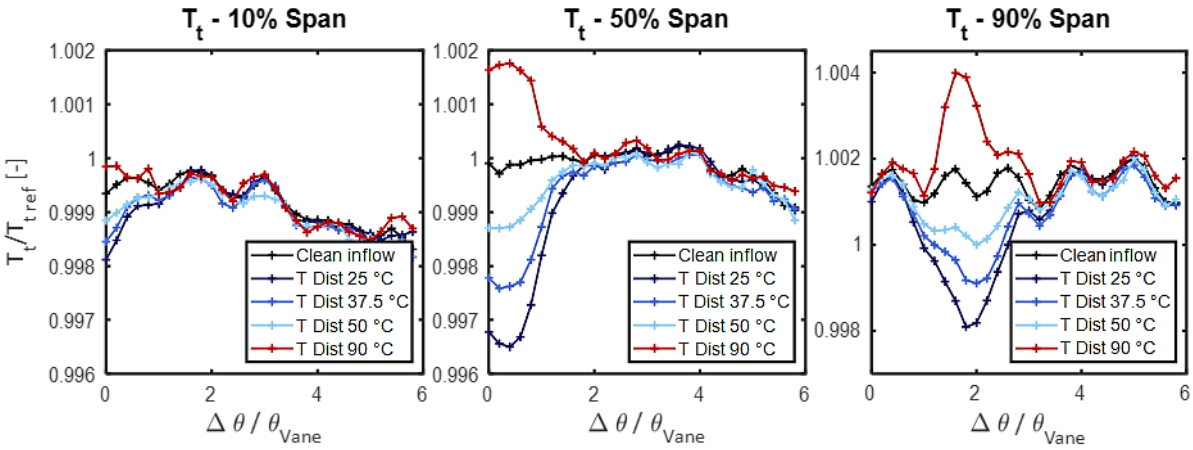

FIGURE 8.7: Circumferential distribution of total temperature at hub (10% span), midspan (50% span) and tip (90% span). 2.5 g/s injection.

The effect of the different injection temperatures is well visible in the plots. In fact, the shape and amplitude of the distortion in the he circumferential distribution of T_t follows very well the trend of the injection air temperature. Combining the information obtained from all the aerodynamic results presented in this section it is possible to conclude that the mass flow and the temperature of the injected air have a strong effect on the resulting total temperature distortion at the LPT stage inlet. In particular, two effects can be highlighted. Firstly, it is evident that the higher is the injected mass flow, the higher is the intensity of the distortion obtained in plane A. Secondly, the total temperature distortion amplitude seems to follow a quite linear relation with the injection temperature. However, it should be noted that the injection of warmer air behaves differently from the injection of colder air, resulting in a different absolute amplitude of the distortion due to the same (negative or positive) difference between the main flow and injected air temperatures. This can be understood observing the temperature profiles in FIGURE 8.6: the amplitude the distortion for case 90 °C is higher than the distortion obtained for case 50 °C, even though the absolute temperature difference between the injected air and the main flow is higher for the second case. These results could be connected to a different mixing behaviour of high temperature, and therefore low density, air injected in the colder main flow, compared to the injection of lower temperature and higher density fluid in warmer air.

8.1.4 PLANE C – TOTAL TEMPERATURE – INJECTED MASS FLOW 2 G/S

The flow field at the outlet of the machine was measured in plane C. The aim of this series of measurements was to study the evolution of the temperature distortion through the stage. The results will be presented for the case featuring 2.0 g/s additional air injection, as this case presented the closest inlet total pressure profile to the reference case and allowed to reach higher injection temperatures.

The distributions of total temperature in plane C measured with air injection of 2.0 g/s at 310.5 K (37.5 °C) and 373 K (100 °C) are presented in FIGURE 8.8. The measurement sector was shifted during the measurements to intercept the distorted flow, and is therefore located at a different circumferential position. In particular, it is centred in 60 degrees from the machines top and covers 6 stator pitches.

Observing the two figures, and by comparing them to the stage out flow presented in FIGURE 6.5, it is possible to notice the presence of a cold spot end a hot spot in the 37.5 °C case and in the 100 °C case respectively. The central positions of the altered temperature regions are highlighted on the contour plots with letters A and B. In particular, for the cold injection configuration, the total temperature in the mid span region is the lowest measured in the sector, suggesting a strong presence of the cold air injected in plane 0 at the rotor outlet. Also the 100 °C case presents a noticeable higher temperature zone in the mid channel.

The interaction of the temperature distortion with the secondary vortices can be seen as well. Letters C and D are positioned near the tip region, where an effect of the temperature alteration on the tip leakage

flow can be observed. In particular, higher temperatures were measured in the tip region of the higher temperature injection case and lower temperature can be observed at the tip of the colder injection case compared to the clean inflow case. Effects of the inlet air injection can be seen also in the hub region, where the temperature of the flow entrained in the hub secondary vortices is influenced by the inlet temperature distortion. Letters E and F superimposed to the temperature contours refer to the localised cold and hot spot that can be seen in both plots in the hub region.

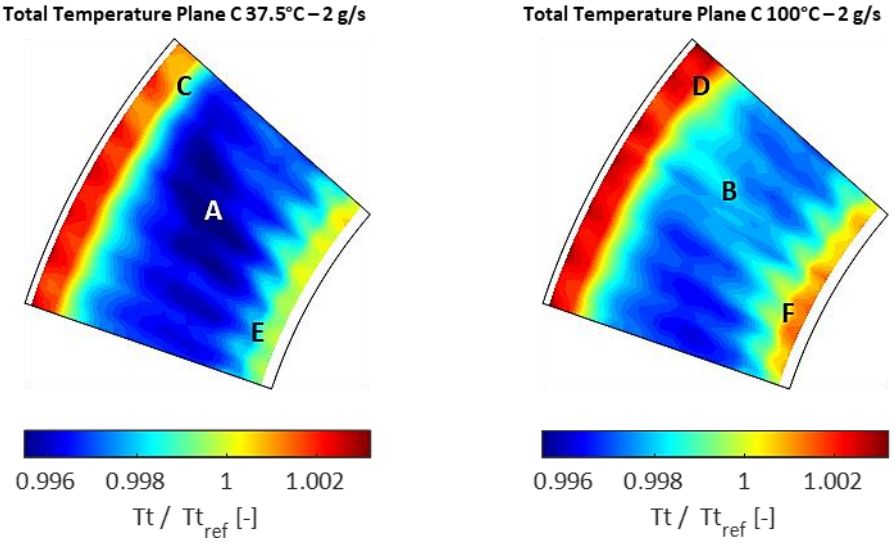

FIGURE 8.8: Total temperature distributions in plane C. 2 g/s. 37.5 °C injection case (left) 100 °C injection case (right).

In order to visualise the effects of the inlet total temperature inhomogeneity on the temperature distribution downstream of the rotor blades, the circumferential T_t distribution in plane C is plotted in FIGURE 8.9 at hub (left), mid-span (centre) and tip (right). The main effects that were highlighted observing the contour plots of FIGURE 8.8 can be found in this visualisation as well. It is interesting to point out that the azimuthal position of the distorted flow in the stage outlet flow field is independent on the temperature of the air injection. The circumferential migration of the T_t alteration with the radial height, that was already observed in plane A is noticeable also in plane C, and appears to be even more significant.

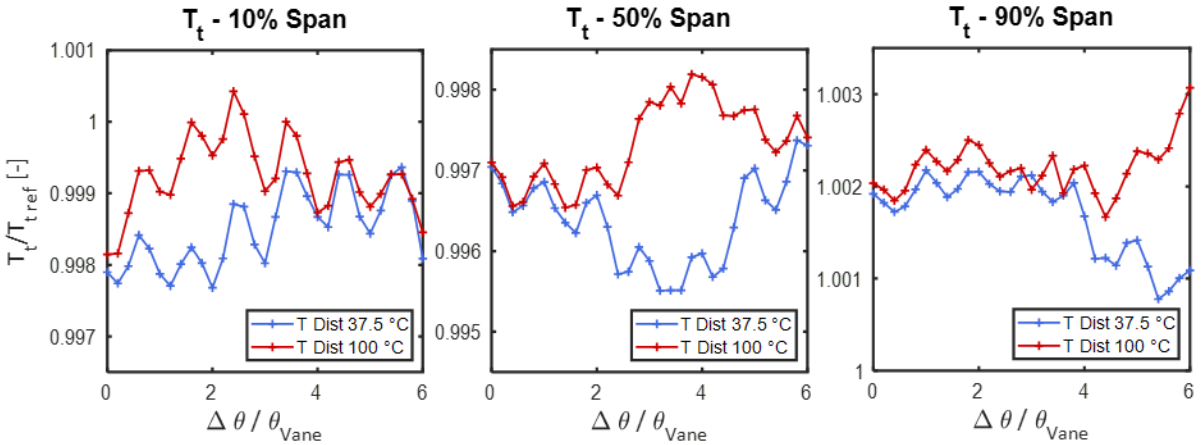

FIGURE 8.9: Circumferential distribution of total temperature in plane C. Hub (10% span), midspan (50% span) and tip (90% span). 2.0 g/s injection.

It is possible to compare the circumferential distributions relative to the 100 °C case and 37.5 °C case to study the differences in the outlet rotor flow between the injection of colder or warmer air. Considering that the effect on the total temperature values seem to be comparable in absolute terms, it can be said that the injection of hot air causes a stronger temperature distortion than cold air injection. In other terms, that the hot temperature distortion is less mixed during stage crossing. This is demonstrated considering that the temperature effect is similar for the two cases, even though the temperature of the injected air is 66% higher than the clean inflow case in the hot injection case and 50% lower in the cold injection case.

8.1.5 ROTOR BLADE VIBRATIONS - INJECTED MASS FLOW 2 G/S

The blade vibration frequency spectra will be presented in the following section to analyse the impact of the inlet temperature distortion on the rotor blade vibratory response.

The strain gauge data were processed following the same procedure presented in the paragraph above about the pressure inlet distortion. An average with respect to the rotational speed and then an FFT was performed. The spectra obtained have a resulting frequency resolution of 5 Hz. The results presented in this work are relative to one strain gauge (SG2).

FIGURE 8.10 shows a comparison of the spectra obtained from the signals of SG2. As for the case above, the results are presented in the form of strain normalised over the amplitude of the first mode of the reference case. A comparison between the spectra enables the recognition of the impact of the temperature distortion on the rotor blade vibrations. In particular, it can be seen that the most affected mode is mode 1F. The amplitude of the first mode obtained for the colder air injection case (37.5 °C) is lower than the level of mode 1F measured for the clean inflow configuration, whereas both the 1F amplitudes measured with an inlet non-uniformity characterised by a profile of warmer air are higher than the amplitude of the reference case. In more details, the 1F amplitude is 16% lower for the 37.5 °C injection, 15% higher for the 95 °C injection and 67% higher for the 100 °C case. The 1F blade vibration amplitudes are directly connected to the total temperature circumferential and radial distributions presented in FIGURE 8.3, FIGURE 8.4 and FIGURE 8.9. In particular, the T_j = 100 °C case corresponds to the highest total temperature positive distortion, in both plane A and C, and to the highest 1F amplitude. The same correspondence between temperature distortion and vibration amplitudes can be observed for the T_j = 37.5 °C case, which exhibits the strongest negative distortion and the lowest 1F. Consequently, the distorted temperature inflow conditions are thought to influence the rotor blades excitation at the first eigenfrequency according to the temperature of the injected air.

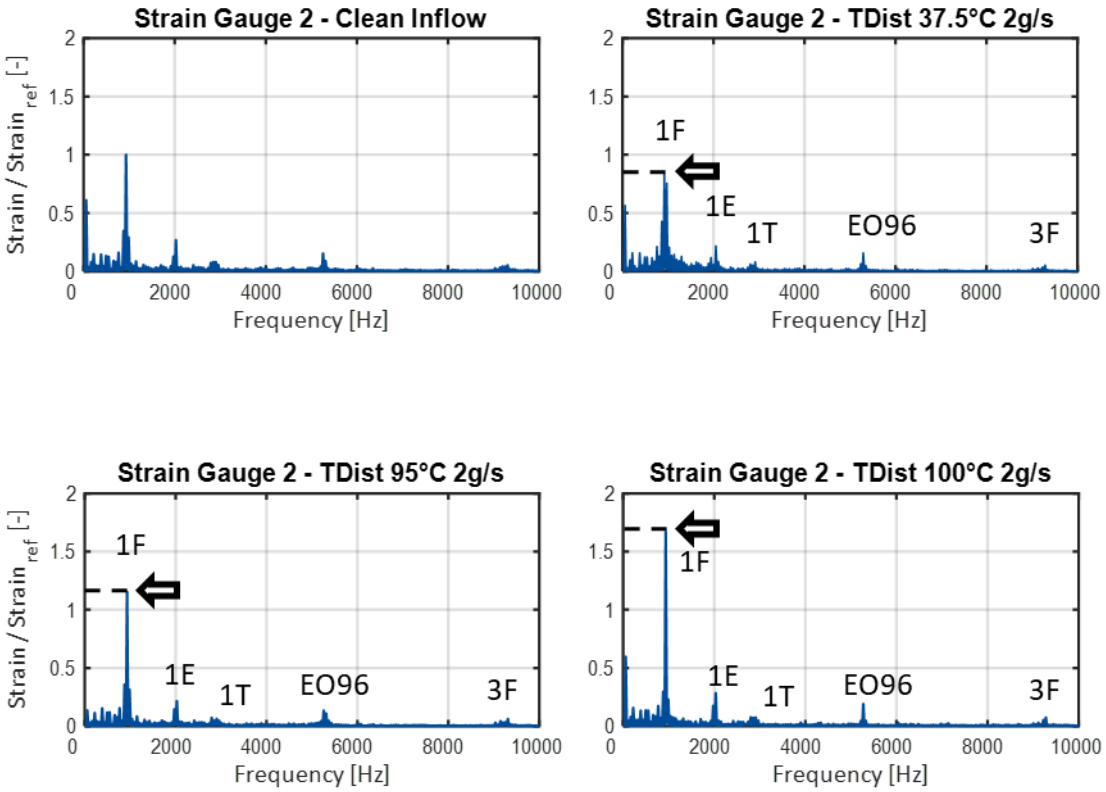

FIGURE 8.10: Forced response spectra of strain gauge 2. 2 g/s injection.

The strain energy evaluation procedure was applied also to this setup, to allow a better comparison of the strain data. The strain energy was evaluated according to Equation (5.24). FIGURE 8.11 depicts the results of this evaluation. Again, since the clean inflow case was taken as reference, it's value is 1 in the bar-plot. Observing the figure, one can note that the trend seen in the 1F amplitude is replicated by the strain energy. The colder air injection case presents lower strain energy over the investigated strain, whereas the T_j=95 °C and T_j=100 °C cases display higher E_{strain}. In particular, the set-up featuring an air injection temperature of 100 °C exhibits the highest strain energy. These results are representative of the impact of the inlet total temperature distortion on the rotor blade force response across the complete vibration frequency spectrum.

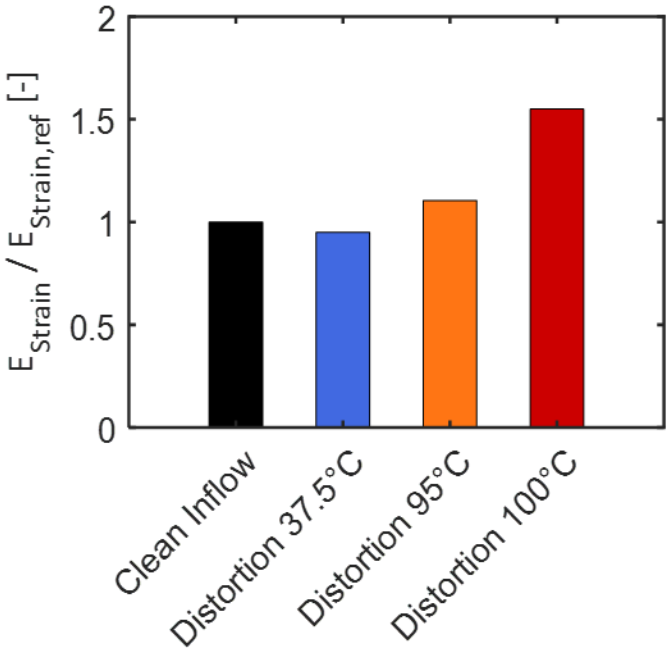

FIGURE 8.11: Strain energy evaluated from SG2 signal for the 2.0 g/s injection cases.

In order to analyse the relationship between the temperature of the inflow distortion and the blades vibrations, the amplitudes of mode 1F obtained for the different cases are plotted in FIGURE 8.12. This visualisation allows to understand the relationship between inlet temperature distortion and blade vibrations amplitudes. In particular, there seems to be a direct relation between the two, so that the warmer air injection determines higher 1F amplitude and colder air injection determines weaker blade forced response at the first eigenfrequency. The effect of the temperature on the aerodynamic damping could be connected to this result. In particular, the region of the passage characterised by a hotter temperature determines a higher forced response of the rotor blades as they cross the distorted flow. The opposite was measured for the colder air injection cases. A possible explanation could be found considering that the major differences between the temperature profiles were found in the tip region, where aerodynamic effects are associated with major changes in the rotor blades vibratory response. In agreement to what observed by Ioannou in [99] and Ioannou and Sayma [128], the temperature excess, or defect, present in the region characterised by the flow distortion determines a variation of the energy flux impinging on the rotor blades, in particular in the tip region. This means that for the cases with injection temperature lower than the inlet total temperature there is a higher concentration of highly energetic fluid at high span, while in the cases where colder air is injected at the stage inlet, the energy of the fluid available in the distorted region is lower. Therefore, this excess or defect of energy in the inlet distortion, could be linked to higher or lower blade vibratory response respectively.

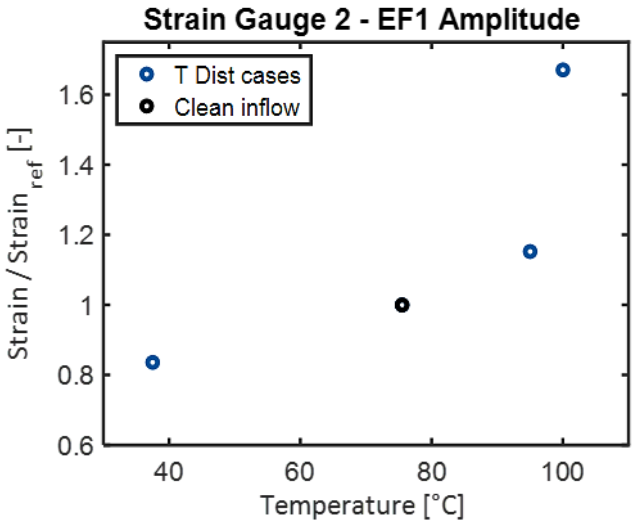

FIGURE 8.12: 1F amplitudes for different air injection temperatures. 2 g/s injection.

8.1.6 ROTOR BLADE VIBRATIONS - INJECTED MASS FLOW 2.5 G/S

The spectra obtained for the cases characterised by a 2.5 g/s mass flow injection at the stage inlet (plane 0) are presented in this section. The FFT spectra of the SG2 signal obtained for different injected air temperatures are presented in FIGURE 8.13. The effect of the temperature distortion on the rotor blade vibrations can be recognised similarly to the lower injected mass flow configuration presented above. The trends are consistent with the 2 g/s injection cases. In particular, the amplitude of the first mode obtained for the 37.5 °C air injection case is lower than the level of the 50 °C case, which in turn results lower than the reference value, measured with clean inflow and a homogenous total temperature inlet of 75.5 °C. In more details, amplitude of mode 1F results 32% lower than the reference case for the T_j = 37.5 °C case and 21% for the T_j = 50 °C. Moreover, the inlet non-uniformity characterised by a profile of hotter air determines a higher first mode amplitude than the reference case. The T_j = 90 °C injection case shows a 1F amplitude 10% higher than the clean inflow case.

The plots shown in the presentation of the aerodynamic results agree with the blade vibration data reported here. In particular, by comparing FIGURE 8.5 and FIGURE 8.13 one can observe that the T_j = 90 °C shows both the higher 1F amplitude and the strongest Total temperature disturbance in the stage inlet flow field. in a similar way, the cases corresponding to the injection of air at a lower temperature than the average temperature at the stage inlet, T_j = 35.5 °C and T_j = 50 °C, determine a negative temperature distortion, and consequently influence the amplitude of the first mode in the spectra presented in FIGURE 8.13, which is smaller than the case with clean inflow.

Consequently, since a very similar trend was shown by the two tested configurations, it is possible to affirm that the temperature of the inlet distortion has a well-defined effect on the rotor blades vibratory response.

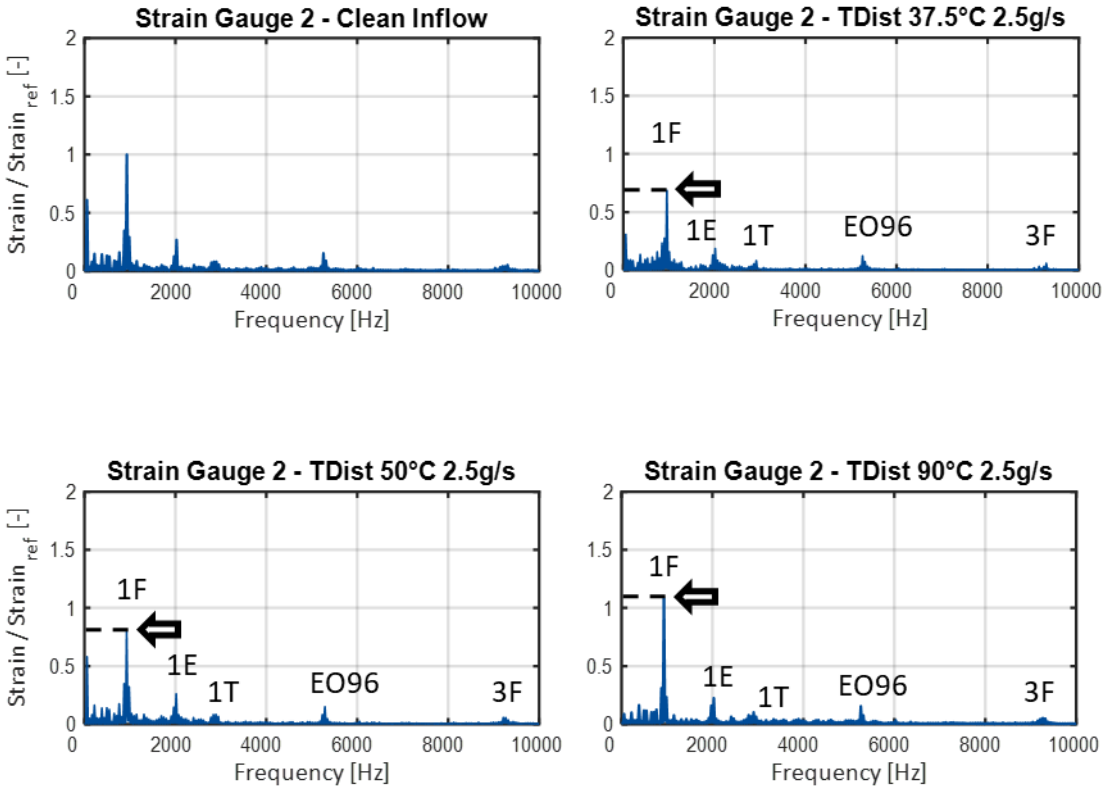

FIGURE 8.13: Forced response spectra of strain gauge 2. 2.5 g/s injection.

The strain energy was evaluated according to Equation (5.24) also for this injection mass flow rate. The results are shown in FIGURE 8.14. Once again, the clean inflow case value is 1 in the bar plot, as it was taken as reference. By comparing the bar plot with the blade vibration spectra, one can note that the strain energy contained in the SG signal follows same trend of mode 1F amplitude. The colder air injection, which determines a strong negative total temperature defect visible in FIGURE 8.5, presents lower strain energy over the investigated frequency range. a similar behaviour can be found for the case with air injection at the temperature of 50 °C, which presents a less intense temperature distortion than the case T_j = 37.5 °C and consequently a higher deformation energy, but still lower than the reference case. The temperature distortion intensity-strain energy trend is confirmed by the E_{strain} evaluated for the set-up featuring an air injection temperature of 90 °C. This case exhibits higher values than the reference case, consistently with the positive temperature energy distortion shown in the presentation of the aerodynamic results relative for this case in FIGURE 8.5 and FIGURE 8.6. therefore, the combined analysis of the 5HP and strain gauges' measurements allows the recognition of a relation between the intensity of the temperature distortion and the rotor blades forced response, which was already visible in the results presented for the 2.0 g/s mass flow injected case and can be found in the 2.5 g/s case data as well.

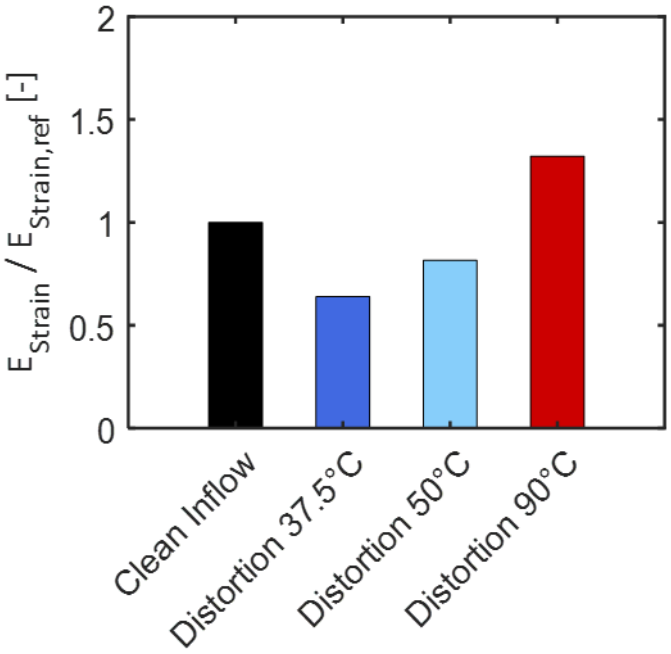

FIGURE 8.14: Strain energy evaluated from SG2 signal for the 2.5 g/s injection cases.

A plot presenting a better visualisation of the relationship between the temperature of the inflow distortion and the blades vibrations for the 2.5 g/s configurations is presented in FIGURE 8.15. The direct relation between the intensity of the distortion generated by the injection of secondary air in the inlet plane of the stage and the amplitude of the first mode, which is the most affected by the inflow inhomogeneity, is evident again in this plot.

The presence of a flow region characterised by higher, or lower, temperature in the stage inflow, is connected to the presence of a zone crossed by the rotor blades with more, or less, energy. This appears to be directly connected to the vibratory behaviour of the blades. Ultimately, the results presented for the 2.5 g/s injection case support the conclusion obtained already for the 2.0 g/s case, confirming that the excess or defect of energy determined by the inflow total temperature distortion could be associated to a direct modification of the blade vibratory behaviour.

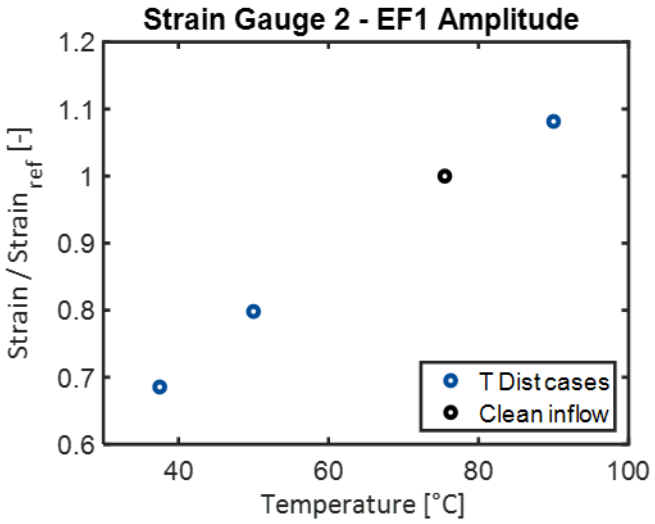

FIGURE 8.15: 1F amplitudes for different air injection temperatures. 2.5 g/s injection.

9. TOTAL TEMPERATURE AND PRESSURE INLET DISTORTION IN PLANE A

This chapter examines the combined effect of a total pressure and temperature distortion in plane A. The results of the measurement campaign presented here are based on the set-up described in 4.4.3. The effects of the generation of a total temperature and pressure distortion very close to the stator inlet of the modern low pressure turbine stage will be highlighted by investigating the flow field downstream of the rotor row and the blades vibratory behaviour. The air injection considered for this part of the experimental campaign is located in the same plane utilised for the generation of the inlet inhomogeneity discussed in section 7.2. moreover, the injection is performed using a similarly shaped device. Consequently, the results presented in 7.2 will be compared with the ones obtained with the current setup. The aim is to investigate the effect of the injection of air at different flow rates and temperatures and its interaction with the distortion created by the wake of the cylindrical total pressure distortion generator.

9.1 PLANE C - AERODYNAMIC RESULTS – INJECTED MASS FLOW 2 G/S

The results of the aerodynamic measurements will be presented and compared in detail in this section. The rotor exit flow field is studied and compared with the clean inflow case and with the P_t distortion cases, in order to evaluate the effects of the inflow distortion on the rotor blade excitation. The effect of the inlet inhomogeneity on the rotor blade vibrations will be analysed starting from the modifications that the temperature and pressure distortion combinations determines on the flow field and consequently on the aerodynamic excitation of the blades.

In order to maintain a consistent behaviour of the air injection system, also for the air injection in plane A, the mass flow rates were 2.0 g/s and 2.5 g/s. The first injection mass flow that was tested was 2 g/s. It was decided to inject the air at the two extreme temperatures used already for the injection in plane 0. In particular, the two cases tested had an injection temperature of 310.5 K (37.5 °C) and 373 (100 °C).

The flow field downstream of the investigated low pressure turbine stage measured by means of 5HP in plane C is presented in FIGURE 9.1. The figure presents an aft-looking-forward visualisation of the time-averaged total pressure (left) and total temperature (right) measured for the two temperature injection cases.

The total pressure distribution displayed in the left plots of FIGURE 9.1 shows areas of low momentum fluid concentrated in the region between 20% and 80% span, highlighted on the P_t contours with the letters A and A'. This low momentum regime is characterized by a drop in total pressure that reaches up to more than 50% of the measured range in the core flow. One can additionally note that the low total pressure flow influences both the wakes and core flow regions originating from the stator vanes. The effect of the injection of air at different temperatures is difficult to understand in this visualisation, but it seems that the higher temperature air determines a stronger total pressure reduction in the centre on the channel. More details about this comparison will be discussed presenting the P_t radial and circumferential distributions.

Another effect of the inflow non-uniformity of total pressure and temperature at the stage inlet can be recognised in the tip and hub regions. Letters B and B' are superimposed to the total pressure contours to signal the region of tip flow in plane C that is influenced by the air injection in plane A. Both cases seem to have a higher total pressure in correspondence of the distorted flow area. In the hub region, C

and C' correspond to an area of low total pressure. Comparing the two air injections, the two cases seem to have a very similar behaviour at this span height.

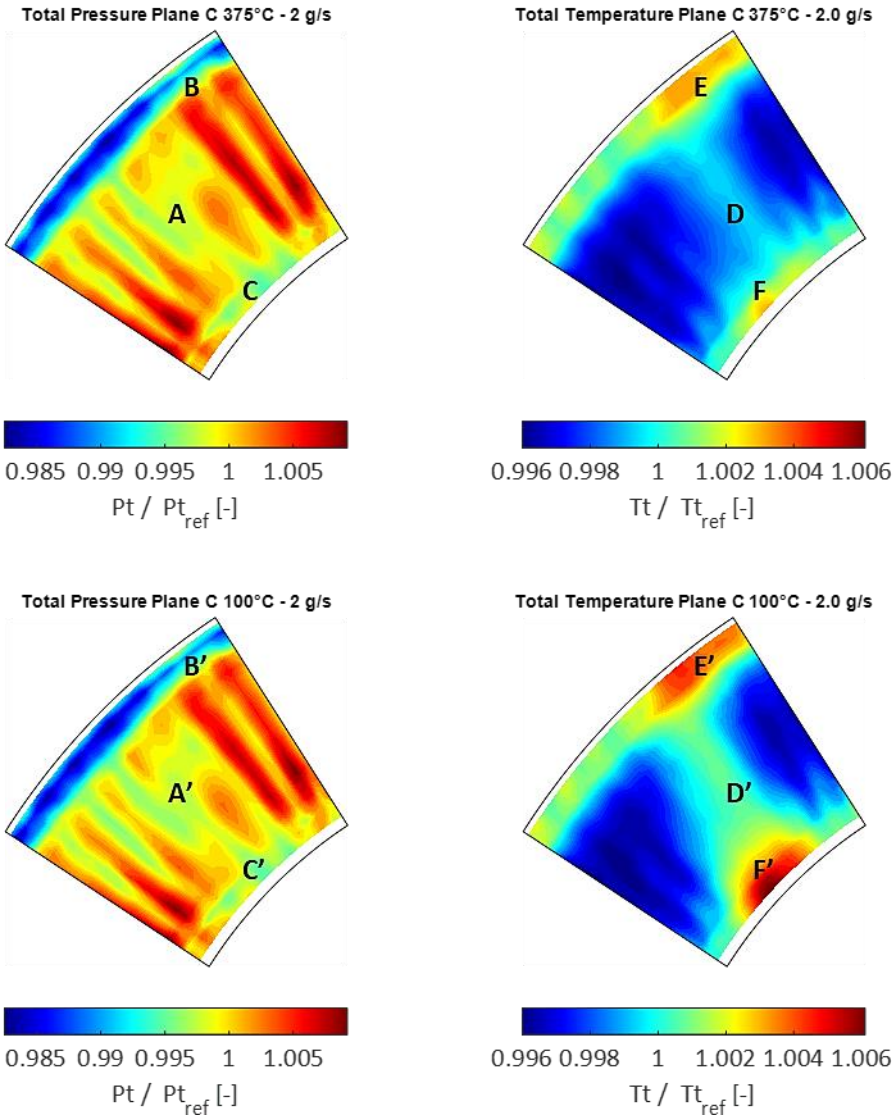

FIGURE 9.1: Total pressure (left) and temperature (right) distribution in plane C for the 37.5 °C (above) and 100 °C (below) cases. 2 g/s injection.

The total temperature field is depicted on the right in FIGURE 9.1. A distributed region of higher total temperature can be recognised in correspondence of the low total pressure areas discussed above. The origin of the higher total temperature can be found in the different way the distorted flow characterised by lower or higher temperature and lower momentum interacts with the rotor blade row and the work extraction in this region. In fact, as it was shown in the section above regarding the stage performance with the presence of a single total pressure inlet distortion, lower work extraction corresponds to a higher total temperature recorded in the wake of the blockage. This is the reason that determines the presence of a higher T_t also in the case of air injection at a temperature lower than the clean inflow reference case temperature.

The effect of the air injection can be noted also in the endwall flows. Letters E and E' are superimposed to the T_t contours to show the effect of the inlet air injection in plane A on the tip leakage flow. The temperature in this area is higher than in the reference case presented in FIGURE 6.2 for both injection temperature cases, with the T_j = 100 °C showing the higher temperature. A similar behaviour

can be observed in the hub region, labelled with letters F and F', where in correspondence of the total pressure reduction, a region of high temperature can be seen.

It is possible to compare the total temperature flow non-uniformity that is visible in the flow field downstream of the LPT rotor for the total temperature and pressure inlet distortion configuration with the higher total temperature region measured for the P_t distortion only cases. The interesting outcome is that the total temperature in the distorted area at the rotor exit is lower for the air injection cases in plane A than for the P_t-only case, suggesting that the air injected at the stage inlet travels through the stage together with the low momentum fluid in the wake of the injector promoting the extraction of more work from the flow than in the P_t distortion only case.

A comparison between the cases concerning the generation of distortions in plane A and the reference case can be facilitated studying the radial distributions of the flow quantities. The total pressure mass averaged radial distribution is plotted in FIGURE 9.2. The figure contains the curves of the clean inflow case, P_t-only, and two curves of the combined effect (in blue and red). The plot on the left refers to the entire measured sector, while the graph on the right focuses only on the area affected by the distorted flow. The graphs are presented to allow the comparison between the total pressure only distortion and the generation of a total temperature and total pressure inhomogeneity in plane A, upstream of the LPT stage.

Observing the plot on the left of FIGURE 9.2 it is possible to note that the injection of air from the distortion generator determines a visible difference between the total pressure profiles of the P_t-and-T_t distortion cases and the P_t only distortion case. It appears that the injection of air has the effect of filling the wake of the cylinder, reducing the intensity of the total pressure inhomogeneity and consequently generating a pressure profile in plane C closer to the profile of the reference case. A strong reduction is still visible in the span region between 15% and 30 %, where the radial distribution is dominated by the vane passages core flow, which therefore results altered also in the P_t-and-T cases with respect to the clean inflow reference. The chart on the right refers only to the part of the measurement sector that is really affected by the distorted flow in plane C. It has been evaluated isolating the region of the measured flow fields where a non-zero difference with the reference case could be evaluated and then averaging the values at each span height along the circumferential direction.

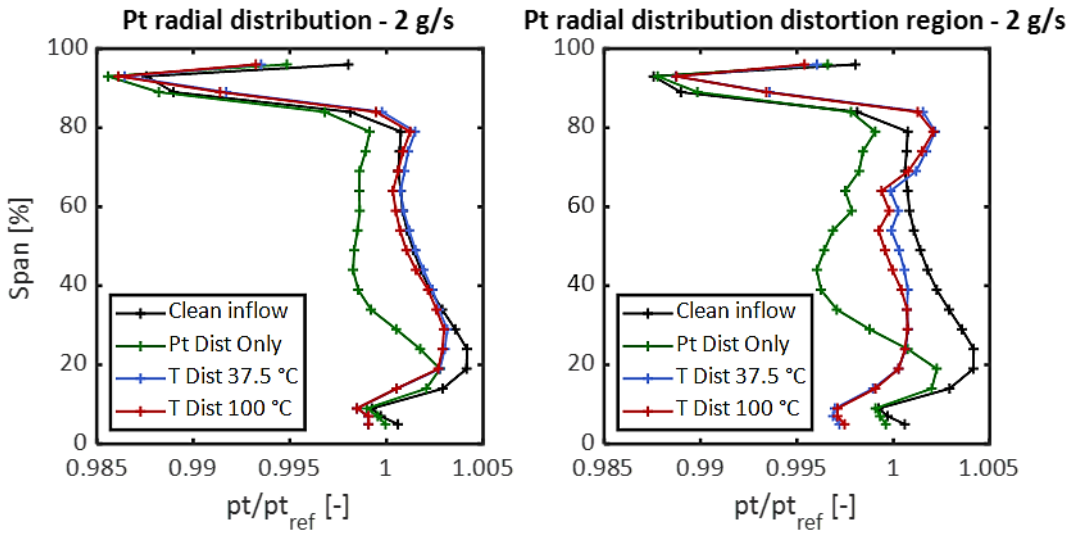

FIGURE 9.2: Radial distributions of circumferentially mass averaged total pressure in the complete measurement sector (left) and in the distorted sector only (right). Plane C. 2 g/s injection.

The effect of the air injection is noticeable comparing the air injection cases with the total pressure distortion only configuration. Both injection cases show a higher total pressure distribution along the span, more like the clean reference case. Higher total pressure values are visible in the tip region as well as in the upper part of the central span region. The air injection determines a reduction of total pressure

more intense in the hub region, where both the T_j = 37.5 °C and T_j = 100 °C display a very similar P_t distribution, which results lower than both the clean case and the P_t distortion only case. This is an evidence that the injected air entrains in both the tip and the hub secondary flows while crossing the stage and determines a detectable modification of the flow field downstream of the rotor row. Together with the endwall flows, the plots clearly show a modification of the inlet distortion also in the mid-span region.

The total temperature radial distributions are depicted in FIGURE 9.3. The left hand side plot is referred to the complete measurement sector. The case featuring air injection at a temperature of 37.5 °C shows a total temperate profile across the sector lower than the reference case, while the 100 °C injection case presents a temperature distribution much more similar to the clean inflow case. The injection of air in plane A determines a reduction of the temperature wake generated by the total pressure distortion generator when used alone, as this case still present the higher T_t in plane C across the whole channel downstream of the rotor row. Observing the plot on the right, which is referred to the sector impacted directly by the inlet distortion flow, one can have a more detailed view of the real effect of the injection of air in plane A on the flow downstream of the rotor. It can be observed that the air injection has a particularly strong effect in the endwall regions. In particular, the T_j = 37.5 °C distribution shows low T_t mainly in the vicinity of the hub, but also close to the tip. In a similar manner, the injection of warmer air determined substantially higher total temperature in the hub region, consistently higher also of the P_t distortion only case. These findings suggest that the air injected in the wake of the inlet distortion generator in plane A is subject to a separation and a radial migration. Specifically, even if the injection was designed to generate radially even distributed inflow inhomogeneity, the air injected is entrained in the secondary flow close to the endwalls and is responsible for the modification of the flow field downstream of the stage.

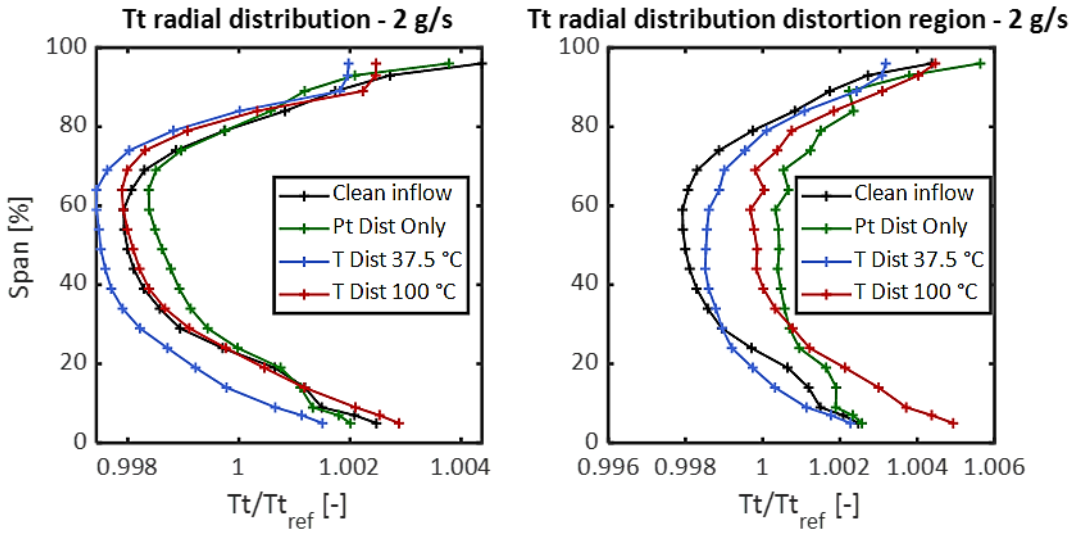

FIGURE 9.3: Radial distributions of circumferentially mass averaged total temperature in the complete measurement sector (left) and in the distorted sector only (right). Plane C. 2 g/s injection.

In order to obtain more information on the aerodynamic flow field downstream of the stage, and to study the forcing on the rotor blades, the radial distributions of static pressure and temperature will be analysed now. FIGURE 9.4 depicts the span wise distributions of static pressure in plane C mass averaged along the circumferential measurement sector. Analysing the plots, it can be seen that the P_t distortion only case determines the highest pressure reduction along the whole span. This is in accordance with the total pressure plots presented in FIGURE 9.2. Contrarily, the cases featuring air injection in plane A display a pressure distribution along the span higher than the clean inflow case. This is visible both in the complete measurement sector and in the plot on the right, which is referred only to the area occupied by the distorted flow. Comparing the two cases, it is evident that the injection of colder

air at the stage inlet leads to a condition of higher pressure downstream of the rotor blades than the 100 °C case.

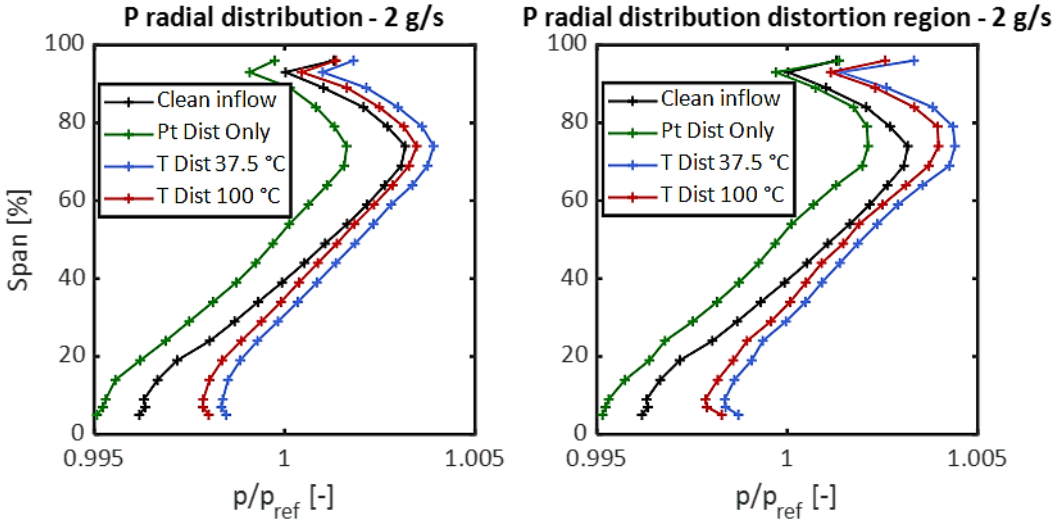

FIGURE 9.4: Radial distributions of circumferentially mass averaged static pressure in the complete measurement sector (left) and in the distorted sector only (right). Plane C. 2 g/s injection.

An analysis of the temperature profiles in plane C can also help the comprehension of the rotor blade aerodynamic excitation due to the temperature distortion. The span-wise temperature distributions are plotted in FIGURE 9.5. As for the previous visualisations, the plot on the left is referred to the measurement sector, while the right hand side plot is concentrated only on the area of distorted flow. The distribution of temperature in plane C is very similar to the distribution of total temperature. The case featuring the inlet distortion generator without air injection shows the highest temperature raise relative to the clean inflow case. The air injection configurations instead, present radial distributions that are consistent with the temperature of the injected air. In particular, studying the plot on the right referred to the distorted region only, it can be seen that the 37.5 °C injection case determines a lower temperature rise than the hot air injection case. An important difference is noticeable in the lower span region close to the hub, where the effect of the temperature distortion generated in the temperature distortion cases appears to be stronger on the radial distribution than the P_t distortion only case.

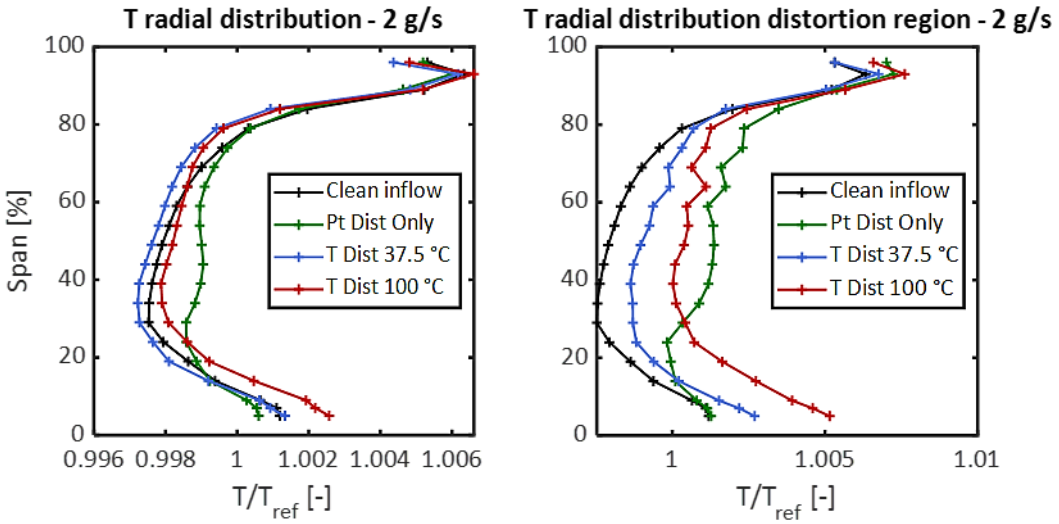

FIGURE 9.5: Radial distributions of circumferentially mass averaged temperature in the complete measurement sector (left) and in the distorted sector only (right). Plane C. 2 g/s injection.

The behaviour of the static pressure and temperature in plane C can be explained considering that the mass flow injection in plane a determines a double effect. On one hand, the air injection fills the region downstream of the injector, reducing the impact of the injector's wake on the turbine performance. In particular, according to the results presented in 7.2.1, the reduction of the wake flow corresponds to an increase in the work extraction in the distorted region. On the other hand, the temperature of the injected air directly modifies the thermodynamic condition of the flow in the distorted region determining the modification of the air temperature at the inlet of the stage. Therefore, the injection of colder air corresponds to lower temperature entering the stator row, while the injection of air at a temperature higher than the main flow corresponds to a localised higher temperature region at the stator inlet. The effect of the injection in plane A is therefore a combined effect of both the injected mass and its temperature.

A description of the flow evolution through the stage based on a schematic T-s diagram is considered useful to explain the effects of the flow injection in plane A. The evolution of the distorted flow can be visualised considering the combined effect of the mass flow injected and the temperature of the injection. The analysis is focused on the evolution of the flow between plane A and plane C. The visualisation of the thermodynamic transformation between the two states is used here as an attempt to introduce a simple model to support the explanation of the results obtained downstream of the LPT stage when a combined total pressure and total temperature distortion is generated at the stage inlet.

A T-s plot representing the thermodynamic transformation of the flow in the stage is presented in FIGURE 9.6. The starting state of the transformation are the flow conditions of the flow in plane A. The end state of the flow in plane C is described by the P and T measured by 5HP for each different case presented in FIGURE 9.4 and FIGURE 9.5. The different values of pressure and temperature measured in plane C for the four investigated cases are related to the different work exchanged through the stage by the flow because of the distortion. It is convenient to begin the description of the plot considering the P_t-distortion only case, which is represented by the green line in the figure. The flow contained in the distorted region exchanges work through the stage with a certain efficiency, which is expected to be the worst one between the investigated cases, considering that the wake of the injector is the most intense for this configuration. The case characterised by warmer air injection is represented in the plot by the red line. In this case, the transformation starts from a higher temperature and since the mass flow injection in the injector wake reduces the intensity of the wake, the efficiency of this transformation is expected to be higher, closer to the clean inflow case one. This is represented in the T-s plot by a more vertical transformation line Therefore, the end state in plane C is characterised by a higher pressure and a lower temperature. A similar behaviour is expected from the colder injection cases, represented by the blue line. The main difference is that in this case the initial state is at a lower temperature. Considering the same injected mass flow for both the warmer and colder cases, the effect on the efficiency of the transformation can be considered similar. This leads to an even lower final temperature, as shown by the final state of the blue line in FIGURE 9.6.

With regards to the effect of the injected mass flow rate, it can be considered that to a higher mass corresponds a stronger effect on the temperature, and a more intense effect on the wake intensity reduction. This leads to an even more relevant improvement in the work extraction in the distorted region.

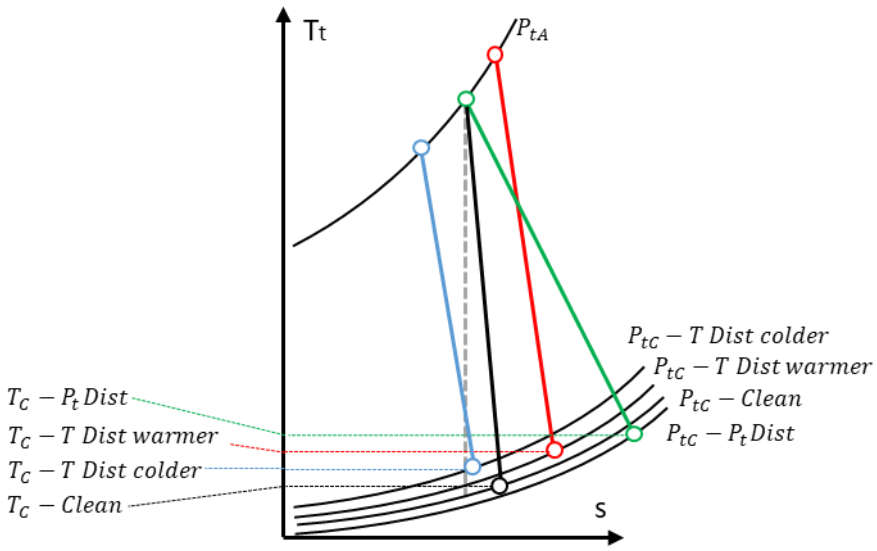

FIGURE 9.6: Schematic T-s plot representing the thermodynamic transformation of the flow between plane A and plane C.

It is useful to study the circumferential distribution of total pressure and total temperature in plane C to highlight a series of interesting aspects related to the air injection at the stage inlet. A visualisation of the total. pressure measured at midspan (centre), hub (left) and tip (right) is depicted in the three plots in FIGURE 9.7. The wakes of the stator vanes are clearly noticeable at all span heights observing the clean inflow case. The effect of the modifications in the temperature profile at the stage inlet determined by the air injection are clearly noticeable in the hub region, where the T_j = 100 °C injection and the T_j = 37.5 °C case are show low values of total pressure. It appears that injected air has a particularly strong effect on the structures related to the stator vanes close to the hub wall. In the mid-span region, the effect on the total pressure results less pronounced and in particular lower than the P_t only distortion case. In the tip region the air injection cases show a trend similar to the P_t only distortion. The higher level demonstrated is due to the additional air merging with the fluid flowing around the injector.

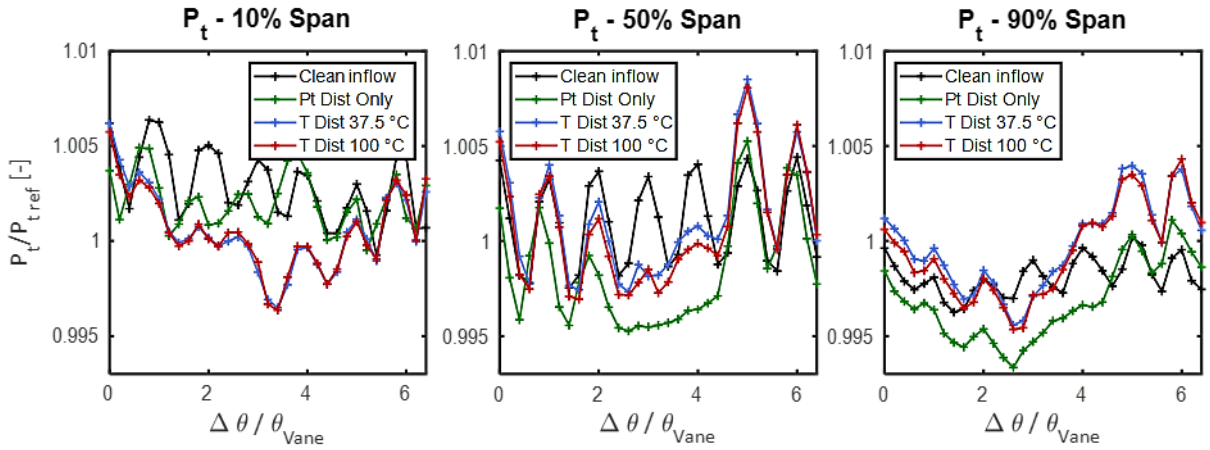

FIGURE 9.7: Circumferential distribution of total pressure at hub (10% span), midspan (50% span) and tip (90% span). Plane C. 2 g/s injection.

The circumferential distribution of total temperature in plane C is presented in FIGURE 9.8. The effects of the injection of secondary air at different temperatures can be seen in the three plots at hub, mid-span and tip. In particular, the distortion generated by an air temperature lower than the clean case inflow temperature determines a strong reduction of T_t in plane C distributed across the whole

circumferential sector in the region. Instead, at the same span height, the T_j = 100 °C case shows an area characterised by a much higher total temperature. At midspan the influence of the air injection appears to be also noticeable, with the T_j = 37.5 °C case showing the lowest temperature profile between the distorted cases. As already discussed in the radial distributions, the effect at midspan is higher for the P_t only case. In the tip region the air injection cases are again determining stronger deviation from the clean case then the P_t only case. This effect is caused by the radial redistribution of the injection air, which even if still present at midspan, is subject to a radial displacement towards the hub and the tip as a consequence of the crossing through the stage.

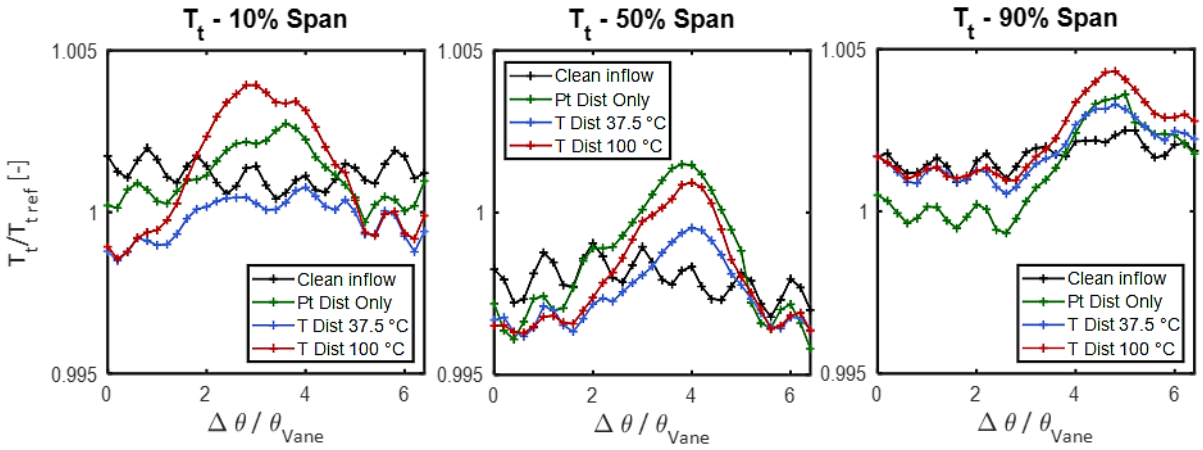

FIGURE 9.8: Circumferential distribution of total temperature at hub (10% span), midspan (50% span) and tip (90% span). Plane C. 2 g/s injection.

The radial displacement of the inflow temperature distortion was observed by Gaetani and Persico in [103] and by Gaetani et al. [104], who presented experiments and numerical simulations focussed on the propagation of hot-streaks through an HPT stage. A strong migration in spanwise direction of the perturbations was reported, especially through the rotor row. Jenny et al. [106] also analysed the flow at the rotor exit under the presence of hot-streaks, demonstrating that the hot gases migrate towards the end walls and interact with the secondary flow structures in the hub region. The authors concluded that there is a radial inward movement of the hot spot towards the hub through the rotor row.

9.2 PLANE C - AERODYNAMIC RESULTS – INJECTED MASS FLOW 2.5 G/S

In order to study the effect of the mass flow injection in plane A, a second set of measurements were performed with $\dot{m}_j = 2.5\ g/s$ injected through the distortion generator. The temperatures used for this part of study was 310.5 K (37.5 °C) and 363 (90 °C).

The presentation of the results follows the same approach of the previous section, The flow field measured by means of 5HP in plane C is presented in FIGURE 9.9. On the left hand side of the figure it is possible to see the time-averaged total pressure and on the right hand and side the total temperature measured for the two temperature injection cases.

Letters A and A' in FIGURE 9.9 highlight the region between 20% and 80% of the flow channel, where areas of low momentum fluid can be seen in the total pressure field. The drop in total pressure in this region reaches a maximum of 50% of the core flow range. Additionally, it can be observed that both the wakes and the stator flow regions are affected by the distorted inflow. Observing the flow in the centre span region, it is possible to notice that the injection of colder temperature corresponds to a slightly lower P_t distortion intensity, i.e. to higher total pressure values in the centre field.

The effect at the tip and hub that was shown in the previous section can be recognised also in this results. Regions of tip flow that are influenced by the T_t and P_t distortion in plane A are signalled with letters B and B'. Higher values of total pressure in correspondence of the distorted tip area can be seen

also in this case. In the region close to the hub, an area of low total pressure can be observed labelled with letters C and C'. The two temperature cases seem to have a similar effect at this span height. All this results are similar to the ones obtained for the 2.0 g/s injection, which permits us to conclude that the injection of more mass flow in plane A does not influence the general behaviour of the distorted flow through the stage, when the total pressure is taken into consideration. More details regarding this will be discussed cornering the temperature and the radial and circumferential distributions.

The right hand side plots of FIGURE 9.9 depict the total temperature field for the two configurations measured. As for the case above, higher total temperature was measured in correspondence of the region characterised by the low momentum fluid, as labelled by letters D and D'. A comparison between the T_t contours in the figure and the ones referred to the $\dot{m}_j = 2\ g/s$ case, allow the analysis of the effects of the injection temperature and of the injected mass flow. Firstly, the injection of a slightly higher mass flow at lower temperature seems to determine a lower impact of the temperature hotspot on the flow field downstream of the rotor row. This means that the temperature of the hot spot at the stage inlet is the parameter that determines the impact of the distorted flow on the stage. Secondly, comparing the Tj = 37.5 °C, it is possible to notice that the temperature is slightly more influenced in the $\dot{m}_j = 2.5\ g/s$ case, in particular in the tip region. The presence of more low temperature flow at that span height is considered to be the cause of this. This comparison will be expanded in the following presentation of the radial and circumferential distributions of P_t and T_t.

As for the previous case, it is interesting to point out the effects of the air injection on the endwall flows. Letters E and E', and F and F' highlight the effects of the inlet air injection in plane A on the tip leakage flow and on the hub secondary flows. In both regions, a total temperature hot spot can be seen.

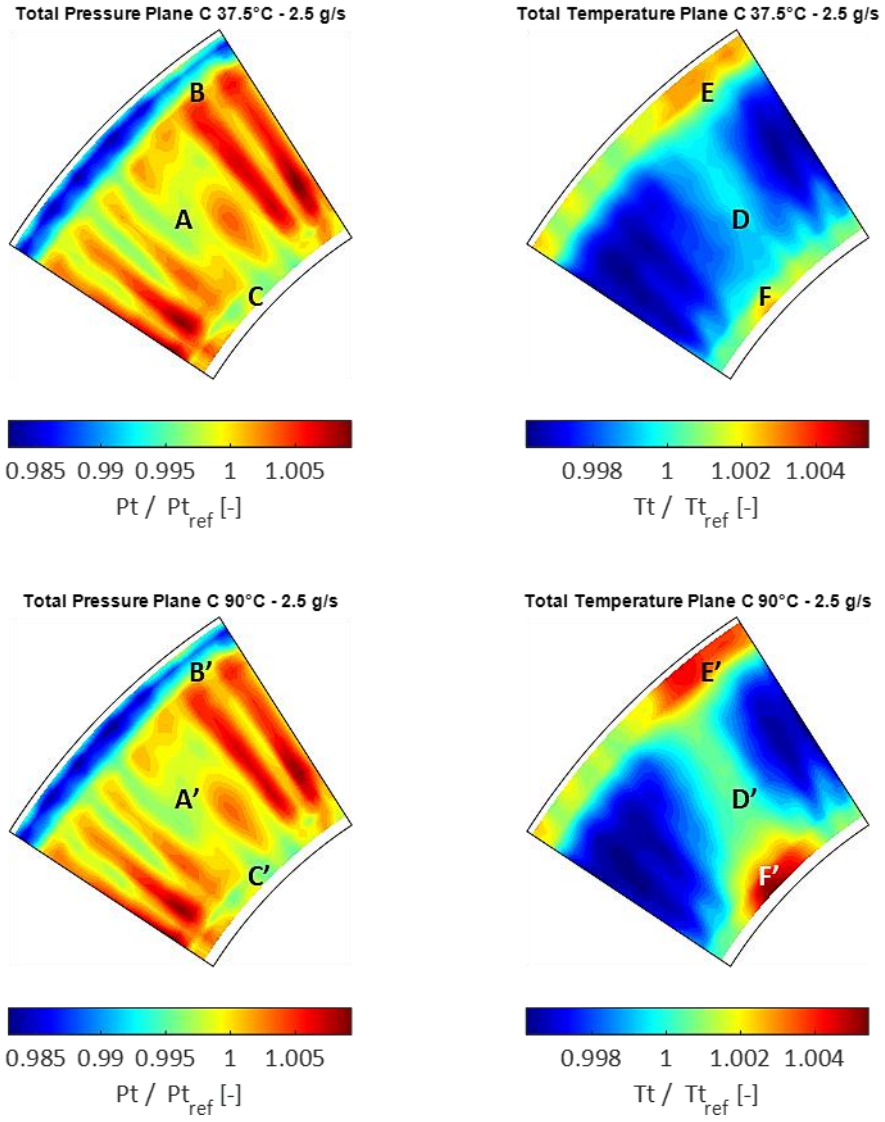

FIGURE 9.9: Total pressure (left) and temperature (right) distribution in plane C for the 37.5 °C (above) and 90 °C (below) cases. 2.5 g/s injection.

The total pressure mass averaged radial distribution corresponding to the $\dot{m}_j = 2.5\ g/s$ case is plotted in FIGURE 9.10. The whole measurement sector is presented on the left, while the distorted area is the focus of the plot on the right.

By comparing the plot on the left of FIGURE 9.10 with the correspondent visualisation depicted in FIGURE 9.2, it is possible to see that the injection of more air from the distortion generator determines only a small difference in the total pressure profile of the measured channel. The effect of filling the distortion generator wake can be seen also here, with the only difference that the distribution seems to be slightly higher in the higher mid-span region, just below the tip flow region, at around 80% span. However, this difference is very small. Studying the plot referring to the distorted region, the effects of air injection can be broken down in the three span wise regions. As for the 2.0 g/s case, higher total pressure was measured in the tip region and a reduction is noticeable close to the hub. It can be also seen that the injection of more mass flow in plane A determines a less intense reduction of total pressure near the hub region and a stronger increase in the tip flow. The detailed analysis of the P_t distribution in the core of the distorted flow therefore allows to see that the increased mass flow of the injection enhances the effect of filling the generator wake. The result is a higher P_t radial distribution across the span, which is then closer to the clean inflow reference case distribution.

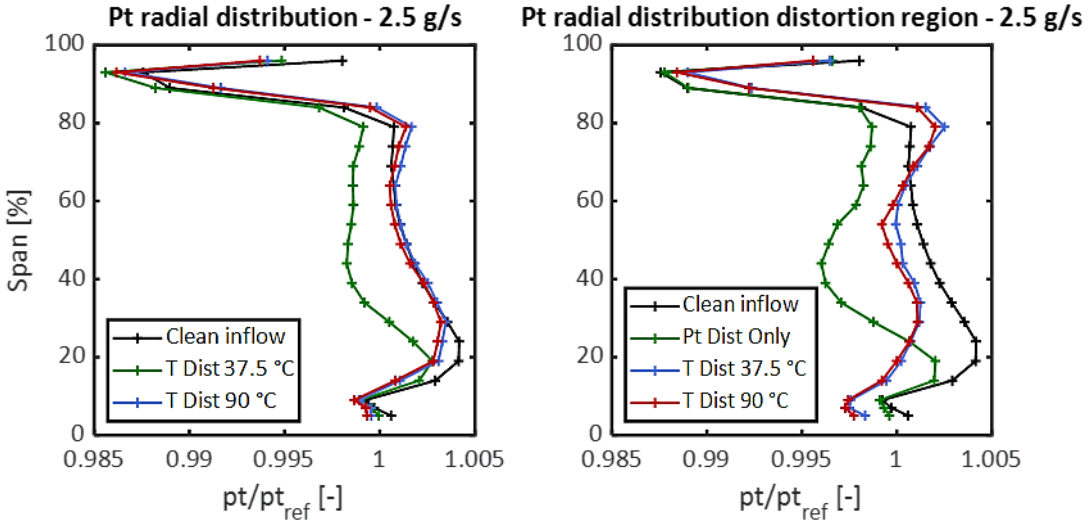

FIGURE 9.10: Radial distributions of circumferentially mass averaged total pressure in the complete measurement sector (left) and in the distorted sector only (right). Plane C. 2.5 g/s injection.

FIGURE 9.11 shows the circumferentially mass averaged total temperature radial profiles. Again, the plot on the left is referred to the complete measurement sector. The injection of air at a rate of 2.5 g/s determines a lower total temperature profile for the colder air injection case and a very similar distribution to the clean inflow case for the 90 °C temperature case. The distributions shown in the plot are very similar to the 2.0 g/s case. The main differences can be analysed considering the plot on the right hand side, which refers only to the sector impacted directly by the inlet distortion flow. In particular, the injection of more mass flow at 37.5 °C determines a colder temperature profile at both tip and hub span heights, but a higher average temperature in the central span area. The effect of the additional mass flow at 90 °C seems to be balanced out by the fact that the lower mass flow case had a higher injection temperature and therefore the temperature profiles appear similar. higher temperature seems instead to be balanced out by the lower temperature. The radial migration effect highlighted in the presentation of the results relative to the lower mass flow case seem to be consistent with the radial distribution presented here. Consequently, it can be seen that he injection of more mass flow determines a stronger effect near hub and tip.

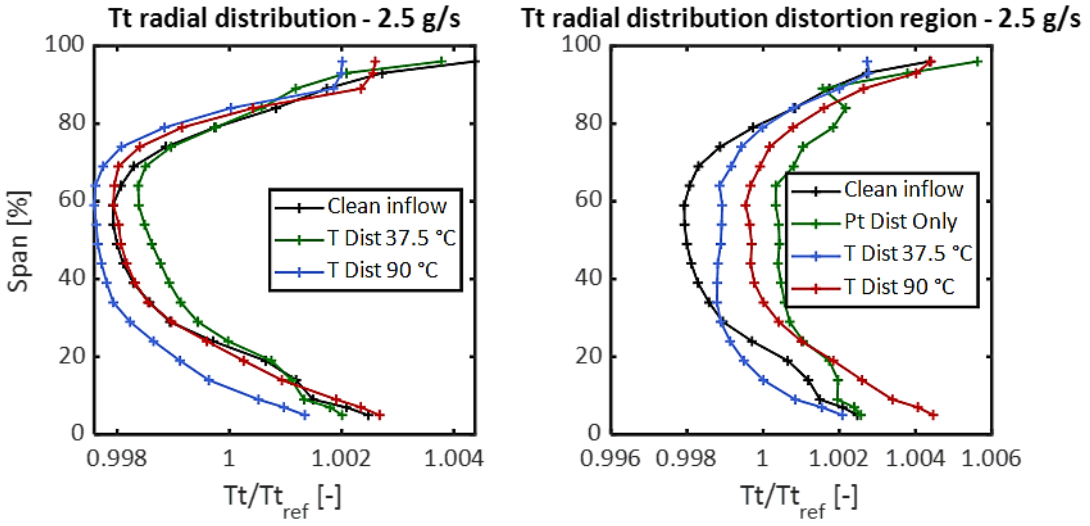

FIGURE 9.11: Radial distributions of circumferentially mass averaged total temperature in the complete measurement sector (left) and in the distorted sector only (right). Plane C. 2.5 g/s injection.

As for the presentation of the results related to the 2.0 g/s injection, also the static pressure and temperature distributions are taken into consideration here. The static pressure radial trends for the cases tested are represented in FIGURE 9.12. Both plots present a very similar distribution to the 2.0 g/s injection case. In particular, the P_t only case still shows the lowest pressure, while the two air injection cases present two pressure profiles higher than the clean case. In particular, in the plot on the right is clear that the 37.5 °C air injection determines the highest pressure in plane C. The injection of air at a temperature higher than the reference case generates a higher temperature distribution in plane C compared to the reference, but lower than the 37.5 °C case.

It is possible to compare the pressure distributions in FIGURE 9.12 with the distributions obtained for the 2 g/s cases. In general, it can be observed that the additional mass flow injected determines a distortion of static pressure in plane C characterised by a very similar static pressure distribution. The only marginal difference that can be seen between the cold air cases, is a slightly higher pressure distribution in the lower channel for the 2.5 g/s case. The injection of hot air at a slightly lower temperature instead seems to determine a relatively smaller reduction of the intensity of the pressure distortion.

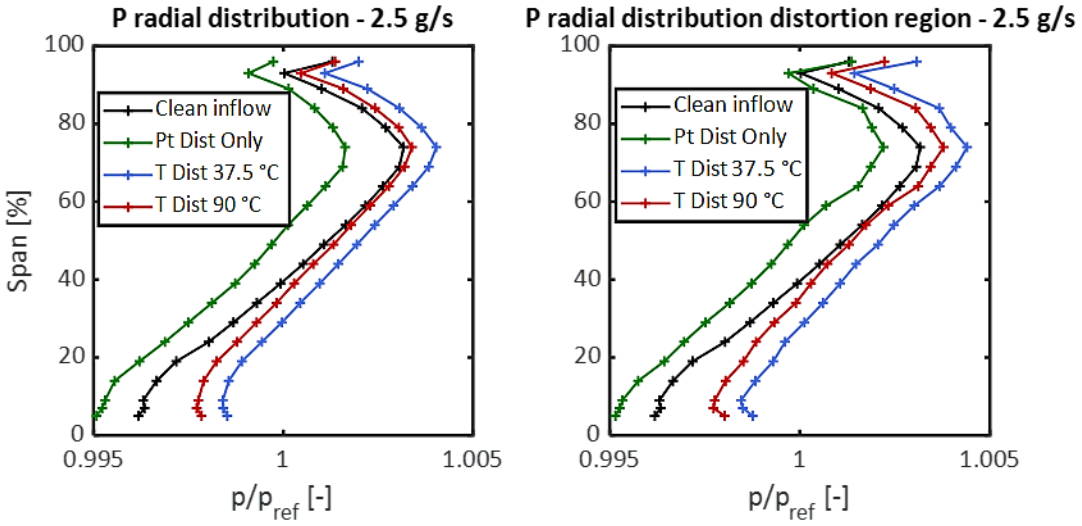

FIGURE 9.12: Radial distributions of circumferentially mass averaged static pressure in the complete measurement sector (left) and in the distorted sector only (right). Plane C. 2.5 g/s injection.

The temperature in plane C for the 2.5 g/s cases is depicted in FIGURE 9.12. As for the static pressure, the temperature follows the same trend of the 2.0 g/s cases. The modifications of the radial distributions are evident in the right hand side plot, with an increasing temperature starting from the clean case to the 37.5 °C injection, to the 90 °C injection and ending with the P_t only distortion case, in which the wake of the injector cylinder is not filled with any injected fluid, resulting in the stronger temperature distortion in the flow field in plane C. By comparing the temperature distributions in the distorted region with the distributions presented in FIGURE 9.5, one can observe that the injection of an additional mass of colder air generates a more intense temperature reduction effect near the hub and tip in the distorted region. Similarly, for the case with hot air injection it seems that the additional injected mass injected at a temperature of 90 °C instead of 100 °C as for the 2 g/s case, determines a lower temperature profile than the one recorder for the 100 °C and 2 g/s configuration.

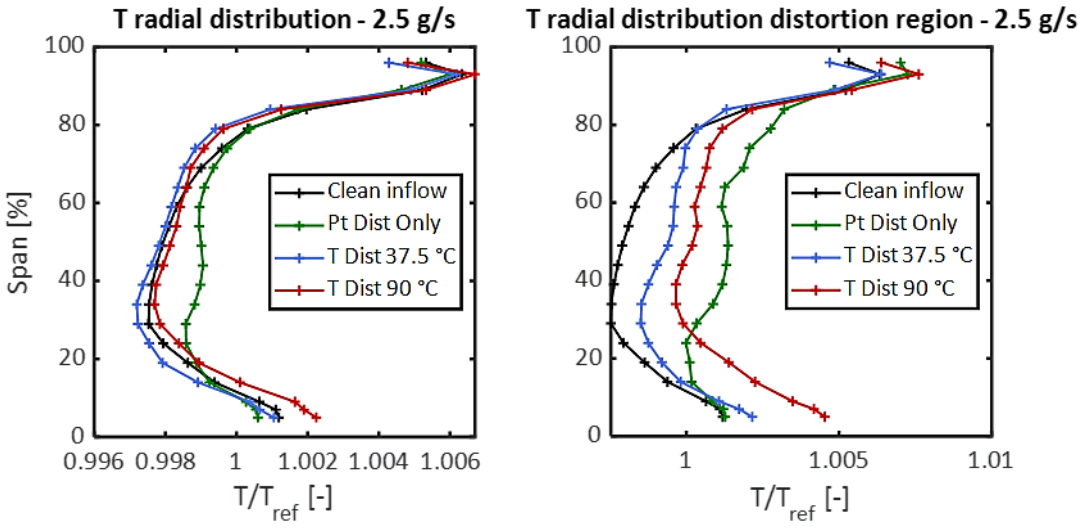

FIGURE 9.13: Radial distributions of circumferentially mass averaged temperature in the complete measurement sector (left) and in the distorted sector only (right). Plane C. 2.5 g/s injection.

These results obtained for the 2.5 g/s injection case are consistent with the explanation already introduced in the previous section, relative to the lower injected mass flow case, as the combined effect of the injected air mass flow and temperature is visible also in the 5HP data measured for this case.

The plots presented in FIGURE 9.14 and FIGURE 9.15 show the total pressure and total temperature distribution along the circumferential direction for the 2.5 g/s case. A comparison between the total pressure plots in FIGURE 9.14 with the previously presented case depicted in FIGURE 9.7 shows that the distributions are very similar, and the same observations already obtained studying the contours and the radial distributions can be made.

Additionally, also the total pressure plots appear to be very similar to the 2.0 g/s cases. A more relevant difference, more important because located in the tip and hub regions, can be observed comparing the plots relative to the total temperature in plane C. In particular, a lower total temperature is determined by the injection of more mass flow in the tip and hub regions for the 37.5 °C case. This is visible in the right hand side plot of FIGURE 9.15. This occurs because more air is located in the hub and tip regions due to the radial shift of injected air and therefore the impact on the temperature is higher. In general, it can be observed that the 2.5 g/s mass cases can be linked to the generation of lower distortions in the temperature flow field in plane C.

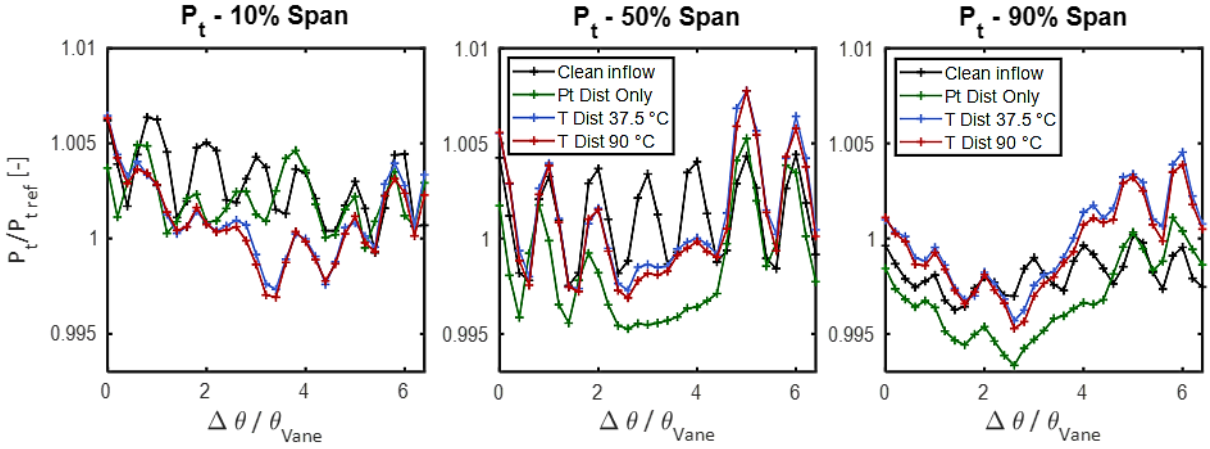

FIGURE 9.14: Circumferential distribution of total pressure at hub (10% span), midspan (50% span) and tip (90% span). Plane C. 2.5 g/s injection.

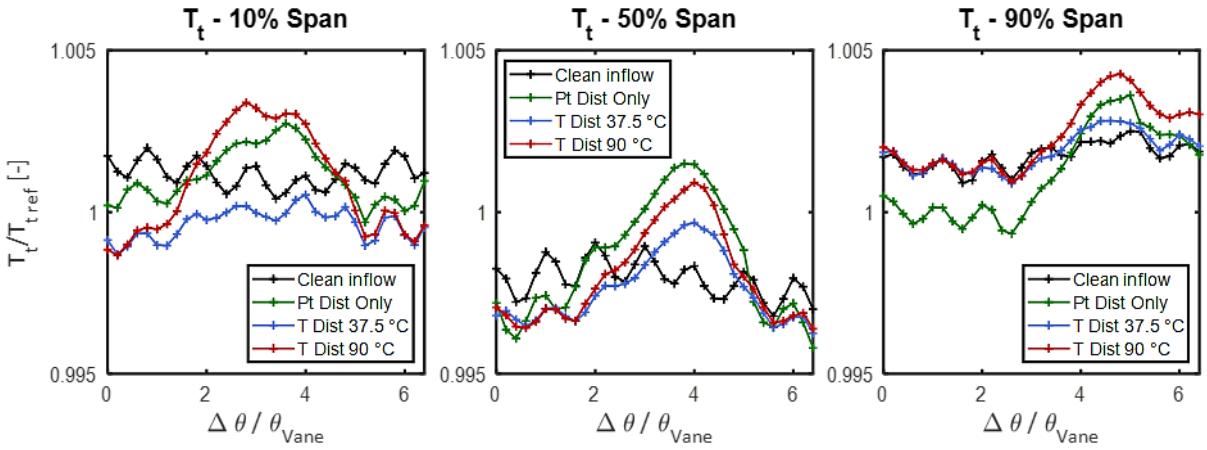

FIGURE 9.15: Circumferential distribution of total temperature at hub (10% span), midspan (50% span) and tip (90% span). Plane C. 2.5 g/s injection.

9.3 ROTOR BLADE VIBRATIONS - INJECTED MASS FLOW 2 G/S

The frequency spectra related to the blade's vibrations acquired for the 2 g/s injection in plane A cases will be discussed in this section. The aim is to study the interaction between the generation of a strong distortion in the flow field close to the stage inlet. Differently for the results presented in chapters 7 and 8, the injection of air in plane A generates an alteration on both the temperature and pressure distributions, as presented in the aerodynamic analysis above, introducing the possibility to study different distortion intensities

The same post processing procedure presented above was used to study the SG data. An FFT was performed after the data were averaged with respect to the rotational speed. The resulting spectra have frequency resolution of 5 Hz. Consistently with the data described above, the results presented in this work are relative to one strain gauge (SG2).

FIGURE 9.16 presents a comparison between the spectra obtained for the air injection cases as well as for the P_t only inlet distortion case. From the signals of SG2. The amplitudes shown in the plots are normalised with the strain of the first eigenfrequency (1F) of the reference case. By comparing the three plots it is possible to observe that the simple total pressure distortion case gives the higher vibration amplitude of the first eigenfrequency, with a value 6.24 times higher than the clean case. The second highest 1F amplitude was measured for the low temperature distortion case, which resulted in a value 5.35 times higher than the 1F amplitude measured for the reference configuration. Finally, the case with T_j = 100 °C shows an amplitude of the mode 1F 5.04 times higher than the clean inflow case.

The trend exhibited by the 1F amplitudes is not simple to interpret. The evidence that was found in the distributions of the first flap wise bending mode amplitudes obtained for the cases with air injection in plane 0 seems to be not valid for the new cases. Consequently, the interpretation of the results is not as straightforward. In order to link the behaviour of the blade forced response to the aerodynamic modifications and disturbances created in plane A with the injection of air right upstream of the stage inlet is necessary to associate the effects of the distortions on both the temperature and the pressure distributions. In particular, observing the pressure and temperature radial distributions depicted in FIGURE 9.4 and FIGURE 9.5, it is possible to see that the cases that determine the higher static pressure disturbance are the T_j = 37.5 °C case and the P_t distortion only. The T_j = 100 °C case instead, shows a pressure distribution that appears to be closer to the clean inflow case. Therefore, it can be said that the influence on the blade vibratory behaviour for these configurations is not only dominated by the temperature distributions, but also by the strong modifications on the pressure fields determined by the combined inlet distortion generation. In the 37.5 °C case, the higher static pressure that characterises the flow field at the rotor exit is strictly connected to a higher static pressure region crossed by the rotor blades in the distorted flow. Consequently, the effect on the temperature field due to the injection of colder air in the wake of the distortion generator is counterbalanced by an increase of static pressure. This determines that the case characterised by the colder air temperature profile in plane C is connected

to a higher vibration level. Furthermore, considering the combined effect of the mass flow and temperature of the injected air it can be stated that the case with the most intense flow distortion is the colder air injection case, considering that at the same mass flow corresponds a higher temperature difference between the injected air and the main flow. To this case corresponds the highest amplitude of the blade vibratory response at the first mode.

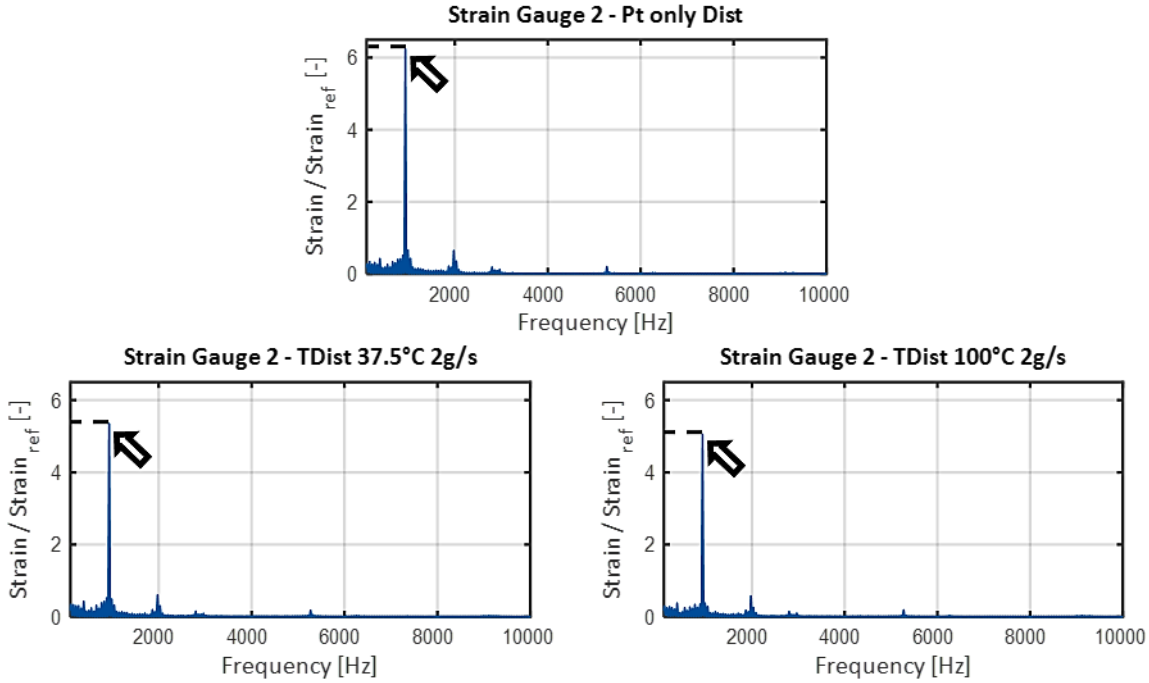

FIGURE 9.16: Forced response spectra of strain gauge 2. 2 g/s injection in plane A.

In order to link the excitation due to the modifications on the flow field due to the presence of the inflow inhomogeneity, the same procedure applied in the previous chapter for the study the EO excitation contained in the aerodynamic flow field measured downstream of the rotor blade was used here. In particular, the Fourier transformation was applied in the circumferential direction to the aerodynamic distributions measured at 50% span. The results of the decomposition of the flow field at mid-span are presented in FIGURE 9.17. The amplitudes reported are only intended to be a qualitative visualisation and are normalised with the amplitude due to the forcing of the stator vanes wakes, corresponding to the EO96 excitation, measured for the clean inflow case.

Analysing the plots, it can be noticed that all the configurations featuring inlet inhomogeneities present high excitation amplitudes at low engine orders. This result was expected for the P_t only distortion case, as in fact this result was already introduced in section 7.2.2. A similar behaviour is visible in the plots referring to the addition of air injection, in the wake of the distortion generator in plane A. The excitation level at low engine orders seems to be higher also for these cases. Therefore, it can be affirmed that the inflow inhomogeneity generated directly in front of the stator vanes, propagates through the stage, causing an additional aerodynamic excitation at low engine order, which determines an alteration of the 1F mode vibratory response.

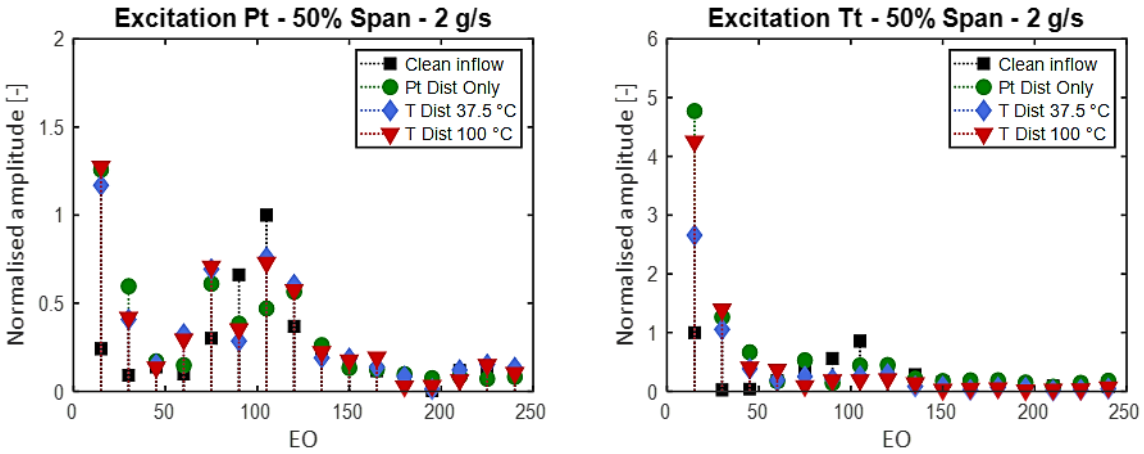

FIGURE 9.17: Engine order excitations evaluated for the clean inflow case and for the distortion cases in plane C. 2 g/s injection in plane A.

In order to facilitate the comparison between the cases, the amplitudes of mode 1F are plotted in FIGURE 9.18 against the temperature of the injected mass flow in plane A. It must be underlined that the injection of warmer air does not correspond to a higher temperature in the measurement plane downstream to the rotor blades. The case registering the highest T in plane C was the P_t distortion only case, which also showed a strong pressure distortion in the region affected by the distorted flow. Considering that the highest 1F amplitudes were measured also for the same configuration, it can be affirmed that there is a strong connection between the rotor blade vibratory behaviour and the combination of the intensities of both the temperature and the pressure distortions measured in the distorted region of flow field.

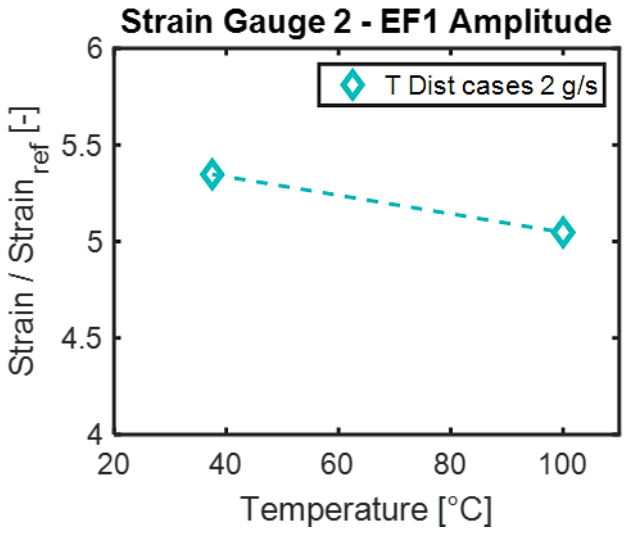

FIGURE 9.18: 1F amplitudes for different air injection temperatures. 2 g/s injection in plane A.

9.4 ROTOR BLADE VIBRATIONS - INJECTED MASS FLOW 2.5 G/S

This section regards the data relative to the cases characterised by a 2.5 g/s mass flow injection in plane A. The FFT spectra presented in FIGURE 9.19 are referred to the SG2 signal obtained for two injected air temperatures configurations and for the P_t distortion only case, which is again used as a reference for the vibration level comparison. The 1F amplitudes trend is consistent with the 2 g/s injection cases presented in FIGURE 9.16. The effect of the distortions in the pressure and in the temperature fields on the rotor blade vibrations can be recognised, likewise to the lower injected mass

flow configuration presented above. In particular, the T_j = 37.5 °C case shows an amplitude of the first eigenfrequency (1F) 5.03 times higher than the reference case. Once again, the higher injection temperature configuration follows with a mode 1F amplitude 4.84 times higher than the clean inflow value.

Even though the amplitudes obtained with the injection of an additional quantity of air follow the same trend as the 2.0 g/s mass flow cases, the absolute amplitudes seem to be slightly lower. This behaviour can be connected to the differences of temperature measured in the region occupied by the distorted flow and to the stronger effect of the additional injected mass flow on the wake of the injection cylinder. In particular, from the analysis of FIGURE 9.13 it was observed that a lower temperature in the end wall regions, due to the additional mass of colder air injected in the 2.5 g/s - 37,5 °C case generates a more intense temperature reduction effect near the hub and tip in the distorted region. In the same way, for the hot air injection case, the injection of more mass at a colder temperature than for the 2.0 g/s case (90 °C instead of 100 °C), determines a lower temperature profile in the distortion region, which is then associated with a lower vibration amplitude of the first mode. Therefore, the combination of mass flow and temperature of the injected air in plane A determines an effect on the blade vibratory behaviour recognisable also in this case.

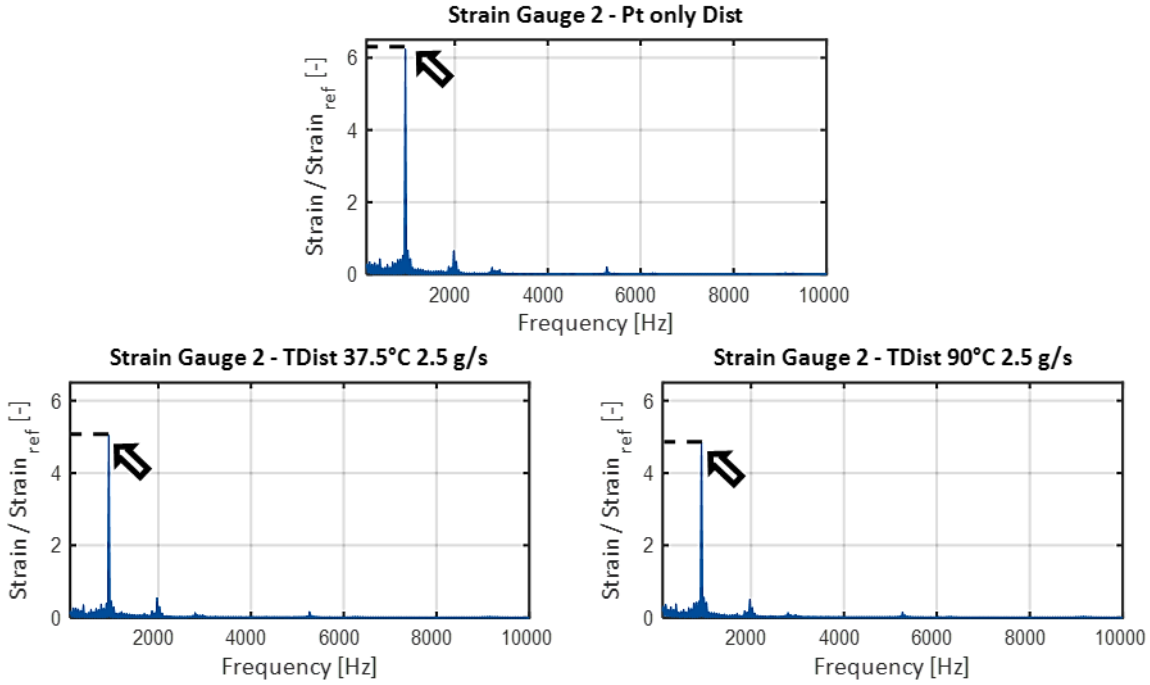

FIGURE 9.19: Forced response spectra of strain gauge 2. 2.5 g/s injection plane A.

As for the section relative to the 2.0 g/s cases, also for the distortion cases characterised by the injection of 2.5 g/s of additional air in plane A, the EO excitation contained in the aerodynamic flow field was studied and the results are collected in the plots in FIGURE 9.20The same procedure described above was applied to these cases.

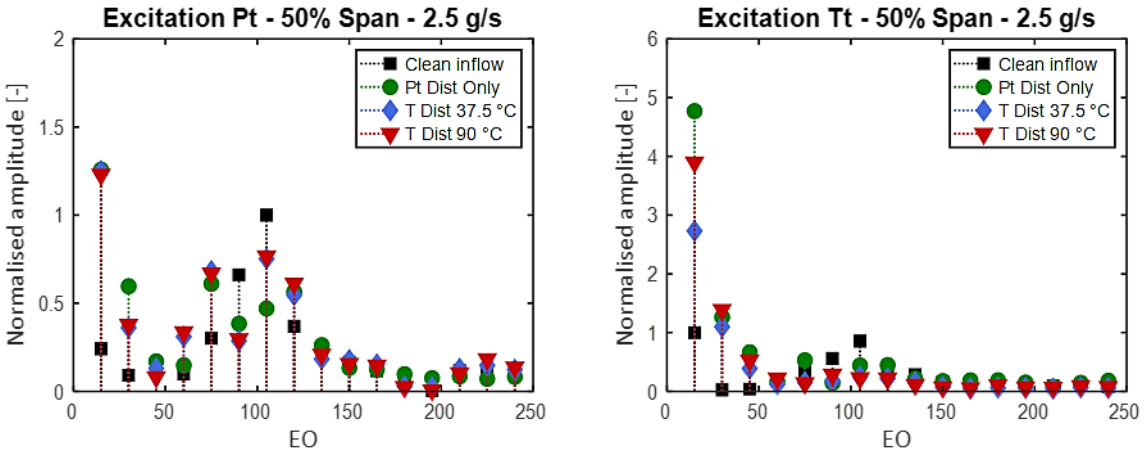

FIGURE 9.20: Engine order excitations evaluated for the clean inflow case and for the distortion cases in plane C. 2.5 g/s injection in plane A.

The plots reported in FIGURE 9.20 show a similar behaviour to the 2.0 g/s cases. In particular, looking at the plots, it can be seen that all configurations with inflow inhomogeneity have a high excitation amplitude at low EO. Consequently, these results confirm that the combination of additional disturbances in the distorted inflow configurations is directly related to of the first natural frequency vibration response excitation (1F). The air injection, and the consequent modification of the aerodynamic characteristics of the inlet inhomogeneity seem to have a direct effect on the excitation of the first eigenfrequency (1F), introducing additional excitation at the low engine orders, similarly to the P_t distortion only case.

FIGURE 9.21 collects the amplitudes of mode 1F obtained for all the cases featuring injection in plane A against the temperature of the injected air. The decreasing trends with the injection temperature is clearly noticeable for both injected mass flows. The ultimate insight that that can be obtained from the data presented in the plot is the fact that the temperature of the air injection in plane A is not enough to describe the intensity of the flow inhomogeneity travelling through the stage. Instead, it is the interaction between the mass flow rate, the temperature of the injected air and the wake of the injector that determines the intensity of the inhomogeneity at the stator inlet. In particular, the lower amplitude values measured for the 2.5 g/s injection case can be linked to a stronger effect of the injected air in reducing the wake of the injector, which is associated with a lower distortion intensity in the flow field and therefore lower forcing of the distorted flow on the blades.

Consequently, it is the interaction between the different effects of the inlet inhomogeneity on the flow field characteristics, which could be tracked to a modification of the rotor blades vibratory behaviour, analysing together the strain gauge data and the aerodynamic measurement.

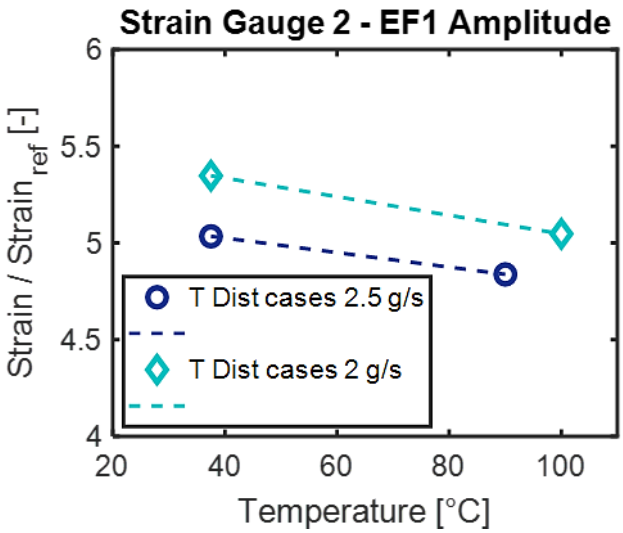

FIGURE 9.21: 1F amplitudes for different air injection temperatures. 2.5 g/s injection in plane A.

10. SUMMARY AND CONCLUSIONS

This chapter presents a summary of the findings that have been presented in the previous sections of this thesis, in relation to the specified objectives, highlighting the conclusions of the aerodynamic and aeroelastic analysis. In this thesis the effect of inlet inhomogeneities on the flow field and on the blade vibratory behaviour were analysed in detail, with particular focus on total pressure and total temperature distortions at the inlet of a modern low pressure turbine stage. A fundamental understanding of the impact of a series of important parameters such as the distortions' intensity and their clocking position, on the propagation through the LPT stage was gained. The experimental investigation enabled the recognition of the effects on aerodynamic excitation and the rotor blade forced response during steady and transient due to the pressure and temperature non-uniformities. A further discussion on the achievements of this thesis is presented in the following subsections. In conclusion, an outlook and some suggestions for future work will be proposed.

10.1 P_T DISTORTION IN PLANE 0

Regarding the total pressure non-homogeneity generated in plane 0 by the wake of a cylinder positioned upstream of the investigated stage, the results of aerodynamic and vibration measurements carried out at engine relevant conditions were presented in order to characterise the response of the rotor blades to a circumferential inlet pressure distortion.

Five-hole-probe and FRAPP measurements, performed upstream of the LPT stage, allowed the description of the main features that dominate the stage inflow with and without distortion generator. The former case showed that the wake of the cylinder strongly affects the flow field and causes the preconditions for the excitation of additional frequencies. The additional excitation was then confirmed during the strain gauge measurements.

The signal of the strain gauges applied on blades surface were analysed in the frequency and in the time domain. The results showed an increase of the amplitude of the first eigenfrequency (1F), which could be linked to the excitation due to the vortices shedding from the distortion generator mounted upstream the LPT stage. High amplitudes of the total pressure fluctuations were indeed measured in the wake of the distortion cylinder. Further, another effect of the once-per-revolution inlet inhomogeneity was observed during the speed ramps, as the response of the 1F mode was found to be consistently higher in the transient measurements acquired with the distortion generator installed.

The presence of the pressure distortion was linked to the excitation of lower EO. In particular, it was evaluated that the spatial inhomogeneity introduced in the flow field by the distortion generator determines high excitation amplitudes at low engine orders. The aerodynamic excitation at EO1 and EO2 resulted much more intense than the one due to the wakes of the inlet guide vanes. The higher 1F response measured during the speed sweeps can be caused by the additional pressure perturbation present in the distorted inflow configuration. Therefore, the analysis of combined aerodynamic data and vibration data shows that the presence of low-momentum fluid in a localised position around the

machine duct, propagating from the inlet through the stage, causes the amplification of low engine order excitation, which in turn determines the increase of the rotor blade vibratory response.

Summarizing, aerodynamic and vibration measurements were studied together to investigate the effects of an inlet total pressure distortion on both the flow field upstream of a low pressure turbine stage and on the forced response of the rotor blades. The distortion creates steady and unsteady aerodynamic alterations, causing direct effect on the rotor vibrations.

10.2 P_T DISTORTION IN PLANE A – EFFECT OF CLOCKING

In a second series of experiments, the total pressure distortion was generated in the inlet flow field of the LPT stage at three different circumferential positions, in order to study the influence of the distortion-stator clocking on the aerodynamic and vibratory performance of the turbine. The non-uniformity in the inflow was generated by the wake of a cylinder positioned upstream of the investigated stage aligned with the leading edge, the suction surface and the pressure surface of a stator vane respectively.

The rotor exit flow field was studied in order to describe the evolution of the low momentum fluid through the stage and to highlight the main differences that characterise the flow depending on the position of the distortion generator. The results showed that the extent of the total pressure reduction region and the amount of additional unsteadiness introduced in the flow by the distortion generator were different for the different investigated cases. In detail, the alignment with the leading edge caused the highest total pressure loss and the wider region of low total pressure, while the highest total pressure RMS were measured for the SS distortion case. Therefore, the interaction between the wake of the cylinder and the stator vanes depended on the distortion-vane relative position, and influenced directly the rotor-stator wakes interaction, as well as the extent of the secondary flows. Additionally, also the repercussions of the distorted inlet flow on the work extracted from the rotor were discussed in detail. It was found that less work is exchanged in the region of the flow field affected by the distortion.

Regarding the blade vibratory behaviour, higher amplitudes were observed for all cases presenting non-homogeneous temperature inflow, both over the whole spectrum and localized at the first eigenfrequency (1F), during steady operation and during speed-sweeps around the nominal operating point. The trend exhibited by the vibration amplitudes over the whole frequency spectrum followed the trend of total pressure fluctuations observed for the different configurations. Consequently, the amplification effect determined by the inlet distortion on the flow unsteadiness could be directly linked to the higher forced response of the rotor blading. Moreover, it was observed that the spatial non-uniformity in the distorted region induced an amplification of the aerodynamic excitation at low engine orders, determining an increase of the vibratory response of the first eigenfrequency (1F).

In conclusion, this part of the project showed that the steady and unsteady alterations created by the distortion in the flow field lead to modifications of the rotor vibration characteristics. The impact of the pressure distortion azimuthal position influence on the LPT stage aerodynamics and vibrations was also examined.

10.3 T_T DISTORTION IN PLANE 0

In this section of the work focussed on the study of total temperature inflow non homogeneities, air injection at the inlet of a low pressure test turbine was used to generate a circumferential total temperature distortion at the stage inlet. The air needed to generate the non-uniformity in the inflow was supplied to an injector by a supply line equipped with an air heater and a temperature control system. This setup permitted to vary the mass flow and temperature of the injected air, allowing the investigation of multitude of different temperature distortions.

The study of the stage inlet flow field allowed the description of the non-uniform temperature circumferential distribution and the effects of the injection on the inlet total pressure and flow angle. Different injection cases varying for injected mass flow and temperature, were analysed and the main

differences that characterise the distorted flow region depending on the mass flow and temperature of the injected air were discussed.

The vibrations data seem to highlight a direct relationship between the temperature of the inlet distortion and the blade vibrations amplitudes. In particular, the injection of warmer air determines a higher rotor blade forced response amplitude, whereas a temperature of the injected air colder than the temperature of the main flow could be liked to lower rotor blade vibratory response. This direct effect of the temperature of the inlet distortion on the first eigenfrequency amplitude could be connected to a modification of the aerodynamic forcing on the rotor blades determined by the variation of the flow energy impinging on the rotor blades driven by the temperature distortion.

To conclude, the alterations created by temperature non-uniformities in the stage inlet flow field and the modifications of the rotor vibration characteristics were investigated. The specific influence on the LPT stage aerodynamics and vibrations of the temperature distortion temperature and amplitude was also examined. Ultimately, this study provided insights on the effects of temperature distortions on localised changes of aerodynamic energy loading on the blades and their direct effect on the rotor blade vibrations.

10.4 P_T AND T_T DISTORTION COMBINATION IN PLANE A

The last part of this theses focussed on the generation of a distortion in the vicinity of the stage stator vanes, combining the presence of a cylindrical distortion generator with the injection of air at different mass flows and temperatures. The analysis of the distorted flow region was carried out by means of 5HP data, which enabled the detection of the main characteristic of the distorted flow after the crossing of the stage, depending on the mass flow and temperature of the injected air in plane A.

The same direct relationship between the vibratory response and the total temperature measured in the distorted region could not be found in the vibrations data of this case, as for the previously described configuration. The comparison between the aerodynamic data and the blade vibrations seem to indicate that the reason of this difference can be found in the additional modification that the injection of air in plane A determines in the flow field in plane C. In particular, it was observed that the injection of colder or warmer air had a double effect on the flow field. On one hand, the additional mass flow injected in the wake of the distortion generator filled this wake, reducing the effect of the distortion, and allowing the stage to work closer to its clean inflow performance. On the other hand, the temperature of the injected air showed direct influence on the temperature of the flow in the disturbed region, which in turn has a direct effect on the stage performance as well. The effect of such modification is visible in the temperature and pressure profiles measured downstream of the stage. In particular, an increase of the pressure distortion was measured downstream of the stage. The amplitude of such distortion was higher for the colder inlet temperature distortion than for the hotter temperature case.

Therefore, it is thought that the generation of the inlet distortion directly upstream of the stator vanes generates additional modification in the flow field that were not present in the inlet distortions studied for the cases featuring air injection in plane 0, further upstream. As a consequence, the additional effect of the combination between mass flow and temperature of the injected air in plane A is thought to be connected to a different aerodynamic excitation, corresponding to a modification of the rotor blades vibratory response. The intensity of the distortions measured in the flow field due to the quantity and the temperature of the injected air could be linked to the changes showed by the amplitude of the blade vibrations.

To summarize, the alterations created by the air injection in the wake of the injector cylinder generated more complex modification in the flow field, determining the separation between the temperature in the distorted flow field and the amplitude of the blade vibrations and revealing the effect of the amount of injected air. Ultimately, the generation a non-uniformity at the stage inlet characterised by both a temperature and pressure alterations, allowed the identification of the combined effect of temperature and pressure localised distortions on the rotor blade vibration characteristics.

10.5 OUTLOOK AND FUTURE WORK

This study provides insights on the effects of inflow circumferential perturbations, more and more important considering the possible excitations caused by struts, flow injections and instrumentations in shorter and lighter engine components. Ultimately, the results presented throughout this work support the importance of the study of the distortions distribution and of the reality effects as a critical stage during the design process, to ensure robust design and safe operation.

Regarding the possibility to expand the work presented in this thesis with more interesting research on the effects of inlet flow field distortion and their repercussions on the rotor blades vibrations, a series of possible topics come to mind.

Considering that the analysis of the propagation of an inlet distortion through a one and a half low pressure turbine stage composed by inlet guide vanes and stator vanes and rotor blades showed that the distortions are visible in the stage outlet flow, the interaction between the distorted flow and potential turbine exit guide vanes positioned downstream of the LPT rotor could be investigated. The work of Simonassi et al. [129] and Schönleitner et al. [68] showed the important effects of different turbine exit casings designs on both the flow field downstream of the LPT rotor and on the blade vibrations. Consequently, it is the opinion of the author that the interaction between inlet distortions and turbine exit guide vanes could generate interesting effects impacting on the machine performance and on the blades vibratory behaviour.

Another interesting research objective could be the in depth study of the alterations caused by inlet distortions to the acoustic performance of the LPT stage. Considering the relevance of noise emissions and noise attenuation, effects like number of inlet distortions and clocking with the inlet guide vanes, stator vanes or TEGV could be studied. The goal of such study would be to provide engine designers with the tools needed to consider the effects of the distribution and the intensity of inlet distortions on the noise generation and propagation through a LPT, in order to ultimately reduce the emission of noise.

11. PUBLICATIONS

JOURNAL PUBLICATIONS

L. Simonassi, M. Zenz, S. Zerobin, T. Selic, F. Heitmeir and A. Marn, *"On the Influence of an Acoustically Optimized Turbine Exit Casing onto the Unsteady Flow Field Downstream of a Low Pressure Turbine Rotor",* ASME Journal of Turbomachinery, Vol. 141, April 2019.

CONFERENCE PUBLICATIONS

L. Simonassi, M. Zenz, S. Pramstrahler, P. Bruckner, F. Heitmeir, A. Marn, *"Aerodynamic and aeroelastic experimental investigation on the propagation of inlet temperature distortions in a low pressure turbine stage",* 14th ETC, Gdansk, Poland, *2021.*

L. Simonassi, M. Zenz, P. Bruckner, S. Pramstrahler, F. Heitmeir, A. Marn, *"Experimental Study on the Effect of Clocking on the Propagation of Inflow Pressure Distortions in a Low Pressure Turbine Stage",* ASME Turbo Expo 2020, London – Virtual Conference, 2020.

M. Zenz, **L. Simonassi**, P. Bruckner, S. Pramstrahler, F. Heitmeir, A. Marn, *"Noise Attenuation Potential Using Helmholtz Absorbers Integrated in Low Pressure Turbine Exit Guide Vanes and Turbine Exit Casing End Walls",* ASME Turbo Expo 2020, London – Virtual Conference, 2020.

L. Simonassi, M. Zenz, P. Bruckner, F. Heitmeir, A. Marn, *"Aeroelastic and Aerodynamic Investigation of a Low Pressure Turbine Under the Influence of a Circumferential Inlet Distortion",* ASME Turbo Expo 2019, Phoenix AZ, 2019.

M. Zenz, A. Hafizovic, **L. Simonassi**, P. Leitl, F. Heitmeir, A. Marn, *"Aeroacoustical and Aerodynamical Investigations of Riblets Applied on Low Pressure Turbine Exit Guide Vanes for Two Different Operating Points",* ASME Turbo Expo 2019, Phoenix AZ, 2019.

L. Simonassi, R. Benauer, Zenz, M., P. Leitl, F. Heitmeir, A. Marn, *"Numerical and Experimental Study of the Aerodynamic and Aeroelastic Performance of a Low Pressure Turbine",* 13th ETC, Lausanne, *2019.*

M. Zenz, A. Hafizovic, **L. Simonassi**, P. Leitl, R. Benauer, F. Heitmeir, A. Marn, *"Aerodynamical and aeroelastic investigations of a riblet design applied on the surface of turbine exit guide vanes of a low pressure turbine",* 13th ETC, Lausanne, *2019.*

L. Simonassi, M. Zenz, S. Zerobin, T. Selic, F. Heitmeir and A. Marn, *"On the Influence of an Acoustically Optimized Turbine Exit Casing onto the Unsteady Flow Field Downstream of a Low Pressure Turbine Rotor",* ASME Turbo Expo 2018, Oslo, 2018.

M. Zenz, F. Schoenleitner, **L. Simonassi**, S. Bauinger, D. Broszat, F. Heitmeir, A. Marn, *"Experimental Determination of the Effectiveness of a Sound Absorbing Turbine Exit Casing"*, 12th ETC, Stockholm, *2017.*

CONFERENCE PRESENTATIONS

L. Simonassi, M. Zenz, F. Heitmeir, A. Marn, *"Numerical and Experimental Study on the Influence of Inlet Distortion on the Aeroelastic and Aerodynamic Performances of a Low Pressure Turbine",* 22nd Blade Mechanics Seminar, Winterthur, 2018.

L. Simonassi, M. Zenz, S. Zerobin, T. Selic, F. Heitmeir, A. Marn, *"On the Modal Analysis of Fast Response Aerodynamic Pressure Probe Data ",* XXIV Biannual Symposium on Measuring Techniques in Turbomachinery, Prague, 2018.

L. Simonassi, F. Schoenleitner, M. Zenz, S. Bauinger, A. Marn, *"On the Influence of Different Design Philosophies of Turbine Exit Guide Vanes on the Vibrational Behaviour of the Upstream Low pressure Turbine Rotor",* 22nd Blade Mechanics Seminar, Winterthur, 2017.

REFERENCES

[1] OWiD, “Global Number of Airline Passengers,” Our World in Data, [Online]. Available: https://ourworldindata.org/grapher/number-airline-passengers. [Accessed 17 December 2020].

[2] H. Ritchie, “Climate change and flying: what share of global CO2 emissions come from aviation?,” Our World in Data, Ocotber 2020. [Online]. Available: https://ourworldindata.org/co2-emissions-from-aviation. [Accessed 17 December 2020].

[3] J. Henne, “Gearing up for High Volume GTF Production - ISABE Conference Keynote,” in *21st ISABE Conference*, Busan, 2013.

[4] A. Collar, “The first Fifty Years of Aeroelasticity,” *Aerospace,* pp. 12-20, 1978.

[5] T. Fransson, Aeroelasticity in Axial-Flow Turbomachines.

[6] F. Holzinger, F. Wartzek, H. P. Schiffer, S. Leichtfuss and M. Nestle, “Self-Excited Blade Vibration Experimentally Investigated in Transonic Compressors: Acoustic Resonance,” *J. of Turbomach.,* vol. 138, pp. 041001-1-12, 2016.

[7] F. Schönleitner, “Schwingungsanregung verschiedener Turbinenaustrittsgehäuse zükunftiger Flugtriebwerkskonzepte,” PhD Thesis - TU Graz, Graz, 2015.

[8] J. M. Tyler and T. G. Sofrin, “Axial Flow Compressor Noise,” *SAE TRans.,* vol. 70, pp. 309-332, 1962.

[9] T. Camp, “A Study of Acoustic Resonance in a Low-Speed Multistage Compressor,” *ASME J. of Turbomach.,* vol. 121, no. 1, pp. 36-43, 1999.

[10] T. Fransson, “Dynamic Aeroelasticity - Important Parameters - Time-Dependent Aerodynamic Nomenclature,” in *Aeroelasticity in Axial Flow Turbomachines (VKI Lecture Series 1999-05)*, Rhode-St-Genese, Belgium, Von Karman Institute for Fluid Dynamics, 1999.

[11] AGARD, “AGARD Manual on Aeroelasticity in Axial-Flow Turbomachines - Volume 2 Structural Dynamics and Aeroelasticity.,” AGARD, 1988.

[12] D. J. Ewins and R. Henry, “structural Dynamics Characteristics of Individual Blades,” in *AGARD Manual on Aeroelasticity in Axial-flow Turbomachines,* AGARD - NATO, 1987.

[13] D. Vogt, "Experimental Investigation of Three-Dimensional Mechanisms in Low-Pressure Turbine Flutter," Phd Thesis - KTH Royal Institute of Technology, Stockholm, Sweden, 2005.

[14] A. V. Srinivasan, "Flutter and Resonant Vibration Characeristics of Engine Blades," in *International Gas Turbine & Aeroengine Congress & Exhibition*, Orlando, Florida, 1997.

[15] J. D. Denton, "Loss Mechanisms in Turbomachines," *ASME J. of Turbomach.,* vol. 115, no. 4, pp. 621-656, 1993.

[16] C. H. Sieverding, "Recent Progress in the Understanding of Basic Aspects of Secondary Flows in Turbine Blade Passages," *ASMe J. Eng. Gas Turbines Power,* vol. 934, pp. 11-26, 1985.

[17] L. S. Langston, "Secondary Flows in Axial Turbines - A Review," *Annuals of the New York Accademy of Sciences,* vol. 934, no. 1, pp. 11-26, 2001.

[18] H. P. Hodson and R. G. Dominy, "Three-dimentional flow in a low pressure turbine cascade at its design conditions," *ASME J. of Turbomach.,* vol. 109, pp. 278-286, 1987.

[19] O. P. Sharma and T. L. Butler, "Prediction of endwall losses and secondary flows in axial flow turbine cascades," *ASME J. of Turbomach.,* vol. 109, pp. 229-236, 1087.

[20] J. D. Coull, "Endwall Loss in Turbine," *ASME J. of Turbomach.,* vol. 139, pp. 081004-1-081004-12, 2017.

[21] P. Lampart, "Investigation of Endwall flows and losses in axial turbines. Part I. Formation of endwall flos and losses," *Journal of Theoretical and Applied Mechanics,* vol. 47, no. 2, pp. 321-342, 2009.

[22] G. Paniagua, R. Dénos and S. Almeida, "Effect of the Hub Endwall Cavity Flow on the flow-Field of a transonic High-Pressure Turbine," *ASME J. of Turbomach.,* vol. 126, no. 4, pp. 578-586, 2004.

[23] P. Jenny, R. S. Abhari, G. M. Rose, M. Brettschneider, K. Engel and G. J., "Unsteady Rotor Hub Passage Vortex Behavior in the Presence of Purge Flow in an Axial Low Pressure Turbine," *ASME J. Turbomach.,* vol. 135, no. 5, p. 051022, 2013.

[24] P. Jenny, R. S. Abhari, M. G. Rose, M. Brettschneider, J. Gier and K. Engel, "Low-Pressure turbine End Wall Design Optimisation and Experimenta Verifcation," in *ISABE, Paper No. 1717*, 2011.

[25] K. Regina, A. I. Kalfas and R. S. Abhari, "Experimental Investigation of Purge Flow Effects on a High Pressure Turbine Stage," *ASME J. of Turbomach.,* vol. 137, no. 4, p. 041006, 2014.

[26] J. Ong and R. J. Miller, "Hot Streak and Vane Coolant Migration in a Downstream Rotor," *ASME J. Turbomach.,* vol. 134, p. 051002, 2012.

[27] J. Dhalqvist and J. Fridh, "Experimental investigation of turbine stage flow field and performance at varying cavity purge rates and operating speeds," *ASMe J. of Turbomach.,* vol. 140, no. 3, p. 031001, 2017.

[28] S. Zerobins, A. Peters, S. Bauinger, A. Bhadravati Ramesh, M. Steiner, F. Heitmeir and E. Göttlich, "Aerodynamic Performance of Turbine Center Frames With Purge Flows—Part I: The Influence of Turbine Purge Flow Rates," *J. Turbomach.,* vol. 140 , no. 6, p. 061009, 2018.

[29] P. Z. Sterzinger, S. Zerobin, F. Merli, L. Wiesinger, A. Peters, G. Maini, M. Dellacasagrande, F. Heitmeir and E. Göttlich, "Impact of Varying High- and Low-Pressure

Turbine Purge Flows on a Turbine Center Frame and Low-Pressure Turbine System," *J. Turbomach.,* vol. 142, no. 10, p. 101011, 2020.

[30] S. A. Sjolander, "Secondary and Tip-Clearance Flows in Axial Turbines: Phisycs of Tip-CLearance Flows," in *VKI Lecture Series,* 1997.

[31] P. Lampart, "Tip Leakage Flow in turbines," *Task Quarterly,* vol. 10, no. 2, pp. 139-175, 2006.

[32] J. Bindon, "The measurement and formation of tip clearance," in *ASME Paper 88-GT-203* , 1988.

[33] J. Moore and J. S. Tilton, "Tip Leakage Flow in a Linear Turbine Cascade," *J. of Turbomach.,* vol. 110, no. 1, 1988.

[34] S. Yoon, E. Curtis, J. Denton and J. Longley, "The Effect of Clearance on Shrouded and Unshrouded Turbines at Two Levels of Reaction," *ASME J. of Turbomach.,* vol. 136, no. 2, pp. 1231-1241, 2013.

[35] M. Sell, M. Treiber, C. Casciaro and G. Gyarmathy, "Tip-clearance-affected flow fields in a turbine blade row," *Proc. Inst. Mech. Eng. Part A J. Power Energy,* vol. 213, pp. 309-318, 1999.

[36] J. D. Coull and N. R. Atkins, "The Influence of Boundary Conditios on TIp Leakage Flow," in *Proceedings of ASME 2013 Turbine Blade Tip Symposium and Course Week*, Hamburg, 2013.

[37] J. Tallman and B. Lakshminarayana, "Numerical Simulation of Tip Leakage Flows in Axial Flow Turbines, With Emphasis on Flow Physics: Part II—Effect of Outer Casing Relative Motion," *ASME J. of Turbomach.,* vol. 123, p. 324, 2001.

[38] A. A. McCarter, X. Xiao and B. Lakshminarayana, "Tip Clearance Effects in a Turbine Rotor: Part II—Velocity Field and Flow Physics," *ASME J. of Turbomach.,* vol. 123, no. 2, pp. 305-313, 2001.

[39] A. Sotillo and J. M. Gallardo, "Study of the Impact of Multi-Row Interaction on Flutter Analysis for a Representative LPT Geometry," in *ASME Turbo Expo 2018: Turbomachinery Technical Conference and Exposition*, Oslo, Norway, 2018.

[40] R. D. Stieger and H. P. Hodson, "The Unsteady Development of a Turbulent Wake Through a Downstream Low-Pressure Turbine Blade Passage," *ASME J. of Turbomach.,* vol. 127, no. 2, pp. 388 - 394, 2005.

[41] A. Binder, W. Förster, H. Kruse and H. Rogge, "An Experimental Investigation Into the Effect of Wakes on the Unsteady Turbine Rotor Flow," *Journal of Engineering for Gas Turbines and Power*, vol. 107, pp. 458-465, 1985.

[42] H. P. Hodson, "Measurements of Wake-Generated Unsteadiness in the Rotor Passages of Axial Flow Turbines," *Journal of Engineering for Gas Turbines and Power,* vol. 107, pp. 467-475, 1985.

[43] O. Sharma, T. L. Butler, H. D. Joslyn and R. P. Drings, "Three Dimensional Unsetady Flow in an Axial Flow Turbine," *J. Propulsion,* vol. 1, no. 1, pp. 29-38, 1985.

[44] N. Arndt, "Blade Row Interaction in a Multistage Low-Pressure Turbine," *ASME J. of Turbomach.,* vol. 115, no. 1, pp. 137-146, 1993.

[45] M. Rose, M. Mansour and P. Schüpbach, "The Thermodynamics of Wake Blade Interaction in Axial Flow Turbines: Combined Experimental and Computational Study," in *Proceedings of ASME Turbo Expo 2009*, Orlando, Florida, 2009.

[46] D. Lengani, T. Selic, R. Spataro, A. Marn and G. E., "Analysis of the unsteady flow field in turbines by means of modal decomposition," in *Proceedings of ASME Turbo Expo 2012*, Copenhagen, 2012.

[47] D. Lengani, B. Paradiso, A. Marn and E. Göttlich, "Identification of Spinning Mode in the Unsteady Flow Field of a Low Pressure Turbine," *ASME J. Turbomach.*, vol. 134, no. 5, 2012.

[48] M. Zielinsky and G. Ziller, "Noncontact Blade Vibration Measurement System for Aero Engine Application," in *Proceedings of ISABE*, 2005.

[49] L. Malzacher, C. Schwarze, V. Motta and D. Peitsch, "EXPERIMENTAL INVESTIGATION OF AN AERODYNAMICALLY MISTUNED OSCILLATING COMPRESSOR CASCADE," in *Proceedings of ASME Turbo Expo 2018 Turbomachinery Technical Conference and Exposition*, Oslo, Norway, 2018.

[50] F. Holzinger, F. Wartzek, M. Nestle, P. Schiffer and S. Leichtfuß, "Self excited Blade Vibration Experimentally investigated in Transonic Compressors Rotating Instabilities and Flutter," in *Proceedings of the ASME TurboExpo 2015*, 2015.

[51] M. Mayorca, "Numerical Methods for 'Turbomachinery Aeromechanical Predictions," Phd Thesis - Department of Energy and Technology, Royal Institute of Technology, Stockholm, Sweden, 2011.

[52] S. Stapelfeldt and M. Vahdati, "IMPROVING THE FLUTTER MARGIN OF AN UNSTABLE FAN BLADE," in *Proceedings of ASME Turbo Expo 2018 Turbomachinery Technical Conference and Exposition*, Oslo, Norway, 2018.

[53] B. Mischo, P. Jenny, S. Mauri, Y. Bidaut, M. Kramer and S. Spengler, "NUMERICAL AND EXPERIMENTAL FSI-STUDY TO DETERMINE MECHANICAL STRESSES INDUCED BY ROTATING STALL IN UNSHROUDED CENTRIFUGAL COMPRESSOR IMPELLERS," in *Proceedings of ASME Turbo Expo 2018 Turbomachinery Technical Conference and Exposition*, Oslo, Norway, 2018.

[54] R. Corral and A. Vega, "Quantification of the Influence of Unsteady Aerodynamic Loading on the Damping Characteristics of Airfoils Oscillating at Low-Reduced Frequency—Part I: Theoretical Support," *J. of Turbomach.*, vol. 139, pp. 031009-1-8, 2017.

[55] a. Vega and R. Corral, "Quantification of the Influence of Unsteady Aerodynamic Loading on the Damping Characteristics of Airfoils Oscillating at Low Reduced Frequency—Part II: Numerical Verification," *J. of Turbomach.*, vol. 139, pp. 031010-1-8, 2017.

[56] L. Pinelli, F. Vanti, A. Arnone, B. Beßling and D. Vogt, "INFLUENCE OF TIP SHROUD MODELING ON THE FLUTTER STABILITY OF A LOW PRESSURE TURBINE ROTOR," in *Proceedings of ASME Turbo Expo 2019: Turbomachinery Technical Conference and Exposition*, Phoenix, Arizona, USA, 2019.

[57] T. R. Müller, D. M. Vogt, K. Vogel and B. A. Philipsen, "INFLUENCE OF INTRAROW INTERACTION ON THE AERODYNAMIC DAMPING OF AN AXIAL TURBINE STAGE," in *Proceedings of ASME Turbo Expo 2018 Turbomachinery Technical Conference and Exposition*, Oslo, Norway, 2018.

[58] D. Ewins, "The Mistuned Blade Vibration Problem Re-Visited," in *Proceedings of the 12th International Symposium on Unsteady Aerodynamics, Aeroacoustics and Aeroelasticity of Turbomachines*, 2009.

[59] D. Ewins, "The Effect of Blade Mistuning on Vibration Response a Survey," in *IFToMM Conference on Theory of Machines and Mechanisms*, 1991.

[60] M. Castanier and C. Pierre, “Modeling and Analysis of Mistuned Bladed Disk Status and Emerging Directions,” *Journal of Propulsion and Power,* vol. 22, no. 2, pp. 384-396, 2006.

[61] Y. J. Chan, “Variability of Blade Vibration in Mistuned Bladed Discs,” PhD Thesis - Imperial Colledge London, London, 2009.

[62] M. Nowinski and J. Panovsky, “Flutter Mechanism in Low Pressure Turbine Blades,” *Journal of Engineering for Gas Turbine and Power,* vol. 122, pp. 82-88, 2000.

[63] N. Glodic, D. Vogt and T. Fransson, “Experimental and Numerical Investigation of Mistuned Aerodynamic Influence Coefficients in an Oscillating LPT Cascade,” in *Proceedings of the ASME TurboExpo 2009,* 2009.

[64] B. Megerle, T. S. Rice, I. McBean and P. Ott, “Numerical and Experimental Investigation of the Aerodynamic Excitation of a Model Low-Pressure Steam Turbine Stage Operating Under Low Volume Flow,” *Journal of Engineering for Gas Turbines and Power,* vol. 135, pp. 012602 -1-7, 2013.

[65] A. Bessone, L. Carassale, R. Guida, Z. Kubin, A. A. Lo Balbo, M. Marrè Brunenghi and L. Pinelli, “EXPERIMENTAL AND NUMERICAL ASSESSMENT OF A LAST STAGE ST BLADE DAMPING AT LOW LOAD OPERATION,” in *Acta Polytechnica CTU Proceedings 20*, Prague, 2018.

[66] J. J. Kielb and R. S. Abhari, “Experimental Study of Aerodynamic and Structural Damping in a Full-Scale Rotating Turbine,” *Journal of Engineering for Gas Turbines and Power,* vol. 1025, pp. 102-112, 2003.

[67] H. Hennings and R. Elliot, “Forced Response Experiments in a High Presure Turbine Stage,” in *Proceedings of the ASME Turbo Expo 2002,* Amsterdam, 2002.

[68] F. Schönleitner, T. Selic, C. Schitter, F. Heitmeir and A. Marn, “Experimental Investigation of the Upstream Effect of Different Low Pressure Turbine Exit Guide Vane Designs on Rotor Blade Vibrations,” in *Proceedings of the ASME Turbo Expo 2016*, Seoul, 2016.

[69] A. Marn, F. Schönleitner, M. Mayr, T. Selic and F. Heitmeir, “On the Effect of Axial Spacing Between Rotor and Stator onto the Blade Vibrations of a Low Pressure Turbine Stage at Engine Relevant Operating Conditions,” in *Proceedings of the ASME Turbo Expo 2016*, Seoul, 2016.

[70] A. P. Plas, M. A. Sargeant, V. Madani, D. E. Crichton and M. Greitzer, “Performance of a Boundary Layer Ingesting (BLI) Propulsion System,” in *AIAA Aerospace Sciences Meeting and Exhibit,* Reno, Nevada USA, 2007.

[71] R. V. Florea, C. Matalanis, L. W. Hardin, M. Stucky and A. Shabbir, “Parametric Analysis and Design for Embedded Engine Inlets,” *Journal of Propulsion and Power,* vol. 31, no. 3, pp. 843 - 850, 2015.

[72] D. Arend, J. D. Wolter, S. M. Hirt, A. Provenza, J. A. Gazzaniga, W. T. Cousins, L. W. Hardin and O. Sharma, “Experimental Evaluation of an Embedded Boundary Layer Ingesting Propulsor for Highly Efficient Subsonic Cruise Aircraft,” in *AIAA Propulsion and Energy Forum,* Atlanta, GA, USA, 2017.

[73] W. T. Cousins, D. Voytovych, G. Tillman and E. Gray, “Design of a Distortion-Tolerant Fan for a Boundary-Layer Ingesting Embedded Engine Application,” in *AIAA/SAE/ASEE Joint Propulsion Conference*, Atlanta, GA, USA, 2017.

[74] D. Perovic, “Distortion Tolerant Fan Design,” PhD Thesis - University of Cambridge, Cambridge, UK, 2019.

[75] J. Longley, “Measured and Predicted Effects of Inlet Distortion on Axial Compressors,” in *ASME 1990 International Gas Turbine and Aeroengine Congress and Exposition*, 1990.

[76] V. Jerez Fidalgo, C. A. Hall and Y. Colin, “A Study of Fan-Distortion Interaction Within the NASA Rotor 67 Transonic Stage,” *J. of Turbomach.*, vol. 134, no. 5, 2012.

[77] E. J. Gunn and C. A. Hall, “Aerodynamics of Boundary Layer Ingesting Fans,” in *ASME Turbo Expo 2014*, Düsseldorf, Germany, 2014.

[78] E. J. Gunn and C. A. Hall, “Non-Axisymmetric Stator Design For Boundary Layer Ingesting Fans,” in *ASME Turbo Expo 2017*, Charlotte, NC, USA, 2017.

[79] D. K. Hall, E. M. Greitzer and C. S. Tan, “Analysis of fan stage conceptual design attributes for boundary layer ingestion,” *J. of Turbomach.*, vol. 139, no. 7, 2017.

[80] A. Provenza, K. Duffy and M. Bakhle, “Aeromechanical Response of a Distortion-Tolerant Boundary Layer Ingesting Fan,” *Journal of Engineering for Gas Turbines and Power*, vol. 141, no. 2, 2019.

[81] M. Bakhle, T. Reddy and R. Coroneos, “Forced Response Analysis of a Fan with Boundary Layer Inlet Distortion,” in *AIAA/ASME/SAE/ASEE Joint Propulsion Conference*, 2014.

[82] J. B. Min, T. S. Reddy, M. A. Bakhle, R. M. Coroneos, G. L. Stefko, A. J. Provenza and K. P. Duffy, “Cyclic Symmetry Finite Element Forced Response Analysis of a Distortion-Tolerant Fan with Boundary Layer Ingestion,” in *AIAA SciTech Forum - 2018 AIAA Aerospace Sciences Meeting* , Kissimmee, Florida , 2018.

[83] S. R. Manwaring, D. C. Rabe, C. B. Lorence and A. R. Wadia, “Inlet Distortion Generated Forced Response of a Low-Aspect-Ratio Transonic Fan,” *J. of Turbomach.*, vol. 119, pp. 665-676, 1997.

[84] J. G. Marshall, J. Denton, L. Xu and J. W. Chew, “PREDICTION OF LOW ENGINE ORDER INLET DISTORTION DRIVEN RESONANCE IN A LOW ASPECT RATIO FAN,” in *Proceedings of ASME Turbo Expo 2000: International Gas Turbine & Aeroengine Congress & Exhibition*, Munich, Germany, 2000.

[85] A. Kammerer and R. S. Abhari, “Experimental Study on Impeller Blade Vibration During Resonance - Part 2: Blade Damping,” in *Proceedings of Asme Turbo Expo 2008*, Berlin, Germany, 2008.

[86] A. Kammerer and R. S. Abbhari, “Experimental Study on Impeller Blade Vibration During Resonance - Part I: Blade Vibration During Resonance Due to Inlet Flow Distortion,” *Journal of Engineering for Gas Turbines and Power*, vol. 131, pp. 1-11, 2009.

[87] A. Kammerer and R. S. Abhari, “Blade Forcing Function and Aerodynemic Work Measurements in a High Speed Centrifugal Compressor With Inlet Distortion,” *Journal of Engineering for Gas Turbines and Power*, vol. 132, pp. 1-11, 2010.

[88] V. Iyengar and H. Simmons, “Effects of Stator Flow Distortion on Rotating Blade Endurance: Part 1—Aerodynamic Excitation Aspects,” in *ASME Turbo Expo 2012: Turbine Technical Conference and Exposition*, Copenhagen, Denmark, 2012.

[89] H. Simmons, V. Iyengar and T. C. Allison, “EFFECTS OF STATOR FLOW DISTORTION ON ROTATING BLADE ENDURANCE PART 2 – STRESS ANALYSIS AND FAILURE CRITERIA,” in *Proceedings of ASME Turbo Expo 2012*, Copenhagen, Denmark, 2012.

[90] M. Oettinger, M. Henke and J. R. Seume, "EFFECT OF DIFFUSER INHOMOGENEITY ON FULL-ANNULUS AXIAL TURBINE PERFORMANCE," in *Proceedings of Global Power and Propulsion Society*, 2020.

[91] S. Biagiotti, J. Bellucci, M. Marconcini, A. Arnone, G. Baldi, M. Ignesti, V. Michelassi and L. Tapinassi, "IMPACT OF TURBINE CENTER FRAME WAKES ON DOWNSTREAM ROWS IN HEAVY DUTY LOW PRESSURE TURBINE," in *Proceedings of ASME Turbo Expo 2019*, Phoenix, Arizona, USA, 2019.

[92] W. Y. Lee, W. N. Dawes and J. D. Coull, "The Impact of Manufacturing Variability on Multi-Passage High Pressure Turbine Aerodynamics," in *AIAA SciTech Forum*, San Diego, California, 2019.

[93] F. Boulbin, N. Penneron, J. Kermarec and M. Pluviose, "Turbine blade forces due to partial admission," *Revue Francaise de Mecanique*, vol. 3, pp. 203-208, 1992.

[94] R. Pigott, "Turbine Blade Vibrations Due to Partial Admission," *Int. J. Mech. Sci*, vol. 22, pp. 247-264, 1980.

[95] J. Fridh, B. Laumert and T. Fransson, "Forced Response in Axial Turbines Under the Influence of Partial Admission," in *Proceedings of the ASME Turbo Expo 2012*, Copenhagen, 2012.

[96] N. B. Hushmandi, J. E. Fridh and T. H. Fransson, "UNSTEADY FORCES OF ROTOR BLADES IN FULL AND PARTIAL ADMISSION TURBINES," in *Proceedings of ASME Turbo Expo 2010: Power for Land, Sea and Air*, Glasgow, UK, 2010.

[97] J. L. Kerrebrock and A. A. Mikolajczak, "Intra-stator transport of rotor wakes and its effect on compressor performance," *Journal of Engineering for Power*, vol. 92, no. 4, pp. 359-368, 1970.

[98] M. Munk and R. C. Prim, "On the multiplicity of steady gas flows having the same streamwise pattern," *Proceedings of the National Academy of Science*, vol. 33, pp. 137-141, 1947.

[99] E. Ioannou, "The effects of temperature distortion on aerodynamics and low engine order forced response in axial turbines," PhD Thesis - City University London, London, 2015.

[100] J. R. Schwab, R. G. Stabe and W. J. Whitney, "Analytical and experimental study of flow through an axial turbine stage with a nonuniform inlet radial temperature profile," *AIAA Journal*, 1983.

[101] T. L. Butler, O. P. Sharma, H. D. Joslyn and R. P. Dring, "Redistribution of an inlet temperature distortion in an axial flow turbine stage," *Journal of Propulsion and Power*, vol. 5, no. 1, pp. 64-71, 1989.

[102] T. Povey and I. Qureshi, "Developments in hot-streak simulators for turbine testig," *J. of Turbomach.*, vol. 131, no. 3, p. 031009–15, 2009.

[103] P. Gaetani and G. Persico, "HOT STREAK EVOLUTION IN AN AXIAL HP TURBINE STAGE," in *Proceedings of 12th European Conference on Turbomachinery Fluid dynamics & Thermodynamics*, Stockholm, Sweden, 2017.

[104] P. Gaetani, P. G., L. Pinelli, M. Marconcini and R. Pacciani, "Computational and Experimental Study of Hot Streak Transport Within the First Stage of a Gas Turbine," in *Proceedings of ASME Turbo Expo 2019*, Phoenix, AZ, 2019.

[105] D. Prasad and G. J. Hendricks, "A numerical study of secondary flow in axial turbines with application to radial transport of hot streaks," *J. of Turbomach.*, vol. 122, 2000.

[106] P. Jenny, C. Lenherr, A. Kalfas and R. Abhari, "EFFECT OF HOT STREAK MIGRATION ON UNSTEADY BLADE ROW INTERACTION IN AXIAL TURBINE," in *Proceedings of ASME Turbo Expo 2010: Power for Land, Sea and Air* , Glasgow, UK, 2010.

[107] F. Simone, F. Montomoli, F. Martelli, K. S. Chana, I. Qureshi and T. Povey., "Analysis on the effect of a nonuniform inlet profile on heat transfer and fluid flow in turbine stages," *J. of Turbomach.,* vol. 134, no. 1, p. 011012–14, 2012.

[108] D. J. Dorney, K. L. G. Burlet and D. L. Sondak, "A survey of hot streak experiments and simulations," *International Journal of Turbo and Jet Engines,* vol. 16, p. 1–15, 1999.

[109] S. Manwaring and K. L. Kirkeng, " Forced response vibrations of a low pressure turbine due to circumferential temperature distortions," in *Proceedings of the 8th International Symposium on Unsteady Aerodynamics and Aeroelasticity of Turbomachines*, Stockholm, 1997.

[110] C. Breard, J. Green and M. Imregun, "Low-engine-order excitation mechanisms in axial-flow turbomachinery," *Journal of Propulsion and Power,* vol. 19, pp. 704-712, 2003.

[111] M. A. Mayorca, R. Bladh and U. Ozturk, "Estimation of burner can-induced excitation levels in an industrial gas turbine," in *ASME Turbo Expo 2013: Turbine Technical Conference and Exposition,* 2013.

[112] H. P. Pirker, H. Jericha and G. Zhuber-Okrog, "Auslegung und Betriebsverhalten einer Verdichteranlage für die Luftversorgung wissenschaftlicher Versuchseinrichtungen," *VDI Berichte, vol. 1208,* pp. pp. 331-347.

[113] M. Moser, G. Kahl, G. Kulhanek and F. Heitmeir, "Construction of a Subsonic Test Turbine Facility for Experimental Investigations of Sound Generation and Propagation for Low Pressure Turbines," in *ISABE Conference 2007*, Beijing, 2007.

[114] T. Selic, F. Schönleitner and A. Marn, "Measurement Report HiSpeeT," Institute of Thermal Turbomachinery and Machine Dynamics, Graz University of Technology, Graz, 2015.

[115] T. Arnold, "Kalibrierbericht 5-Loch Sonde," 2008.

[116] T. Selic, "Experimental Investigation of the Aerodynamic and Acoustic of Exit Guide Vanes for Future Aircraft Engines," PhD Thesis - TU Graz, Graz, 2016.

[117] G. Presico, P. Gaetani and A. Guardone, "Design and analysis of new concept fast response pressure probes," *Measurement Science and Technology,* vol. 16, pp. 1741-1750, 2005.

[118] D. Lengani, B. Paradiso and A. Marn, "Method for the Determination of Turbulence Intensity by Means of a Fast Response Pressure Probe and its Application in a LP Turbine," *Journal of Thermal Science,* vol. 21, 2012.

[119] S. Zerobin, S. Bauinger, A. Marn, A. Peters, F. Heitmeir and E. Göttlich, "The Unsteady Flow Field of a Purged High Pressure Turbine Based on Mode Detection," in *Proceedings of ASME Turbo Expo 2017,* Charlotte, NC, USA, 2017.

[120] K. Hoffmann, An Introduction to Stress Analysis and Transducer Design using Strain Gauges, HBM.

[121] F. Schönleitner, L. Traussnig, A. Marn and F. Heitmeir, "Modal Characterisation, Strain Gauge Setup and 1-Way FSI of a Low Pressure TUrbine Rotor Blading," in *Proceedings of the ASME Turbo Expo 2015,* Montreal, 2015.

[122] M. Bär, "Bedienungsanleitung Telemetriesysteme," Manner Sensortelemetrie, 2014.

[123] F. Schönleitner, T. Selic, L. Traussing, F. Heitmeir and A. Marns, "Experimental Blade Vibration Mesurements on Rotating Turbomachinery," in *20th Blade Mechanics Seminar*, Winterthur, Switzerland, 2015.

[124] J. Szwedowicz, S. M. Senn and R. S. Abhari, "Optimum strain Gage Application for Bladed Assemblies," *J. of Turbomach.*, vol. 124, pp. 606-613, 2002.

[125] M. D. Sensmeier and K. L. Nichol, "Minimizing Vibratory Strain Measurement Error," in *Proceedings of the 1998 International Gas Turbine & Aeroengine Congress and Exibition*, Stocholm, 1998.

[126] M. D. Sesmeier and K. L. Nichol, "Optimum Placement of Sensors for Vibration Measurements on Turbine Engine Blades," in *American Institute of Aeronautics and Astronautics AIAA*, 1998, 1998.

[127] M. T. Schobeiri and J. John, "A Study of the Developement of Steady and Periodic Unsteady Turbulent Wakes Through Curved Channel at Positive, Zero and Negative Streamwise Pressure Gradients," Texas A&M University, College Station, Texas, 1996.

[128] E. Ioannou and A. Sayma, "Full anulus numerical study of hot streaks propagation in a hydrogen-rich synges fired heavy duty axial turbine," *J. Power and Energy,* vol. 231, no. 5, pp. 344-356, 2017.

[129] L. Simonassi, M. Zenz, S. Zerobin, T. Selic, F. Heitmeir and A. Marn, "On the Influence of an Acoustically Optimized Turbine Exit Casing onto the Unsteady Flow Field Downstream of a Low Pressure Turbine Rotor," in *Proceedings of ASME Turbo Expo 2018*, Oslo, 2018.

LIST OF FIGURES

LIST OF TABLES